ABSTRACT

FUSCO, MICHAEL. Multilayer Protective Coatings for High-Level Nuclear Waste Storage Containers. (Under the direction of Dr. Mohamed A. Bourham and Dr. John G. Gilligan).

Corrosion-based failures of high-level nuclear waste (HLW) storage containers are potentially hazardous due to a possible release of radionuclides through cracks in the canister due to corrosion, especially for above-ground storage (i.e. dry casks). Protective coatings have been proposed to combat these premature failures, which include stress-corrosion cracking and hydrogen-diffusion cracking, among others. The coatings are to be deposited in multiple thin layers as thin films on the outer surface of the stainless steel waste basket canister. Coating materials include: TiN, ZrO_2, TiO_2, Al_2O_3, and MoS_2, which together may provide increased resistances to corrosion and mechanical wear, as well as act as a barrier to hydrogen diffusion.

The focus of this research is on the corrosion resistance and characterization of single layer coatings to determine the possible benefit from the use of the proposed coating materials. Experimental methods involve electrochemical polarization, both DC and AC techniques, and corrosion in circulating salt brines of varying pH. DC polarization allows for estimation of corrosion rates, passivation behavior, and a qualitative survey of localized corrosion, whereas AC electrochemistry has the benefit of revealing information about kinetics and interfacial reactions that is not obtainable using DC techniques. Circulation in salt brines for nearly 150 days revealed sustained adhesion of the coatings and minimal weight change of the steel samples.

One-inch diameter steel coupons composed of stainless steel types 304 and 316 and A36 low alloy carbon steel were coated with single layers using magnetron sputtering with compound targets in an inert argon atmosphere. This resulted in very thin films for the metal-oxides based on low sputter rates. DC polarization showed that corrosion rates were very similar between bare and coated stainless steel samples, whereas a statistically significant decrease in uniform corrosion was measured on coated, as opposed to bare, mild steel. Passivation and passive breakdown was largely unaffected by the coating materials. Activation parameters were determined for corrosion rates and passive breakdown potential based on

measurements performed between 20°C and 80°C to simulate elevated waste canister temperatures due to decay heat.

Electrochemical impedance spectroscopy (EIS) was used to study the metal-electrolyte interface and the passive film formed on types 304 and 316 stainless steel. Capacitance values were calculated by utilizing the constant phase element and a conversion technique proposed in the literature. This method was shown to remove the frequency dependence of the capacitance that is often seen in electrochemical analysis. The dielectric constant was estimated from impedance and potentiostatic current measurements, and film defect densities were calculated to be on the order of 10^{20} cm^{-3}, which is consistent with highly-doped semiconductive films.

EIS was also employed to study reactively-sputtered TiO_2 films on stainless steel type 304, which was substantially thicker than initial TiO_2 coatings. The impedance spectra of TiO_2-coated stainless steel exhibited several distinctions from its uncoated counterpart and were clearly dominated by the dielectric coating material. Film defect density was on the order of 10^{17} cm^{-3}, which is several orders of magnitude lower than the bare steel and is more consistent with solid-state semiconductors.

This research shows the potential of these coating materials to alter the corrosion behavior of the outer surface of a HLW storage canister. Although the initial single layered coatings had little effect on the corrosion and passivity of the stainless steel substrates, it is possible that with a thicker multi-layered coating system the substrate may be sufficiently isolated from the environment. Moreover, the thin single layer coatings were able to reduce corrosion of A36 steel, showing the promise of these coating materials in reducing uniform corrosion. Further optimization of deposition parameters and testing of multilayer coatings is necessary for serious consideration of these coatings in the future.

Multilayer Protective Coatings for High-Level Nuclear Waste Storage Containers

by
Michael Fusco

A dissertation submitted to the Graduate Faculty of
North Carolina State University
in partial fulfillment of the
requirements for the degree of
Doctor of Philosophy

Nuclear Engineering

Raleigh, North Carolina

2016

APPROVED BY:

Dr. Mohamed A. Bourham Co-chair of Advisory Committee	Dr. John G. Gilligan Co-chair of Advisory Committee
Dr. Korukonda. L. Murty	Dr. Alexei V. Saveliev

DEDICATION

To my family and to Emma for their unwavering support, encouragement, and patience.

BIOGRAPHY

Michael Fusco was born on May 19, 1991 in Livingston, NJ. He grew up in Rockaway Township in northern New Jersey before moving to Waxhaw, NC in 2005. He attended Weddington High School in Matthews, NC, graduating in June of 2009.

Michael attended North Carolina State University, where he earned his Bachelor's degree in Nuclear Engineering in 2013. He then earned his Master's of Nuclear Engineering one year later under the direction of Dr. Mohamed Bourham as a part of the Accelerated Bachelor's/Master's (ABM) program studying pellet acceleration using electrothermal plasma launchers. He has spent the last few years performing electrochemical corrosion testing on protective coatings for high-level waste storage containers. Michael would like to continue to research the corrosion behavior of coatings and new alloys, specifically in the context of nuclear reactors and nuclear waste storage. However, despite his new research focus, he will forever be fascinated by the realm of plasma physics and the ever-lingering possibility of sustainable fusion energy.

ACKNOWLEDGMENTS

I would like to first thank my advisor and mentor, Dr. Mohamed Bourham. His guidance and support has brought me to this point in my career. He afforded me the ability to work independently and carve my own research path, for which I am forever grateful. Dr. Bourham always found time to read my papers and answer my emails amidst his unbelievably busy schedule, and he is largely responsible for getting me through my graduate studies in a timely manner. For that and his devotion to his students, I sincerely thank him. One day I hope to follow his example and become a professor myself.

I would also like to thank my committee members Dr. John Gilligan, Dr. K.L. Murty, and Dr. Alexei Saveliev. Their comments on and support of my research have been invaluable, and their willingness to meet on short notice has helped streamline this process.

I would like to thank the Department of Energy (DoE) Nuclear Energy University Program (NEUP) for providing financial support for this project under contract DE-NE0000736 Project NEUP 13-5427.

Significant recognition must be given to Dr. Leigh Winfrey and her group, both at Virginia Tech and the University of Florida. Dr. Winfrey served as the P.I. and kept the project moving amidst significant adversity, and she coordinated our research efforts very effectively. Her graduate students Abigail Casey and John Echols deserve my full appreciation for the paramount role they played in the success of this project. They consistently provided me with samples to test coupled with excellent characterization of those samples. Their efforts made my life easier, and I thank them for that. Dr. Winfrey's undergraduates also earn my appreciation for their part in the project, including among others, Caroline Campbell, Alexis Tuason, Jordan Schweigert, and Sean Kerrigan.

A group of people from NC State are also due proper gratitude for their assistance throughout this process. First and foremost, Yasar Ay for single-handedly building and managing the circulators and performing the accompanying measurements, which was an immense help for this project. Four undergraduate students also contributed to this work in varying capacities that included solution mixing, sample preparation, data organization, and optical imaging. They are Jasmin Alsaied, Alexander Pharr, Richard Skowron, and Kathryn Bailey, and I thank them for the time and effort they invested in this work.

I am eternally grateful for the fellowships that have supported me throughout my graduate studies. I extend my thanks to the NC State College of Engineering for granting me the Dean's Doctoral Fellowship to help me through my first year of graduate school. Likewise, I am beholden to the NRC for providing funding for the GFINE to support my next two years of school. These fellowships have allowed me to focus my time and effort on my research, which has been unbelievable helpful.

Finally, I would like to express my sincerest gratitude to the NC State Department of Nuclear Engineering. The department has supported me unconditionally through three degrees and has fulfilled my every request along the way. I have seen the department grow and advance over the years, and I am grateful for the opportunities it has given me. I cannot express how much this department has meant to me over the years. It will no doubt be a bittersweet departure.

TABLE OF CONTENTS

LIST OF TABLES

LIST OF FIGURES

CHAPTER 1

INTRODUCTION

The push to increase the generating capacity of nuclear reactors to combat climate change over the next several decades will make storage of nuclear waste quite important. Radioactive waste is classified into four categories: high level waste (HLW), transuranic (TRU) waste, uranium mill tailings, and low level waste (LLW) [1]. Of primary interest is HLW, which comprises greater than 99% of the total radioactivity contained in nuclear waste in the United States [2]. HLW includes defense and weapons waste, as well as spent fuel from commercial nuclear reactors (in a once-through fuel cycle) [3]. Due to the potential health hazards of HLW, its storage requires the most stringent control and performance standards. HLW storage containers are required to provide complete containment of the radioactive waste for 1000 years, after which very slow release of radionuclides is permitted, in accordance with U.S. Nuclear Regulatory Commission (NRC) rule 10CFR60 [4], [5]. Hence, the selection of materials to house high level radioactive waste requires significant care and consideration.

Spent (or used) nuclear fuel (SNF) from commercial reactors constitutes upward of 93% of the total HLW radioactivity in the U.S. [2], and is growing consistently each year from power reactor operation. Spent fuel is stored on-site at the reactors producing it due to a lack of centralized waste storage. Yucca Mountain in Nevada was to be used as a centralized geological repository for permanent storage of HLW before the suspension of the project in 2010. Used nuclear reactor fuel is not reprocessed in the U.S. to reduce the radioactivity and volume of the waste, as a fuel recycling process has yet to be licensed by the NRC. The only current option for long-term fuel storage in the United States is above-ground dry cask storage.

The goal is to make the dry cask storage system as robust as possible to ensure complete containment of radioactivity during transport and disposal of nuclear waste.

Eventually, SNF will require permanent storage, though the storage method and type of environment has not been decided. The environments to which the nuclear waste packages could possibly be exposed include ground water, sea water, sea air, and salt deposits, just to name a few. Permanent storage options may or may not include use of the current dry cask designs, but they will require, at the very least, a primary container to prevent dissemination of radionuclides. This primary container (or canister) is the main focus of this research.

This dissertation is organized as follows: Chapter 1 provides an introduction to used nuclear fuel and current dry cask storage systems. The composition and radioactive concentrations of typical fuel removed from nuclear power reactors is discussed, along with examples of dry cask storage designs and their chosen materials. Chapter 2 discusses the properties of various steels, which are most often used for the primary waste storage container. It also presents and details failure mechanisms of interest for waste storage containers. Chapter 3 presents the concept of passivity of metals and details the formation and breakdown of the passive film for stainless steels according to the prevailing theory. In Chapter 4, the coating materials proposed to mitigate potential catastrophic failures of the steel canisters are described. This chapter also presents a brief review of available coating deposition methods and depicts the method chosen for this study. Chapter 5 explains the various experimental methods used throughout this research, particularly electrochemical corrosion methods. Chapters 6 and 7 provide results based on two different classes of electrochemical experiments: DC and AC corrosion techniques. Chapter 8 presents a study of TiO_2-coated stainless steel using AC electrochemistry, and Chapter 9 discusses some overarching conclusions and work to be pursued in the future. The remaining chapters are a compilation of published works detailing the radiation shielding properties of various materials for use in dry cask storage systems.

1.1 Nuclear Fuel

Fresh fuel for light water reactors (LWR) consists of cylindrical fuel rods filled with uranium dioxide (UO_2) pellets, which are arranged in arrays to form fuel assemblies. The uranium is enriched to between 3 and 5 atom percentage uranium-235, representing the necessary amount of fissile material to generate the desired energy output and power profile throughout the reactor core. Natural uranium consists of 0.72% ^{235}U with the remainder being ^{238}U and a trace amount of ^{234}U. Natural uranium may be used as fuel for heavy water moderated reactors due to the much lower thermal neutron absorption cross section of the isotope deuterium (^{2}H) compared to a hydrogen atom (^{1}H). However, light water moderated reactors, which constitute the vast majority of nuclear reactors around the world, require mined uranium to be enriched.

The fuel is kept in the reactor for three to four refueling cycles (between 1 and 2 years) for a total in-reactor time between 3 and 5 years on average. Following removal from the reactor the used fuel assembly is placed in a storage pool (Figure 1-1) where it is allowed to cool for upward of five years. The decay heat is substantially reduced after several years of pool storage, allowing the fuel assembly to be transferred to dry storage, where heat removal is accomplished by the fill gas in storage casks. The fuel is considered ‘spent’ at this point for a once-through fuel cycle, although it contains large quantities of actinides that could be reprocessed and reused to fuel light water and fast reactors. Table 1-1 gives the breakdown of long-lived isotopes present in spent fuel that contribute most to the total radioactivity. The fuel isotopic composition was calculated using the ORIGEN code package from Oak Ridge National Laboratory using operating conditions from the Surry Nuclear Power Plant with fuel burnup of 38.6 gigawatt-days per metric ton of uranium (GWd/MTU) after a 22 year decay [6]. Only isotopes that contribute activity greater than 1 Ci/MTU are included in Table 1-1.

Radioactivity from spent fuel bundles is almost entirely due to low and intermediate energy gamma rays, emitted during the decay of various radionuclides in Table 1-1. Alpha and beta

particles also contribute significantly to the activity of spent fuel, but they are much easier to shield and are not much cause for concern once the spent fuel is placed in storage containers. Neutrons are a small component of radiation emitted from spent fuel, and high density, low atomic number materials are added to spent fuel containment to provide neutron shielding and criticality safety.

Table 1-1: Long-lived radionuclide activity per MTU – 38.6 GWd/MTU Surry Plant – 22 yr. decay [6].

Nuclide	**Activity/MTU (Ci)**	**Nuclide**	**Activity/MTU (Ci)**
Cs-137	7.61E+04	Np-239	3.63E+01
Ba-137m	7.19E+04	Am-243	3.63E+01
Pu-241	5.34E+04	Cd-113m	1.55E+01
Y-90	4.97E+04	Tc-99	1.54E+01
Sr-90	4.97E+04	Cm-243	1.42E+01
Am-241	3.42E+03	Te-125m	9.09E+00
Pu-238	3.11E+03	Co-60	8.78E+00
Kr-85	2.43E+03	Am-242m	7.40E+00
Cm-244	2.20E+03	Am-242	7.37E+00
Eu-154	1.34E+03	Cm-242	6.09E+00
Pu-240	5.95E+02	Pu-242	2.96E+00
Pm-147	5.48E+02	Sn-121m	2.18E+00
Sm-151	3.79E+02	Eu-152	1.79E+00
Pu-239	3.33E+02	Sn-121	1.69E+00
H-3	2.48E+02	Ni-63	1.64E+00
Eu-155	1.32E+02	Zr-93	1.34E+00
Cs-134	1.20E+02	U-237	1.28E+00
Sb-125	3.72E+01	U-234	1.11E+00

Table 1-2: Photon activity by energy per MTU – 38.6 GWd/MTU Surry Plant [7].

Mean Photon Energy (MeV)	Activity/MTU (Photons/sec)	% Energy Activity
0.015	3.08E+09	0.00000
0.02	7.03E+09	0.00000
0.03	1.55E+14	0.31680
0.04	4.67E+13	0.12730
0.05	2.82E+12	0.00960
0.06	4.61E+13	0.18850
0.08	2.38E+12	0.01300
0.10	2.22E+13	0.15130
0.15	1.59E+10	0.00020
0.20	3.74E+12	0.05100
0.30	4.39E+11	0.00900
0.40	7.19E+11	0.01960
0.50	6.34E+11	0.02160
0.60	2.32E+15	94.8505
0.80	2.25E+13	1.22650
1.00	1.53E+13	1.04250
1.50	1.93E+13	1.97260
2.00	2.91E+06	0.00000
Total	**2.66E+15**	

Table 1-2 shows the breakdown by energy of the photon activity, in photons emitted per second, per metric ton of uranium for the radionuclide concentrations in Table 1-1 [6], [7]. The highest activity gamma group has a mean energy of 0.6 MeV, which is mainly attributable to the 661.7 keV photon emitted following the beta decay of ^{137}Cs to the metastable state of ^{137}Ba.

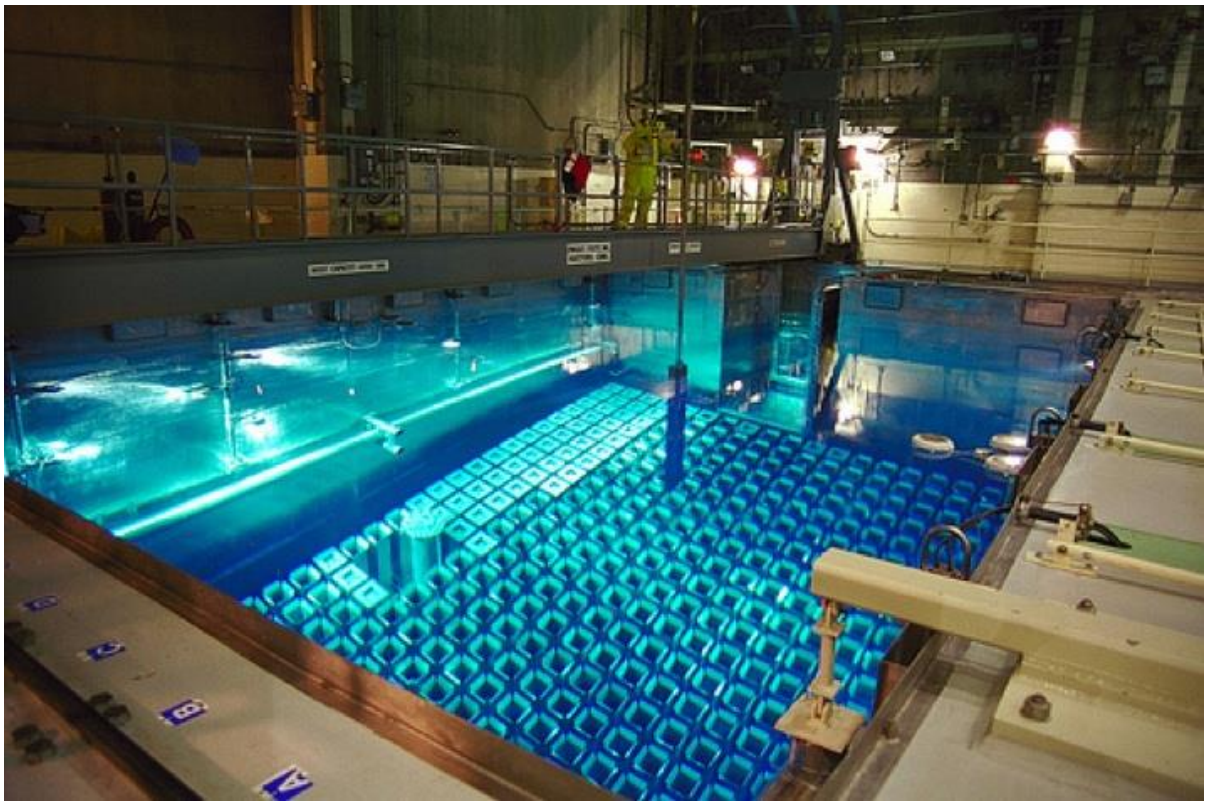

Figure 1-1: Example spent fuel storage pool. Available from: http://ansnuclearcafe.org/2014/06/10/spent-fuel-pool-fire-risk-goes-to-zero-a-few-months-after-reactor-shutdown/#sthash.K9eqGp4J.dpbs

1.2 Dry Cask Storage

As was mentioned at the start of this chapter, HLW must be fully contained for hundreds of years and at least partially contained for thousands more. The current method for "*permanent*" storage of spent nuclear fuel (SNF) and other types of HLW is to place the waste inside canisters encased in steel or concrete overpacks, termed dry casks. Spent fuel bundles are transferred to dry casks after at least 5 years of cooling in spent fuel pools. A simple illustration of a spent fuel bundle (assembly) and dry storage cask is shown in Figure 1-2. Storage casks contain spent fuel bundles within a cylindrical canister surrounded by several layers that may include shielding liner materials and a concrete overpack, which is several feet thick, or a thinner outer steel shell. The canister is filled with inert gas and sealed before being placed in the remainder of the cask. Two designs of dry storage casks, from Holtec International and AREVA Transnuclear, are provided in Figure 1-3 courtesy of a U.S. NRC presentation [8]. Both designs are dual storage and transportation casks and utilize a stainless steel waste basket canister, though they differ in their shielding. The HI-STORM 100 implements a thick concrete overpack for shielding and impact protection, whereas the TN-68 has a low alloy steel outer wall and a polypropylene layer for shielding. Typical dry casks can hold several dozen spent fuel assemblies: Figure 1-3 shows that the HI-STORM 100 generally holds 24 pressurized water reactor (PWR) bundles, and the TN-68 stores 68 boiling water reactor (BWR) bundles.

Once the casks are fully loaded and sealed, they are either placed vertically on very large concrete pads or horizontally in storage vaults, both above ground. Notice from Figure 1-3 that the casks are of substantial size. They may range from 14 – 20 ft. in length and from 8 – 12 ft. in diameter; casks holding BWR fuel are shorter and wider to reflect the size of the fuel bundles in comparison to PWR fuel. The word *permanent* was placed in quotes in the previous paragraph to emphasize that above-ground dry cask storage is not a permanent storage option, although currently it is the only option available. Eventually, the spent fuel will necessitate a

transfer to a permanent storage facility, whether it be in bore holes, in underground tunnels, or possibly in seawater. However, the container in which the fuel will ultimately be stored may bear similarities to the current dry casks.

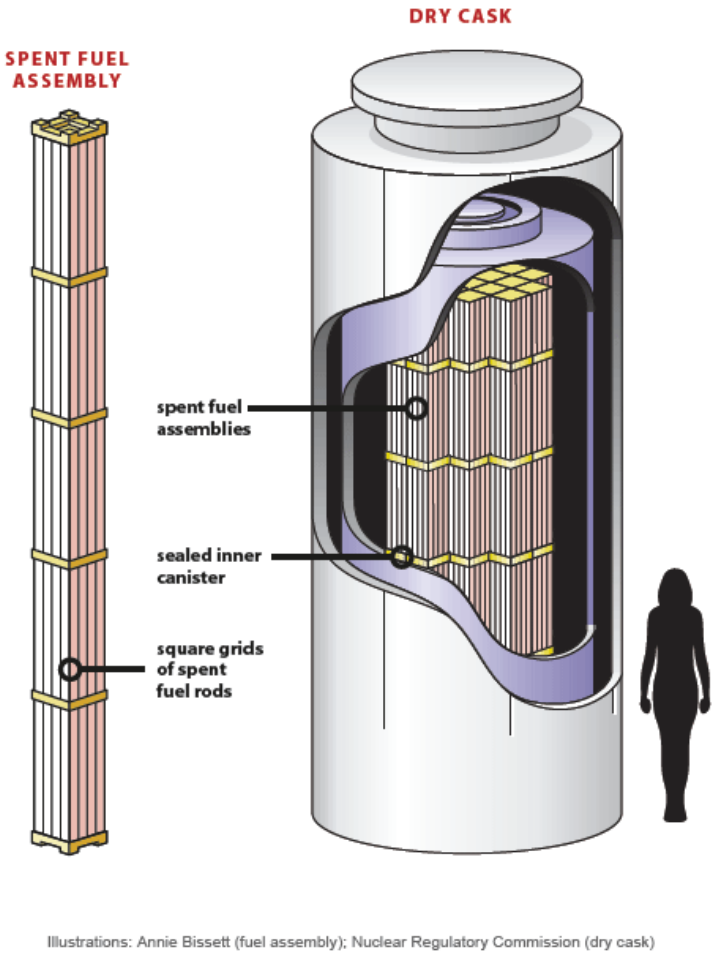

Figure 1-2: Illustration of a typical spent fuel assembly and simple dry cask for HLW storage with an outline of an average-sized human to show scale. Available from: http://www.ucsusa.org/publications/catalyst/su-13-the-growing-threat-of-nuclear-waste.html#.V356__krLRY

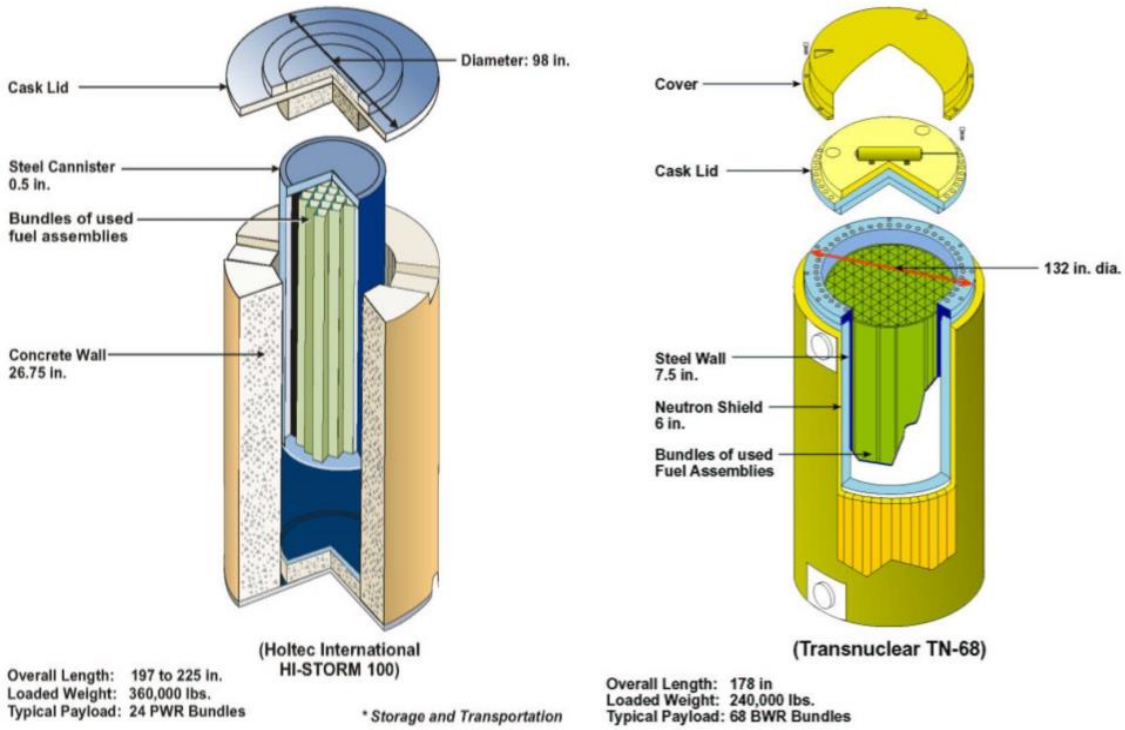

Figure 1-3: Two example dry storage cask designs – Holtec International HI-STORM 100 (left) for PWR fuel and Transnuclear TN-68 (right) for BWR fuel. Image taken from U.S. NRC presentation [8].

The first casks were loaded in 1986, and while there has been no radiation release as a result of dry storage to date, it is unknown how the casks will continue to age. A spent fuel storage cask was opened and inspected in 1999-2000 at Idaho National Laboratory (INL) after 14 years of service. The cask was a CASTOR-V/21 PWR storage container from Gesellschaft für Nuklear-Service (GNS) loaded with 21 spent fuel assemblies from Dominion's Surry Power Station. The cask consisted of a cast-iron body with a stainless steel fuel basket, and results showed no signs of safety-compromising degradation [9]. The fuel pellets and cladding from the fuel assemblies that were removed from the storage cask were also inspected and tested at Argonne National Laboratory. Findings showed that very little cladding damage had

occurred during storage [10]. While these findings are promising for the future of dry cask storage, 14 years is an insignificant period of time compared to the thousands of years required for radioactive waste storage.

According to a report by the Nuclear Energy Institute (NEI) there were 1,613 casks in operation as of June 2012, which together contained 19,000 MTU and 67,691 fuel assemblies [11]. The projections extend to nearly 3,000 casks by 2020 and over 5,000 by 2040. As the number of casks in operation increases, more permanent storage locations must be found, and routine inspection will become less practical. Hence, significant research is needed to ensure that the best options for dry storage are being implemented.

1.3 Dry Cask Materials

In order to assess the viability of dry cask storage as a long term waste storage option, the properties of the materials used must be thoroughly understood. These include the waste canister, concrete overpack (or steel shell), and intermediate shielding and structural layers, which include glass and lead among other materials. The most essential of these are the structural materials of the cask responsible for proper containment of the radioactive material, which are the waste package canister and overpack. These must remain intact for the foreseeable future to avoid any significant release of radiation.

Materials to be used for waste storage applications must be assessed based on a number of important properties: mechanical strength and toughness, fabricability and cost, resistance to uniform and localized corrosion, and resistance to possible failure mechanisms, namely stress corrosion cracking (SCC), hydrogen embrittlement, and radiation-enhanced degradation.

1.3.1 Overpack

The overpack is made of thick concrete, as can be seen in Figure 1-3. Concrete is one of the most widely used construction materials. It is inexpensive, easy to cast in many shapes and sizes, and has high enough strength to be used as a structural material. Concrete is commonly used in many nuclear applications, including as the containment building for nuclear reactors around the world. By using proper additives, concrete can easily be tailored to many different applications, including long-term radiation shielding.

The concrete overpack is an effective shielding and structural material, and is useful as an impact absorbing layer. Recently, many studies have been conducted on the use of additives to increase the density and attenuation properties of the overpack for gamma-ray shielding [12]–[14]. These studies show that the density and effective attenuation coefficient of the concrete may be increased significantly by utilizing various proportions of heavy metal additives, including lead and iron. This is particularly useful, as the storage casks may be made with thinner overpacks to decrease the cask footprint without sacrificing shielding capability. This is important for fuel transport casks as well. The use of specialty concrete for shielding of spent nuclear fuel is detailed in Chapters 10, 11, and 12.

1.3.2 Outer Steel Shell

Rather than a concrete overpack, some storage cask designs utilize a steel or cast iron shell that is significantly thinner than the concrete layer. These casks require additional shielding layers to compensate for the loss of the thick overpack, but they may be made smaller and lighter without the concrete. The outer shell is made of very high strength steel (usually carbon steel) or cast iron that is capable of being structurally sound for long term use. Unlike the overpack, long term oxidation and corrosion damage may be of concern for steel and cast iron dry casks.

1.3.3 Glass Shielding

There has been much interest recently in high density glass compositions with high effective atomic number for radiation shielding [15]–[18]. Glass is transparent to visible light and possesses high thermal stability. Ordinary glass is composed mainly of silicon dioxide (SiO_2). Similarly to concrete, additives may be included to create glass with desirable properties. When compounded with relatively simple compositions of heavy metal oxides (i.e. PbO), glass has the potential to be an extremely versatile shielding material. The effects of a thin glass layer on the shielding properties of dry storage casks is discussed in detail in Chapters 11 and 12.

1.3.4 Waste Package Canister

The waste package wall (or canister) is the first barrier to radionuclide release, apart from the fuel cladding, and as such, it is the focus of this research. Selection of proper canister material is paramount to safe containment of HLW. Many materials have been considered for the waste canister based on some desirable properties for the potentially harsh conditions of radiation exposure coupled with thermal output from the spent fuel. Additional considerations were given to possible environmental conditions for permanent HLW storage. Much of the work that was done in assessing HLW storage materials was completed assuming that Yucca Mountain would be the permanent storage location for HLW. Although the Yucca Mountain project has been suspended, the materials research still applies to other possible permanent storage locations.

These candidate materials for HLW canisters include: iron and iron alloys (steels), stainless steels, titanium alloys, and nickel alloys, among others [19]. Copper was briefly considered based on its natural abundance and apparent durability in the Yucca Mountain environment, but it is known to perform poorly in radiation fields [1]. Titanium alloys are strong and

corrosion-resistant but are unusually susceptible to hydrogen embrittlement and are difficult to machine and weld. Nickel alloys are often used as alternatives to titanium alloys because they possess similar properties and are easier to weld. However, they are often prohibitively expensive [1].

That leaves the various types of steel or cast iron. Steel is easily the most widely used structural alloy based on its low cost and high workability compared to other materials for similar applications. Carbon steel is extremely strong and sturdy, and being composed of mostly iron, it has been well characterized. It is not particularly corrosion resistant due to a lack of alloying elements, but it has a predictable service life as it is less susceptible to catastrophic failure in most circumstances. Stainless steel, on the other hand, is extremely corrosion resistant because of its high alloying content, but it is predisposed to failure due primarily to stress corrosion cracking. The lower strength of stainless steel compared to carbon steels or cast iron translates to an increase in ductility, reducing the possibility of brittle failure. Both carbon steel and stainless steel will be investigated as possible waste package materials for this study.

CHAPTER 2

PROPERTIES OF STEEL AND FAILURE MECHANISMS FOR HLW STORAGE CONTAINERS

The materials for HLW storage containers considered in this study are mild low-carbon steel and stainless steel. These materials are already in use in current dry cask storage systems. In order to enhance the protection and lifetime of these materials for nuclear waste storage applications, the relevant properties and downfalls of these steels must be established. Many dry cask designs utilize stainless steel as the canister material because of its good mechanical strength and corrosion resistance stemming from its ability to form passive surface films [1], [20], [21]. However, a ductile form of cast iron and carbon steel have also been considered and implemented for the canister and outer cask shell [22], [23]. Stainless steel offers the ability to use a very thin canister to contain the fuel bundles because the corrosion rate is so low. Whereas cast iron or carbon steel container walls must be made thicker to account for measurable corrosion, they are less likely to suffer from localized corrosion and stress corrosion cracking. This study focuses on the waste basket canister, and considers it to be the primary barrier to radionuclide release. The cladding is not considered as providing long term containment for the spent fuel pellets because it undergoes significant deformation and chemical modification inside the reactor. The long-term effects of intense pressure, heat, and radiation on the ability of the cladding to prevent leakage have not been determined, which is the reason that the focus is placed on the storage container. It should be noted that the cladding from the PWR cask opened at INL was still intact and showed few signs of wear after 14 years of storage [10]. However, 14 years is hardly indicative of the deterioration that will inevitably occur over

thousands of years. Moreover, the cladding is optimized for use in a LWR environment, rather than for long term storage. Instead, the primary waste basket may be designed especially to withstand degradation in a number of environments over an extended period of time, and hence the focus is placed on the waste package canister.

2.1 Steel Composition and Structure

Three steel compositions have been chosen for study to represent the canister material: stainless steel type 304 (SS304), stainless steel type 316 (SS316), and A36 low-alloy carbon steel. Each of these are commercially available steel alloys and are relatively inexpensive. Nominal compositions of each are given in Table 2-1, with the important differences between each alloy highlighted in red. SS304 is an austenitic, standard composition stainless steel, which can be considered as a solid solution of interstitials within a face-centered cubic (FCC) lattice [24], used in nearly all industries for myriad applications. SS316 is similar to SS304 with increased nickel content and the addition of molybdenum for additional protection against localized corrosion [25], [26]. The 300-series stainless steels represent variations of the standard and widely used 18-8 formula, which stands for 18% Cr and 8% Ni by weight.

A36, unlike the two previous steels, is a ferritic carbon steel and is the most commonly used mild steel. It possesses a body-centered cubic (BCC) iron (α-Fe) lattice with interstitial atoms (primarily carbon) [24] and minimal addition of alloying components. Stainless steels are better suited for many industrial applications, but carbon steel is still preferred in many cases for its superior strength, including as the primary material for LWR pressure vessels.

The primary crystal structure of the stainless and carbon steels is depicted in Figure 2-1. The microstructure of each steel has significant implications on the properties of interest for HLW storage. The atoms in a BCC material are not as tightly packed as in FCC crystal structure. A result of having a more loosely-packed structure is that the available slip planes in a BCC lattice do not correspond to close-packed planes [24]. Thus, slip is more difficult and

requires higher shear stress, making BCC materials harder and less malleable with lower ductility, introducing the possibility of brittle fracture. FCC materials are more tightly packed than BCC materials, leading to higher ductility at the expense of some strength. A FCC lattice has fewer possible slip systems, but the slip planes are more closely packed, requiring lower shear stress to deform. A consequence of easier deformation is that austenitic steels tend to be mostly immune to brittle cracking.

Table 2-1: Nominal compositions of steels utilized as canister materials for this study

Steel	SS316	SS304	A36
Element	%	%	%
C	**0.08**	**0.08**	**0.26**
N	0	0.1	0
S	0.03	0.03	0.05
P	0.045	0.045	0.04
Si	1	0.75	0.4
Ni	**10-14**	**8-12**	**0**
Cr	**16-18**	**18-20**	**0**
Mn	2	2	0.75
Mo	**2-3**	**0**	**0**
Cu	0	0	0.2
Fe	Bal.	Bal.	98.3

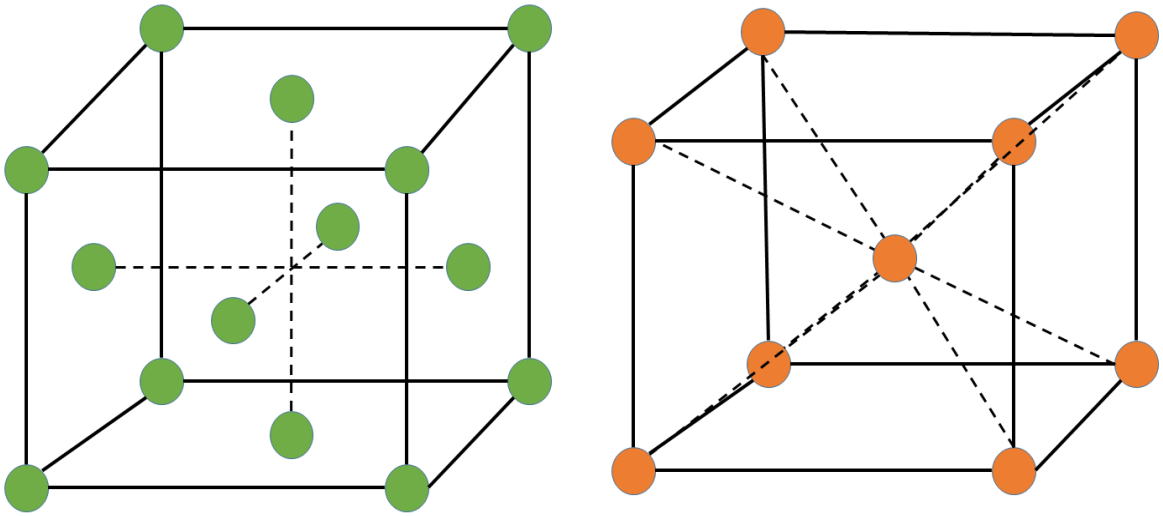

Figure 2-1: Crystal structure: face-centered cubic – austenitic steel (left); body-centered cubic – ferritic steel (right)

The crystal structure of the steels also plays an important role in hydrogen uptake and diffusion. Hydrogen, along with small atoms such as oxygen, nitrogen, and carbon, is able to occupy interstitial sites within the lattice structure. The FCC lattice has fewer interstitial sites available to be occupied than the BCC lattice, meaning fewer hydrogen atoms may be trapped in the interstitial lattice sites. Moreover, because the atoms are more tightly packed in an FCC lattice, the hydrogen has lower mobility, whether inhabiting an interstitial site or not. This provides austenitic steels with substantial immunity to hydrogen embrittlement and cracking, although interstitial impurities like nitrogen increase the likelihood of brittle intergranular cracking [27]. On the other hand, the increased number of interstitial sites and the increased mobility of hydrogen in a BCC lattice promotes trapping in ferritic steels, making them more susceptible to hydrogen cracking and embrittlement [28]. This point will be touched upon again further along in this chapter.

2.2 Alloying Components

Iron forms the matrix of all steels, providing them with their structural properties. It is strong, tough, ductile, and malleable, making it a versatile construction material. It is also inexpensive and compatible with a large variety of alloying elements. However, iron by itself has several flaws including its weight and propensity to corrode readily. This led to the creation of steel alloys, which contain additional elements to compensate for the shortcomings of pure iron. The most important alloying components are discussed here.

i. Chromium

Steel is considered to be "stainless" when it contains at least 12% chromium by weight. Chromium is primarily responsible for the good oxidation resistance of stainless steel. Its ability to combine with oxygen to form passive oxide films greatly increases resistance to corrosion. Increasing the amount of chromium alloyed with iron increases the chromium enrichment of the passive film barrier layer, acting to increase its stability. Also, Cr-Fe alloys have good mechanical properties and are easily fabricated [27]. Additional benefits of chromium include increased tensile strength, hardness, and toughness. The corrosion resistance afforded by adding chromium to steel is nullified if the carbon content is too high because of the tendency of chromium to form carbides. This will be discussed in more detail later in this chapter.

ii. Nickel

Nickel is the element mostly responsible for giving the 300-series stainless steels their austenitic FCC structure, which contributes to their strength and ductility. The nickel also contributes to the retention and stability of austenite upon quenching from high temperatures,

and it improves thermal stability and machinability [27]. Nickel is resistant to atmosphere, alkalis, and non-oxidizing acids. It is active enough to form oxide surface films, but the films are significantly less stable than chromium oxides. Finally, nickel is mostly resistant to chloride stress corrosion cracking and high temperature oxidation, which is the reason that steam generator tubes are often made from nickel alloys. Accordingly, nickel content above 8% in austenitic steel alloys increases resistance to stress corrosion cracking in chloride solutions [29]. This constitutes the nominal nickel content in the 18-8 (300 series) stainless steels.

iii. Molybdenum

Molybdenum is well known to increase resistance to localized corrosion (pitting, crevice, intergranular, etc.) when used as an alloying element, which is the reason it is included as a component in higher-grade steel alloys like SS316. The exact mechanism by which molybdenum acts to reduce susceptibility to localized corrosion is uncertain. The proposed theories involve either a strengthening of the passive film at the film/solution interface or a concentration of molybdenum at the metal/film interface that limits the metal dissolution rate [26], [30], [31]. There is experimental evidence for both theories, but more recently it is believed that molybdenum preferentially promotes the formation of Cr_2O_3 in the passive film, effectively increasing its stability [26], [31]. This also aids in re-passivation of areas of the film that have ruptured, such that pits may not be able to form or propagate after passive breakdown. It has been shown to block active sites, such as pits, to decrease or prevent further attack [32], [33]. A higher Mo content means better protection in chloride environments.

Another important role that molybdenum plays, particularly in steels, is that it readily forms stable compounds, namely carbides, which reduces the amount of carbon available to bond with chromium [24]. Thus, addition of molybdenum preserves the chromium content such that it is continually available to form and reform passive films. This increases resistance to

intergranular and crevice corrosion because chromium tends to be depleted in the vicinity of grain boundaries and surface defects, leading to local film breakdown and possibly cracking.

iv. Carbon

Carbon is added to iron to create cast iron, carbon steel, and other mild steels. It causes the tensile strength and hardness to increase at the expense of the inherent ductility and malleability of pure iron. The decrease in ductility and machinability as carbon content increases introduces an upper carbon limit based on the application. The carbon content in cast iron is greater than 2%, resulting in a very brittle material with high strength. Most structural applications opt for mild or low-carbon steels with less than 0.5% carbon by weight. These have increased strength from the presence of carbon without a complete loss of ductility and machinability.

The carbon content is generally minimized in austenitic stainless steels. A high carbon content is detrimental to corrosion resistance, as chromium tends to form carbides within the material. This results in decreased passivity and a higher likelihood for localized corrosion, specifically near grain boundaries or in and around crevices. The formation of some carbides is beneficial for hardening, though a majority of the desired increase in hardness and strength is achieved using other alloying components. Reducing carbon content comes at a substantial cost [27], so the adverse effects of having a small amount of carbon may be counteracted using other alloying elements (i.e. molybdenum).

v. Minor Alloying Elements

The remaining alloying elements are generally found in very small amounts in most steels. They include N, S, Si, Cu, Mn, and P, among a few others, and are included to enhance some of the properties provided by major alloying components. Some of these minor alloying

elements are essentially impurities, and removing them entirely is not feasible based on the cost associated with this. Many of these elements are beneficial in minute amounts but quickly become detriments above certain concentrations.

Among these, it is worth mentioning that nitrogen has been shown to increase localized corrosion resistance and to stabilize thermal and mechanical properties in stainless steels [27], [34]. Specifically, it increases pitting resistance in chloride media, making it a low-cost alternative to other alloying components [35]. Nitrogen also increases strength without reducing ductility and disrupts the formation of chromium carbides along grain boundaries. However, nitrogen is not added to low alloy steels (i.e. A36 mild steel) due to the inclination to form brittle nitrides [36].

2.3 Possible Failure Mechanisms

It is currently unknown how dry storage casks will age in the harsh environment of decay heat and radiation exposure. The nuclear industry has only 30 years of practical dry storage experience, and it is difficult to predict how the HLW storage landscape will change in the future. There are many options being investigated for more permanent storage options other than the above ground, on site dry storage. A majority of these options utilize some sort of storage container, which may be subjected to any number of environments. The current dry casks will also need to be moved to permanent storage at some point. That being said, the waste package canister must be able to withstand a number of different environments depending on the location of the ultimate disposal. The most likely environments are salt-containing, which include sea water, sea air, ground water, geologic brines, and dry salt deposits. This is a serious issue for stainless steels, as well as other candidate alloys, because halogen ions are particularly aggressive in causing corrosion-based cracking.

The key to improving canister integrity lies in the ability to understand and protect against catastrophic failure. Failure mechanisms that are relevant to HLW storage are mechanical failures that are initiated and/or enhanced by external factors, and they are difficult to predict. These include fatigue, creep, rupture, fracture, cracking, and embrittlement that are caused by corrosion, hydrogen permeation, and radiation exposure. Each of these failure mechanisms affects materials differently, and it is imperative to understand which mechanisms are most likely to cause failure for each material. This study focuses primarily on corrosion and corrosion-based failures, though other failure mechanisms are recognized and discussed.

2.3.1 Hydrogen Damage

The introduction of hydrogen into the lattice of a metallic element or alloy can have disastrous effects on the reliability of the material. Hydrogen atoms typically occupy interstitial sites in the lattice, making certain materials more vulnerable to hydrogen damage than others (see discussion in section 2.1). The process of hydrogen damage involves the ingress of hydrogen atoms into the material, typically via adsorbed hydrogen on the surface. The hydrogen will then inhabit interstitial lattice sites and possibly diffuse throughout the material. The atomic hydrogen may combine to form hydrogen gas or a different gas (methane, for example). These molecular gases are typically too large to diffuse through the metal and create an internal pressure, resulting in a decrease in strength and ductility and the possibility of cracking. Hydrogen cracking is especially problematic in ultra-high strength alloys.

Hydrogen can be introduced into the system either during manufacturing or during operation. Welding, casting, electroplating, and pickling are possible sources of hydrogen within the metal because of the higher solubility of hydrogen in liquids rather than solid states [33]. It is also often the product of electrolysis or corrosion reactions such as reduction of water molecules or oxidation. The diffusion of hydrogen into a metal usually results in a decrease in

ductility. Stresses below the original yield stress of the material are then able to cause cracking and possible brittle failure. Cracking and blistering can also occur in the absence of applied or residual stress if the swelling due to hydrogen recombination within the metal is severe.

Austenitic stainless steels are unlikely to suffer from hydrogen cracking because of a higher hydrogen solubility and lower diffusion based on crystal structure [27]. Ferritic-pearlitic carbon steels (A36) are more susceptible to hydrogen cracking than austenitic steel, but still significantly less so than martensitic steel. The low solubility and high hydrogen mobility through BCC structure [28] allows hydrogen to permeate into ferritic steels and become trapped. Many cases of severe hydrogen cracking in carbon steels have been misdiagnosed as stress corrosion cracking, as the visual signs of cracking are similar between the two mechanisms [37].

Heat treatment is an effective way to reduce hydrogen embrittlement, particularly following manufacturing of the metal. High temperatures allow the trapped hydrogen to diffuse out of the material and recombine. Additionally, higher temperatures promote hydrogen evolution, removing adsorbed species from the metal surface. Likewise, a suitable coating can inhibit the ingress of hydrogen [33], [38].

2.3.2 Environmentally Induced Cracking

Environmentally induced cracking (EIC) causes brittle fracture of a normally ductile material and includes three types of failure: hydrogen-assisted cracking, stress corrosion cracking (SCC), and corrosion fatigue cracking (CFC) [29], [33]. EIC occurs in the presence of an environment that causes minimal uniform corrosion for the alloy in question. Being ductile alloys with low uniform corrosion rates, austenitic stainless steels are vulnerable to EIC in a number of environments.

i. Stress Corrosion Cracking

The most widely acknowledged likely failure mechanism for stainless steel waste storage canisters is stress corrosion cracking (SCC). SCC occurs due to a combination of sufficient tensile stress and an aggressive environment and leads to the cracking of alloys well below their ultimate tensile strength (UTS) [29].

Cracking is initiated in several ways, the most likely of which are localized corrosion, hydrogen embrittlement, or film induced cleavage [37]. In the case of localized corrosion, and active dissolution path forms where corrosion is accelerated despite the bulk of the material being passive and corroding very slowly. Localized corrosion occurs due to the breakdown or inadequate formation of the passive film on the metal surface; the passive film will be discussed in detail in the subsequent chapter. Hydrogen embrittlement was discussed previously and can lead to cracking by increasing local plastic deformation and decreasing ductility. Finally, film-induced cleavage can occur from a crack initiated in a brittle coated film, which can propagate into the ductile metal beneath. The brittle film may be intentionally or unintentionally coated on the metal or unintentionally formed, such as de-alloyed surface layers. Regardless of the mechanism, once a crack initiates, the stress (either applied or residual) may act to open the crack, increasing corrosion and propagation of the crack tip and preventing the crack from re-passivating [37].

Stainless steels are susceptible to SCC in chloride-containing solutions. Chlorides are particularly aggressive at initiating localized corrosion, which will be explained in Chapter 3. The real threat of failure by stress corrosion cracking is that the residual stress from welding is enough to cause SCC in stainless steels. Dry storage canisters contain several welded regions based on their size and shape, making them likely targets for cracking to occur.

SCC is known to be an anodic process, which is expected based on the corrosion required to propagate the crack tip. Thus, SCC can be mostly prevented by cathodic protection, or providing an electrical path between the metal of interest and a sacrificial anode that is more

active than the protected metal [39]. This causes preferential corrosion of the more active metal, protecting the more important metal from accelerated corrosion of cracks that may form.

ii. Hydrogen-Assisted Cracking

Hydrogen dissolved in a metal lattice tends to be attracted to regions of high tensile stress where the metallic structure is distorted. This causes embrittlement of the metal in regions that already possess tensile stresses that are higher than in other regions. Brittle cracking becomes much easier at this point. Hydrogen cracking often dominates over SCC in high strength alloys such as low alloy and carbon steels, and some titanium and aluminum alloys [29], whereas it is unlikely for steels with yield strengths less than roughly 600 MPa [37].

Hydrogen induced cracking manifests itself in similar ways to SCC, and it is often difficult to decide if the failure was due to hydrogen cracking or SCC based on the crack morphology. What makes hydrogen-assisted cracking distinct from SCC is the growth mechanism of the crack. SCC is accelerated by anodic polarization, indicating that crack growth is primarily controlled by corrosion. In contrast, hydrogen cracking is enhanced by cathodic polarization or protection, indicating a non-corrosive crack growth mechanism [29], [37].

Cathodic corrosion generates hydrogen, which accounts for the acceleration of cracking. The reduction of oxygen given by Equation (2.1) is a cathodic reaction that produces hydroxide ions. These ions may dissociate producing hydrogen ions capable of diffusing into the metal lattice. This reaction occurs preferentially at the cathode surface and is enhanced by cathodic polarization, leading to the generation of additional hydrogen.

$$O_2 + 2H_2O + 4e^- \rightarrow 4OH^- \tag{2.1}$$

iii. Corrosion Fatigue Cracking

Corrosion fatigue cracking (CFC) may occur in a corrosive environment when a metal is subjected to cyclic stresses. The stress is often well below the tensile strength of the material. The number of cycles to failure decreases with increasing stress and in the presence of a corrosive environment. Some materials, particularly steels, possess an endurance limit, which is the minimum stress required for fatigue to set in. Below this limit, fatigue cracking is unlikely no matter how many stress cycles the material undergoes. A corrosive environment is capable of significantly decreasing or even eliminating the endurance limit of a material, which can lead to cracking at even lower stress levels [29], [39]. Cyclic stresses are not expected to be present in dry cask storage, thus it is unlikely that CFC will pose a threat to canister integrity.

2.3.3 Intergranular Corrosion

Intergranular corrosion (IGC) is the corrosion attack or preferential corrosion along the grain boundaries of a material. The grain boundaries can become susceptible to corrosion through the depletion of protective or passivating elements. IGC is a common problem in alloys but generally does not affect pure metals [29].

Austenitic stainless steels are a common example for situations that favor IGC. Stainless steels may be sensitized during heat treatment or cold working [27], predisposing them to intergranular attack. The sensitization of austenitic stainless steels consists of the precipitation of chromium-rich carbides ($Cr_{23}C_6$) at grain boundaries, which is depicted in Figure 2-2. This substantially depletes the elemental chromium content in areas immediately surrounding the grain boundaries, making passive film formation more difficult in these regions. Often the grain boundary regions are depleted to chromium contents well below the required 12% to maintain the corrosion resistance of stainless steel. With the grain boundaries lacking the

essential chromium content required to initiate passivity, localized corrosive attack is likely to take place [24], [29].

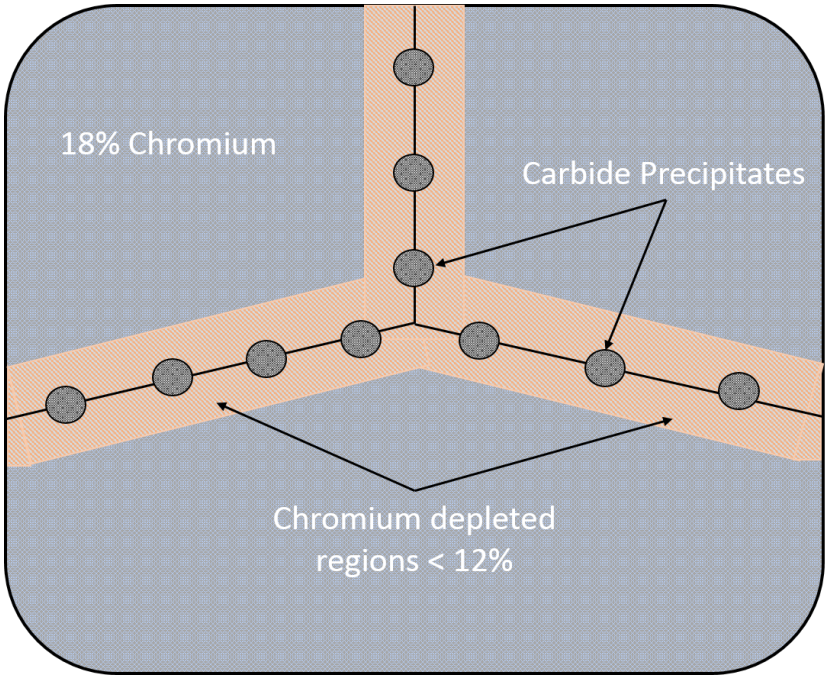

Figure 2-2: Chromium carbide precipitation at grain boundaries due to sensitization of austenitic stainless steel. Adapted from [24].

Sensitization of stainless steels may take place during welding, making IGC especially likely in the welded regions of dry storage containers. There are, however, several prevention methods. The steel may be rapidly cooled following heat treatment (i.e. welding) to prevent chromium carbides from forming and/or migrating and precipitating at grain boundaries. Also, special grades of stainless steel have reduced susceptibilities to IGC. One class has extremely low carbon content (SS304L and SS316L) to decrease carbide formation. The other class is stabilized with reactive elements that tend to form carbides in the place of chromium (SS316,

SS324, etc.). These elements include molybdenum, niobium, titanium, and several others, which are capable of reducing chromium depletion by aggressively forming carbides themselves [24]. Thus, of the two types of austenitic stainless steels discussed in this chapter, type 316 is expected to be more resistant to both pitting and intergranular corrosion based on the molybdenum addition, which is not present in type 304 stainless steel.

2.3.4 Crevice Corrosion

Corrosion is greater inside crevices, which are usually created by contact between two materials. This includes a metal in contact with another material, either metallic or nonmetallic, creating a region that is partially shielded from the external environment, often with a narrow opening (crevice). As an example, crevices are often formed by bolts or washers, though they may also be formed by some type of deposition on the metal surface [29].

Crevice corrosion occurs due to a difference in oxygen concentration inside and outside the crevice. Inside the crevice, there is an oxygen deficiency, which makes passivation very difficult and does not allow the cathodic reactions to consume corrosion products from the anodic reactions. Thus, the inner portion of the crevice becomes the anode of the corrosion system, greatly increasing the corrosion rate. The situation is exacerbated in the presence of aggressive anions. The corrosion products (cations) that build up in the crevice due to the lack of oxygen attract anions from the surrounding medium. If chloride ions are present, for example, highly acidic chloride solutions become concentrated in the crevice, and corrosion rates increase drastically. Crevice corrosion may also initiate from the retention of water or a corrosive solution inside a crevice after some type of immersion, which will again create deleterious concentration gradients [24], [29], [33]. Crevices are an easy target for localized corrosion, though they can be prevented with changes in geometry and proper contact between materials.

2.3.5 Radiation Damage

Ionizing radiation has a substantial effect on the properties of exposed materials. Materials inside reactors undergo significant microstructural changes due primarily to neutrons and fission fragments. Intense nuclear radiation is capable of causing vacancies, interstitials, impurities, depleted zones, voids, thermal spikes, etc., all of which can be considered radiation damage. Irradiation generally acts to harden and decrease ductility of materials. Detailed discussion of the different aspects of radiation effects is found in Ref. [24]. Gamma rays are also capable of inducing radiation damage, but not to nearly the same degree as neutrons and heavy particles.

An important manifestation of radiation effects on failure mechanisms of steel is irradiation-assisted stress corrosion cracking (IASCC). IASCC is the enhancement of SCC due to irradiation and is a major cause of failure in LWR components [27], [40]. The mechanism by which irradiation affects SCC is unknown, but one popular theory is radiation-induced segregation [24]. Prolonged irradiation of austenitic stainless steels in particular is known to result in chromium depletion along grain boundaries, increasing susceptibility to SCC. It has been shown that minor alloying components play a significant role in IASCC [40], owing to the complexity of the radiation damage mechanisms. The cracking is often intergranular, hence the focus on depletion along grain boundaries. Other theories include: radiation hardening leading to SCC, localized deformation, internal oxidation, and irradiation creep [24].

IASCC is mostly the cause of high neutron flux, which causes the largest changes in material microstructure. The radiation emitted from spent fuel is primarily gamma rays (Chapter 1) that do not cause nearly as much damage as neutrons and heavy particles. It is not expected that IASCC is of significant concern for HLW storage.

CHAPTER 3

THE PASSIVE FILM

The primary resistance to corrosion for many metals stems from the ability to form passive films. The passive film inhibits corrosion of an otherwise active substrate, even in aggressive environments. Metals are considered passive if they corrode very little despite a marked tendency to react in a given environment, or despite significant anodic polarization. Metals that are generally inert, such as gold and platinum, are not considered to be passive. As was mentioned in the previous chapter, a number of the corrosion-based failures of interest for dry cask storage canisters initiate as localized breakdowns in the passive film. This puts great importance on understanding the formation and breakdown of the passive film to better protect against premature failure.

3.1 Background

The concept of passivity was first observed for iron immersed in nitric acid (HNO_3) as early as the mid-1700s [41]. It was noted that iron corrodes readily in dilute nitric acid but does not react in concentrated nitric acid. However, the first recorded use of the term “passivity” to describe an induced lack of reactivity was not until the mid-1800s by the German chemist Christian Schönbein [27], [41].

Since its discovery, the passivity of naturally reactive metals has been studied extensively for a myriad different combinations of metal and environment. Theories about passivity and its origins have been proposed since the earliest observations of decreases in corrosion of otherwise active metals. Herbert H. Uhlig explains that the various theories may be arranged

into four categories: metal modification, reaction rate, oxide film, and adsorption [41]. These four categories of theories about the initiation of passivity will be described briefly here, but a detailed description of each may be found in the work of Uhlig [41].

i. Metal Modification

The metal modification theory stipulates that the passive state of a metal results from a physical change in the metal itself. This theory suggests that the passive state of a metal results from a physical change in the valence state of that metal. An extension of the valence theory advocates that allotropes of an element dictate active or passive states. Allotropes are structural modifications of an element. For example, diamond and graphite are allotropes of carbon that consist of carbon atoms bonded in different manners and possess distinct properties. Several research groups conceived that Fe^{3+} represented the passive allotrope of iron, whereas Fe^{2+} was its active counterpart [41]. The idea of metal modification and electronic structure changes leading to passivity was modified and expanded several times to match newer experimental results.

ii. Reaction Rate

This theory attributes passivity to slow rates of metal dissolution, which is not dependent on surface films. The dissolution rate was decided to depend on the rate of hydration of metal ions in the lattice, which is a necessary precursor to their solubility in water. This view was modified to allow hydrogen to be the primary determinant of the corrosion state. It was postulated that metals are in the passive state until hydrogen enters the metal lattice, causing them to become active. The hydrogen was said to catalyze the reaction by expanding the lattice, giving rise to the "hydrogen activation theory." This theory was the frontrunner at the 1913 international symposium on passivity [41].

iii. Oxide Film

The titular oxide film is allegedly formed via oxidation of the metal surface. It was hypothesized that the oxide film would be invisible due to its very low thickness and would be impervious to acids. This oxide film would shield the metal surface from the environment, such that it could not be attacked nor could it be dissolved due to anodic polarization. Essentially, the film would act as a diffusion barrier to limit the mobility of ions or atoms through the film. However, the protective properties of the supposed film could not be accounted for thermodynamically assuming any of the known oxides of the metal, namely iron. Additionally, ellipsometry measurements on 18-8 stainless steel have showed surface films only a few angstroms thick. These two points led researchers to believe the mechanism to be different from the oxidation theory [41].

iv. Adsorption

Rather than limited mobility through an oxide film, the adsorption theory attributes passivity to a chemisorbed (or physically adsorbed) surface layer that blocks further chemical reactions. The surface layer is considered to be adsorbed oxygen, often compounded with ions from the metal surface. This theory differs from the oxide film theory in the formation of the passive layer and the kinetic blocking, rather than diffusion barrier, nature of the film. It is supported by the fact that very thin films, sometimes one or two monolayers, lead to passivity. Also, the unfilled d electron shell of the transition metals (for which passivity primarily applies) favors a chemisorbed oxygen bond [41]. Finally, increasing anodic polarization favors additional oxygen to be incorporated into the film, causing film growth. This is indeed what is observed in that increasing the film formation potential will increase film thickness.

Adsorption proceeds according to Figure 3-1, in which oxygen ions adsorb (usually chemisorb) to the metal surface. This is followed by interaction with metal ions, forming a monolayer oxide film. Subsequently, additional oxygen may adsorb to the initial layer, and over time metal ions will make their way into the film, forming a stoichiometric oxide layer [27], [42]. Though the exact mechanism is yet unknown, the adsorption theory is generally favored as the initiation of passivity.

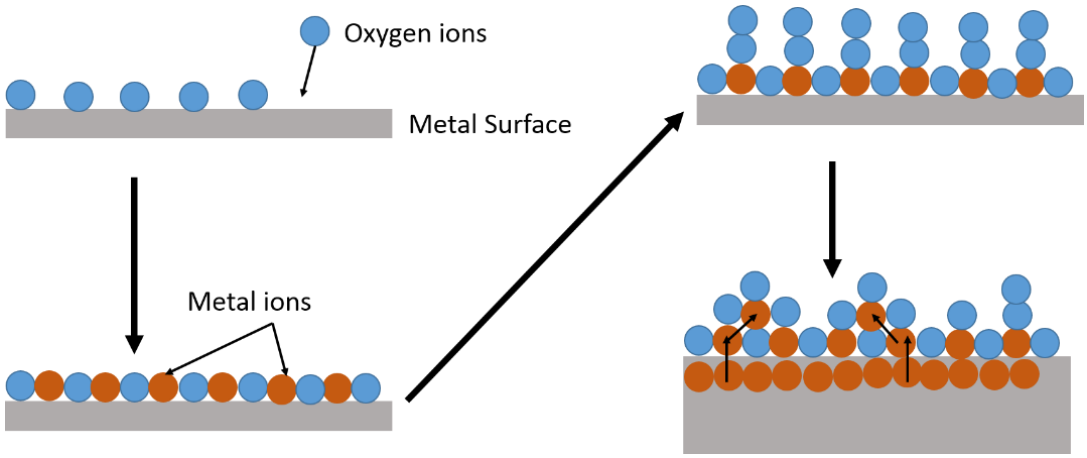

Figure 3-1: Adsorption theory of oxide passive layers on metal, adapted from [27], [42]

3.2 Passive Film Growth – Point Defect Model

Irrespective of the initiation mechanism, it is generally accepted that the passivity of most metals may be ascribed to the formation of an oxide film between the metal and the environment. Once passivity has been initiated, the growth mechanism of the passive film is of interest. Film growth kinetics have been shown experimentally to follow either a logarithmic law or an inverse logarithmic law, given by Equations and , respectively [43].

$$L = A_0 + A_1 \ln(t) \tag{3.1}$$

$$\frac{1}{L} = B_0 - B_1 \ln(t) \tag{3.2}$$

Where: L is the film thickness,

t is time,

And A_0, A_1, B_0, and B_1 are constants.

Several theories have been proposed to explain either or both of the film growth laws that are observed. Currently, the Point Defect Model (PDM) represents the most comprehensive prevailing theory on protective oxide or hydroxide films that form on metals under anodic polarization [43]–[47]. A review of previous passive film growth models is provided in the work of Chao et al. [43].

The Point Defect Model is based on several tenets [43], [46]:

- The passive film generally forms in one or two layers: an inner barrier layer and a porous outer layer
  - Passivity is linked to the barrier layer
- The passive film contains a high concentration of point defects, which are primarily cation and anion vacancies
- The defects are generated and consumed at the film/solution and metal/film interfaces
- Film formation and breakdown is controlled by vacancy transport,
- Passive layers are characterized by high electric field strengths on the order of 10^6 V/cm
- Passive films behave as highly-doped semiconductors
  - The "dopants" are vacancies
- Ion transport through the film occurs via vacancy motion
- Film growth and dissolution eventually balance to form a steady state film

The development of the model extends from the elementary reactions that result in vacancy generation and annihilation. These reactions occur at the metal/film and film/solution interfaces and may either contribute to the growth, dissolution, or conservation of the film. These reactions are summarized in Figure 3-2 specifically for a film stoichiometry of M_2O_3 (M=metal), as is the case for stainless steel, which shows the film growth and dissolution based on vacancy transport. Cation vacancies are generated at the film/solution interface and are consumed at the metal/film interface, denoted by reactions 3 and 1, respectively. The opposite applies for anion (oxygen) vacancies, which are generated at the metal/film interface and are consumed at the film/solution interface, given by reactions 2 and 4. Reactions 1, 3, and 4 represent the movement of ions across boundaries and thus are lattice-conserving reactions. Reaction 2 does not conserve the lattice because it results in film generation represented by $[M_M + (3/2)V_O]$. Reaction 5 is responsible for destruction, or dissolution, of the film and also is not lattice-conserving. Each of these reactions has an associated rate constant responsible for determining the net effect on the film. Under steady state conditions, the growth and dissolution rates will equal each other to form a film with a constant thickness [44]. Note that cation interstitials have been neglected in this formulation, though they will also contribute to the film lattice.

PDM analysis beginning with these elementary reactions results in kinetic equations to predict the evolution of the film thickness and charge exchange current with time, voltage, and solution pH based on fundamental properties. These properties include reaction rate constants, diffusivities, and electric field strength, among others. Detailed analyses will not be repeated here, as they are presented thoroughly in the work of Macdonald et al. [43]–[47].

The PDM has been applied successfully in matching experimental current response and film growth for a number of metals including iron, stainless steels, nickel and chromium alloys, tungsten, tantalum, and zirconium [43], [48], [49]. From first principles, it is capable of exactly

predicting the logarithmic growth of the passive film with time that is frequently observed in experiment, which is a primary reason for its popularity and frequent application.

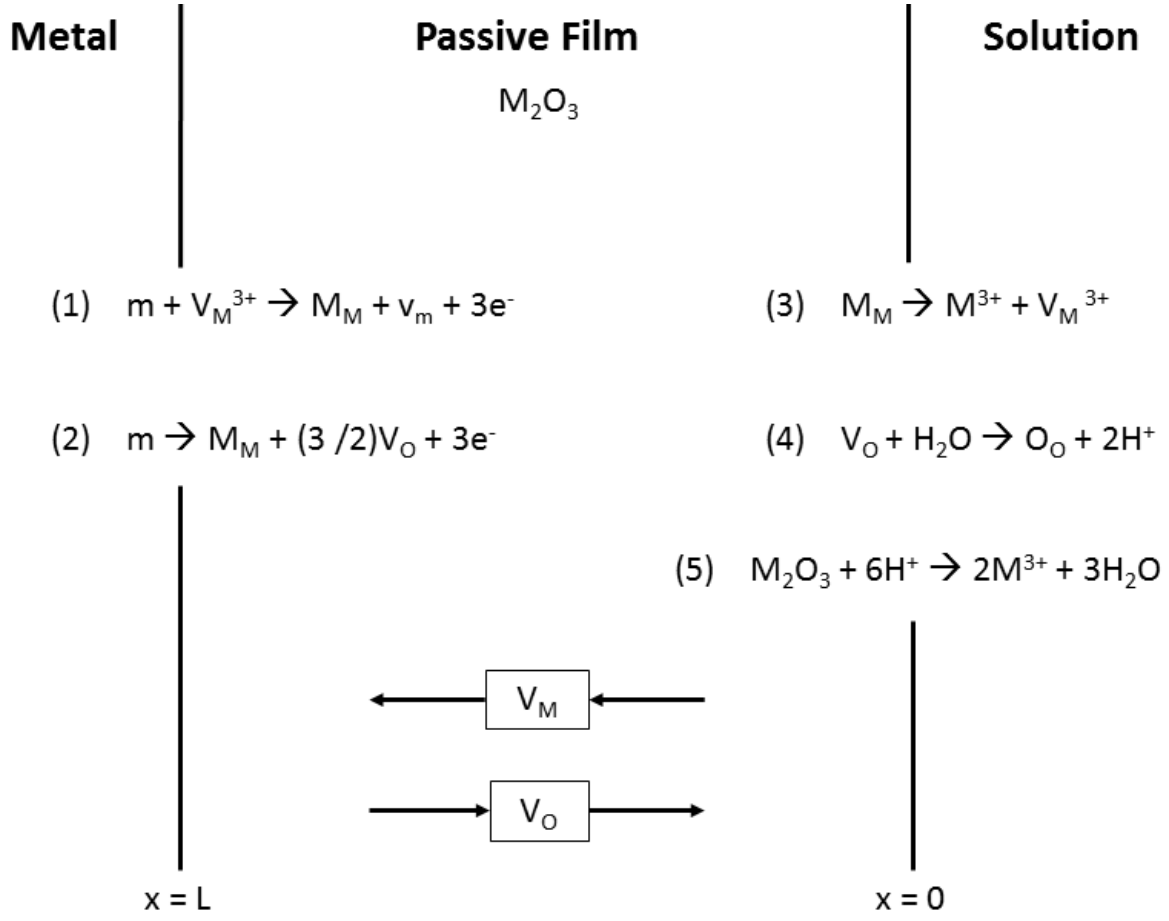

Figure 3-2: Elementary reactions responsible for growth and dissolution of the passive film according to the PDM, adapted from [44], [47]. M_M = metal cation in film lattice site, O_O = oxygen anion in film lattice site, m = metal atom, $VM^{(\chi/2)+}$ = cation vacancy, V_O = oxygen (anion) vacancy, and v_m = vacancy in metal substrate.

3.3 Passivity and Passive Breakdown of Stainless Steel

Though the motivation for this study is stainless steel, most of this discussion about passivity is general and applies to a wide variety of metals. The focus will be on stainless steel because it passivates much more readily in many environments than does mild and carbon steel. For 18-8 stainless steels, the principle thin film formed in oxidizing environments is a combination of chromium (III) oxide (Cr_2O_3) and iron (III) oxide (Fe_2O_3). Typically, it forms in two layers: an inner layer of primarily Cr_2O_3 and an outer layer of mostly Fe_2O_3, although a third hydroxide layer may also form in acidic solutions [30]. The formation of a bilayer film has been confirmed by several researchers using auger electron spectroscopy (AES) [50]–[53] and x-ray photoelectron spectroscopy (XPS) [30], [54], among other techniques. The passive film on stainless steel forms in both wet and dry media as long as a source of oxygen is present due to the pronounced oxygen affinity of chromium. This further supports the adsorption theory of the initiation of passivity [27].

As mentioned previously, the formation and breakdown of the passive film are considered to be driven by vacancy transport. Figure 3-2 stipulates that the cation (metal ion) vacancies are formed at the film/solution interface and are consumed at the metal/film interface; the opposite is true for oxygen vacancies. The film forms “into the metal” beginning with adsorbed oxygen ions on the metal surface, and proceeds by reactions 2 and 4 in Figure 3-2. Initially, reaction 2 proceeds at a faster rate than reaction 5. This continues until a steady state is reached at which point formation and dissolution of the film are in equilibrium. The film growth occurs due to anion (oxygen) vacancy transport from the metal/film interface, through the passive layer, to the film/solution interface, where the film may take on more oxygen. Film dissolution or destruction occurs via motion of cation (metal) vacancies in the opposite direction.

If the cation vacancies cannot be consumed quickly enough at the metal/film interface, they may coagulate creating the vacancy condensation seen in Figure 3-3. This may eventually lead to local film detachment or rupture, resulting in the breakdown of the passive film. The

important parameters in determining passive breakdown are vacancy concentrations and diffusion coefficients. Both larger concentrations of cation vacancies and higher diffusion rates increase the likelihood of local film breakdown. Under normal circumstances, the passive film will remain intact indefinitely. However, the previous chapter detailed the possible failures of stainless steel resulting from passive breakdown due to the presence of chloride ions. Mechanisms of chloride-enhanced passivity breakdown will be discussed.

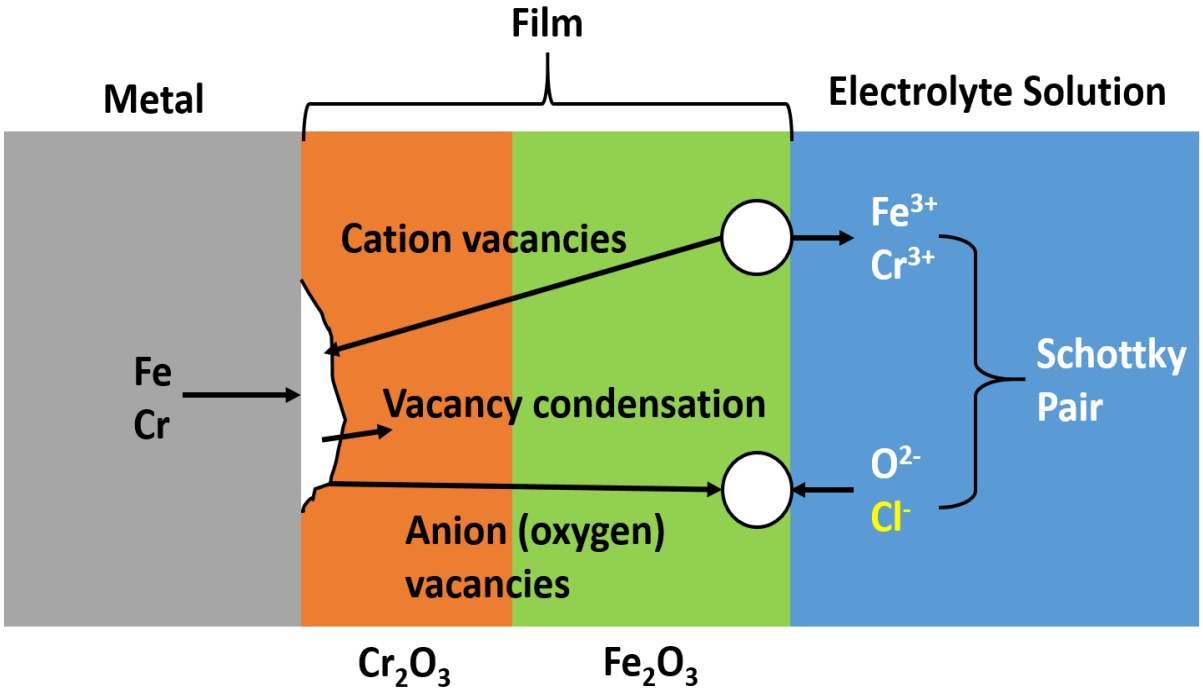

Figure 3-3: Film formation and breakdown mechanisms of stainless steel with a bilayer passive film. Adapted from the work of D. D. Macdonald [44].

3.3.1 Effect of Aggressive Anions

Aggressive anions are capable of competing with oxygen to occupy oxygen vacancy sites at the film surface. The problematic anions for many metals including stainless steel are halogen ions, of which the most aggressive is often the chloride ion. Absorption of anions other than oxygen into surface vacancies results in the generation of cation vacancies by two different mechanisms: Schottky pair reactions or cation extraction. For the first case, a pair of cation and oxygen vacancies are created from ejection of metal cations and anions from the film lattice in a Schottky-type reaction. In the second situation, the absorbed anion reacts with surface cations and desorbs into solution, also forming cation and anion vacancies. In each case the newly-vacant oxygen site is capable of interacting additional anions, effectively repeating the process. This makes the generation of cation vacancies autocatalytic, leading to an increased number of cation vacancies than would be formed if only oxygen were present, as well as an increase in the dissolution rate [29], [44], [55]. The effect can be so pronounced in high anion concentrations that the metal may not readily passivate due to the enhanced film dissolution [27].

Once the anion and cation vacancies have been formed, they have two potential reaction paths. The pair may coalesce and annihilate, resulting in lattice destruction. This is considered anion-enhanced film dissolution that occurs on the macro-scale and has the same outcome as reaction 5 in Figure 3-2. Alternatively, particularly if cation mobility is moderate to high, the cation vacancy can be transported through the film to the metal surface. If the increase in cation vacancies due to aggressive anion absorption cannot be consumed quickly enough, they will condense at the surface of the metal to form localized voids. The condensation of vacancies causes local film detachment, which prevents the film from growing because reaction 2 in Figure 3-2 cannot occur. However, film dissolution (reaction 5) continues, causing local thinning of the passive film. Eventually, this leads to film rupture either due to complete dissolution of the film locally or mechanically due to stress induced in the barrier layer [44].

The particular effectiveness of the chloride ion in inducing passive breakdown of stainless steel over other halogen ions has to do with two competing processes. In order for the anion to absorb into an oxygen vacancy, it must first dehydrate, which has an associated energy. Following dehydration, the oxygen vacancy must expand to accommodate the larger anion. These two energies prove to be in competition: the decreasing tendency for ions to hydrate as their size increases, resulting in a smaller dehydration energy, is offset by the increasing energy required to expand the oxygen vacancy. In the case of stainless steel, as well as many other metals, chlorides represent the most favorable combination of energy for absorption into an oxygen vacancy compared to other halogen ions. However, depending on the size of the oxygen vacancy, absorption of anions other than Cl^- may become more favorable, as is the case for titanium, which is more likely to breakdown in the presence of bromide than chloride [44], [55]. Halogen ions have lesser effect on metals such as titanium, tantalum, molybdenum, tungsten, and zirconium due to their high oxygen affinity, making it difficult for halides to displace oxygen and occupy vacancies [27].

3.3.2 Pitting Corrosion

Localized breakdown of the passive film creates an active dissolution path where corrosion is accelerated, producing an active-passive cell (Figure 3-4). A local breach in the passive film results in preferential corrosion of the metal that has been exposed. This creates a region of actively corroding metal amidst the passive metal surface with a much lower corrosion rate. A potential difference develops between the cathode (passive metal) and anode (active metal), resulting in rapid dissolution of the active metal surface, known as pitting. The corrosion products that are concentrated in the pit draw anions into the actively-corroding region, ensuring that the pit continues to grow. The low oxygen concentration within the pit, depicted in Figure 3-4, prevents the active pit walls from re-passivating.

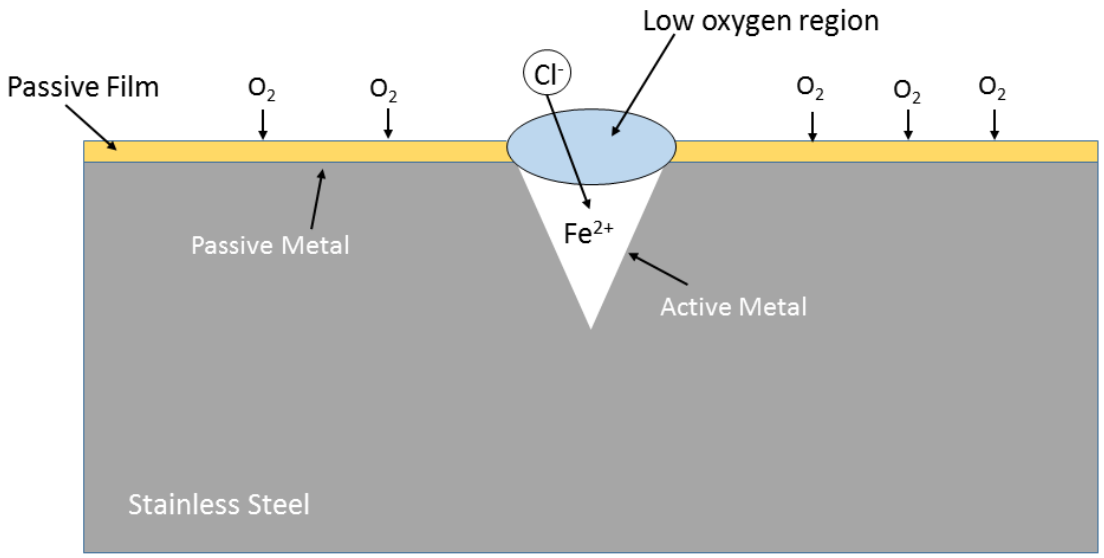

Figure 3-4: Active-passive cell leading to pitting corrosion

Pitting corrosion occurs in two stages: pit initiation, in which the passive film is breached, and pit propagation [27]. Pit initiation requires that the corrosion (or equilibrium) potential exceed the critical pitting potential (CPP) at which the passive film begins to breakdown. Various corrosion couples can cause the necessary increase in equilibrium potential. Initiation of a pit results in an active-passive cell with sufficient voltage difference to induce high current density and a high corrosion rate within the pit. Sustaining the pit requires the large voltage difference within the active-passive cell that has formed and causes the pit to propagate. The pit will continue to grow until a new passive film has formed over the pit, which typically requires the voltage to drop below the re-passivation potential of the metal.

As was mentioned, exceeding the critical pitting potential is necessary for stable pitting to take place. Increasing the voltage above the corrosion potential draws more negative ions to the metal surface, increasing the likelihood of breakdown by the mechanisms discussed in the previous section. Eventually, the aggressive anion presence at the metal surface is enough to cause the passive film to breakdown at many localized sites. The potential at which this occurs

is known as the CPP [56], [57]. Refer to Figure 5-4 for a plot showing the measurement of the breakdown and re-passivation potentials, where the re-passivation potential is the point at which the pits may re-passivated and cease propagating following a stable pitting regime. It is important to note that pitting may occur below the CPP, and even at equilibrium conditions depending on the chloride concentration. These pits tend to re-passivated quickly and are unable to propagate and remain active as they are above the CPP. This regime is known as metastable pitting, and the pits have a lifetime associated with them depending on the potential at which they are formed [58].

Materials are also known to have characteristic critical pitting temperatures (CPT), which is the lowest temperature at which stable pitting can occur under a given set of conditions. The CPT decreases due to several factors, most notably an increase in chloride concentration [59]. The standard CPT for 18-8 grades of stainless steel in chloride-containing media is several tens of degrees centigrade. The exact temperature is dependent on the composition of the steel and the chloride concentration. HLW containers will likely be operating above this temperature range due to the decay heat from long-lived isotopes, making stable pitting a possibility in most chloride environments.

A final point to make about pitting corrosion is that pitting will occur in areas where the passive film is more likely to breakdown. This includes surface defects or flaws, inclusions, grain boundaries, sensitized areas, and areas of high cation mobility. Surface defects, grain boundaries, and sensitized areas represent regions that present obstacles to forming stable passive films. High cation mobility, on the other hand, means faster diffusion of cation vacancies, resulting in an increased likelihood of passive film rupture. Consequently, metals forming passive films that are poor cation conductors are better protected against pitting, although this is not necessarily the case for other types of corrosion.

Optical images of stainless steel type 304 are provided in Figure 3-5 showing pitting corrosion after a one week immersion in chloride solution. The solution is a combination of three chlorides - 0.33 M NaCl + 0.33 M KCl + 0.33 M $MgCl_2$ – producing a 1 M chloride

solution. The images show significant pitting after exposure to chlorides for one week, showing the potential for passive breakdown despite no applied potential. The substantial effect that molybdenum has on the susceptibility of stainless steel to localized corrosion can be seen in Figure 3-6. The stainless steel type 316 sample shows a much lower density of corrosion pits than type 304 after exposure to the same solution for the same amount of time. Reasons for the added protection to localized corrosion provided by molybdenum were discussed in the previous chapter.

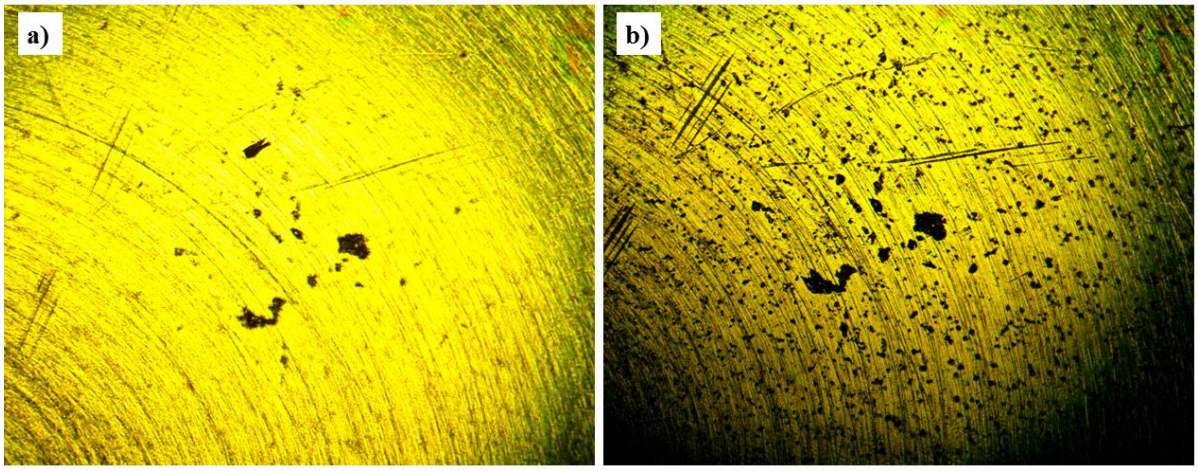

Figure 3-5: Optical images at 4x magnification of SS304 before (a) and after (b) immersion in a 1 M chloride solution for one week showing pitting corrosion

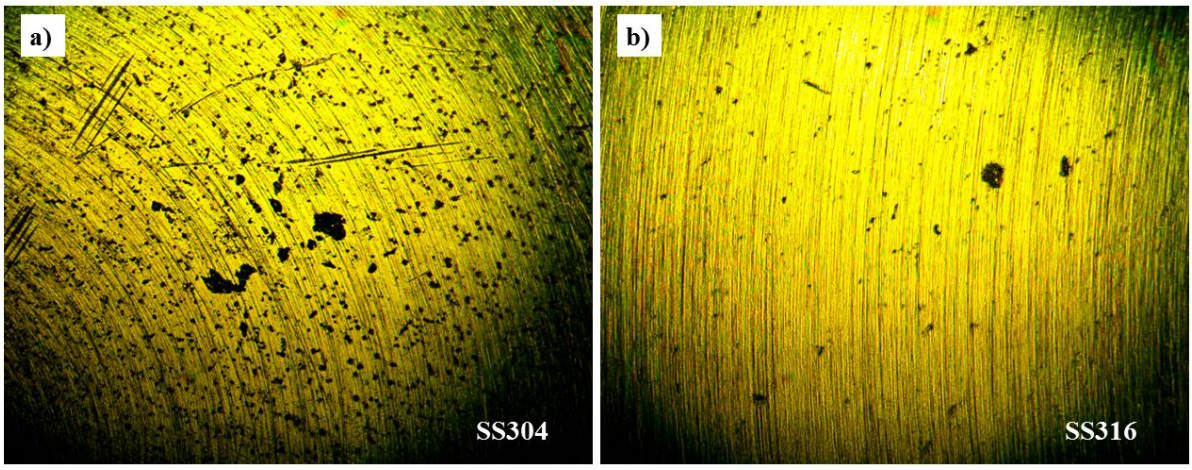

Figure 3-6: Optical images at 4x magnification of SS304 (a) and SS316 (b) after immersion in a 1 M chloride solution for one week showing the effect of molybdenum on pitting corrosion

CHAPTER 4

MULTILAYER PROTECTIVE COATINGS FOR HIGH-LEVEL WASTE STORAGE CONTAINERS

In light of the potential pitfalls of steel canisters discussed in the previous two chapters, several coating materials have been proposed: TiN, ZrO_2, TiO_2, Al_2O_3, and MoS_2 [60]. These coatings have been shown to be good barriers to corrosion, hydrogen diffusion, and mechanical wear [38], [61]. They are to be deposited on the outer surface of the steel HLW storage canister in multiple layers with the goal of isolating the waste package wall (canister) from the surrounding environments to which the storage containers may potentially be exposed. Figure 4-1 depicts the coating setup within the confines of dry cask storage. Refer to Figure 1-2 and Figure 1-3 for dry storage cask geometry and configurations.

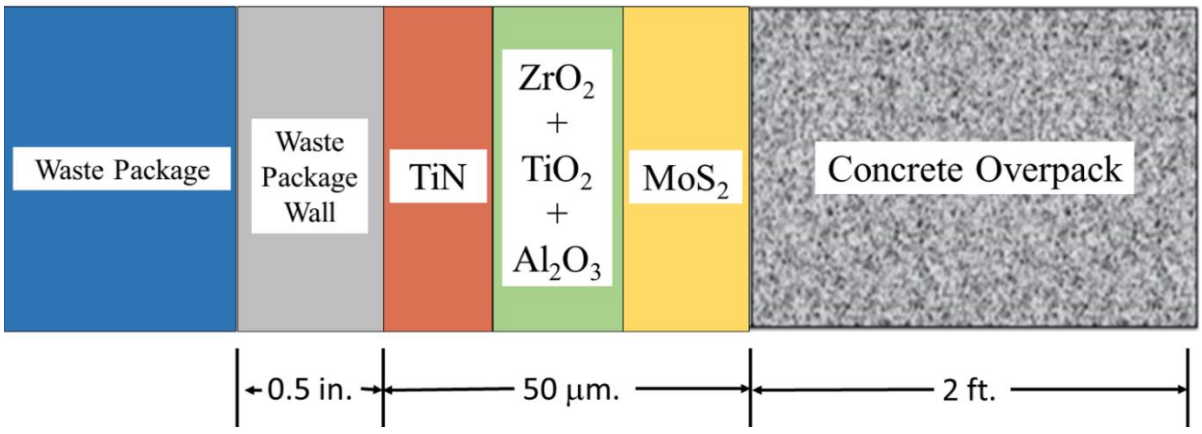

Figure 4-1: Multilayer protective coatings for high-level waste storage (not to scale)

The first layer is titanium nitride, which has excellent corrosion resistance and high mechanical strength. The second compound layer is known as 'Zirconolite' and is a compound of the three metal-oxide materials. It is insoluble in water and provides additional hardness and corrosion resistance. Finally, the outer layer is molybdenum disulfide, which is a common solid lubricant that offers physical wear resistance. It is believed that the combination of these coating layers with a total thickness of 50 μm or less is capable of protecting the primary waste storage container from environmentally-induced failures for the foreseeable future. The merits and properties of each of these materials will be discussed in detail.

4.1 Coating Materials

4.1.1 Titanium Nitride (TiN)

Titanium is one of the most abundant structural materials in the Earth's crust and has a number of desirable properties that make it and its alloys widely used. Titanium has high strength, low elasticity, high melting point, and good corrosion resistance. Its high strength-to-weight ratio makes it particularly useful as a lightweight structural material [27], [62]. Titanium is quite reactive and readily forms protective passive films, primarily TiO_2, giving it excellent resistance to corrosion. It is resistant to attack in chloride media, and thus is very noble on the galvanic series in seawater [63]. Pure titanium is supremely resistant to pitting and stress corrosion cracking in chloride solutions, although its alloys are susceptible to SCC and crevice corrosion under certain circumstances. The one drawback to titanium is that it is entirely dependent on forming and continually reforming a passive oxide film. Because of this, it is subject to attack in aggressive, non-oxidizing environments such as concentrated sulfuric and hydrochloric acids.

By compounding titanium to create titanium nitride, its properties are enhanced to include those of both covalent compounds – high hardness and high melting point – and metals – high

thermal and electrical conductivity. Titanium nitride has been used successfully as a coating material and acts as an effective diffusion barrier [64], as well as forming good Ohmic contacts with underlying metals [65]. Finally, TiN is used extensively to coat high-speed cutting tools to improve wear and corrosion resistance [66].

Based on its high mechanical strength, good corrosion resistance, and ability to act as a diffusion barrier, as well as the overwhelming abundance of titanium, TiN is an ideal first barrier layer to protect HLW canisters. It has the ability to sufficiently isolate the steel substrate from potentially harmful environments and can withstand mechanical and corrosive wear. Likewise for most coatings, the properties of TiN thin films are subject to the deposition method and the deposition conditions. As such, experimental testing of coating materials is a necessity.

4.1.2 Metal-Oxides (ZrO_2, TiO_2, and Al_2O_3)

Oxide ceramics have been used as surface coatings to improve wear, erosion, cavitation, fretting, and corrosion resistance. They are especially useful when wear and corrosion resistance are simultaneously needed [67], [68]. The three oxide materials under consideration - zirconia, titania, and alumina – may either be compounded or co-deposited to create a composite material known as zirconolite. The exact properties of zirconolite are highly dependent on the relative concentrations of each of the three oxides. Hence, the properties of each oxide individually must be understood in order to create the best possible combination of zirconolite.

i. Zirconium Dioxide (ZrO_2)

Zirconium is the primary component of the fuel rod cladding that contains UO_2 fuel pellets in LWRs. It is used because of its good mechanical properties, low thermal neutron cross section, and excellent corrosion resistance. Zirconium is an active metal that forms very stable passive films over a wide range of conditions and has mechanical properties similar to titanium and stainless steel described previously. Zirconium is resistant to alkalis and most acids that do not contain fluorine. Its corrosion resistance breaks down in the presence of high temperature air and chloride compounds [27].

Zirconium dioxide, or zirconia, much like pure zirconium, has properties similar to those of stainless steel and has been called "ceramic steel" [69]. Because of its high permittivity it has been considered as a replacement for SiO_2 in the semiconductor industry [70]. It is extremely stable chemically and thermo-mechanically, leading to a plethora of potential applications, specifically as a coating material [71]. Most importantly, it has shown significant promise as a coating for corrosion protection of stainless steel [72], and it has much better resistance to chloride solutions than pure zirconium.

ii. Titanium Dioxide (TiO_2)

Titanium dioxide, or titania, has been the most widely investigated metal-oxide in the field of surface science since the discovery of its ability to split water in a photoelectrochemical cell in 1972 [73], [74]. Since this time, TiO_2 has been used in an extraordinary number of applications including: as a photocatalyst in solar cells, as a gas sensor, as a white pigment, for optical coatings, in electric devices, as a coating on medical implants, and to help degrade organic molecules such as pollutants [73]. Much like ZrO_2, it is a prime candidate to replace SiO_2 in dielectric gate devices due to thickness limitations created by electron tunneling [73]. Undoubtedly, the thermal, chemical, and mechanical stability of titania are partly responsible

for its plethora of applications [62]. However, the use of TiO_2 as a coating for corrosion protection is of interest for this study. Titanium dioxide has frequently been studied as a corrosion-resistant coating, specifically on stainless steel [68], [75], [76], and has proven successful in many cases. Titania is especially resistant in chloride solutions [68], as was previously discussed for passive films on titanium metal, making it an obvious choice for protection of stainless steels.

iii. Aluminum (III) Oxide (Al_2O_3)

Aluminum is another lightweight structural material with good corrosion resistance and electrical and thermal conductivity [27]. As with the other metals that have been discussed, aluminum is active until it reacts with oxygen to form a protective passive film, which is primarily Al_2O_3 in sufficiently oxygenated environments. Aluminum is subject to pitting and crevice corrosion in chloride-containing media and is sensitive to corrosive attack in a number of other environments. Despite this, aluminum alloys still find use because of their remarkable strength-to-weight ratios, particularly in aerospace manufacturing. However, when weight is not the most dominant limiting factor, it is often better to use aluminum as an alloying component to make use of its desirable properties. For example, the addition of as little as 3-5% Al as an alloying component allows corrosion resistance in air up to exceptionally high temperatures [27].

Aluminum (III) oxide, or alumina, is the final component of the tri-oxide composite coating to be deposited on the outer surface of the HLW storage canister. Alumina, much like zirconia and titania, is a hard ceramic that is thermally stable and resistant to chemical attack [77]. Al_2O_3 is particularly effective at improving chemical wear and erosion [67]. Alumina is most often used for its abrasive properties and its abrasion protection. It is used in sandpaper and metal polishing as an effective substitute for diamond, as well as a common coating on cutting tools to prevent abrasive wear during use [67]. Alumina provides significantly improved

corrosion resistance compared with aluminum metal in addition to its unique wear resistance [78].

iv. Zirconolite ($ZrO_2 + TiO_2 + Al_2O_3$)

Oxides are frequently combined to form even more effective coatings, as they tend to blend well together. For example, Al_2O_3 coatings have shown better resistance to corrosion and better deposition uniformity when combined with TiO_2 [62], [79]. Furthermore, wear resistance of alumina/titania compound coatings has been shown to increase over alumina coatings alone. This increased wear resistance may be compounded by also adding ZrO_2 to the oxide mixture [67]. The same goes for corrosion and dissolution resistance, which lends credence to the blending of the three oxides to form an even more protective coating layer – zirconolite.

Zirconolite is very hard, resistant to corrosion, and insoluble in water. As mentioned previously, the properties of zirconolite are specific to the relative concentrations of each of the three oxides used to prepare the coating. Zirconolite possesses the most desirable properties of each of zirconia, titania, and alumina, making it ideally suited to be used as a protective coating in many types of environments.

4.1.3 Molybdenum Disulfide (MoS_2)

The benefits of molybdenum as an alloying component in steels have been described in Chapter 2. Molybdenum disulfide, in contrast, does not afford much corrosion resistance, but rather is used as a dry lubricant and to provide wear resistance. It possesses especially low friction in the absence of liquids and humidity [80]. The low coefficient of friction of MoS_2 leading to desirable lubricating properties is intrinsic in its crystal structure [81]. MoS_2 consists of covalent bonds and is arranged in a layered, triangular prism with alternating layers of

molybdenum and sulfur atoms [80], [82], [83]. The layered structure results from the strong polarization of sulfur atoms, which also creates greater spacing between layers. This extra spacing combined with weak bonds reduces the shear stress required to cleave the layers [80]. The relative ease with which basal cleavage occurs in molybdenum disulfide gives the molecule its low friction and good lubrication. Also, despite shearing of atomic layers, MoS_2 is able to retain its structure and its good adhesion to metallic substrates, making it an ideal solid lubricant [80], [82].

4.2 Common Coating Deposition Methods

There are a number of methods that are commonly used or have been used to deposit coatings on many types of substrates. Selection of an appropriate deposition method depends on the type of substrate, the material being deposited, and the desired application of the coating. A majority of deposition techniques may be grouped into four categories: physical methods, chemical methods, physical-chemical or hybrid methods, and dry etching methods for pattern delineation [84]. Each of these categories will be discussed in terms of their most popular techniques and the overarching utility of each class of method.

4.2.1 Physical Deposition Methods

Physical deposition methods are a class of coating deposition technique that results because of a physical reaction in which the deposited material is physically moved onto the substrate. A majority of physical deposition techniques fall under the umbrella of physical vapor deposition (PVD), which is a set of processes used to deposit thin films using vacuum technology to produce a vapor of material, which is then deposited on the substrate. Thermal

spraying methods dwell outside the realm of PVD techniques but will also be discussed as physical deposition mechanisms.

i. Evaporation Techniques

The first class of PVD techniques involve evaporation of the material to be deposited, which occurs in a vacuum environment. Standard evaporation techniques involve heating of the deposition material, either thermally, resistively, or using electron or neutral beam heating, until evaporation occurs. The gaseous material is then transported to the substrate and condenses on the surface, leading to film growth. The low pressure ensures as few interactions as possible between the evaporation source and the substrate. A reactive gas may be included in the chamber to form compounds prior to condensation on the substrate, which is aptly termed "reactive evaporation." The reactive evaporation process may also be enhanced by forming a plasma within the vacuum chamber, aiding the compound-forming reaction [84]. Evaporation techniques produce uniform coatings and have good deposition rates but are limited to materials that may be efficiently heated to the point of evaporation.

A specialized evaporation method that has gained significant traction over the past 30 years is molecular beam epitaxy (MBE). This is an ultrahigh vacuum (UHV) evaporation method for depositing high quality thin films [84]. The process involves atomic or molecular "beams," generated via evaporation or already gaseous sources, which are allowed to crystallize on the substrate surface. MBE is capable of producing extremely uniform films with properties very similar to those of the bulk material. The benefit to MBE over standard evaporation techniques is a lower growth temperature, which limits diffusion and allows for abrupt boundaries between layers and thickness control down to single atomic layers [84]. This makes MBE ideal for manufacturing semiconductor devices, where it is used extensively. A significant drawback to MBE is the extremely high vacuum that is required – often 10^{-11} Torr or better – to grow

uniform, single-crystal coatings. Significant expense and design constraints accompany the need for UHV conditions.

ii. Sputter Deposition

The second set of PVD processes, and possibly the most widely used class of deposition methods, are the various sputtering techniques. Sputtering is the process of physically removing material from a target by bombarding it with energetic particles. The particles that have been removed may then deposit onto the substrate. Sputtering differs from evaporative methods in that the particles enter the vapor phase due to momentum (or impulse) transfer rather than thermal excitation leading to evaporation. This gives sputter deposition significant versatility; virtually any material is subject to sputtering without regard for its thermal limitations or vaporization requirements. Sputter coatings also have good uniformity and smoothness, as well as good adhesion to many substrates. Thickness of sputtered coatings is relatively simple to control, and sputtering is highly adaptable, especially to the size of the substrate [84].

Sputtering may be performed in a number of ways, most of them involving ions as the bombarding particle. The ions are typically generated in a plasma discharge, though ion beams generated in other manners are also used. Plasma chambers used for sputter deposition include DC discharges, cathode arcs, and RF (radio frequency) discharges, in various geometries and configurations. Similarly to evaporation processes, sputtering takes place under vacuum conditions so that ions and sputtered atoms (or molecules) are relatively unimpeded on the way to their targets, producing more uniform films. Low pressure also reduces the energy input required to form the plasma discharge. Magnetron sputter deposition is the method of choice for this research and will be described in detail in a subsequent section.

iii. Ion Plating

Ion plating was developed as an alternative to the other PVD methods, which produce deposition particles with insufficient energy for some applications. Evaporation processes produce particles with energies less than 1 eV, and sputtering produces atoms with energies up to 10 eV [84]. In order to enhance the deposition energies, the substrate and growing film are continuously bombarded by high energy ions. Ions bombard the surface before and during deposition to increase adhesion by cleaning the substrate surface and to influence the properties of the coating during growth [85]. The constant bombardment of the growing coating often leads to a dense structure with fine grain boundaries [84]. However, the deposition rate decreases because of re-sputtering of the coating from the substrate. The properties of the impinging ions significantly affect the coatings and must be closely maintained to ensure optimal deposition conditions.

Ion plating can be added to almost any PVD technique because it can use any source of ions. Ions may be produced as a part of the deposition method, as with plasma-assisted sputtering, or they may be introduced from a source external to the main deposition process. For example, a negative bias applied to the substrate in addition to the target in a DC or RF plasma discharge will simultaneously accelerate ions toward the substrate and sputter the target material. If instead the ion source is a separate ion gun, it may be applied to any standard PVD method, including evaporative, non-plasma methods, in which case it is known as ion beam assisted deposition, or IBAD.

iv. Thermal Spraying

Thermal spraying is a class of methods that is often used on an industrial scale to coat large items quickly. A high density heat source is used to melt the coating material and accelerate it toward the substrate, where it rapidly cools. There are many types of thermal spraying methods

including plasma sprays, which are among the most widely used of the thermal spray techniques. Plasma spraying utilizes a plasma jet that is hot enough to melt nearly all materials and provides significant acceleration to the coating material.

Thermal spraying methods have deposition rates that are several orders of magnitude higher than PVD and chemical deposition methods, allowing for coatings up to several millimeters thick. Other major benefits are that thermal spraying does not require low pressure, thus saving cost and effort on vacuum equipment, and very large components may be coated rather quickly. The main disadvantages are porous coatings and often poor adhesion. The drawbacks to thermal spraying make it practical only for thick coatings on relatively large substrates, as small devices require greater precision and better uniformity.

4.2.2 Chemical Deposition Methods

As the name implies, chemical deposition methods are techniques that utilize chemical reactions to deposit coatings. The methods are divided based on the phase utilized to transport the coating material. The first group uses a gas phase and vacuum technology to deposit material and consists of chemical vapor deposition (CVD) and atomic layer deposition techniques. The second group employs the liquid phase as the mass transfer medium and primarily involves sol-gel processing [86]. The fundamental difference between chemical deposition and physical deposition is that the coating materials are chemically altered from the form of the precursor to the final film deposition. The manner in which the alteration occurs is dependent on the specific chemical technique.

i. Chemical Vapor Deposition (CVD)

Chemical vapor deposition is one of the most important film deposition technologies and is used extensively in the fabrication of solid-state microelectronics. CVD presents versatility for depositing many types of compounds with high precision [87]. The principles of CVD involve the introduction of gaseous constituents, either as part of the process or from a separate process, which are made to chemically react and form a solid film on a substrate. Standard CVD methods are performed under vacuum conditions ranging from low to ultrahigh vacuum, though CVD is also done at atmospheric pressure for certain applications. There are many subclasses of CVD depending on the application, though the fundamental processes are the same. Thermal chemical vapor deposition, organometallic vapor phase epitaxy (OMVPE), and photochemical vapor deposition are notable variations of CVD but will not be discussed further [84].

The basic CVD sequence begins with reactions leading to the formation of gaseous film precursors followed by transport to the substrate and adsorption of the film precursors to the substrate surface. Diffusion (often thermally-activated) and further chemical reactions of adsorbed film precursors result in film growth [84]. Thermodynamics are important in predicting the rates of the possible chemical reactions, and the continual need for more advanced and intricate coatings places significant importance on the underlying chemistry.

The advantages of CVD include its uniform film deposition, allowing for elaborate substrate geometries. Additionally, CVD often boasts relatively high deposition rates and a lower vacuum requirement than PVD techniques, as well as high purity films. However, the precursors to the film composition must be gaseous at the operating temperature. This requires very complex and frequently hazardous precursors for low temperature operation, or elevated temperatures requiring more sophisticated equipment and control.

ii. Atomic Layer Deposition (ALD)

Atomic layer deposition (also known as atomic layer epitaxy or molecular layering) is a form of CVD that has been developed to meet the ever-growing needs of semiconductor manufacturing. ALD is based on self-limiting chemical reactions, which accounts for the atomic layer control that is possible with ALD. Most ALD processes utilize a well-designed precursor to deposit binary films in sequential layers. In this case, the reaction may be divided into two half-reactions each reaction proceeds in the presence of its own precursor, which, in turn, readies the surface for the next precursor-reaction pair. The reactions take place only at surface sites, leading to self-limiting film growth; each layer stops growing when the surface sites have been exhausted [88], [89].

Angstrom-level thickness control is available with ALD, which is the biggest advantage it provides over other deposition techniques. It is also capable of producing extremely thin, uniform, defect-free films that are necessary for semiconductor and microelectronics manufacturing, as well as some other applications. The self-limiting nature of ALD produces continuous films because no surface sites are left unoccupied – this is especially important for dielectric films. Finally, ALD is extendible to large and varied-geometry substrates because the gaseous precursors do not require line-of-site to the substrate, as with PVD methods [89].

iii. Sol-Gel Processing

Sol-gel processing describes the class of methods in which a solution or sol undergoes a transition to a rigid, porous mass (gel). A sol is a liquid containing suspended, insoluble particles [84]. Sol-gel reactions are a series of hydrolysis and condensation reactions that promote the growth of the suspended particles in a network, representing the sol to gel transition [90]. The important reagent (or precursor) in most sol-gel reactions is a metal alkoxide [84], where an alkoxide is the conjugate base of an alcohol, which is the compound

that is left over after the alcohol loses a proton in a chemical reaction. For coatings, the solution undergoes the sol-gel transition once it is in contact with the substrate, going from liquid phase to a solid-liquid gel [84].

Sol-gel processing has the advantages of low temperature operation and uniform, homogeneous, high purity films. Also, any unused material can be recovered and reused, making the use of potentially precious and expensive materials quite efficient [84]. The major downside of sol-gel is the cost of precursors. It is useful for thin films where material costs are not an issue, but there are more practical methods for creating or depositing bulk materials [84]. Additionally, it is difficult to avoid film fracture and porosity upon drying of the gel phase.

iv. Electrochemical Deposition

Electrochemical deposition is a process by which ions in a solution may be deposited in the form of a solid film onto a conducting substrate. Deposition in this manner may be achieved by two different processes: electrodeposition, involving externally applied power, or electroless deposition, involving a spontaneous deposition with no applied power [91]. In an electrodeposition, or electroplating, process the external power source generates a current causing material dissolved in solution to be reduced and flow toward the substrate, where it is deposited. Electroless deposition relies on clever solution compositions to drive the electrochemical potential toward the spontaneous deposition of dissolved material. In this case, the solution itself provides the necessary electrons to reduce ions in solution, allowing them to be deposited on the substrate surface. Electrochemical deposition techniques are frequently utilized in semiconductor and microelectronics manufacturing [91]. They are generally limited to conducting materials, making those methods less versatile than other deposition methods. However, this is made up for by the deposition rates of electrochemical techniques, which are

much higher than other chemical deposition methods. Additionally, electrochemical deposition systems can be very simple and inexpensive to manufacture.

A closely related technique to electrodeposition and electroless deposition is electrophoretic deposition, which coats a substrate with particles suspended in a solution using electrical currents. The generated electric field causes suspended particles to move toward the substrate electrode (electrophoresis), where the particles may coagulate and deposit [92], [93]. Electrophoretic deposition is often applied to deposit ceramics and other dielectric materials, though it is limited to materials that can be suspended properly in solution. This requires proper matching of deposition material and liquid to ensure insolubility. Many oxides have been deposited electrophoretically, including TiO_2, ZrO_2, and Al_2O_3 [93].

4.2.3 Hybrid (Physical-Chemical) Deposition Methods

Physical-chemical, or hybrid, deposition methods combine aspects of physical and chemical deposition to enhance the deposition process. Hybrid methods are able to overcome the disadvantages of one technique by complementing it with another and have become quite popular because of this. The types of hybrid deposition systems are numerous, but there is one of particular interest that has gained significant traction: plasma-enhanced chemical vapor deposition (PECVD).

Plasmas are able to enhance chemical reactions much more efficiently than other methods. Because of that, PECVD has been made more cost efficient than thermally-activated CVD in most cases. An example of this is the deposition of silicon nitride films. Thermal CVD techniques require temperatures between 700 and 900°C, whereas PECVD reduces these temperatures to less than 350°C by substituting electrical energy from the plasma for thermal energy [84]. Moreover, dissociation of the gaseous species that occurs within a plasma is often desirable for augmenting the chemical reactions required for deposition. Lower temperatures

are significantly better for substrates and structural materials of the deposition device, which is why PECVD has become an established commercial deposition technique for a wide array of applications.

4.2.4 Etching and Pattern Delineation Processes

Etching is the selective removal of a material to create a specific pattern or design. This is typically accomplished by placing a mask over the area where material removal is not desired. Etching may be divided into two broad categories: wet and dry etching. Wet etching includes most types of chemical etching and generally is capable of removing material much faster than dry etching. However, it is typically isotropic because the liquid etchant is capable of getting underneath the mask. In cases where precision is required, dry etching is normally the method of choice. Dry etching includes plasma-assisted etching, ion beam etching, laser etching, as well as other physical and dry chemical etching processes. Physical dry etching uses high kinetic energy particles to remove atoms from the substrate, similar to sputtering, whereas dry chemical etching utilizes chemical reactions between the gaseous etchant and the substrate. It is possible to create anisotropic etches with dry etching methods, which is preferred to isotropic wet etching. However, the greater control of dry methods comes at the expense of etch rate, which is significantly lower than for wet etching.

Etching processes are often used in microelectronics fabrication using photoresist on silicon wafers, though they are also used to deposit thin films in desired patterns. Etching is not an ideal method for the uniform, protective coatings that are desired for HLW storage containers, and this description has only been included for completeness.

4.3 Magnetron Sputter Deposition

In light of the pros and cons of the deposition methods described in the previous section, magnetron sputter deposition was chosen as the method to be used for the deposition of thin film coatings on steel for this research. To recap, the advantages of sputter deposition are: good film uniformity and thickness control, film deposition with bulk properties, excellent versatility in selection of target and substrate materials, good adhesion, and moderate deposition rates [84].

Magnetron sputter deposition is a form of PVD that has a relatively high deposition rate and produces quality films. It has adequate scalability and good adaptability, which were important factors in choosing a deposition technique [94], [95]. Due to the overwhelming size of spent fuel storage containers, the deposition technique must be appropriately scaled up in order to be practical to implement. Moreover, there is a broad range of materials to be deposited, and there may be an even wider variety in the future to account for different situations and environments. Sputter deposition is capable of handling almost any coating material and it may be scaled up by building a larger discharge chamber. Although there are other techniques that produce higher quality, lower defect coatings (i.e. ALD and PECVD), or have higher deposition rates (i.e. thermal spraying), or are more easily applied on a large scale (i.e. thermal spraying and electrodeposition), there are very few deposition methods that combine all of these desirable properties. The exceptional adaptability of magnetron sputtering combined with high quality films, moderate deposition rates, thickness control, and acceptable scalability make it one of the most well-rounded deposition techniques. Furthermore, sputtering is relatively simple to control and automate, so it is not a technique that is solely confined to research laboratory use.

4.3.1 Glow Discharge

The basis of the sputtering operation is the glow discharge plasma that is used as the source of ions. In fact, glow discharges are the basis for many types of plasma-based deposition processes including sputter deposition, plasma etching, and PECVD, among others [84]. These plasmas are generally weakly ionized at well below atmospheric pressure. The basics of plasmas will not be rehashed here, as they can be found in any introductory plasma textbook, though it is important to discuss the specifics of processing plasmas and the way they are controlled.

Glow discharges are often sustained by applying a high power to a set of electrodes within the discharge chamber. A simple schematic of a capacitive plasma discharge is given in Figure 4-2. The power source, which may be DC voltage or RF power, passes current through the gas (normally low pressure) between two parallel plate electrodes, eventually causing the gas to ionize or "break down" to form a plasma. The discharge is then sustained by energetic electrons. When the voltage is shut off, ionization ceases and recombination of electrons and ions produces neutral fill gas again, effectively turning off the plasma. There are many other types of plasma discharge configurations, but the focus here will be on planar, capacitive discharges.

Glow discharges for processing are typically low pressure discharges with gas pressures between 1 mTorr and 1 Torr, though some applications require higher vacuum [96]. High pressure processing discharges are also used as a means of delivering high heat to the target or substrate. There is a delicate balance of gas pressure for plasma sputtering: too low of a pressure leads to an insufficient number of ions, whereas too high of a pressure reduces the mean free path (MFP) of sputtered atoms, causing too many interactions before reaching the substrate. Because of this, gas pressure is an important control parameter in determining film deposition rate and film uniformity and morphology.

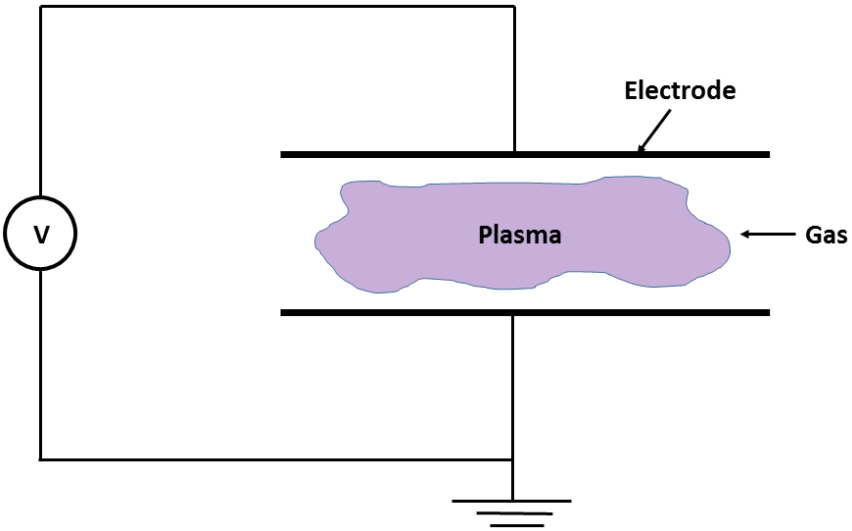

Figure 4-2: Simple capacitive plasma discharge – adapted from [96]

4.3.2 Physical Sputtering

To reiterate what was stated previously, sputtering is the process of bombarding a target with energetic particles to dislodge atoms and/or molecules. The material that is removed may then be deposited onto a substrate if desired. In the case of glow discharge sputtering, the source of energetic particles is the plasma itself. Heavy ions in the plasma are accelerated toward the negatively-biased target, gaining enough kinetic energy along the way to displace material upon contact with the target. In Figure 4-3, the plasma is generated in the negative glow region, and ions are accelerated through the sheath (or "dark space"), which is mostly devoid of electrons, toward the cathode. The sputtered atoms that are ejected from the cathode are then deposited on the substrate. The setup in Figure 4-3 is the simplest form of plasma sputtering, and it may be controlled by altering the potential through which the ions are accelerated and by changing the gas pressure.

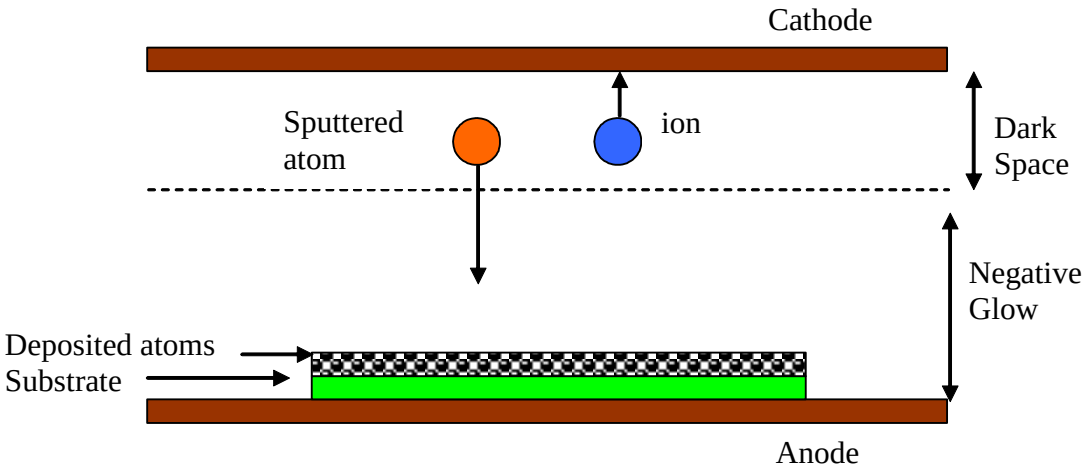

Figure 4-3: Planar cathodic sputter deposition configuration

The primary collision between an energetic ion and a target atom may or may not cause sufficient energy transfer to eject the impacted atom. This is dependent on the energy and angle of incidence of the bombarding ion. For ions on a path perpendicular to the target, the primary collision likely forces the atom further into the substrate rather than toward the surface. However, the ion and atom from the first collision are capable of colliding with other atoms, which may, in turn, collide with additional atoms, and so on. Eventually, one or more atoms may gain the appropriate velocity to leave the substrate. Thus, sputtering typically occurs due to multiple collisions involving a cascade due to a single incident ion [97]. The cascade is capable of spanning a significant volume inside the substrate, meaning that the damage extends beneath the surface. Evidently, the incident ion must have sufficient energy to dislodge an atom from its lattice position such that a cascade may initiate.

With this description of the sputtering process in mind, it is clear that the sputtering yield, or the number of atoms ejected from the target per impinging particle, will be different for each material. The transfer of energy among atoms depends on the size, density, and placement of atoms within the material, along with the energy of the incident particle. Sputtering yield

monotonically increases with incident ion energy because each ion possesses more energy to transfer to the target atoms, leading to greater recoil energies and longer, more energetic collision cascades. Ion energies for sputtering are usually between 200 and 1000 V, which is roughly 10 times the threshold sputtering energy for most materials [96]. Sputtering yield is also sensitive to the type of ions used to bombard the target. The most efficient energy transfer occurs between two similarly-weighted particles. Thus, sputtering yields are increased if the ion and target atoms are close in mass. Argon and xenon are most often selected as the sputtering fill gas, though other atmospheres are also used, particularly for reactive sputtering. The sputtering yield can range from 0.1 atoms ejected per incident ion up to several tens of atoms per ion, depending on the factors discussed above. Sputtering yield is an essential parameter in determining the film deposition rate and becomes exceedingly important for co-sputtering of several targets simultaneously or for compound materials, such as the coatings chosen for this study.

4.3.3 Planar Magnetron Sputtering

In order to get around the balance between a dense plasma and a sufficient mean free path of the sputtered neutral atoms, magnetic fields may be introduced. Magnetic fields, alongside the ever-present electric fields, are used to increase the efficiency of the deposition system. The introduction of magnetic fields changes the motion of charged particles. Both electrons and ions move in circular orbits around magnetic field lines. Except for very high strength magnetic fields, ion motion remains mostly unaffected because of its mass. Electron orbits, though, are substantially altered even by weak magnetic fields. Thus, electrons may be manipulated without affecting ions or neutral particles by applying (or inducing) magnetic fields of appropriate strength.

Magnetrons are a class of sputter sources with applied magnetic fields that run parallel to the target. The magnetic fields, in tandem with electric fields persisting in the plasma, are capable of confining low energy electrons close to the target surface, causing more ionization and increasing the plasma density locally [84], [98]. The local increase in plasma density leads to a greater number of ions and increases the sputtering efficiency, effectively increasing the film deposition rate. Many of the electrons that become trapped near the target surface are secondary electrons emitted upon ion impact. These electrons generally have lower energy than electrons in the plasma bulk and thus can be confined with weaker magnetic fields. The importance of the secondary electrons in the sputtering process is evidenced by the attention given to the secondary electron emission yield in the literature [99]. Increasing the deposition rate in this fashion avoids the negative effect that increasing the sputter gas pressure has on the sputtered atoms that are to be deposited on the substrate. A properly designed magnetron is capable of operating at low pressures (< 10 mtorr) without losing out on sputtering efficiency., which is an important feature that makes magnetrons widely used for sputter deposition. However, depending on the configuration of the magnetic field, the target material may be preferentially sputtered over smaller areas. This causes poor target utilization and wasted materials and is the main disadvantage of the planar magnetron system, though it can be overcome by moving the target with respect to the magnets (i.e. rotating cylindrical magnetron) [84].

Figure 4-4 shows two pictures of a typical planar magnetron sputter deposition system. Each pictures shows ideal magnetic fields lines given the magnets shown, albeit the more realistic field profile may be found in picture (b). Picture (a) displays the concentration of electrons near the target surface leading to an increased local plasma density and increased sputtering. The effect of preferential sputtering may be seen in (b) with the depletion of the cathode between the magnets. Cooling of the sputtering target is essential due to the heat generated from the energy transferred during ion impact. It is evident in (b) that given the proper configuration of magnets, the bulk of the plasma may be confined to a region away

from the substrate, decreasing the ion flux to the substrate surface. This is desirable in many cases to avoid significant re-sputtering of the deposited film.

4.3.4 Reactive Sputtering

To this point, the case has been made for avoiding any interactions between the sputtered atoms and the background gas by operating at low pressure. However, adding a reactive gas to the discharge (i.e. oxygen or nitrogen) opens the door for what is known as reactive sputter deposition. Reactive sputtering is a process where the sputtered atoms react with the gas in the discharge chamber before depositing on the substrate to form a compound coating. For example, aluminum may be sputtered in an argon-oxygen atmosphere to deposit an aluminum (III) oxide (Al_2O_3) coating, rather than sputtering an Al_2O_3 ceramic target in a non-reactive plasma.

The case for reactive sputtering is two-fold. First, compound materials typically have much lower sputtering yields than elemental targets, leading to low deposition rates [100]. This has to do with the inefficient energy transfer between particles of dissimilar mass. The disparity in sputtering yield between compound and elemental materials is exemplified by aluminum oxide. The sputtering yield of pure aluminum for argon ions with energy of 600 eV is 0.83 atoms per incident ion, and it drops to 0.18 atoms per incident ion for Al_2O_3 [96], [101]. The sputtering yield is over 4.5 times greater for pure aluminum compared to its oxide form, resulting in a significantly higher deposition rate of aluminum metal. Sputtering pure aluminum and allowing it to react with oxygen in the discharge chamber can overcome the poor yield of Al_2O_3 and greatly increases the deposition rate of aluminum oxide coatings. This vast discrepancy between sputtering rates of elemental and compound targets is not always the case. The sputtering rates of zirconium and zirconia using 600 eV argon ions are 0.42 and 0.32, respectively, and the sputtering rate of TiO_2 is actually twice as high as that of elemental

titanium for the same energy argon ions [101]. For many cases, though, the sputtering rate makes a significant case for the use of reactive sputter deposition.

Another important aspect of depositing reactively sputtered coatings deals with the selection of the power source. Metal targets are capable of dissipating power efficiently and therefore are compatible with DC and RF power delivery, which are the typical choices for sustaining a plasma discharge. Dielectric targets (i.e. oxide and nitride compounds) are insulating and thus cannot handle high DC power without cracking. Instead, the sputtering of insulating materials requires RF power and carefully-controlled target cooling. Not only are systems with DC power delivery simpler to setup and operate, DC power is much easier to scale up to higher power levels. The concerns with RF power upon scaling up include: nonuniform power delivery, RF leakage, cross-talk between components, arcing, and the high cost of RF power supplies [84]. Metallic targets are easier to purify, machine, and cool, making them more efficient to use than insulating compound targets [84], [102].

Control of gas flow rates into the discharge chamber is very important for reactive sputtering. The metallic target is capable of interacting with the reactive gas prior to sputtering, causing a compound layer to form on the surface of the target. This is known as target poisoning and will greatly reduce the deposition rate for reasons mentioned previously [100], [102]. Flow of the reactive gas must be acutely controlled to prevent target poisoning due to too much of the reactive gas, and to avoid depositing metallic coatings from an insufficient supply of the reactive gas to form compounds with sputtered atoms. The stoichiometry of reactively sputtered films is also very sensitive to the concentration of the reactive gases in the discharge. This places a premium on gas flow control in order to maintain the desired film composition and stoichiometry, though it also provides considerable control over film deposition [102]. This makes reactive sputtering considerably more difficult to implement than nonreactive sputtering.

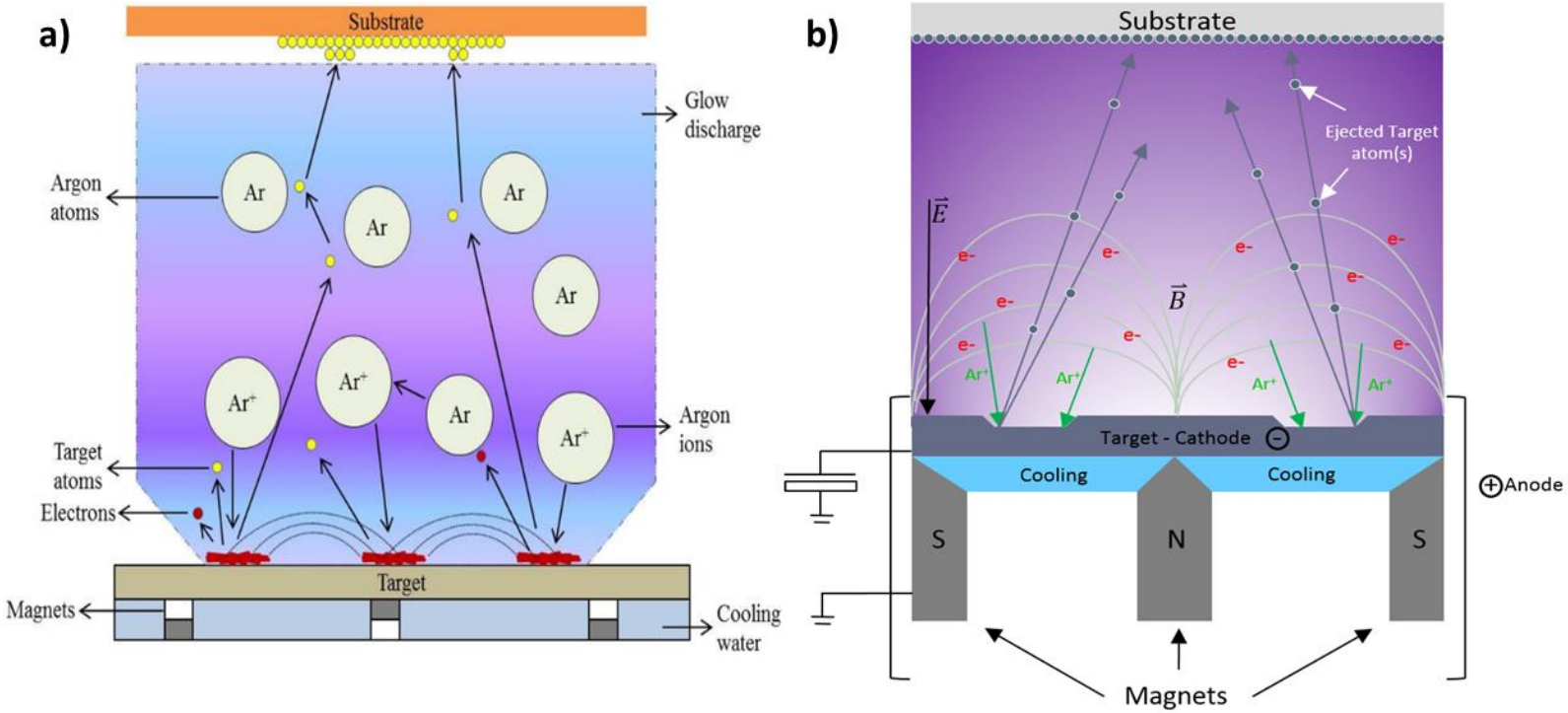

Figure 4-4: Depiction of magnetron sputter deposition: a) argon discharge showing effects of background gas; b) argon discharge with preferential sputtering depicted between magnets

4.3.5 Experimental Magnetron System

The system utilized for coating deposition in this study is pictured in Figure 4-5. It is a CMS (Combinatorial Materials Science) – 18 Multi-Source magnetron sputter deposition system from the Kurt J. Lesker Company. The deposition system is located in the Department of Materials Science and Engineering at the University of Florida at Gainesville.

The processing chamber is a 15”-high cylinder with an 18” diameter and made of stainless steel. It is capable of functioning anywhere from atmospheric pressure to UHV (roughly 10^{-10} Torr). This magnetron has a rotating mount up to 40 rpm that supports up to 6” substrates and substrate heating up to 800°C. RF and DC power delivery are supported for sputtering either conducting or insulating materials, both magnetic and non-magnetic. Finally, the chamber can house 4 sputter targets simultaneously and is capable of multi-gas injection for reactive sputter deposition.

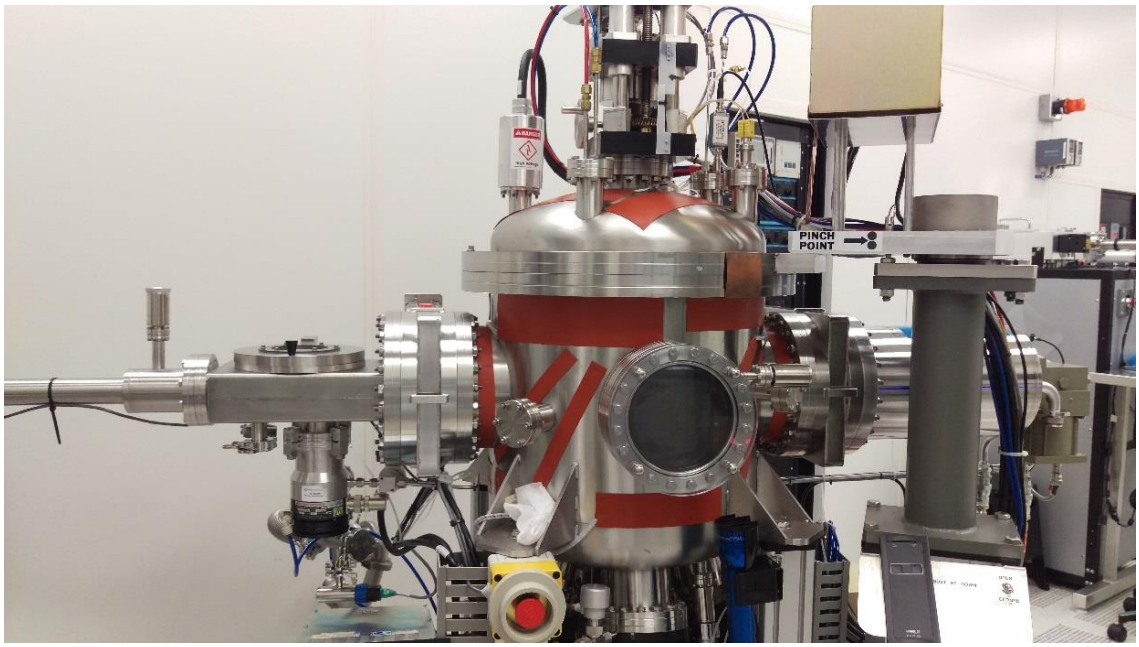

Figure 4-5: Magnetron sputtering system – Dept. of Materials Science and Engineering, Univ. of Florida, Gainesville

4.4 Coating Characterization

Following deposition, the coatings are imaged and characterized to ensure uniformity and good adhesion to the substrate. Imaging techniques include optical microscopy, scanning electron microscopy (SEM), and focused ion beam (FIB) imaging. Optical imaging provides a quick method to determine differences in surface morphology, whereas electron imaging allows for much higher magnification to capture fine microstructure. FIB imaging is useful for milling out regions and observing cross sectional areas with very high magnification.

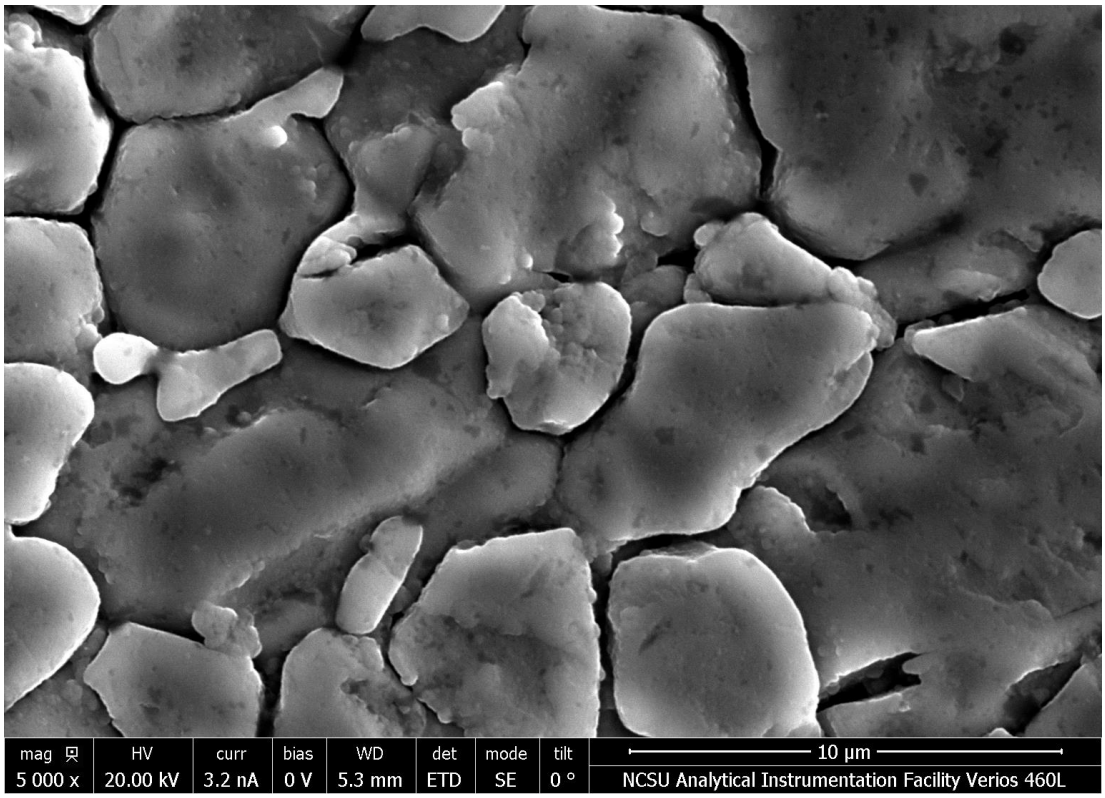

Figure 4-6: SEM image of titanium nitride on SS316 – cathodic arc deposition – 5 k x magnification

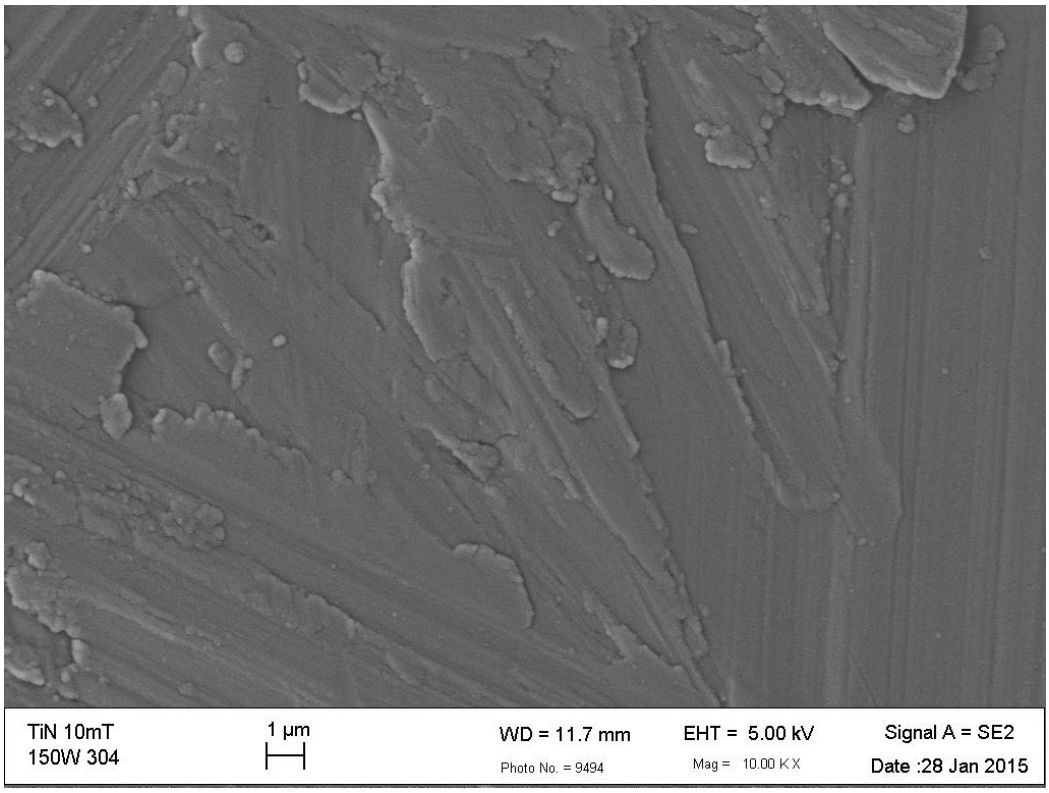

Figure 4-7: SEM image of titanium nitride on SS304 – magnetron sputter deposition – 10 k x magnification

Figure 4-6 and Figure 4-7 show SEM images titanium nitride coatings on two different stainless steels deposited using two different methods, cathodic arc and magnetron sputtering. These images demonstrate the ability of electron microscopes to differentiate between microstructure. It is also clear that magnetron sputtering (Figure 4-7) is capable of producing uniform coatings, which is one of the reasons it was chosen as the deposition technique. Each coating was imaged in a similar manner following deposition.

The power of FIB imaging may be gathered from Figure 4-8, which shows a surface region milled out using an ion beam and the same region blown up to measure the thickness of the protective surface coating.

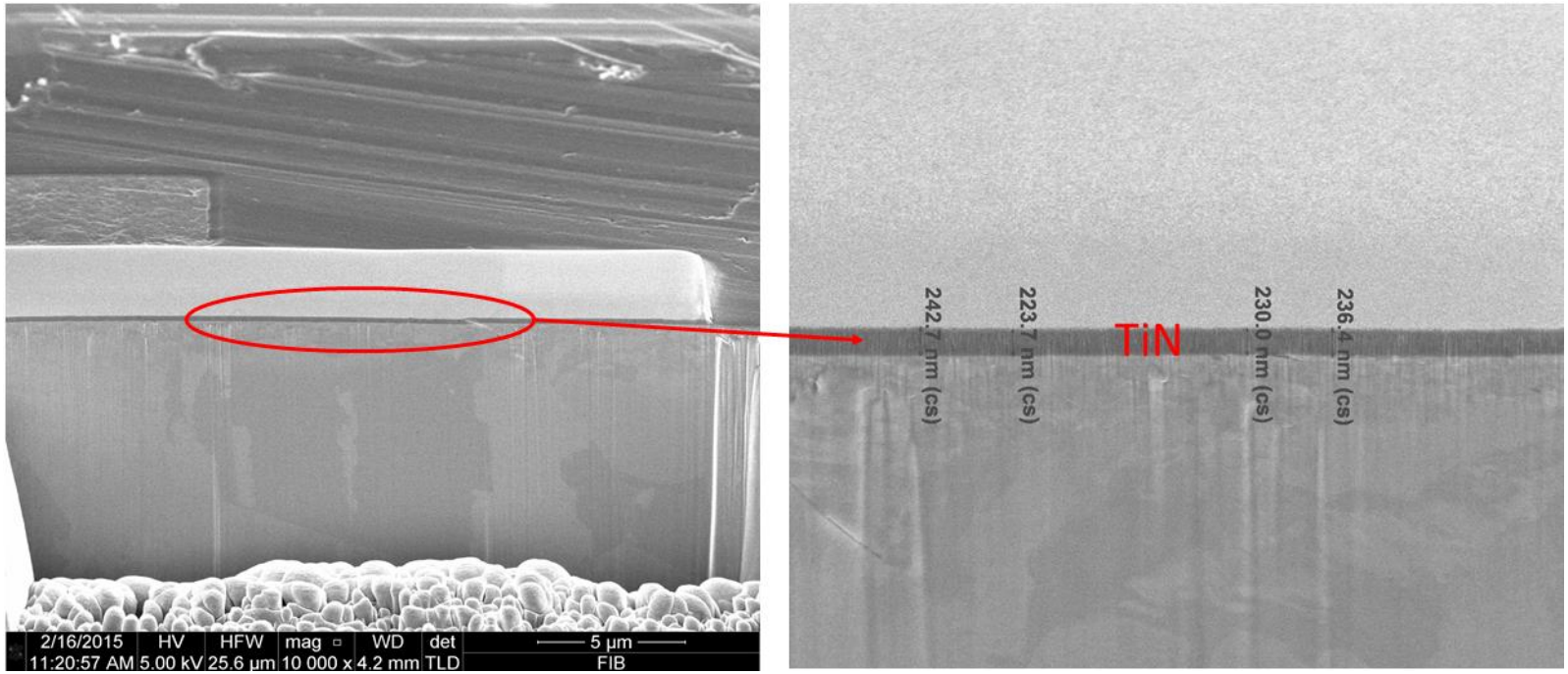

Figure 4-8: FIB image of titanium nitride coating on SS304; milled-out region (left) and an extremely high magnification view of the coating layer (right)

Figure 4-8 shows a fairly uniform coating thickness of roughly 235 nm over a portion of the surface of a SS304 disk. Using FIB imaging, TiN proved to be the thickest coating out of the five materials selected for the same deposition duration. The higher thickness for TiN is based on the fairly high sputtering yield of TiN compound targets. On the other hand, a TiO_2 coating on SS304 may be seen in Figure 4-9 showing a coating thickness around 30 nm, which is roughly an order of magnitude thinner than the TiN coating. Each of the metal-oxide coatings proved to be less than 100 nm thick, owing to the very low sputtering yield of oxide targets. The extremely thin oxide coating layers make a good case for the use of reactive sputtering, which was discussed earlier in this chapter. The effect of the protective coating thickness will be addressed in a subsequent chapter.

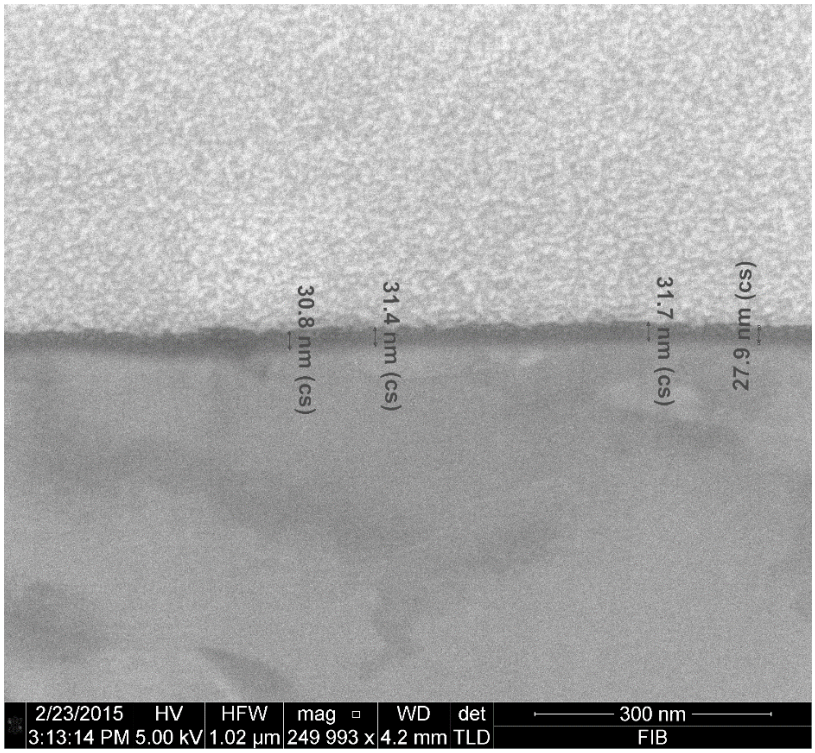

Figure 4-9: FIB image of a TiO_2 coating on SS304 with thickness marked on the image – 250 k x magnification

CHAPTER 5

CORROSION TESTING

The primary focus of this study is on the corrosion performance of the bare and coated steel canister materials. Two types of corrosion experiments are implemented: electrochemical polarization and prolonged exposure in circulating corrosive solutions. These two testing mechanisms provide significant information about the bare and coated steels in a number of environments.

5.1 Electrochemical Polarization

Electrochemical polarization has become an extremely popular technique to assess the corrosion of various materials. The technique consists of measuring the flow of electrons (current) from the oxidation and reduction reactions that collectively cause corrosion. External voltage or current is applied to disturb the equilibrium state, which is known as "polarization." By artificially creating non-equilibrium conditions, corrosion is accelerated, allowing for rapid assessment of the corrosion behavior. Electrochemical polarization measurements allow corrosion to be observed and quantified over a much shorter timescale than would be necessary in the absence of an applied bias and subsequent response current [103].

A diagram of the experimental setup for polarization measurements is provided in Figure 5-1. Electrochemical testing is completed using the MULTIPORT™ corrosion cell kit and the Interface 1000 potentiostat, both from Gamry Instruments (https://www.gamry.com/). The potentiostat is the controlling unit of the test cell that applies and measures the voltage and current signals using the software provided with the unit. The experimental arrangement is the

standard 3-electrode configuration employing a working electrode, a counter electrode, and a reference electrode.

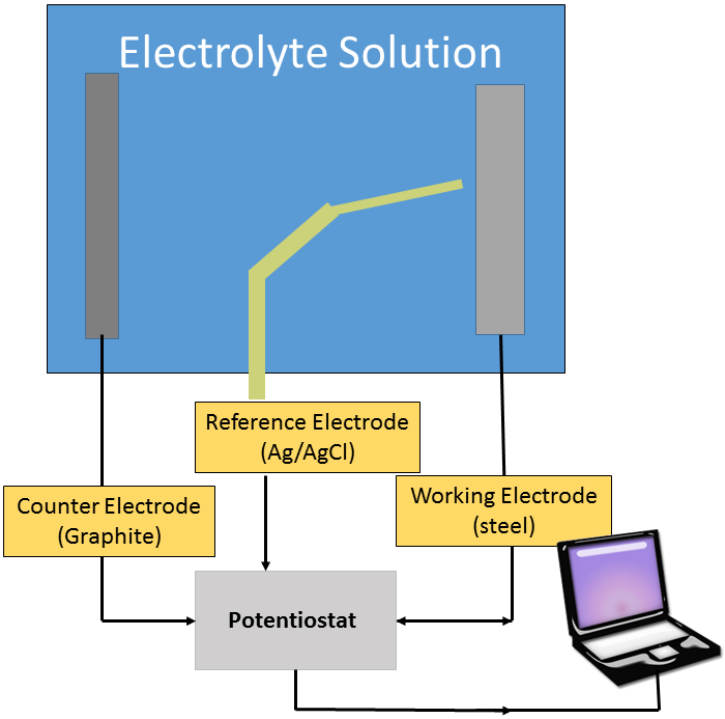

Figure 5-1: Diagram of the setup for electrochemical polarization measurements

The working electrode is the material undergoing corrosion, which is one of three steel alloys in this case. A saturated silver/silver chloride (Ag/AgCl) reference electrode sets the potential against which voltage is measured, or the reference potential. An inert graphite rod is placed in the cell to balance the reactions occurring at the surface of the working electrode and is known as the counter electrode. The purpose of the counter electrode is to act as an electron sink to avoid passing substantial current through the brittle reference electrode. Each of these electrodes is connected to the potentiostat, which is controlled by computer software.

Temperature is measured using a thermocouple placed in solution connected to a multimeter. Figure 5-2 shows a labeled picture of the experimental setup to perform electrochemical measurements.

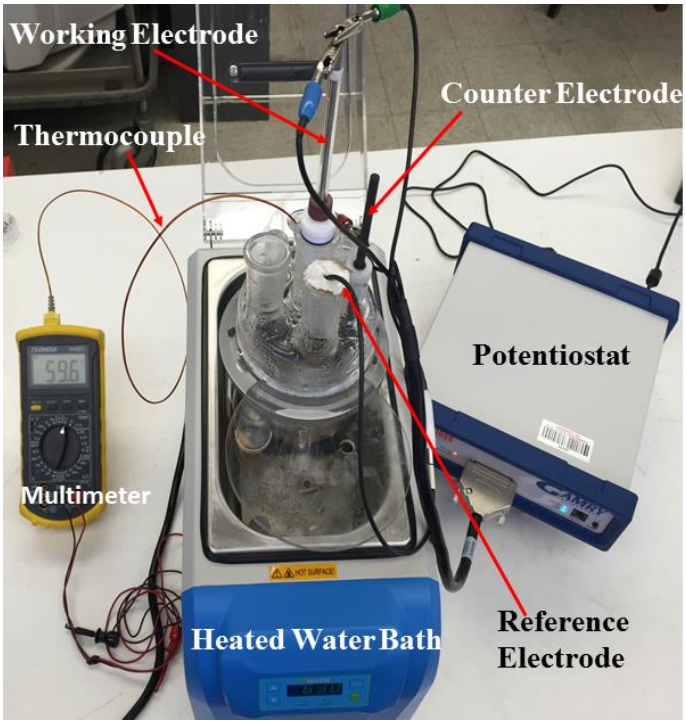

Figure 5-2: Electrochemical polarization setup with labeled components

5.1.1 DC Electrochemistry

DC electrochemistry consists of applying static voltage or current signals and measuring the system response. The DC electrochemical measurements utilized in this study will exclusively control voltage and measure current. Two forms of voltage control that will be employed are potentiostatic and potentiodynamic measurements, the difference between them

being that the voltage is either held constant (potentiostatic) or changes at a prescribed scan rate (potentiodynamic).

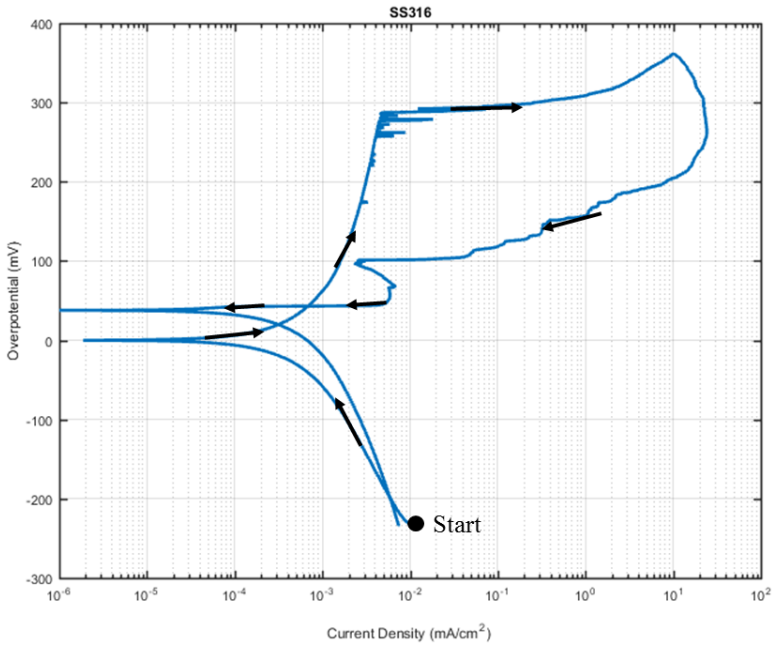

Figure 5-3: Cyclic polarization curve for stainless steel type 316 in 1 M NaCl solution. Arrows indicate direction of voltage scan

5.1.1.1 Cyclic Potentiodynamic Polarization Curves

Potentiodynamic current-voltage curves provide a majority of the information that can be gathered from DC measurements. A special application of potentiodynamic techniques known as a cyclic polarization curve may be seen in Figure 5-3. The voltage scan initiates at the start point noted in the figure and continues in the noble (positive) direction following the direction of the arrows. Upon reaching the apex, the scan reverses and terminates at the starting voltage.

Significant information may be garnered from cyclic polarization curves including corrosion rate, passive breakdown potential, re-passivation potential, and the propensity for localized corrosion in a given environment.

Figure 5-4 shows the same polarization curve as that provided in Figure 5-3 with the passive breakdown (E_{BD}) and re-passivation (E_{RP}) potentials noted on the graph. The passive region is the portion of the curve that is noble to the equilibrium potential (zero overpotential) and is marked by a small change in current over a large voltage range. Passive breakdown is denoted by E_{BD} in Figure 5-4 and spells the end of the passive region and the onset of localized corrosion. This is indicated by the large increase in current that ensues. The passive breakdown potential is equivalent to the critical pitting potential in the absence crevice corrosion and is the point at which corrosion pits begin to form and propagate [56], [57].

Re-passivation is the point at which corrosion pits cease propagating and the passive film is able to reform. It is noted in Figure 5-4 as the point at which the reverse scan crosses over the forward scan. The positioning of the breakdown and re-passivation potentials with respect to the equilibrium potential speaks to the passivation behavior of the material. Furthermore, the severity of the localized corrosion (mostly pitting) may be qualitatively determined from the hysteresis in the cyclic polarization curve. In the absence of pitting and crevice corrosion, the reverse voltage scan would lie directly on top of the forward scan. The size of the loop marked “localized corrosion” in Figure 5-4, or the area under the curve, is proportional to the amount and severity of the localized corrosion. This is evidenced by the fact that the reverse scan measures the same current magnitude for a much lower voltage, which is attributable to pits that have formed and continue to grow.

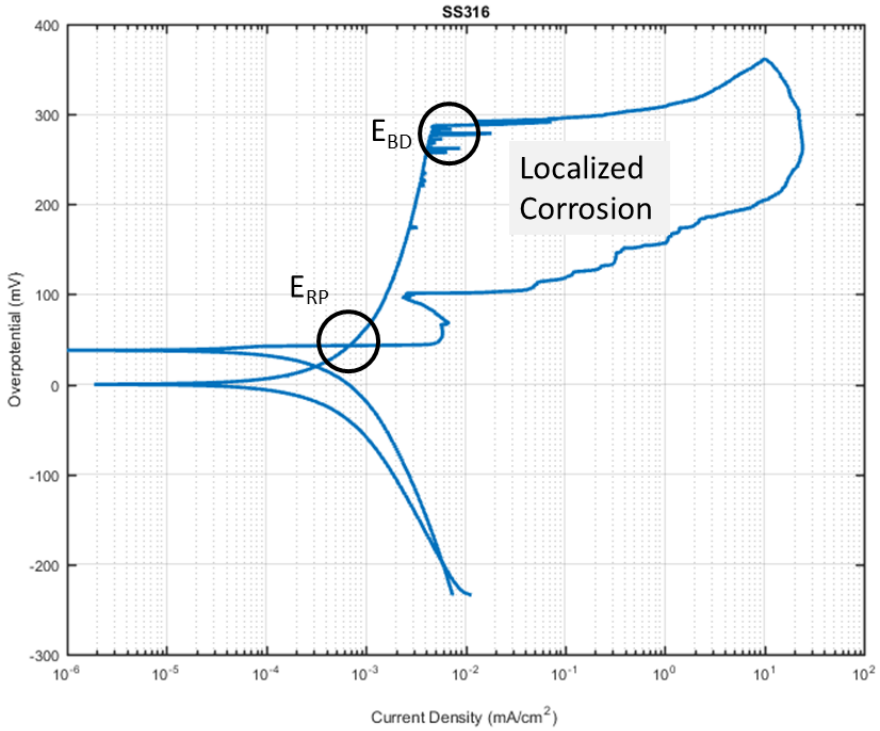

Figure 5-4: Cyclic polarization curve for SS316 showing the passive breakdown (E_{BD}) and re-passivation (E_{RP}) potentials as well as the region associated with localized corrosion

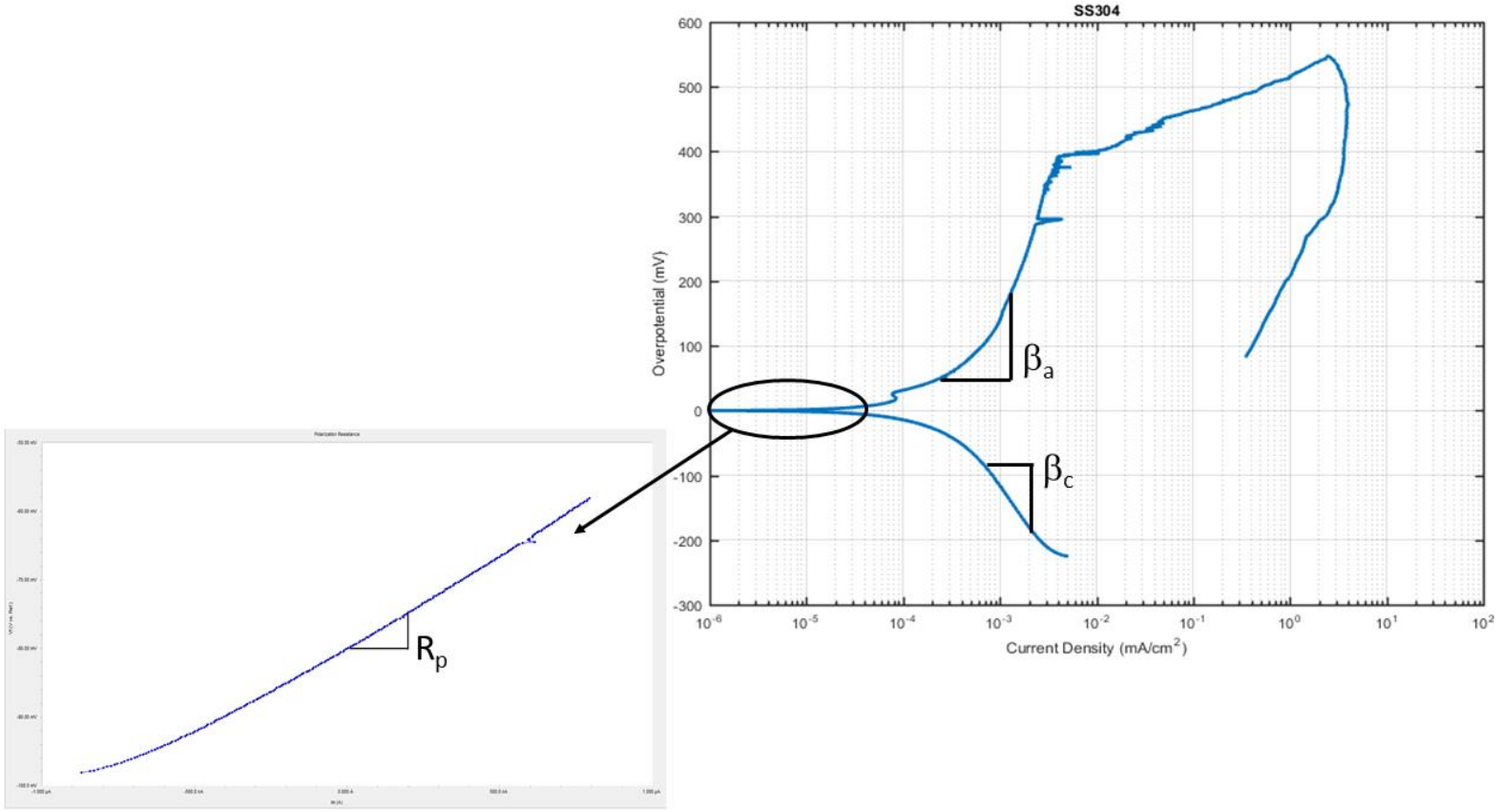

Figure 5-5: Cyclic polarization curve (right) and polarization resistance curve (left) for stainless steel type 304. Parameters are determined from the slope of the curves, as shown. R_p is the polarization resistance and β_a and β_c are the anodic and cathodic Tafel coefficients, respectively.

5.1.1.2 Corrosion Rate

In addition to providing information about passivity and localized corrosion, potentiodynamic polarization may also be used to determine uniform corrosion rates. Figure 5-5 shows the information relevant to determining corrosion rates that may be gathered from cyclic polarization curves. The process of calculating corrosion rates from polarization curves is described below.

The Butler-Volmer equation (Eq. (5.1)) is often used to describe the relationship between potential and current for a system undergoing a combination of anodic and cathodic electrochemical reactions.

$$I = I_{corr}\left(\exp\left[\frac{\alpha_a nF\left(E - E_{corr}\right)}{RT}\right] - \exp\left[\frac{-\alpha_c nF\left(E - E_{corr}\right)}{RT}\right]\right) \qquad (5.1)$$

Where: α_a, α_c are anodic and cathodic charge transfer coefficients,
F is Faraday's constant (= 9.6485E+04 C/mol),
n is the number of electrons involved in the reactions,
R is the universal gas constant (= 8.3144598 J/(K-mol)),
T is the absolute temperature (K),
E_{corr} is the corrosion (equilibrium) potential (V),
I_{corr} is the corrosion (equilibrium) current (A),
And I is the measured current (A).

The quantity 2.3RT/αnF is typically denoted as β [104], in which case Eq. (5.1) can be rewritten as:

$$I = I_a + I_c = I_{corr}\left(\exp\left(\frac{2.3\eta}{\beta_a}\right) - \exp\left(-\frac{2.3\eta}{\beta_c}\right)\right) \tag{5.2}$$

Where: I_a, I_c are anodic and cathodic currents (A),

η is the overpotential ($\eta = E - E_{corr}$, V),

And β_a, β_c are anodic and cathodic Tafel slopes (V/decade).

This gives a relationship between the current and the deviation from the equilibrium potential (overpotential) in terms of parameters characteristic of the coupling of the material and environment, the corrosion current and Tafel slopes, which is valid assuming kinetic control of the corroding system under observation. Measured potential versus current data may be fit to Eq. (5.2) using least squares fitting with I_{corr}, β_a, and β_c as the fitting parameters.

By restricting the potential to a region very close to the corrosion or equilibrium potential (low overpotential region), the exponentials can be expanded in a Taylor series about $\eta = 0$, resulting in the Stern-Geary equation [105]:

$$\left.\frac{d\eta}{dI}\right|_{\eta\to 0} = \frac{\beta_a\beta_c}{2.3I_{corr}\left(\beta_a + \beta_c\right)} \tag{5.3}$$

The left hand side of Eq. (5.3) is the slope of the potential versus current curve in the immediate vicinity of the equilibrium potential and is known as the polarization resistance, R_p. This is depicted in the picture on the left in Figure 5-5.

In the high overpotential region, it is simple to show that either the anodic or cathodic region dominates. The region of high positive overpotential, $\eta > 0$, is dominated by the anodic region, whereas the high negative overpotential region, $\eta < 0$, the cathodic reaction dominates. When anodic current dominates, Eq. (5.2) reduces to:

$$I \approx I_a = \exp\left(\frac{2.3\eta}{\beta_a}\right) \tag{5.4}$$

Rearranging Eq. (5.4), the overpotential may be written as:

$$\eta = a + b\log(I) = \frac{\beta_a}{2.3}\left[\ln(I) - \ln(I_{corr})\right] \tag{5.5}$$

Therefore, the anodic Tafel coefficient, β_a, is proportional to the slope of the voltage versus log current curve in the region of positive overpotential. The same applies for the cathodic Tafel coefficient, β_c, in the negative overpotential region. See Figure 5-5

Solving Eq. (5.3) for the corrosion current gives:

$$I_{corr} = \frac{\beta_a \beta_c}{2.3R_p(\beta_a + \beta_c)} \tag{5.6}$$

All terms on the right hand side of Eq. (5.6) can be determined experimentally, in which case the equilibrium current is immediately obtainable. Once the corrosion current has been calculated, Eq. can be used to relate corrosion current to corrosion rate for a given material undergoing oxidation and reduction reactions.

$$K_{corr} = \frac{I_{corr} \cdot k \cdot EW}{\rho \cdot A_e} \tag{5.7}$$

Where: ρ is the mass density (g/cm^3),

EW is the equivalent weight of the electrode (g),

A_e is the electrode area exposed to corrosion (cm^2),

k is a constant (= 3272 mm/(A-cm-year)),

And K_{corr} is the corrosion rate in millimeters per year (mmpy).

5.1.2 AC Electrochemistry

5.1.2.1 Theory

Applying a voltage signal $v(t) = V_m \sin(\omega t)$, consisting of a single frequency $f = \omega/2\pi$, to a cell will result in a steady state current $i(t) = I_m \sin(\omega t + \theta)$, where t is the time and V_m and I_m are peak amplitudes. This measured current will be of the same frequency as the applied voltage but will have shifted phase. The phase shift θ is the phase difference between the voltage and current and is zero for a purely resistive response [106]. Whereas resistive behavior is simple to characterize, the response of capacitive and inductive elements to sinusoidal voltage and current signals is not so trivial. For a capacitor: $i(t) = [dv(t)/dt]C$, and for an inductor: $v(t) = [di(t)/dt]L$, where C and L stand for capacitance in Farads and inductance in Henrys, respectively.

Fourier transformation allows for a simpler treatment of the resulting system of equations. The sinusoidal voltage and current signals may be rewritten as: $v(t) = V_m \exp(j\omega t)$ and $i(t) = I_m \exp(j\theta) \exp(j\omega t)$, where $j = \sqrt{-1}$. In order to simplify the use of these time-varying signals, Fourier transforms may be implemented. The Fourier transformations for the voltage and current are defined in Eqs. (5.8) and (5.9), which convert voltage and current signals from the time domain to frequency space.

$$F\{v(t)\} = V(j\omega) = \int_{\frac{-\pi}{2}}^{\frac{\pi}{2}} v(t)e^{-j\omega t}dt = \int_{\frac{-\pi}{2}}^{\frac{\pi}{2}} V_m e^{j\omega t}e^{-j\omega t}dt = \pi V_m \tag{5.8}$$

$$F\{i(t)\} = I(j\omega) = \int_{-\frac{\pi}{2}}^{\frac{\pi}{2}} i(t)e^{-j\omega t}dt = \int_{-\frac{\pi}{2}}^{\frac{\pi}{2}} I_m e^{j\theta}e^{j\omega t}e^{-j\omega t}dt = \pi I_m e^{j\theta} \tag{5.9}$$

By applying the definitions for capacitive and inductive elements above, these equations become:

$$F\left\{i(t) = \frac{dv(t)}{dt}C\right\} = I(j\omega) = \int_{\frac{-\pi}{2}}^{\frac{\pi}{2}} C\frac{dv(t)}{dt}e^{-j\omega t}dt = \int_{\frac{-\pi}{2}}^{\frac{\pi}{2}} j\omega CV_m e^{j\omega t}e^{-j\omega t}dt \tag{5.10}$$

$$= j\omega CV_m\pi = j\omega CV(j\omega)$$

$$F\left\{\mathrm{v}(t) = \frac{di(t)}{dt}L\right\} = V(j\omega) = \int_{\frac{-\pi}{2}}^{\frac{\pi}{2}} L\frac{di(t)}{dt}e^{-j\omega t}dt = \int_{\frac{-\pi}{2}}^{\frac{\pi}{2}} j\omega LI_m e^{j\theta}e^{j\omega t}e^{-j\omega t}dt \tag{5.11}$$

$$= j\omega LI_m\pi e^{j\theta} = j\omega LI(j\omega)$$

$$Z(j\omega) = V(j\omega)/I(j\omega) \tag{5.12}$$

Where Z, V, and I are the frequency-dependent impedance, voltage, and current, respectively.

Thus, Eq. (5.10) gives the relationship between current and voltage in the frequency domain for a capacitor, and Eq. (5.11) gives the same relationship for an inductor. Together with Eq. (5.12), the impedance of a capacitor and inductor in frequency space may be expressed as:

$$Z_C = \frac{1}{j\omega C} \tag{5.13}$$

And

$$Z_L = j\omega L \tag{5.14}$$

Both of these equations are much easier to implement than the expressions involving time derivatives given above, proving the utility of the Fourier transform. Impedance is a complex quantity consisting of both resistive and reactive components and is useful for characterizing circuits in terms of a single parameter. The following equations round out the necessary information required for a complete representation of impedance:

$$Z_R = R \tag{5.15}$$

$$Z = Z' + jZ'' \tag{5.16}$$

$$|Z| = \sqrt{(Z')^2 + (Z'')^2} \tag{5.17}$$

$$\theta = \tan^{-1}(Z''/Z') \tag{5.18}$$

$$Re(Z) = Z' = |Z|\cos\theta \tag{5.19}$$

$$Im(Z) = Z'' = |Z|\sin\theta \tag{5.20}$$

Where R is resistance, |Z| is the modulus of impedance, θ is the phase angle, and *Re*(Z) and *Im*(Z) are the real and imaginary components of impedance (resistance and reactance).

5.1.2.2 Application

Impedance measurements applied to systems under electrochemical control is termed Electrochemical Impedance Spectroscopy (EIS). Impedance spectroscopy has been widely applied to electrochemical systems because the impedance contains all of the information available to be extracted from the electrochemical system that can be captured using purely electrical measurements [107]. EIS allows for determination of fundamental properties of electrochemical systems and has become increasingly popular in the field of corrosion science as instruments have become available to extend measurements into the mHz range and below.

The impedance of a cell at a given frequency can be determined by applying a time-varying current perturbation and measuring the voltage response, or, more commonly, by applying a sinusoidal voltage perturbation with known amplitude and measuring the response current. This approach is referred to as potentiostatic (voltage-controlled) impedance spectroscopy (IS) and is generally preferred over galvanostatic (current-controlled) IS because it offers greater control over the kinetics in the cell. Repeating this measurement over a wide range of input frequency produces an impedance spectrum, which may be analyzed to produce information about the electrode-electrolyte system under investigation.

In practice, impedance measurements are limited by several factors. High frequency measurements are plagued by the inductance of the current- and voltage-measuring wires. The time varying current that flows through the wires generates a magnetic field, which causes inductive behavior in adjacent wires. The wire inductance can be as large as several hundred nH (nano Henrys). According to Eq. (5.14), the impedance of an inductor scales linearly with frequency. Thus, the impedance due to the mutual inductance of the measurement wires becomes significant above 50 to several hundred kHz depending on the arrangement of the wires. Fortunately, high frequency inductance is easy to spot in an impedance spectrum and is almost always an artifact of the measurement instrument. The cross talk between wires may be minimized by changing the wire geometry.

On the other end of the spectrum, low frequency measurements are susceptible to instabilities. Many electrochemical systems are not stable enough to allow for consistent measurements for frequencies below several mHz. This is especially true for impedance spectra intentionally measured away from equilibrium conditions. Resolution of very low (mΩ) or extremely high (TΩ) impedances is also dependent on instrument function, though typical electrochemical systems lie between these two extremes. Finally, and arguably most importantly, the impedance response must be linear. That is, the response to the sum of two simultaneous input signals must be the same as the response to the signals applied separately. In other words, the impedance must be independent of the magnitude of the AC voltage perturbation. As long as the perturbation amplitude is less than the thermal voltage (25 mV at 25°C), the governing equations become approximately linear [106]. This severely limits the use of simultaneous multi-frequency measurements, as the sum of all sinusoidal input signals must still be less than the thermal voltage for linearity to apply. Measured impedance spectra may (and should) be checked for linearity and stability by using the Kramers-Kronig relationships [107].

Raw impedance spectra provide little information about the system undergoing measurement. Analysis is required to extract desired information. This is typically

accomplished by fitting the impedance spectra to an equivalent circuit model consisting of circuit elements that can be linked to physical phenomena. For example, the Randles circuit depicted in Figure 5-6 is often used to fit impedance spectra of corroding metals. It consists of a resistor in series with a standard RC circuit. The series resistor is related to the uncompensated Ohmic resistance of the electrolyte solution, and the parallel resistor represents the charge transfer resistance of the electrode. The sum of the two resistances is equivalent to the polarization resistance, which was discussed in a previous section. Finally, the capacitor represents the geometrical capacitance, which captures any insulating behavior in the system. This is often linked to the Helmholtz capacitance of the double layer that forms at the electrode-electrolyte interface. Note that R.E. and W.E. stand for the reference electrode and working electrode, respectively, and are included to show the application of the equivalent circuit to EIS measurements.

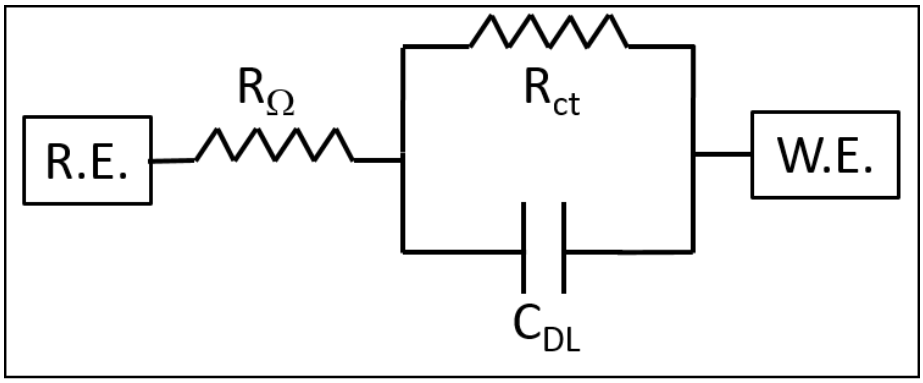

Figure 5-6: Randles circuit for EIS equivalent circuit modeling. R.E. and W.E. are the reference and working electrodes, R_Ω is the ohmic (electrolyte) resistance, R_{ct} is the charge transfer resistance of the working electrode, and C_{DL} is the double layer (Helmholtz) capacitance. Note that $R_p \sim R_\Omega + R_{ct}$.

The impedance response of the Randles circuit is displayed in Figure 5-7 and Figure 5-8. The impedance modulus and impedance phase angle are provided in Figure 5-7, which is

known as a Bode plot. The low frequency limit of impedance is equivalent to the polarization resistance (R_p), whereas the high frequency limit represents the Ohmic resistance of the cell (R_Ω). Figure 5-8 shows another characteristic response of a Randles circuit, which consists of a semicircle in the complex plane.

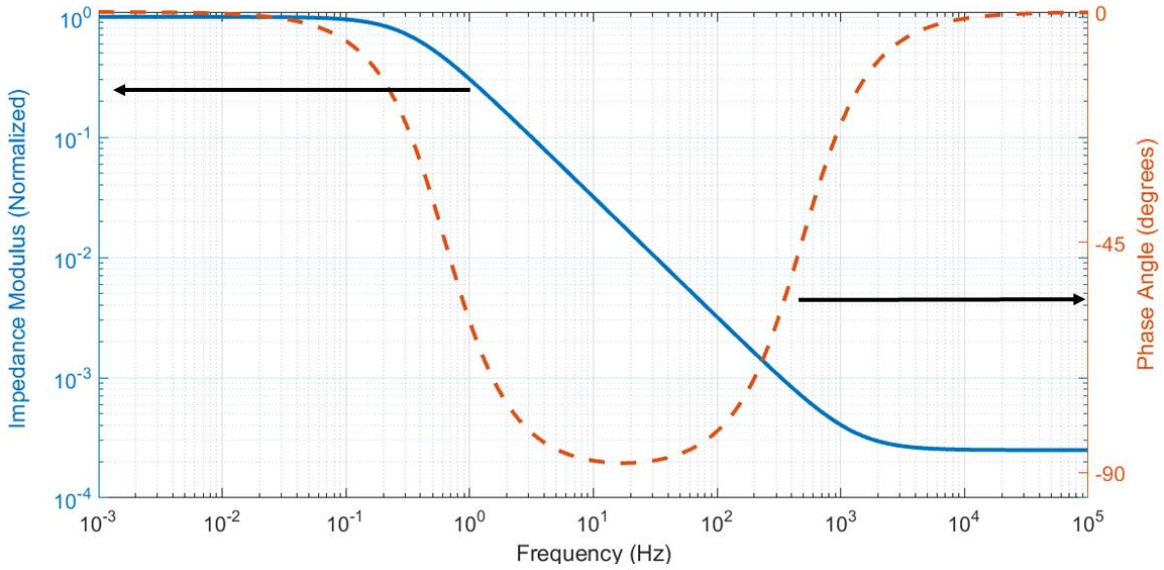

Figure 5-7: Normalized impedance response of a Randles circuit – impedance modulus and phase angle (Bode plot)

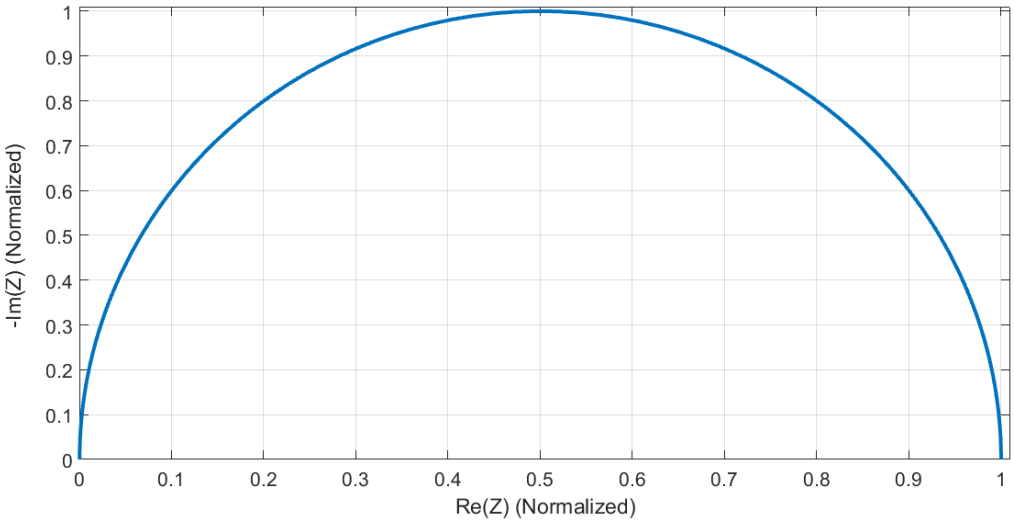

Figure 5-8: Normalized reactance versus resistance for a Randles circuit (Nyquist plot)

Any measured impedance may be modeled by an electrical circuit containing a finite number of elements (resistors, capacitors, and inductors) arranged in various configurations. Clearly, adding more appropriately-placed elements to an equivalent circuit will improve the fit to experimental data. The key, though, is to limit the circuit to elements that can be assigned physical analogs.

More complicated equivalent electrical circuits may be employed in the cases where the impedance response may not be represented by a single RC circuit. Adding additional circuit elements creates different combinations that produce the same impedance spectra. An example of this may be seen in Figure 5-9, which shows two different circuit combinations with the same number of elements. Both of these circuits are capable of modeling the same impedance response with appropriately-valued circuit elements. This introduces another layer of uncertainty in the impedance modeling. Prior knowledge of the proper range of values for elements in the equivalent circuit is required to choose between circuits in this case.

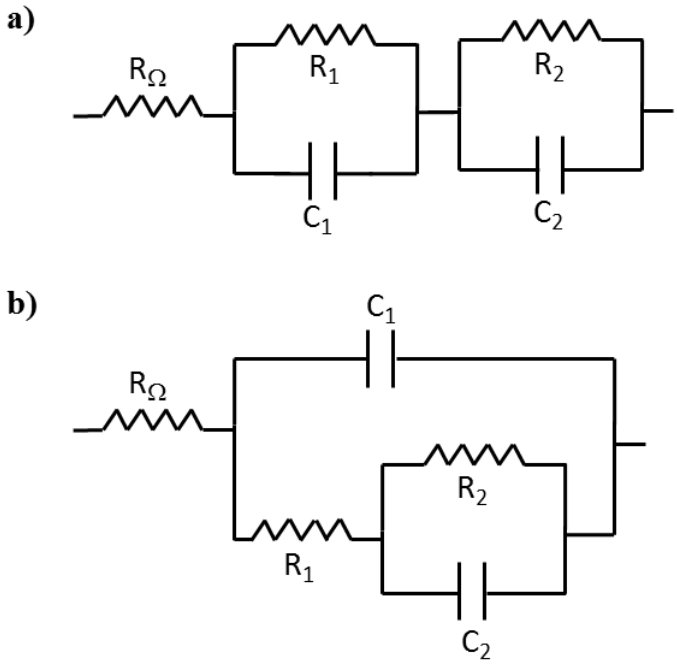

Figure 5-9: Two equivalent electrical circuits producing the same impedance response

The Echem Analyst from Gamry Instruments is used to fit impedance spectra to equivalent circuits. The program employs a simple user interface for circuit building and performs nonlinear least squares (NLLS) fitting between the measured impedance and the simulated impedance of the equivalent electrical circuit. Least squares fitting is based on minimizing the sum of the squares of the errors between data points and a given function, and the Echem Analyst gives the user a choice between two algorithms for NLLS: Levenberg-Marquardt and Simplex. The Levenberg-Marquardt algorithm [108] is a more robust version of the Gauss-Newton algorithm and is realized by using numerical derivatives of the error function. It is susceptible to being trapped by local minima instead of converging to the global minimum. The simplex algorithm [109] randomly generates initial points around starting values to work downhill in the error surface toward the function minimum. It is generally slower than the Levenberg-Marquardt method but avoids the pitfalls of getting stuck in local minima.

Generally, the simplex method is useful for an initial fit, and the L-M method can be implemented for final convergence. In this work the simplex method is preferred because the selection of initial values is more forgiving and it reaches final convergence more efficiently, but both algorithms produce nearly identical NLLS parameters in the end.

5.1.2.3 Constant Phase Element

A primary difficulty of fitting experimentally-obtained impedance data using standard circuit elements is that many metal-electrolyte systems do not exhibit ideal capacitive behavior. This deviation from ideality gives rise to the use of the constant phase element (CPE) to replace the capacitor in equivalent circuit models of measured impedance data. The CPE, which is purely a mathematical construct, has impedance given by:

$$Z_{CPE} = \frac{1}{(j\omega)^{\alpha} Q} \tag{5.21}$$

Where α and Q are the characteristic CPE parameters. The CPE exponent α varies between 0, corresponding to an ideal resistor, and 1, for an ideal capacitor. Q has units of Ω^{-1} s^{α} and is equivalent to capacitance for α = 1 (Ω^{-1} s = F).

Unlike a resistor or a capacitor, the CPE has both resistive and reactive components of its impedance. This comes from the fact that $j^{\alpha} = \cos(\alpha\pi/2) + j \sin(\alpha\pi/2)$. The real and imaginary components of the CPE impedance are given in the following equations:

$$Z'_{CPE} = Re\left(Z_{CPE}\right) = \frac{\cos\left(\alpha\frac{\pi}{2}\right)}{\omega^{\alpha}Q} \tag{5.22}$$

$$Z''_{CPE} = Im\left(Z_{CPE}\right) = \frac{-\sin\left(\alpha\frac{\pi}{2}\right)}{\omega^{\alpha}Q} \tag{5.23}$$

The CPE parameters may be determined from impedance spectra by NLLS fitting to a proper equivalent circuit, or by employing Eq. (5.24), which is obtained by rearranging Eq. (5.23). Calculation of Q and α comes from the slope and intercept of a linear fit to ln(Z'') vs. ln(ω). This method has the advantage of not needing to assume an equivalent circuit if one is not known.

$$\ln\left(Z''\right) = -\alpha\ln\left(\omega\right) + \ln\left(\sin\left(\alpha\frac{\pi}{2}\right)Q^{-1}\right) \tag{5.24}$$

It is clear from Eq. (5.24) that the CPE exponent α may also be calculated as a function of frequency using [110], [111]:

$$\alpha\left(\omega\right) = \left|\frac{d\ln\left(\left|Z''\left(\omega\right)\right|\right)}{d\ln\left(\omega\right)}\right| \tag{5.25}$$

The CPE fits a wide range of experimental conditions with only two adjustable parameters, but it is not rooted in any physical processes. Because of this, the origin of CPE behavior in electrochemical systems has been significantly debated. However, it was initially proposed by

Cole and Cole in 1941 [112], who attributed the behavior to a distribution of time constants ($\tau = RC$), which may occur due to a distribution of capacitance or resistance (or both). This is generally considered to arise from distributions of physical properties. In the literature, the origin of CPE behavior in electrochemical systems has been attributed to porosity, surface roughness, grain boundaries, material inhomogeneity, dielectric relaxation, double layer effects, etc. [113]. The prevailing theory was that the frequency dispersion of the measured capacitance related in some manner to the surface roughness. For example, the CPE exponent, which is a measure of the deviation from ideal capacitive behavior, has been shown to decrease monatonically with increasing surface roughness for platinum electrodes [114], pointing toward increasing frequency dispersion with an increase in surface roughness. However, theories crafted to relate capacitance dispersion solely to the electrode geometry have failed to capture the frequency dependence of the capacitance in the frequency range that is measured experimentally [115], [116]. More recently, CPE behavior has been related to surface energetics and atomic-scale heterogeneity [111], a theory which is supported by the work of Kerner and Pajkossy [116], [117], in which annealing of the electrode prior to testing was shown to decrease capacitive dispersion. They also showed that after sufficient annealing, and in the absence of Faradaic reactions and anion adsorption, single crystalline noble metals could attain very nearly-ideal interfacial capacitance ($\alpha \sim 1$). This seems to point toward differences in surface energetics, which includes compositional differences, ion adsorption, etc., as a prime candidate for the origin of capacitive dispersion [118], though further investigation is certainly required. Despite that the origin of constant phase behavior remains uncertain, it is widely used in impedance modeling to improve the fit of equivalent circuits.

5.2 Corrosion in Circulating Salt Brines

As an additional source of corrosion testing, bare and coated steel samples are placed in circulators with brines of different pH for as long as 150 days. A picture of the circulators is provided in Figure 5-10. Piping is made from PVC and the pumps used are capable of circulating liquid at 1 gallon per minute. The mass of each sample is measured at regular intervals to determine the change in weight due to corrosion. The compositions of the corrosive solutions are given in Table 5-1. Circulating solutions are simulated concentrated waters (SCW) meant to emulate ground water compositions that are present in Yucca Mountain [119]. The solutions contain significant concentrations of chlorides and cover a wide pH range.

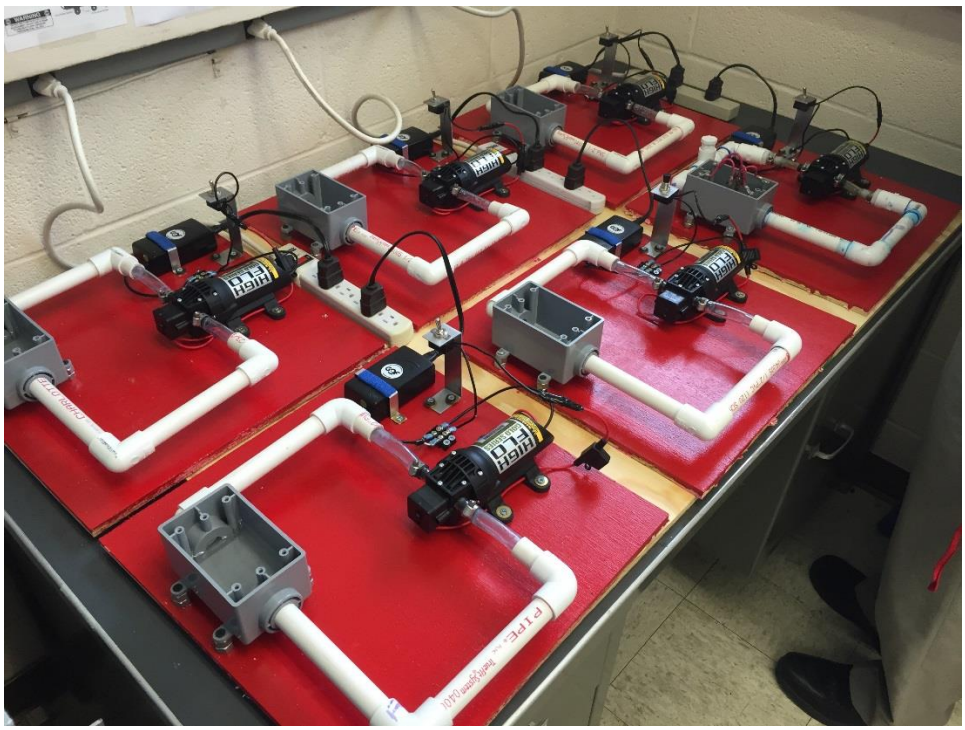

Figure 5-10: Circulators used for extended corrosion testing

Table 5-1: Composition of simulated concentrated water solutions used in circulators

pH = 2.4		**pH = 8.2**		**pH = 13.15**	
Compound	**Quantity**	**Compound**	**Quantity**	**Compound**	**Quantity**
H_2O	1000 mL	H_2O	800 mL	H_2O	800 mL
NaCl	70 g	KCl	120 g	KCl	90 g
KCl	70 g	Na_2SO_4	20 g	NaCl	80 g
KNO_3	15 g	NaCl	90 g	Na_2SO_4	15 g
$MgSO_4$	15 g	$MgSO_4$	30 g	NaOH	20 mL
NaOH	5 mL	KNO_3	15 g		
H_2SO_4	3 mL				

5.2.1 Results

Bare and coated stainless steel samples showed no measurable weight change over a 140-day period in any of the three solutions. More importantly, the coatings were still intact following extended submersion. This confirms good corrosion resistance and adhesion of the protective coatings.

Carbon steel samples saw measurable corrosion in all solutions, with up to 3% weight loss after almost 5 months. Corrosion in the low pH solution was highest, as sulfuric acid makes for an aggressive solution. It is expected that carbon steel will experience measurable corrosion, especially in acidic conditions. Figure 5-11 shows graphs of measured mass over time for four coated steels in each of the three SCW solutions. Mass remains nearly unchanged for all but the carbon steels in the acidic solution. Coated and bare steels show the same trends.

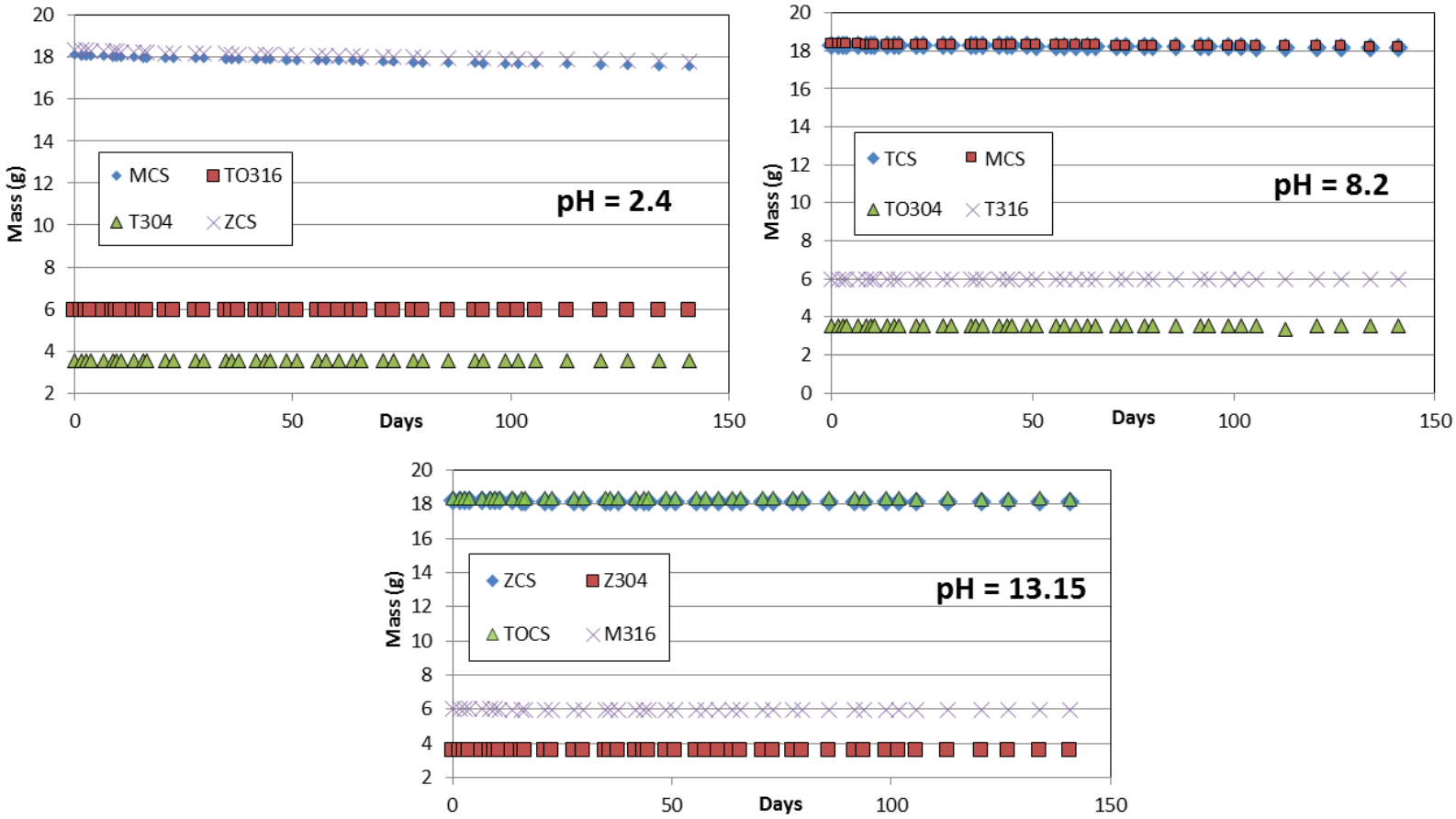

Figure 5-11: Measured mass over time of coated steels in three different SCW solutions – solution pH is provided

CHAPTER 6

CORROSION OF SINGLE LAYER PROTECTIVE COATINGS ON STEEL SUBSTRATES

A portion of this chapter is published in the journal Progress in Nuclear Energy: "Corrosion of single layer thin film protective coatings on steel substrates for high level waste containers," Michael A. Fusco, Yasar Ay, Abigail H.M. Casey, Mohamed A. Bourham, and A. Leigh Winfrey, Vol. 89, pp. 159-169, May 2016, DOI: 10.1016/j.pnucene.2016.02.016.

6.1 Experimental Methods

Electrochemical testing was completed using the MULTIPORT™ corrosion cell kit and Interface 1000 potentiostat from Gamry Instruments, along with the DC105 electrochem software. A standard three electrode setup with a graphite counter electrode and saturated Ag/AgCl reference electrode is used. The reference electrode is placed directly in the corrosion cell to avoid problems posed by a salt bridge. The samples are placed in a holder conducive to testing disks of vary thickness, such that the total exposed surface area to the aerated 1 M NaCl solution is 4.15 cm^2.

Prior to testing, the stainless steel samples are immersed in the testing solution for 15 to 24 hours, allowing the open circuit potential to stabilize. Carbon steel samples equilibrate much more rapidly and need only be placed in solution 1-3 hours before testing. Temperature is controlled using a water bath and thermocouple placed inside the polarization cell. Voltage

drop due to resistance of the NaCl solution is accounted for by the software controlling the potentiostat using the current-interrupt method [120].

Cyclic potentiodynamic polarization curves are measured for each sample to determine corrosion rate and passivation capabilities. These curves encompass both high and low overpotential regions and thus can provide corrosion rates without additional testing. The data gathered can be used for quantitative analysis provided the voltage scan rate is slow. The scan rate used for all electrochemical analysis presented here is 0.6 V/hr (0.1667 mV/s), in accordance with ASTM standard G61-86 [121]. The forward voltage scan is measured from 250 mV below the open circuit potential (E_{oc}) to 1.2 V above E_{oc}, or until a critical current density is reached. The reverse scan begins immediately following the forward scan and proceeds at the same scan rate. The reverse san determines the localized corrosion behavior in the form of a hysteresis in the voltage-current relationship. These tests are completed at temperatures of 20, 40, 60, and 80°C to simulate elevated canister temperatures due to decay heat.

Slopes of the anodic and cathodic half reactions are determined separately from the Echem Analyst™ software from Gamry Instruments, using an 'E log I' fit within 250 mV of the corrosion potential (high overpotential region), which is the region in which Eq. (5.5) applies. Polarization resistance is then calculated by extracting the data within the low overpotential region (± 5 mV from E_{corr}) and performing a linear regression. R_p is established as the slope of this line. From this, Eqs. (5.6) and (5.7) are used to compute the corrosion current and corrosion rate. Several samples of each material at each of the four temperatures are tested; the values of corrosion current presented are averages. The MoS_2 coatings suffered from adhesion issues and thus were not included in this study.

6.2 Kinetic Activation

The corrosion current (or corrosion rate) has been shown to follow an Arrhenius relationship with temperature [122]–[124]:

$$i_{corr} = A \cdot \exp\left(\frac{-E_a^0}{RT}\right) \tag{6.1}$$

Where: i_{corr} is the corrosion current density ($\mu A/cm^2$),
A is the pre-exponential factor ($\mu A/cm^2$),
And E_a^0 is the apparent activation energy (kJ/mol).

A larger activation energy is indicative of a higher energy barrier for corrosion to occur [125]. The activated, or transition state, complex can be formed faster and easier for smaller activation energies. The apparent activation energy has been shown to decrease as the concentration of acid in the corrosive solution increases [126]. This further supports that the activation energy represents an energy barrier to corrosion.

Alternatively, a more appropriate relationship between corrosion rate and temperature may be expressed using the Eyring equation derived from transition state theory [125]–[127]:

$$i_{corr} = \frac{RT}{N_a h}\exp\left(\frac{\Delta S_a^0}{R}\right)\exp\left(\frac{-\Delta H_a^0}{RT}\right) \tag{6.2}$$

Where: N_a is Avogadro's number (= 6.022e23 mol^{-1}),
h is Planck's constant (= 6.626e-34 J-s),
And ΔS_a^0 and ΔH_a^0 are the entropy and enthalpy of activation, respectively.

Eq. (6.2) encompasses the fact that the activation energy may be misleading if significant reordering occurs during the corrosion process such that entropy is large. It also provides a more complete relationship between corrosion rate and temperature, as it accounts for the total free energy, and the pre-exponential factor is not empirical, as in Eq. (6.1). Eq. (6.2) may be rewritten in order to determine the activation enthalpy and entropy from the slope and intercept of a linear fit to ln (i_{corr}/T) versus the reciprocal of temperature:

$$\ln\left(\frac{i_{corr}}{T}\right)=\left[\ln\left(\frac{R}{N_a h}\right)+\frac{\Delta S_a^0}{R}\right]-\left(\frac{\Delta H_a^0}{R}\right)\frac{1}{T} \tag{6.3}$$

The Gibbs free energy of the corroding system can be calculated from entropy and enthalpy:

$$\Delta G=\Delta H-T\Delta S \tag{6.4}$$

Kinetic properties are typically used to describe corrosion in the presence of an inhibitor [122], [124]–[126]. Whereas there is no inhibitor dissolved in the testing solution, the coatings themselves may be considered to function as inhibitors. The coverage of the steel surface by the coatings could influence the corrosion rate, as is typically the case with inhibitors. Transition state theory has also been applied to describe corrosion in the presence of oxide films on metals [127], representing the primary corrosion resistance of stainless steel.

6.3 Results and Discussion

6.3.1 Corrosion Rate of Bare and Coated Steels

Average corrosion current density versus temperature is plotted in Figure 6-1, Figure 6-2, and Figure 6-3 for bare and singly-coated steels in 1 M NaCl. The corrosion current density increases exponentially with temperature and can be described by either Eq. (6.1) or Eq. (6.2), as discussed previously. Corrosion current (Eq. (5.6)) is more indicative of corrosion behavior than the corrosion rate calculated using Eq. (5.7). Proper calculation of the corrosion rate requires an appropriate mass density and equivalent weight of the corroding surface. This can be ambiguous with porous coatings of sub-micron thickness because the coating material and steel substrate together constitute the corrosion system. Determining mass density and equivalent weight requires knowledge of the maximum depth from which ions from the steel could reach the surface and desorb into solution. Instead, corrosion current can be calculated with no material properties and better represents the propensity for the material to corrode in a given solution.

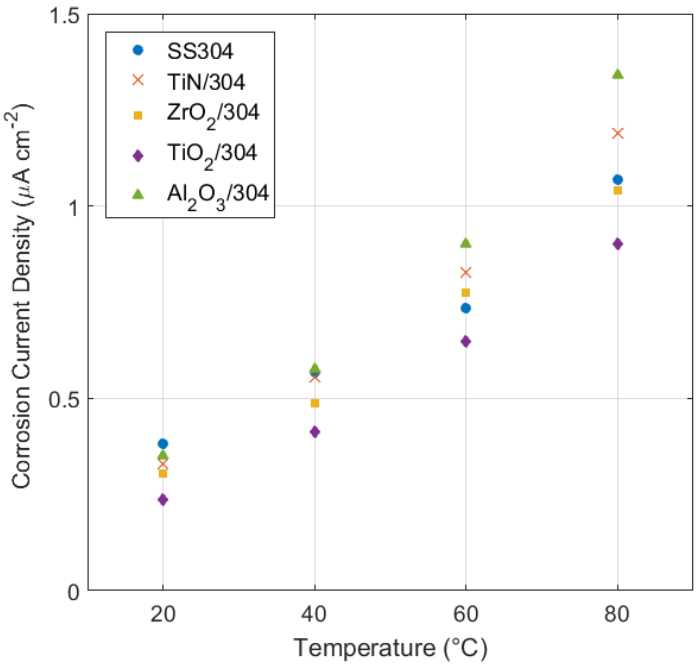

Figure 6-1: Average corrosion current density vs. temperature – SS304

The values of corrosion current for the coated steels are quite similar to the bare steel, suggesting that the steel substrate is corroding along with the surface coatings. Considering that the coatings are thin (most are less than 100 nm thick), it is likely that the coatings are porous, causing ions from both the substrate and coating to flow into the solution. However, the coated samples also do not show significantly higher corrosion rates, indicating that corrosion is not enhanced by placing a more noble metal in contact with steel.

Carbon steel samples show corrosion currents several orders of magnitude larger than stainless steel. This is expected, as A36 steel lacks Ni and Cr, which are essential to the corrosion resistances exhibited by type 304 and 316 stainless steels. Figure 6-3 shows that the coated samples have consistently lower corrosion rates than the bare carbon steel. This signifies that the coatings may be able to protect carbon steel, which corrodes more readily than stainless, if the thickness and number of coating layers increases.

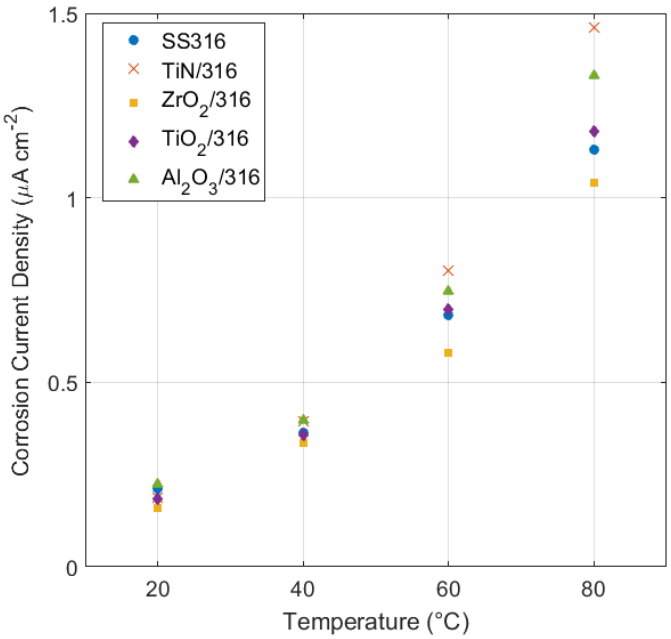

Figure 6-2: Average corrosion current density vs. temperature – SS316

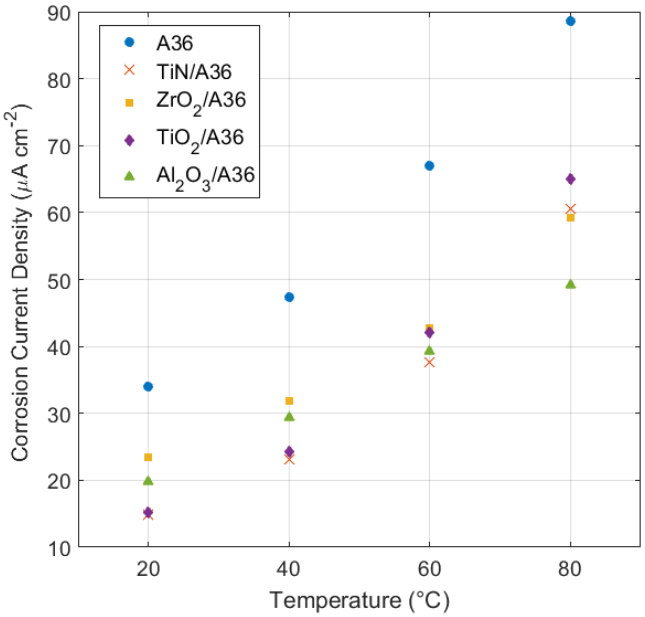

Figure 6-3: Average corrosion current density vs. temperature – A36

6.3.2 Kinetic Activation

Figure 6-4, Figure 6-5, and Figure 6-6 show the logarithm of the corrosion current density divided by absolute temperature, $\ln(i_{corr}/T)$, versus the inverse of absolute temperature. The materials tested show linear trends, in accordance with Eq. (6.3), displaying their activation-type behavior.

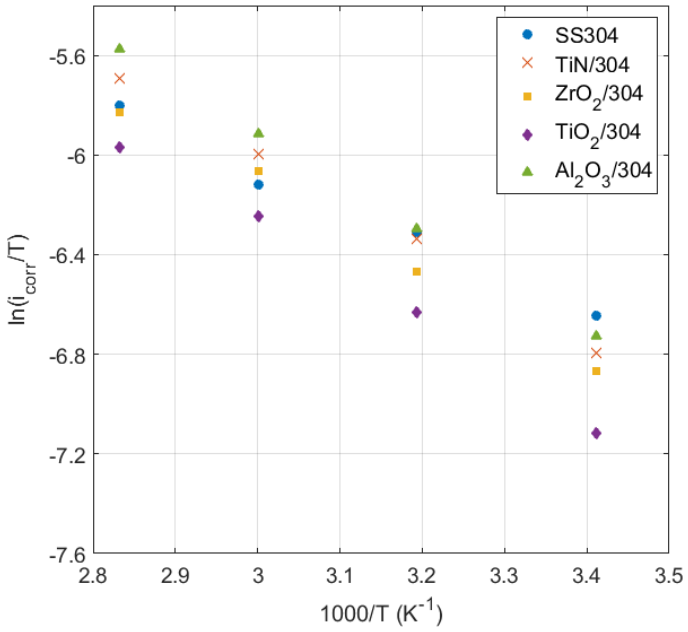

Figure 6-4: Activation kinetics: application of the Eyring equation for SS304

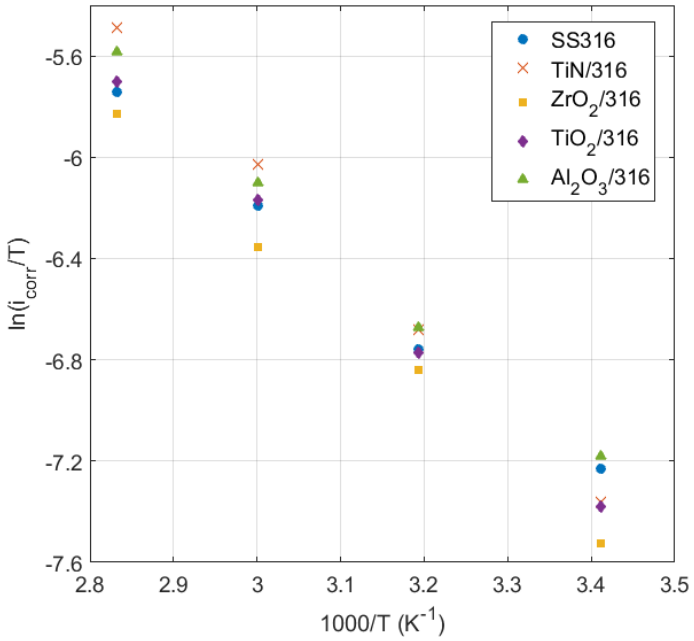

Figure 6-5: Activation kinetics: application of the Eyring equation for SS316

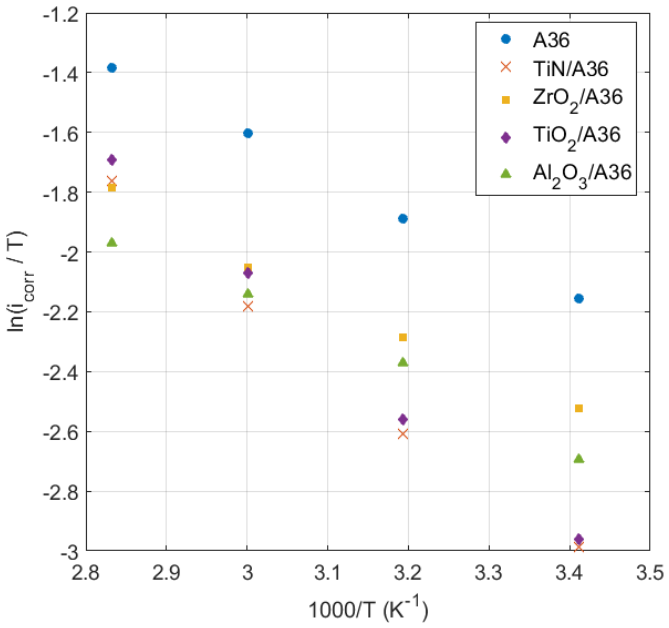

Figure 6-6: Activation kinetics: application of the Eyring equation for A36

The kinetic parameters computed using Eqs. (6.1) and (6.2) are presented in Table 6-1, Table 6-2, and Table 6-3 for the materials studied in aerated 1 M NaCl. Ln(A) is the natural logarithm of the pre-exponential factor in Eq. (6.1) and E_a, H_a, and S_a are the apparent activation energy, activation enthalpy, and activation entropy, respectively. The standard deviations are calculated using uncertainty propagation assuming independent (non-correlated) variables and account for experimental uncertainty and uncertainty from the linear regression.

Table 6-1: Activation parameters – SS304

Material	**Ln(A)**	**E_a (kJ/mol)**	**H_a (kJ/mol)**	**S_a (kJ/mol)**	**E_a - H_a**
SS304	4.96	14.45 ± 4.85	11.78 ± 4.85	-212.61 ± 15.39	2.67
TiN / 304	6.44	18.38 ± 5.74	15.71 ± 5.74	-200.3 ± 17.99	2.67
ZrO_2 / 304	6.13	17.82 ± 4.15	15.15 ± 4.15	-202.88 ± 13.18	2.67
TiO_2 / 304	6.47	19.2 ± 5.63	16.54 ± 5.63	-200.1 ± 17.72	2.67
Al_2O_3 / 304	6.83	19.19 ± 4.37	16.52 ± 4.37	-197.12 ± 13.62	2.67

Table 6-2: Activation parameters – SS316

Material	**Ln(A)**	**E_a (kJ/mol)**	**H_a (kJ/mol)**	**S_a (kJ/mol)**	**E_a - H_a**
SS316	8.37	24.27 ± 4.09	21.6 ± 4.08	-184.28 ± 13.06	2.67
TiN / 316	10.48	29.65 ± 11.32	26.95 ± 11.5	-166.79 ± 35.3	2.67
ZrO_2 / 316	9.15	26.76 ± 2.95	24.09 ± 2.95	-177.83 ± 9.45	2.67
TiO_2 / 316	9.38	27.02 ± 4.47	24.35 ± 4.47	-171.91 ± 11.8	2.67
Al_2O_3 / 316	9.01	25.72 ± 5.12	23.05 ± 5.11	-186.46 ± 10.2	2.67

Table 6-3: Activation parameters – A36

Material	Ln(A)	E_a (kJ/mol)	H_a (kJ/mol)	S_a (kJ/mol)	E_a - H_a
SS316	9.2	13.85 ± 6.53	11.18 ± 6.53	-177.41 ± 20.36	2.67
TiN / 316	10.95	20.21 ± 6.58	17.55 ± 6.57	-162.82 ± 20.72	2.67
ZrO_2 / 316	8.54	13.17 ± 6.65	10.51 ± 6.65	-182.86 ± 20.8	2.67
TiO_2 / 316	11.35	21.12 ± 6.41	18.45 ± 6.41	-159.46 ± 20.12	2.67
Al_2O_3 / 316	8.35	13.02 ± 3.68	10.35 ± 3.68	-184.42 ± 11.69	2.67

Positive values of enthalpy and apparent activation energy reflect the endothermic nature of the dissolution process. Negative entropy values represent that the activated complex is in a more ordered state relative to the initial state. In other words, the system becomes less chaotic as corrosion occurs

The apparent activation energy and activation enthalpy are seen to behave according to the following equation, which stems from comparison of the Arrhenius (Eq. (6.1)) and Eyring (Eq. (6.2)) equations for activation:

$$E_a - H_a = RT \tag{6.5}$$

Where: E_a is the apparent activation energy (kJ/mol),

And H_a is the enthalpy of activation (kJ/mol).

E_a – H_a = 2.67 kJ/mol for each material, and the average of RT over the applicable temperature range is 2.69 kJ/mol. This confirms that the corrosion process is a unimolecular reaction with a single transition state [128].

The coated stainless steels have activation energies (and enthalpies) that are within one standard deviation of each other. Both bare steels show markedly lower activation energy than their coated counterparts but still lie within statistical significance. This difference may become more significant as coating thickness increases and multilayer coatings are introduced, resulting in better corrosion resistance. The activation parameters are significantly different between SS304 and SS316. SS304 has lower activation enthalpy but higher entropy than SS316. However, Figure 6-7 and Figure 6-8 show that the Gibbs free energy of SS304 and SS316, both bare and coated, are nearly identical for each temperature tested. This indicates analogous corrosion behavior. Differences in free energy between bare and coated stainless steel substrates are within standard deviation. The Gibbs free energy (Eq. (6.4)) incorporates both activation enthalpy and entropy and provides the simplest way to compare activation behavior. Ultimately, the free energy determines the relationship between corrosion rate and temperature, as is exhibited by combining Eqs. (6.2) and (6.4) to obtain an alternate form of the Eyring equation:

$$i_{corr} = \frac{RT}{N_a h} \exp\left(\frac{-\Delta G}{RT}\right) \tag{6.6}$$

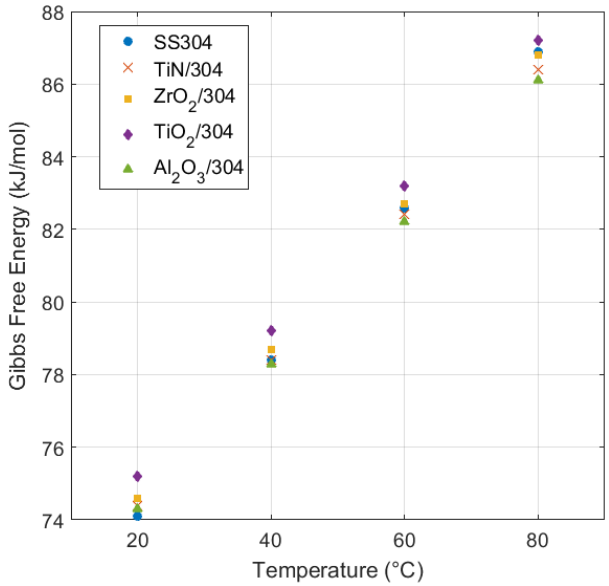

Figure 6-7: Gibbs free energy of activation versus temperature – SS304

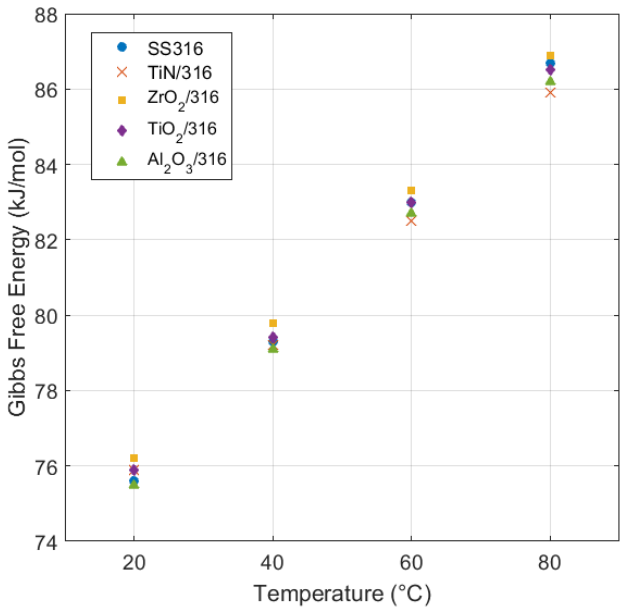

Figure 6-8: Gibbs free energy of activation versus temperature – SS316

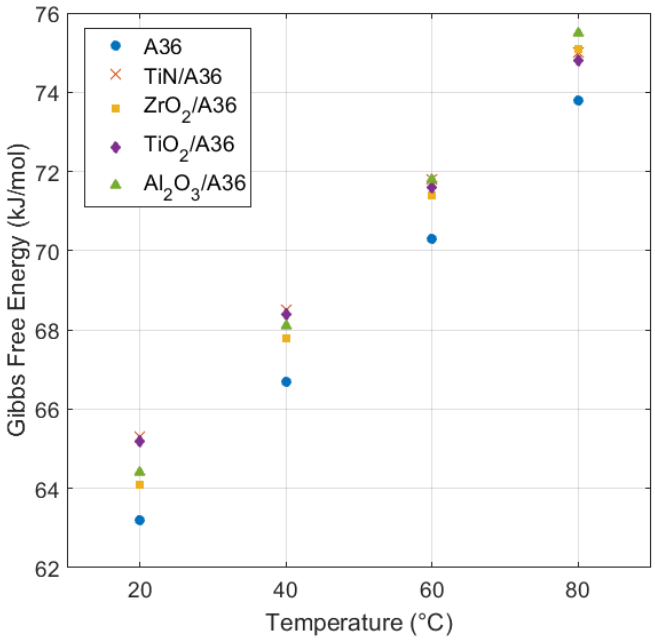

Figure 6-9: Gibbs free energy of activation vs. temperature – A36

Coating materials on A36 steel show two distinct slopes in Figure 6-6. Titanium-containing compounds (TiN and TiO_2) have activation energy of approximately 20 kJ/mol, whereas the remaining oxide compounds (ZrO_2 and Al_2O_3) exhibit activation energy hovering around 13 kJ/mol. Bare A36 steel also has an activation energy slightly above 13 kJ/mol, demonstrating that zirconia and alumina may not provide the same level of protection from corrosion as the titanium compounds. However, the oxide coatings are all under 100 nm thick, so increasing the thickness of the coating will likely improve corrosion resistance. The Gibbs free energy of activation is plotted in Figure 6-9 for A36 steel. The values of free energy are lower for uncoated A36 but lie within uncertainty of the values for coated A36. These values are lower than for the two types of stainless steel, which is natural because a larger Gibbs free energy represents a larger corrosion barrier to be overcome. This can be seen in Figure 6-10, which depicts the free energy of the three types of steel (uncoated) with corresponding error bars.

Both stainless steels lie very close together and are well within uncertainty of each other. Although the large error bars for A36 infringe on the uncertainty range of SS304 and SS316, its free energy is still distinctly lower for each temperature.

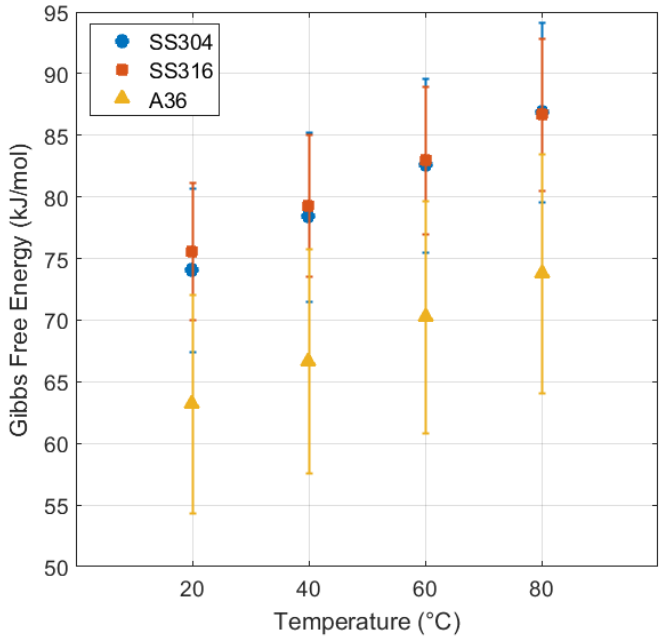

Figure 6-10: Gibbs free energy of activation vs. temperature – all steel substrates with error bars

6.3.3 Passivity and Passive Breakdown

The capacity for passivation can be determined from cyclic polarization curves, examples of which are shown in Figure 6-11, Figure 6-12, and Figure 6-13. The passive region is defined by a small change in current over a large potential range, which corresponds to a near-vertical

line on the polarization curves. A discussion of the acquisition of polarization curves and the features of interest may be found in Chapter 5.

All of the materials studied show decreasing passivity, in the form of a smaller passive region, with increasing temperature. Raising the temperature enhances the diffusion of oxygen and chloride ions and vacancies in the passive film, increasing the likelihood of passive breakdown. In most cases, the polarization curves reveal that passivity is nonexistent at 80°C, showing that temperature has a significant effect on corrosion resistance. The shape of the cyclic polarization curves is very similar for all coatings, which is the reason that curves for only one coating on each steel are provided. This suggests that the corrosion of all samples is influenced by the steel substrate regardless of the coating material.

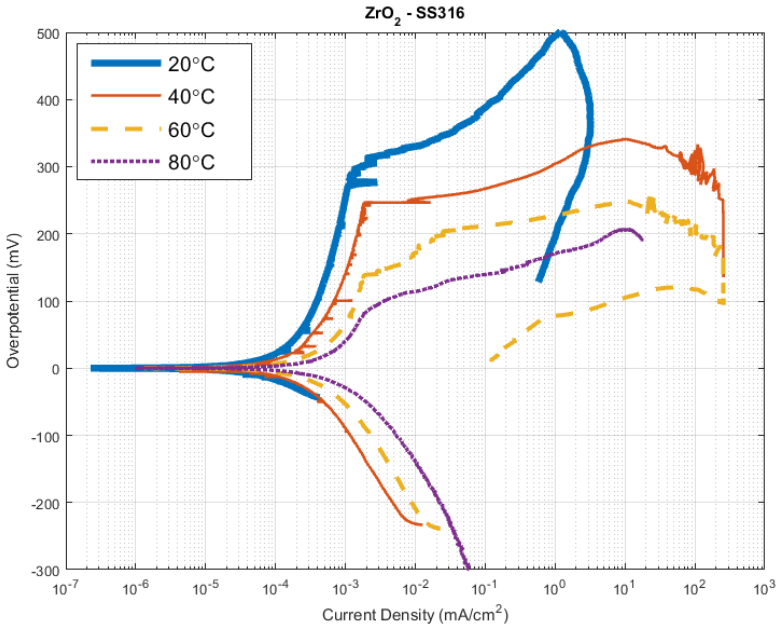

Figure 6-11: Cyclic polarization curves – ZrO_2 / SS316

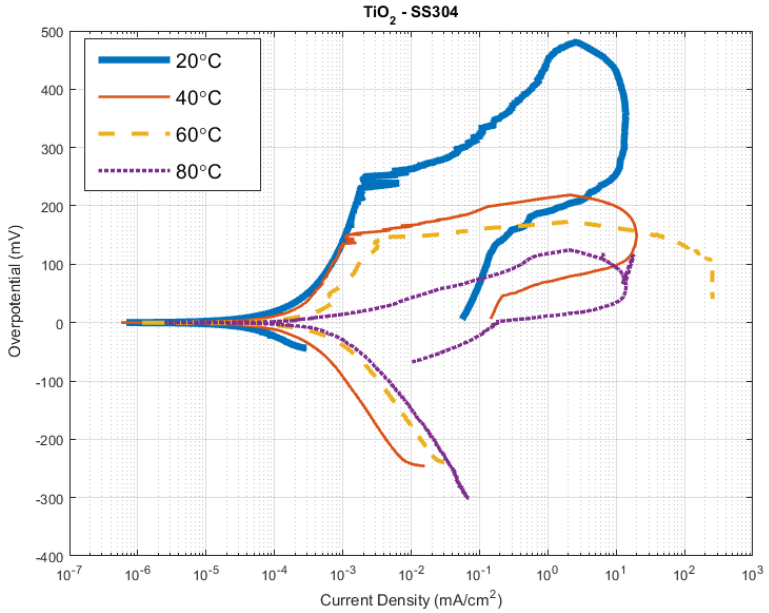

Figure 6-12: Cyclic polarization curves – TiO_2 / SS304

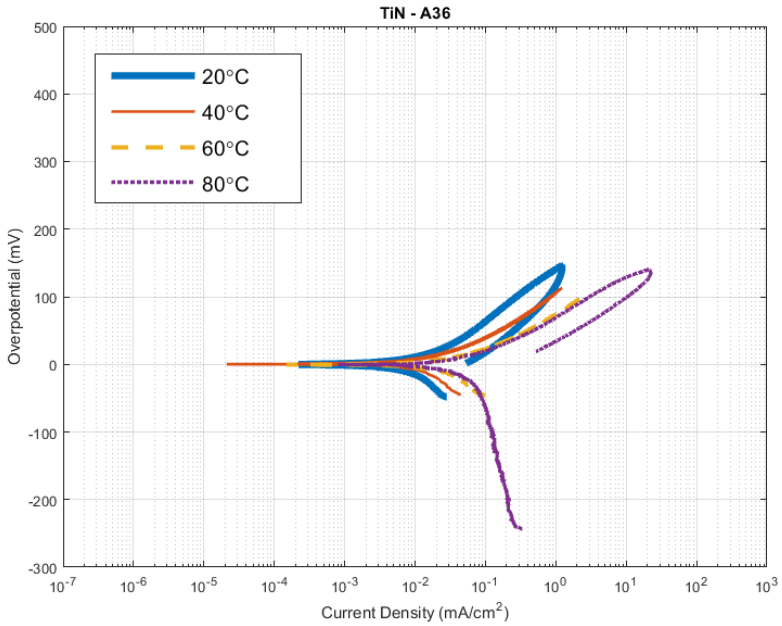

Figure 6-13: Cyclic polarization curves – TiN / A36

The A36 steel exhibits no discernible passivity because it corrodes uniformly at a much higher rate than stainless steel. Most iron oxide films that form on the surface are readily dissolved by corrosion on the surface of the metal. Iron (and low-alloy steels) is capable of passivating at in certain environments at very high critical current densities (~ 1-10 A/cm^2), though current above 1 A cannot be measured by the potentiostat in use, so current densities were kept well below the supposed critical values for iron. Thus, no passive behavior was observed for A36 mild steel. However, not forming a protective passive film means no breakdown and limited localized corrosion. The cyclic polarization curves for A36 show very little hysteresis, indicative of minimal pitting or crevice corrosion. The corrosion of carbon steel is quite predictable in what seems to be the absence of significant localized corrosion. Although carbon steel would require thicker containers to account for steady corrosion, it is not nearly as susceptible to SCC and pitting, which are the primary downfalls of stainless steel. Having a predictable service life may be of interest, especially in nuclear waste storage.

The breakdown voltage can be used as a measure of the passive capabilities of a material. A larger overpotential for initiation of pitting characterizes more desirable passive behavior. A majority of bare and coated stainless steel samples showed signs of crevice corrosion at points of contact with the sample holder, which occurs following interruption of the passive film. The passive breakdown voltage cannot be linked to the critical pitting potential until crevice corrosion is eliminated. Rather, the breakdown voltage marks the onset of localized attack, including pitting and crevice corrosion. It should be noted that elimination of crevice corrosion was later achieved by masking portions of the sample prone to forming crevices in the sample holder. A lack of crevice corrosion did very little to influence the breakdown voltage but proved important in the size of the hysteresis loop and in determining the re-passivation potential.

Similarly to corrosion current density, experimental values of breakdown overvoltage show an exponential relationship with temperature. The effective passive range decreases with temperature, also decreasing the breakdown potential. As was explained in Chapter 3, passive

breakdown is primarily controlled by vacancy diffusion, and so the Arrhenius-type behavior, given by Eq. (6.7) , of the breakdown potential is intuitive. The breakdown potential may be associated with an activation energy that is congruent to the activation energy for vacancy formation and diffusion.

$$\eta_{BD} = C \cdot \exp\left(\frac{-E_a^0}{RT}\right) \tag{6.7}$$

Where: η_{BD} is the breakdown overpotential (V),

C is the pre-exponential factor

And E_a^0 is the activation energy for passive breakdown (kJ/mol).

The exponential behavior of the passive breakdown overpotential with temperature is displayed in Figure 6-14 and Figure 6-15 for both types of stainless steel. A36 steel is omitted because it displayed no discernible passivity and thus no passive breakdown. The logarithm of breakdown overvoltage (η_{BD}) versus inverse temperature may be fit to a straight line, according to Eq. (6.7), to determine the breakdown activation energy, which are given in Table 6-4 for bare and coated stainless steel.

Both stainless steels and each coating material exhibit very similar breakdown behavior. The activation energies are all nearly identical within the confidence range. The alumina coatings on both steels are outliers in terms of apparent activation energy. The activation energy for the alumina coating on the type 316 stainless steel is lower than expected, and it is higher than expected on type 304 stainless steel. The true value likely lies between these two extremes, considering the corrosion behavior and shape of the cyclic polarization curves for alumina coatings was identical to that of other materials.

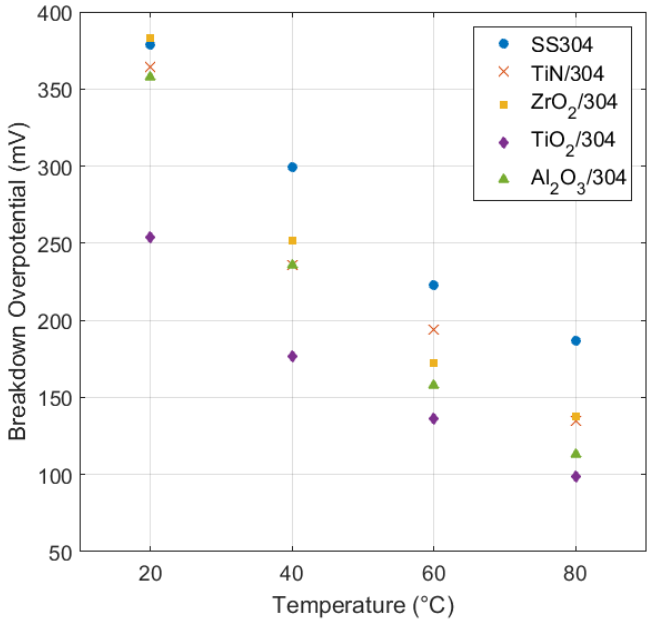

Figure 6-14: Average breakdown overvoltage vs. temperature – SS304

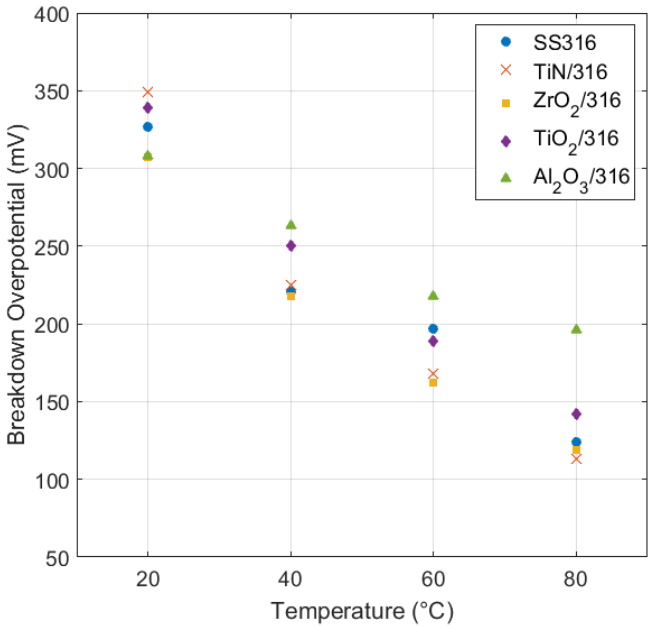

Figure 6-15: Average breakdown overvoltage vs. temperature – SS316

Table 6-4: Apparent activation energy for passive breakdown of stainless steel

Material	**E_a (kJ/mol)**	**Material**	**E_a (kJ/mol)**
SS304	10.35 ± 1.6	SS316	12.93 ± 7.04
TiN / 304	13.65 ± 2.21	TiN / 316	15.82 ± 2.6
ZrO_2 / 304	14.83 ± 5.86	ZrO_2 / 316	13.49 ± 5.44
TiO_2 / 304	13.35 ± 3.58	TiO_2 / 316	12.38 ± 3.25
Al_2O_3 / 304	16.61 ± 1.29	Al_2O_3 / 316	6.66 ± 1.2

6.4 Conclusions

Singly-coated steel substrates have been tested for resistance to corrosion, both uniform and localized. The two stainless steels (type 304 and 316) are clearly more corrosion resistant than the A36 carbon steel. Based on corrosion rates calculated from electrochemical means, the coated samples corrode at similar rates to bare samples. This is likely due to the corrosive solution reaching the substrate through pores in the coatings. This can possibly be alleviated by increasing coating thickness, adding additional layers, and/or adding a metallic buffer layer to improve adhesion and reduce porosity. Moreover, different coating mechanisms have been shown produce coatings with reduced defects and pores, namely atomic layer deposition, sol-gel, and electrochemical plating, compared to plasma deposition [129]. However, the reasons for choosing magnetron sputtering as the deposition method have been detailed in Chapter 4.

Corrosion rate tends to increase exponentially with increasing temperature for all materials tested, following an Arrhenius-type equation. Passive breakdown voltage, and hence the initiation potential for pitting, decreases exponentially with increasing temperature, demonstrating the impact of temperature on macroscopic and localized corrosion.

Corrosion among bare and coated stainless steel samples is comparable. The corrosion current and passive breakdown potential does not vary significantly between bare and coated materials, as the corrosion rates are all well within one standard deviation for each sample. The very thin coatings function similarly to passive films that form on the bare steel. It remains to be seen if thicker, multilayer coatings are able to protect against pitting and other forms of localized corrosion that plague passive stainless steels.

The coated carbon steel samples show more inhibited corrosion than the bare steel. Coated samples of A36 steel have measured corrosion rates that are less than that of the bare steel by greater than one standard deviation. This may indicate that the coatings are able to reduce the rate of uniform corrosion experienced by carbon steels.

Finally, it should be noted that the coatings did not act to accelerate corrosion despite titanium and zirconium being nobler than either stainless or carbon steel.

CHAPTER 7

EIS STUDY OF THE PASSIVE FILM ON AUSTENITIC STAINLESS STEEL

7.1 Introduction

Fully understanding the formation and breakdown of the passive film on various pure metals and alloys is the key to preventing corrosion-based failures. There has been no shortage of significant research done to this end. However, despite prolonged investigation on the passive behavior of metals, the formation and breakdown of passive barrier layers is still somewhat uncertain because it is highly dependent on the conditions under which the films are formed and are exposed after their formation. Currently, the point defect model (PDM) represents the most comprehensive prevailing theory on protective oxide or hydroxide films that form on metals [43]–[47]. The PDM asserts that the passive film exhibits semiconductor-like behavior with high concentrations of point defects, which are primarily oxygen and cation vacancies. Transport of these vacancies controls the formation and breakdown of the passive film, and thus the concentration of vacancies may be used as a measure of the stability of the film. Refer to Chapter 3 for a detailed discussion of the passive film and the specifics of the PDM.

Impedance spectroscopy is widely utilized in electrochemistry because of the range of information that can be captured in a single experiment. Applying perturbing signals to the cell enables the kinetics of the electrode-electrolyte system to be studied to a degree that is unavailable with DC techniques. The vast improvement in potentiostat capabilities over the last few decades allows for greater simplicity in performing impedance measurements. The

remaining difficulty in implementing impedance spectroscopy lies in the analysis of impedance spectra. This is particularly true when the capacitance of the passive film is a necessary component of the analysis, as with Mott-Schottky plots. Determining capacitance provides significant information about the system under study, especially the passive film and the various interfaces that are present. A number of different methods have been presented in the literature to calculate capacitance and to create Mott-Schottky plots from impedance data; many of them have conflicting results. In this research we utilize a method capable of removing the frequency dependence typically found in capacitive analysis. The methods used here are focused specifically on diagnosing the passive film but are directly applicable to analyzing coated materials. As such, this study may be extended to include detailed analysis of the coatings presented in Chapter 4 using the same impedance-measuring methods.

This study focuses exclusively on the passive film in sodium chloride solution, which is abundant in many of the locations that are being considered for ultimate waste disposal. Also, as was mentioned several times, chlorides are particularly aggressive in causing corrosion-based failures of stainless steel. Thus, testing the steels in a 1 M NaCl solution represents a worst-case scenario.

7.2 Experimental Methods

7.2.1 Sample Preparation

Test samples are 1 mm thick, 25.4 mm diameter disks made of AISI type 304 (SS304) and AISI type 316 (SS316) stainless steels that have been mechanically polished to a mirror finish. Samples are degreased in isopropanol and rinsed in distilled water prior to immersion in the testing solution. The disks are secured in a holder, exposing only one face to the electrolyte

solution. The samples are also covered with 3M™ Electroplating Tape 470 to mitigate crevice corrosion, resulting in a total exposed surface area of 1 cm^2.

7.2.2 Testing Procedure

Electrochemical testing has been conducted using a standard three electrode cell with a graphite rod counter electrode and a saturated Ag/AgCl reference electrode. All potentials are referenced to the Ag/AgCl electrode unless otherwise specified. The cell is situated inside a Faraday cage and held at a constant temperature of 20°C. Experiments are controlled by an Interface 1000 potentiostat from Gamry Instruments and are carried out in 1 M NaCl solution.

Samples are immersed in solution for several hours prior to testing to allow the open circuit (or corrosion) potential to equilibrate. The corrosion potential is determined from a polarization resistance measurement as the potential at which zero current would be measured. Following initial immersion and prior to testing, samples are conditioned at negative 1.2 V for 30 seconds to remove air- or aqueously-formed films. Subsequently, the samples are held at a potential 0.1 V above the corrosion potential for 1 hour to allow the passive film to form. Testing ensues immediately following the passivation period.

The impedance data is collected from 50 kHz to 10 mHz at 10 frequencies per decade unless otherwise noted. Impedance spectra are measured at various applied DC voltages with a superimposed RMS AC signal of 10 mV.

7.2.3 Data Analysis

The Echem Analyst software from Gamry Instruments is used to fit equivalent electrical circuit components to the impedance spectra using non-linear least squares (NLLS). All other analyses are carried out in MATLAB.

Quantitative data are presented with uncertainty based on the Monte Carlo method of uncertainty propagation. This method utilizes the fact that uncertainty in measured values represents the statistical properties of the populations of possible values for each source of error. Description of the method and its implementation is detailed in the work of Ferrar et al. [130].

Measured data are assumed to contain 10% error of the measured value for the purpose of uncertainty propagation. This was found to be sufficiently conservative, as this is well above the measurement error noted by the potentiostat manufacturer. The goal is to determine the parameters that contribute most pointedly to propagation of error throughout the analysis. Physical constants and electrode area have been neglected as potential sources of uncertainty in this study; micro-roughness on the electrode surface is capable of substantially altering the electrode area and is still present despite mirror polishing. This warrants additional consideration in the future.

7.3 Results and Discussion

7.3.1 Film Formation and Thickness

Passive films for this analysis are grown potentiostatically for 1 hour before testing, during which the current is measured to keep track of film formation. Passive film thickness is directly proportional to the charge required to form the film. According to the PDM this may be expressed as Eq. (7.1), assuming a metal-oxide film with Stoichiometry $MO_{\chi/2}$ (or $M_{\chi/3}O_{\chi/2}$, as is the case here) [49].

$$i - i_p = \left(\frac{\chi F}{\Omega} \right) \frac{dL}{dt} \tag{7.1}$$

Where i is the current density (A/cm^2), i_p is the passive, or steady state, current density (A/cm^2), F is Faraday's constant (9.6485 x 10^4 C/mol), Ω is the molar volume per cation of the film (cm^3/mol), χ is the number of electrons participating in the reaction, and dL/dt is the time derivative of the film thickness.

Eq. (7.1) may be rewritten to solve for the film thickness, L:

$$L = \left(\frac{\Omega}{\chi F} \right) \int_0^{\tau} \left(i - i_p \right) dt \tag{7.2}$$

For a given passive film composition, the film thickness may be estimated from potentiostatic experiments by integrating the measured current over time and applying Eq. (7.2). The two main components of the passive films formed on austenitic stainless steel, Cr_2O_3 and Fe_2O_3, have molar volumes of 29.12 cm^3/mol and 30.46 cm^3/mol, respectively, and both Cr and Fe have an oxidation number of 3. Thus, there will be little impact on the calculated film thickness by assuming one composition over the other in Eq. (7.2).

Figure 7-1 shows the evolution of current over time at a fixed potential for SS304 and SS316. The decrease in current with time is indicative of the passive film starting to form, and within one hour the current generally reaches its steady state value.

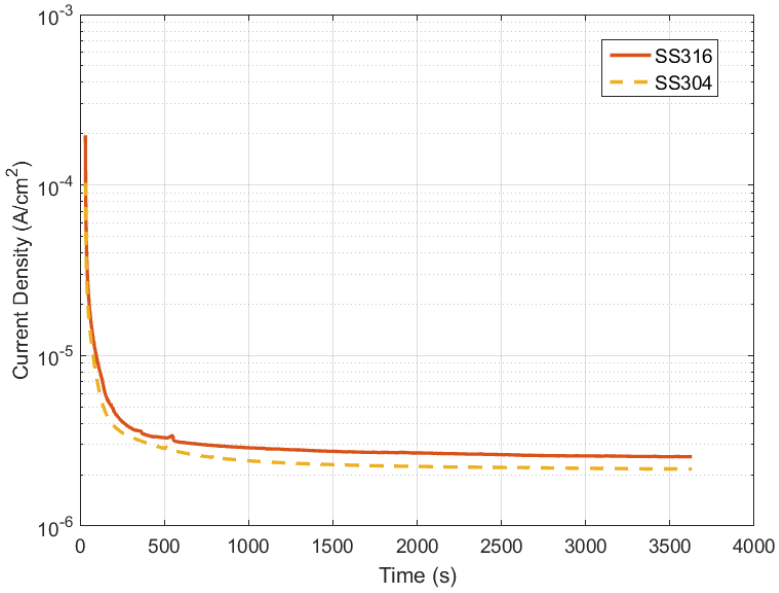

Figure 7-1: Current vs. time at a fixed potential 0.1 V above E_{corr} – type 304 and 316 stainless steel

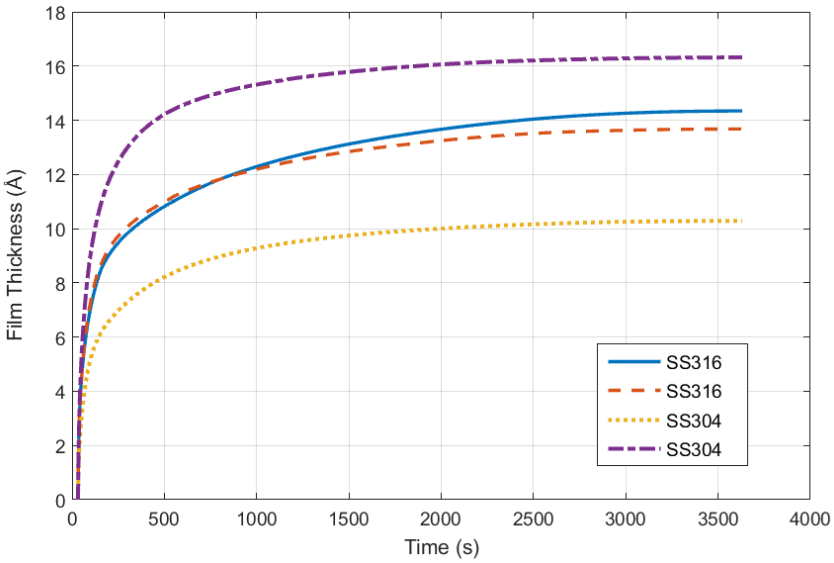

Figure 7-2: Film thickness vs. time at a fixed potential 0.1 V above E_{corr} – type 304 and 316 stainless steel

Assuming that the film thickness at a given time may be estimated using Eq. (7.2), the growth of the passive film may be determined and is displayed in Figure 7-2. The steady state film thickness varies between 1 and 2 nm for a film formation potential 0.1 V above the corrosion potential. The average values of the steady state passive current and film thickness are given in Table 7-1 for both types of steel. They prove to behave quite similarly, indicating the structure and formation of the passive film is analogous between them. This is expected because both steels contain similar concentrations of the major alloying components that are known to affect the film composition (Fe, Cr, Ni, etc.).

Table 7-1: Steady state current density and film thickness – average values and standard deviation

	i_p [μA/cm^2]	Lss [nm]
SS304	1.31 ± 0.54	1.23 ± 0.32
SS316	1.61 ± 0.83	1.35 ± 0.43

Eq. (7.2) assumes that all of the accumulated charge goes toward forming the passive film, making the calculated thickness only a rough estimate. However, the passive film thicknesses are within the range of 1-4 nm, which is considered to be the thickness attained for most oxide films [55], and the values are comparable to film thicknesses measured using AES and XPS for AISI 304 stainless steel [30], [53], as well as for Cr_2O_3 films on nickel-based alloys [131]. Film thickness generally increases with formation potential and the pH value [53]. Thus, the thickness of the films in this study should be on the lower end of the spectrum for a relatively low formation potential and a neutral electrolyte solution. It should be noted that this likely corresponds to the space-charge layer of the passive film, which may be thinner than the film itself; the space-charge layer is important when discussing semiconductive properties.

The uncertainty in the film thickness is dominated by the error assigned to the steady state current density (i_p) equal to 10% of the measured value. This value is critical to properly estimating the film thickness using Eq. (7.2). It should be noted that the uncertainty provided with the passive current density in Table 7-1 is based on the standard deviation of the measurement of many samples.

7.3.2 Impedance Spectroscopy

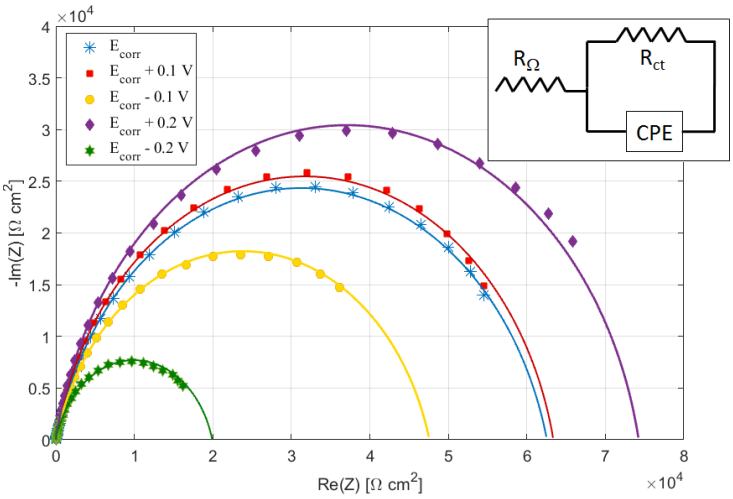

Figure 7-3: Nyquist plot with equivalent circuit model for DC potentials relative to corrosion potential – SS304

The impedance is measured as a function of frequency over a range of DC potentials for both types of steel. Figure 7-3 shows the negative of imaginary impedance plotted against real impedance (Nyquist plot) for type 304 stainless steel and demonstrates the effect of applied voltage relative to corrosion potential, which is -100 mV versus Ag/AgCl in this case. Markers

denote measured data points, and solid lines represent a best fit to the equivalent circuit displayed in Figure 7-3 extrapolated to lower frequencies than were measured. The shape of the curve at each potential is quite similar, but the polarization resistance, represented by the intersection of the curves with the *Re*(Z) axis, changes significantly. Similar behavior can be seen for SS316 in Figure 7-4.

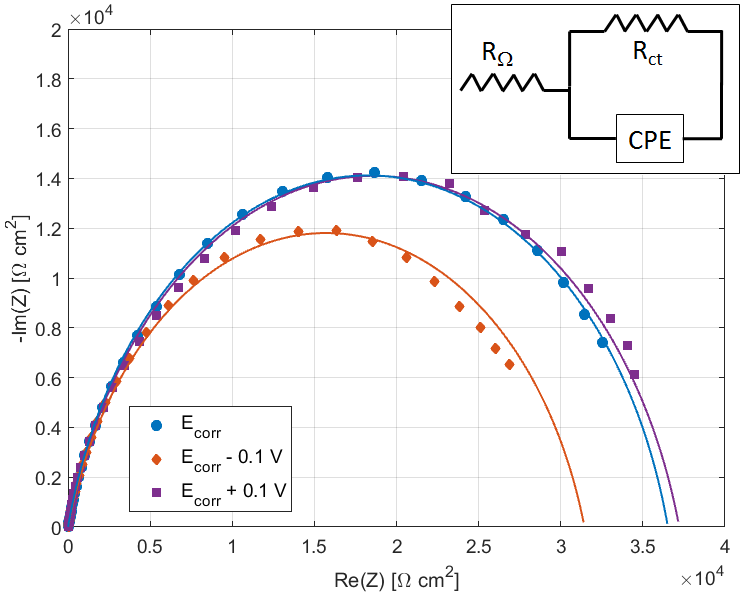

Figure 7-4: Nyquist plot with equivalent circuit model for DC potentials relative to corrosion potential – SS316

At most tested potentials, the impedance spectrum could be described by a single semicircle in the complex plane. The impedance response can then be fitted with a single capacitor (or constant phase element), resulting in a RC circuit in series with the Ohmic resistance of the cell, known as a Randles circuit, as is shown in Figure 7-3 and Figure 7-4. The lone capacitance that is displayed in these impedance spectra is likely the space-charge capacitance of the passive film. However, as the applied potential moves in the cathodic

direction, the capacitance tends toward a two capacitor response as the film capacitance approaches the Helmholtz capacitance in magnitude. This may be demonstrated by the impedance phase angle:

$$\Phi = \tan^{-1}\left(\frac{Im(Z)}{Re(Z)}\right) \tag{7.3}$$

The magnitude of the phase angle decreases as voltage decreases as a result of the increasing deviation from ideal capacitive behavior. This is also seen as the degree of depression of the semicircle in the complex plane plot. Furthermore, the phase angle changes shape as the voltage approaches -0.6 V, indicating that the impedance response is no longer that of a single RC circuit. Upon further reduction of the applied potential, the phase angle returns to its initial behavior. This is displayed in Figure 7-5 and Figure 7-6 for SS304 and SS316, respectively. In each case the corrosion potential is approximately -0.1 V, and the phase angle is plotted versus frequency at several applied voltages. The phase angle shows a shift in frequency and shape starting at -0.35 V in Figure 7-5 and -0.3 V in Figure 7-6. However, the most noticeable difference occurs at -0.6 V in both cases, with is 0.5 V below the corrosion potential. The shift to lower frequencies suggests the influence of a second capacitance, namely the Helmholtz capacitance. As mentioned, Figure 7-5 shows that the phase angle returns to its previous position as the potential is decreased further.

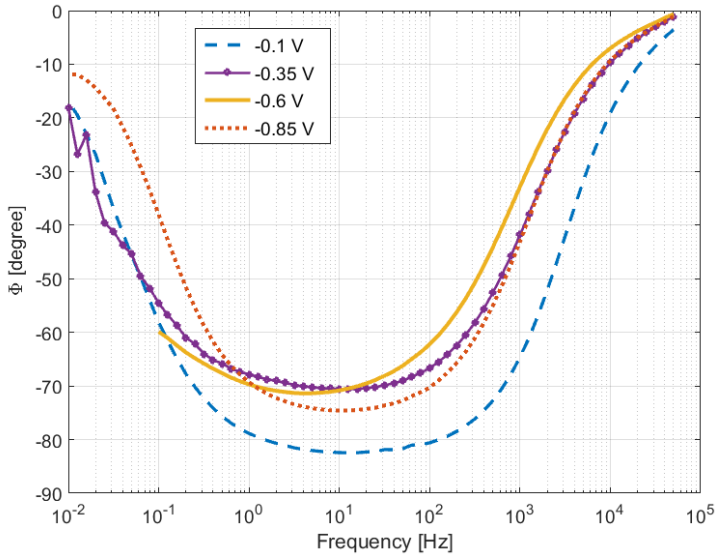

Figure 7-5: Phase angle plotted versus frequency at several applied DC voltages – SS304

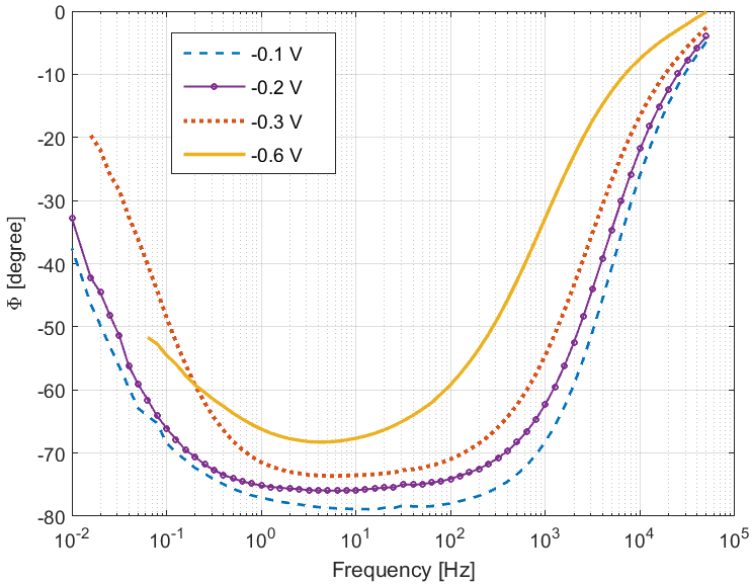

Figure 7-6: Phase angle plotted versus frequency at several applied DC voltages – SS316

The effect of the potential on the impedance response is even more apparent in Figure 7-7 and Figure 7-8, where the resistance and reactance are plotted against voltage. The impedance drops rapidly until reaching a minimum in the vicinity of -0.6 V, which is the same region as the shift in phase angle. Both components of impedance then begin to increase as the voltage continues to decrease. This will have a substantial impact on the apparent capacitance of the passive film.

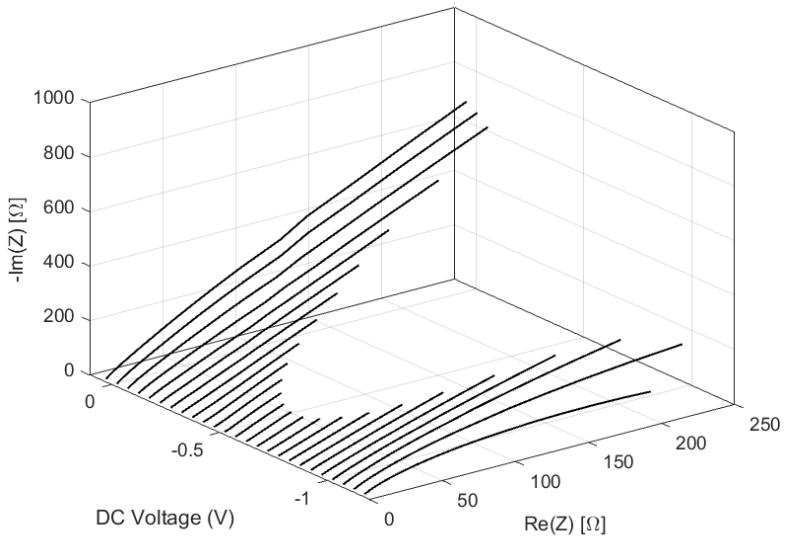

Figure 7-7: Measured impedance spectra for SS304 – Frequency range: 50 kHz – 10 Hz, DC voltage [0.05, -1.2] V

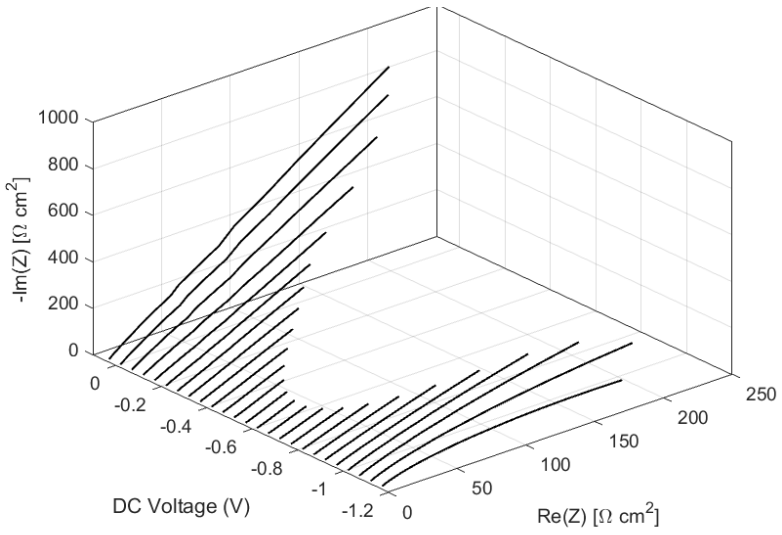

Figure 7-8: Measured impedance spectra for SS316 – Frequency range: 50 kHz – 10 Hz, DC voltage [0.05, -1.2] V

7.3.2.1 Extracting Capacitance from Impedance

Calculating the capacitance directly from measured impedance is strictly correct only if the impedance response of the electrode may be modeled using an ideal capacitor, in which case the capacitance calculated using Eq. (7.4) is independent of frequency. Otherwise, Eq. (7.4) does not hold and the frequency dependence of the supposed capacitance should be accounted for by considering a constant phase element (CPE). The constant phase element was presented in Chapter 5, and the impedance of the CPE is given by Eq. (5.23).

$$C = \frac{1}{\omega Z''} \tag{7.4}$$

Where C is the capacitance, ω is the angular frequency (rad/s), and $Z'' = Im(Z)$ is the imaginary component of the impedance (reactance).

The utility of the CPE in modeling is limited by the ability to extract capacitance from the CPE parameters. The capacitance is extremely important in the characterization of oxide passive films that form on metals. The CPE parameter Q in Eqs. (5.23) and (5.24) is often directly substituted for capacitance in the literature; the implications of this approach have been detailed in Refs. [125] and [126]. Those that decide to extract an effective capacitance from Q and α typically use one of two methods. The first, developed by Brug et al. [132], assumes a distribution of time constants across (parallel to) the electrode surface and is derived for a Randles circuit (Figure 5-6) with a CPE substituted for the capacitor. The effective capacitance using the Brug method (C_B) is:

$$C_B = Q^{1/\alpha}\left(R_\Omega^{-1} + R_{ct}^{-1}\right)^{\frac{1-\alpha}{\alpha}} \tag{7.5}$$

In this formulation, the effective capacitance is sensitive to the Ohmic resistance of the system. Since the Ohmic resistance is generally much smaller than the charge transfer (or polarization) resistance ($R_{ct} >> R_\Omega$), Eq. (7.5) simplifies to:

$$C_B = Q^{1/\alpha} R_\Omega^{(1-\alpha)/\alpha} \tag{7.6}$$

The second capacitance formula was presented by Hsu and Mansfeld [133] and is given by:

$$C_{HM} = Q\left(2\pi f''_{\max}\right) \tag{7.7}$$

Where f''_{max} is the frequency at which the magnitude of the imaginary component of the impedance reaches a maximum. Eq. (7.7) is derived assuming a distribution of time constants normal to the electrode surface, which prioritizes larger resistances and is not sensitive to the cell's Ohmic resistance. Figure 7-9 shows the distribution of time constants parallel to and normal to the electrode surface.

Eq. (7.6) has frequently been applied for passive oxide films even though surface distributions of time constants are generally inconsistent with oxide films. Despite this, Eq. (7.6) has proven superior to Eq. (7.7) in extracting capacitance in many cases [134]–[136]. Eq. (7.7) has been shown to considerably underestimate the passive film thickness measured by external techniques due to overestimation of the effective capacitance [134].

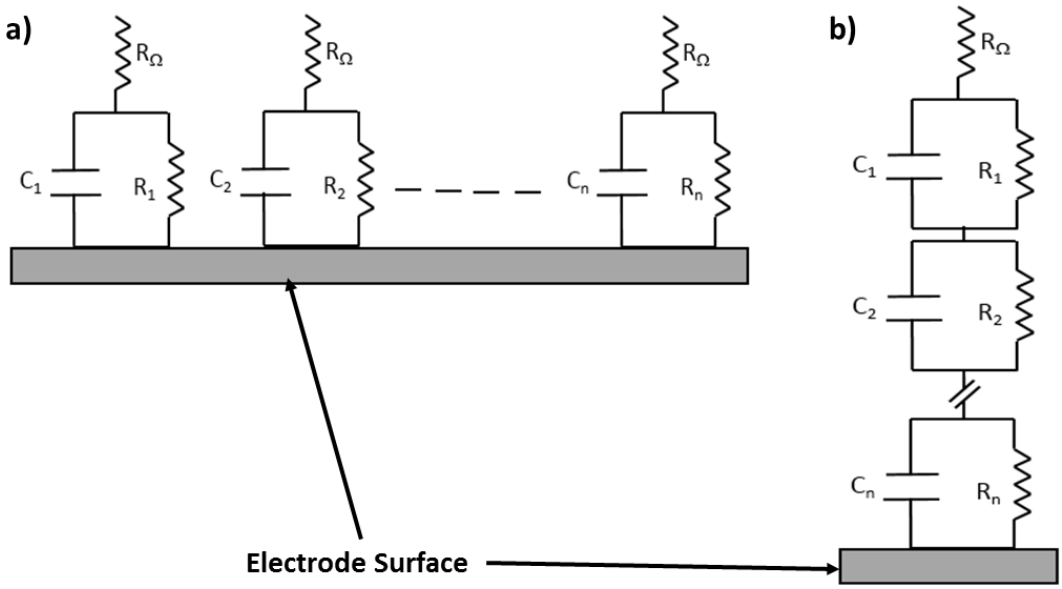

Figure 7-9: Distribution of time constants: parallel to **(a)** and normal to **(b)** the electrode surface, where $\tau_i = R_i C_i$

Whereas these two methods are widely used in the literature, neither is the result of a physical model that gives rise to constant phase behavior. More recently, Hirschorn et al. [137], [138] showed that a power-law distribution of resistivity normal to the electrode surface (along the film thickness) is capable of producing a constant phase response. They developed a method of determining the effective capacitance from CPE parameters based on the resistivity at the film-electrolyte interface [138]:

$$C_{PL} = Q\left(\rho_\delta \varepsilon_r \varepsilon_0\right)^{1-\alpha} g = Q\left(2\pi f_\delta\right)^{\alpha-1} g \tag{7.8}$$

Where ρ_δ is the resistivity at the film-electrolyte interface, ε_r is the dielectric constant of the film, ε_0 is the permittivity of free space (8.85 x 10^{-12} F/m), f_δ is the characteristic high frequency point at which the impedance response transitions from CPE behavior to capacitive, and g is given by an empirical fit:

$$g = 1 + 2.88\left(1-\alpha\right)^{2.375} \tag{7.9}$$

The power-law model (Eq. (7.8)) has been applied successfully for predicting dielectric layer thickness for oxide films on several types of stainless steel, aluminum, and niobium, as well as other non-oxide-forming materials [134], [138], [139]. It has the benefit of requiring only high frequency impedance data provided the transition to capacitive response occurs within the measured frequency range. This transition point can lie within the possible measurement range for oxide films on stainless steel, though it may not for other metals. If the transition is not observed, the maximum capacitance may be determined using the highest measured frequency, or the resistivity at the film-electrolyte interface may be estimated using the film thickness and dielectric constant. A detailed description is found in the work of Hirschorn et al. [138].

7.3.3 Dielectric Constant

Using the calculated film thicknesses presented in Table 7-1 and the capacitance of the film, it is possible to estimate the dielectric constant by applying Eq. (7.10).

$$\varepsilon_r = \frac{C_{PF} L}{\varepsilon_0 A} \tag{7.10}$$

Where C_{FP} is the capacitance of the passive layer measured at the film formation potential, L is the film thickness, and A is the electrode area.

This approach assumes that the passive film acts as a dielectric between two parallel conducting plates, and that the capacitance of the barrier layer may be approximated by the space-charge capacitance, which will be the primary capacitance measured away from the flatband potential, which is the potential of zero charge.

To determine the dielectric constant, impedance spectra were measured from 50 kHz – 10 Hz at the film formation potential. This frequency range captures the capacitance of the passive film (space-charge), as is explained in the next section. The capacitance at the film formation potential has been evaluated using the three methods discussed previously, with utilization of Eqs. (7.6), (7.7) and (7.8) to determine their effect on calculated dielectric constants. The results are summarized in Table 7-2.

The uncertainty in the capacitance used to populate Table 7-2 is calculated assuming error in the CPE parameter Q, the cell Ohmic resistance (R_Ω), and the frequency of maximum reactance (f''_{max}) equal to 10% of their measured values. The frequency of deviation from CPE behavior (f_δ) is assigned an uncertainty of 20% of its value, and the CPE exponent α has an error of 5% of its value. Combining this with the uncertainty in the film thickness presented in Table 7-1 produces the uncertainty in the values of the dielectric constant. In each case, the dielectric constant calculated for SS304 and SS316 fall within one standard deviation of each

other, which is expected because of the similar passive film structure between the two types of steel. However, the uncertainties are small enough that conclusions may still be drawn about the effectiveness of each method. The CPE exponent has the largest impact on the uncertainty of the capacitance and hence the dielectric constant, whereas the frequency of deviation from CPE behavior contributes little to the uncertainty, indicating that Eq. (7.8) is not overly sensitive to changes in this value.

Table 7-2: Passive film dielectric constant calculated using the three methods described in the previous section

	SS304 ε_r	**SS316** ε_r
Eq. (7.8)	13.55 ± 3.54	15.55 ± 4.95
Eq. (7.7)	96.64 ± 25.18	183.54 ± 60.69
Eq. (7.6)	16.74 ± 4.38	20.15 ± 7.37

The value of the dielectric constant typically used in literature for Fe_2O_3 and Cr_2O_3 passive films is either 12 [134], [140]–[144] or 15.6 [50], [145]–[152]. The dielectric constants calculated using the power-law approach (Hirschorn et al., Eq. (7.8)) agree with the values commonly assumed in the literature. The method developed by Brug et al. (Eq. (7.6)) predicts larger dielectric constants, though they still mostly agree with the literature given the uncertainty associated with each. Finally, the Hsu and Mansfeld approach (Eq. (7.7)) predicted values of the dielectric constant an order of magnitude larger than the other two methods resulting in a drastic overestimation. These results agree with what has been shown regarding the impact of each of these methods on the value of the film capacitance [134]–[136]. Moving forward, the power-law method represented by Eq. (7.8) will be used to calculate capacitance from measured impedance data.

7.3.4 Mott-Schottky Analysis

The concentration of vacancies in the film is akin to dopant concentrations in semiconductors, which can be described by Mott-Schottky (M-S) analysis. The measured capacitance at the semiconductor-electrolyte interface is due to the depletion region and the Helmholtz layer in series and can be written [153]:

$$C = \left[\frac{1}{C_{SC}} + \frac{1}{C_H} \right]^{-1} \tag{7.11}$$

Where C is the measured capacitance, C_{SC} is the space-charge capacitance of the depletion layer, and C_H is the capacitance of the Helmholtz layer.

Using Eq. (7.11) and the space-charge capacitance of the depletion region of a semiconductor, the equation describing the semiconducting properties of passive films is given by [52], [153]:

$$\frac{1}{C^2} = \frac{1}{C_H^2} + \frac{2}{\varepsilon_r \varepsilon_0 q A^2 N_{A,D}} \left(E - E_{FB} - \frac{kT}{e} \right) \tag{7.12}$$

Where ε_r is the dielectric constant of the passive film, q is the electron/hole charge, A is the electrode area, $N_{A,D}$ is the acceptor/donor density (film defect density), E_{FB} is the flatband potential, T is the temperature, k is the Boltzmann constant (1.38065 x 10^{-23} J/K), and E is the applied potential.

For the purpose of M-S analysis, impedance spectra are measured successively from 50 kHz – 10 Hz at 50 mV intervals from the film formation potential to -1.2 V. This follows a 1 hour passivation period with constant voltage 0.1 V noble to the corrosion potential. The CPE

parameters and the frequency at which the transition to capacitive behavior occurs are determined at each voltage by fitting the linear portion of the logarithm of the reactance versus log frequency.

This method affords the ability to extract capacitance from the impedance spectra using one of the methods described above, which is not possible for impedance measurements made at a single frequency. Generally, the space-charge capacitance is the smallest capacitance that will be measured, and its behavior will be best captured in the higher-frequency range. Additionally, the measurements at each potential are significantly hastened by removing the low frequency portion of the scan, such that the film is sufficiently unchanged during the series of measurements. Impedance scans were also halted at 100 and 1000 Hz rather than at 10 Hz, and differences in capacitance values were negligible, indicating that this method is capable of removing the frequency dependence that often plagues M-S analysis of passive films.

The CPE exponent, plotted in Figure 7-10 versus voltage, follows the trend seen in Figure 7-7 and Figure 7-8. The value of the CPE exponent changes significantly over the voltage range and must be determined by analyzing an impedance spectrum at each voltage; it will determine how the measurement frequency affects the magnitude of the impedance. This indicates that assuming a CPE exponent in order to calculate the parameter Q based on impedance measured at a single frequency is not a viable option, as small changes in the CPE exponent have pronounced impact on the effective capacitance.

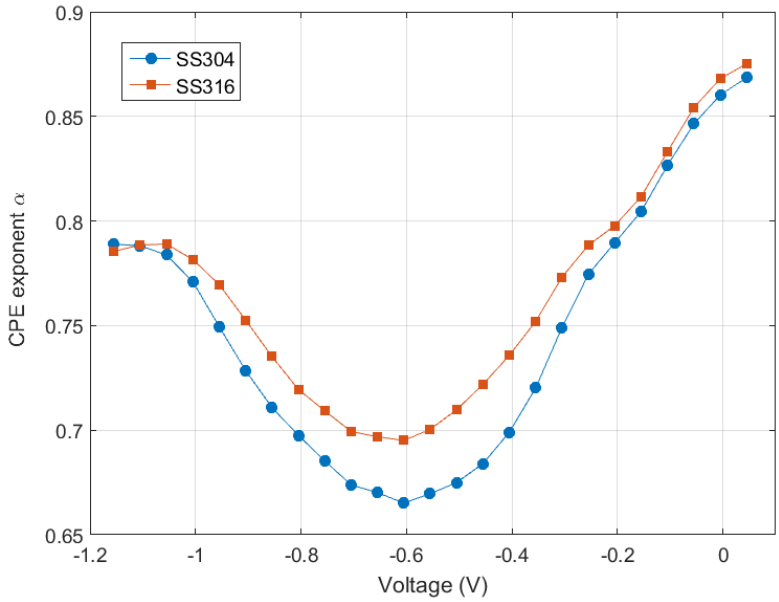

Figure 7-10: CPE exponent (α) versus voltage – SS304 and SS316

The capacitance in Figure 7-11 is calculated using Eq. (7.8) and the power-law resistivity method. The maximum value of the capacitance may be taken as the Helmholtz capacitance and should occur roughly at the flatband potential where the passive film is primarily conductive and contributes little to the measured capacitance [52]. For both types of electrodes the maximum value of capacitance consistently lies in the range 25 – 35 $\mu F\ cm^{-2}$ and occurs very near to -0.6 V. These values are indicative of the Helmholtz capacitance.

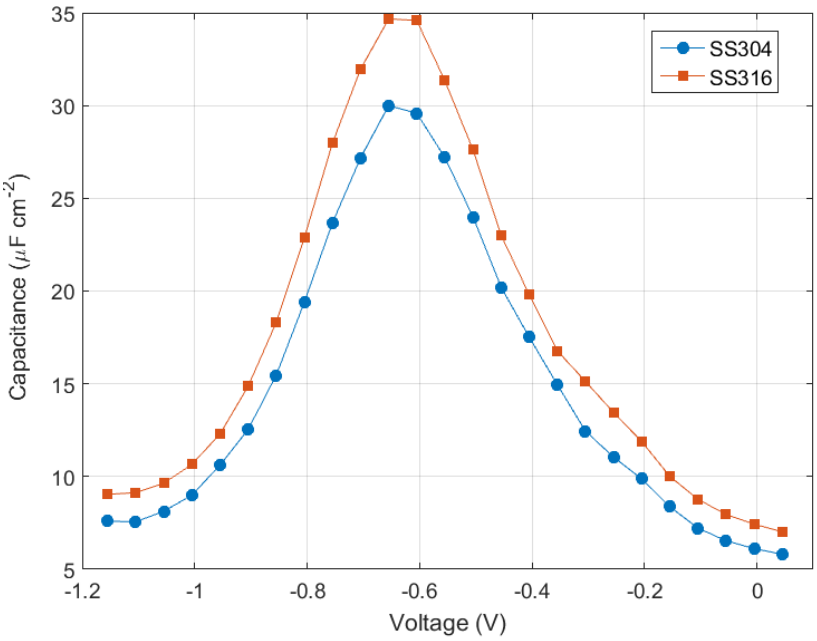

Figure 7-11: Capacitance calculated using Eq. (7.8) from measured impedance spectra: 50 kHz – 10 Hz. Uncertainty in the capacitance falls in the range of 14-15% of given values

According to Eq. (7.12) the slope of the inverse square capacitance with respect to voltage is unaffected by the magnitude of the Helmholtz capacitance. Thus, the M-S curves may be corrected for the Helmholtz capacitance by subtracting the inverse square of the maximum capacitance from the total, leaving only the space-charge capacitance of the passive film. The resulting curves are provided in Figure 7-12, which clearly shows the dual behavior of the passive film formed on stainless steel. The positive slope in the region noble to -0.6 V is attributed to the n-type semiconductor-like behavior of the anion-conducting Fe_2O_3 outer layer film. Likewise, the negative slope in the potential region active to -0.6 V stems from the p-type propensity of the cation-conducting Cr_2O_3 inner film layer. This behavior has been detailed in several studies [35], [50]–[52], [143], [149].

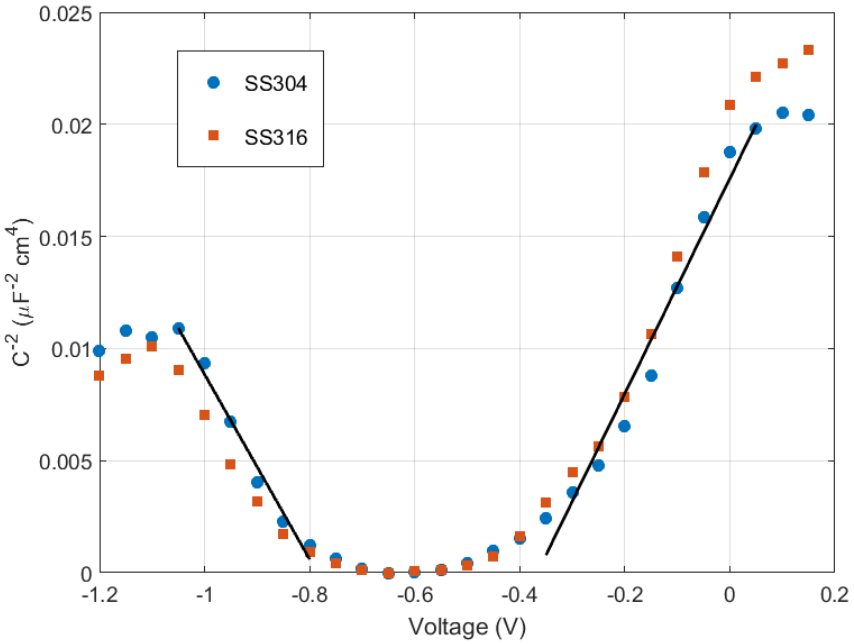

Figure 7-12: Mott-Schottky plot corrected for double layer effects – solid lines represent linear fits to SS304 data

From the slope of the linear portions of the curves depicted in Figure 7-12 and the dielectric constants tabulated using Eq. (7.10) in Table 7-2, the donor and acceptor defect densities may be estimated according to Eq. (7.12). These values are found in Table 7-3.

The dopant densities are essentially identical between the two types of steel. The donor densities (n-type) are slightly lower than acceptor densities (p-type), but the differences are well within uncertainty. Values in Table 7-3 agree with what is presented in the literature [52], [143]. The 'dopants' in these passive films are vacancies (primarily oxygen), and lower vacancy concentrations lead to more protective films. Vacancy concentration is particularly important with regard to passive breakdown, which is driven by vacancy diffusion according to the PDM. A larger vacancy concentration allows more sites for chloride ions to occupy oxygen vacancies and promote localized film breakdown. Thus, stainless steel type 304 and

316 should undergo passive breakdown in a similar manner. This has been shown in a previous study [154].

Uncertainty in the vacancy concentration stems from the slope of the M-S curve and the dielectric constant, which, in turn, are primarily dependent on the CPE exponent and the steady state current density (through the film thickness).

Table 7-3: Dopant densities calculated from M-S data (10^{20} cm^{-3})

	SS304	**SS316**
Donor Density (n-type)	2.82 ± 1.07	2.48 ± 1.61
Acceptor Density (p-type)	3.05 ± 1.20	2.97 ± 1.63

Regardless of whether the curves are corrected for the Helmholtz capacitance or not, the two linear portions clearly show that two separate flatband potentials will be calculated; the Helmholtz capacitance merely causes a 30 or 40 mV offset to each if accounted for. The linear fit for the n-type region predicts a flatband potential around -0.4 V (in agreement with [155] for a solution similar pH) whereas the p-type region predicts another flatband potential around -0.8 V. The true flatband potential is likely between these two values since the maximum value of the capacitance is attained near -0.6 V. Also, plots of the phase angle presented previously (Figure 7-5 and Figure 7-6) are not indicative of multiple flatband potentials. Most models of the electronic structure of highly-disordered oxide films predict a single flatband potential despite many cases of experimental data similar to Figure 7-12. All things considered, the flatband potential of electrodes displaying bilayer passive film formation (i.e. austenitic stainless steel) may be better characterized by the minimum of the Mott-Schottky curve (or maximum of capacitance) where the passive film is contributing very little to the measured capacitance.

7.4 Conclusions

The passive films on AISI types 304 and 316 stainless steel respond very similarly to electrochemical diagnostics. The values calculated for the steady state current density, passive film thickness, dielectric constant, and film vacancy concentration all agree with what has been presented in the literature. Conservative values of measurement uncertainty were assumed and propagated through the entire analysis using the Monte Carlo method. The resulting uncertainty in the calculated values is low enough that conclusions may still be drawn. This analysis allowed determination of the sensitivity of calculations to input parameters. The steady state passive current density (i_p) and CPE exponent (α) contribute the most to the uncertainty of calculated values. This may warrant additional investigation into properly quantifying the uncertainty in these values to reduce propagated errors.

The power-law resistivity method presented by Hirschorn et al. [137], [138] was employed and compared with the Brug et al. [132] and Hsu-Mansfeld [133] methods for calculating capacitance from CPE parameters. The power-law method given by Eq. (7.8) proved to be superior to the other two methods in calculating the dielectric constant of the passive film, in agreement with previous findings.

Mott-Schottky analysis was performed by measuring impedance spectra from 50 kHz to 10 Hz over a range of voltage. This in tandem with the power-law method for extracting capacitance proved reliable in calculating film vacancy concentrations. The analysis was repeated with impedance spectra measured to a lower frequency limit of 100 and 1000 Hz for comparison. Differences in capacitance based on frequency were negligible, showing that this method is capable of removing the measurement frequency dependence that is so often seen in capacitance data. With current technology, measuring impedance over this wide range is still fast enough to prevent significant film reorganization during experiments.

Frequency-dependent values of capacitance have often been reported in studies of passive films formed on metal electrodes and have been explained in a number of ways: variable

conductivity, dielectric relaxation, surface roughness, inhomogeneous films, double layer effects, etc. While some of these characteristics may be contributing to the impedance response of the passive film, it has been shown that proper treatment of the constant phase behavior is capable of relieving the capacitance of its frequency dependence. This is clear from examining the CPE exponent (α) versus voltage for SS304 and SS316 because the magnitude of the CPE exponent will determine how different measurement frequencies affect the apparent capacitance. This is further complicated by the fact that the CPE exponent changes with voltage leading to changes in magnitude and shape of M-S curves if the constant phase behavior is not appropriately handled. The contribution of the CPE exponent to uncertainty mentioned previously further stresses the need to measure impedance spectra to determine capacitance of thin passive films rather than single-frequency impedance values.

Variation of the impedance phase angle and capacitance with voltage suggest that the flatband potential for passive films on austenitic stainless steel lies in the vicinity of -0.6 V. This is at odds with Eq. (7.12), which suggests two separate flatband potentials based on the slope and intercept of the two linear regions of the M-S plots. Studies of passive films on stainless steel often point toward separate flatband potentials for Fe_2O_3 and Cr_2O_3, and passive films on pure chromium are seen to have a flatband potential that is very different from those formed on stainless steel [52]. Despite this, models of the electronic structure of passive films on stainless steel generally account for a single flatband potential and in some cases have successfully matched experimental data. This suggests that the flatband potential of the highly-doped, possibly degenerate [45], semiconductor junction that is the passive film on stainless steel cannot fully be described using Eq. (7.12).

CHAPTER 8

EIS STUDY OF REACTIVELY-SPUTTERED TiO_2 COATINGS ON STAINLESS STEEL

8.1 Introduction

In order to optimize the coating deposition process, the quality and protective nature of the coatings must be characterized. This is essential in determining the required thickness of each coating layer in order that the substrate may be sufficiently isolated from its surroundings. The thickness needed directly impacts the deposition conditions and, more importantly, the time required to deposit the coatings.

Electrochemical impedance spectroscopy (EIS) is a relatively simple method of diagnosing coatings and protective films, specifically for semi-conductive materials. EIS was presented and discussed in detail in Chapter 5, and was applied to the passive film on stainless steel in Chapter 7. The methods used to analyze the passive film formed on bare stainless steel are also applicable to the semiconducting protective coatings that were studied in Chapter 6.

8.2 Coating Deposition

The TiO_2 coatings are deposited via magnetron sputtering using the apparatus in Figure 4-5 with applied RF power of 400 W for 30 minutes. The deposition is performed using a metallic titanium target with a base argon pressure of 10 mTorr with the oxygen flow rate

controlled to ensure uniform deposition of TiO_2. Coatings are deposited on stainless steel disks, both type 304 and 316.

8.3 Testing Procedure

Electrochemical testing was conducted using the same equipment as was described in Chapters 6 and 7. The samples are immersed in 1 M NaCl solution for approximately 1 hour prior to testing. Corrosion potentials are determined from linear polarization measurements in the voltage range very close to the open circuit potential. In this case, potentiostatic measurements are not performed, as the focus is on the coatings, rather than the growth of the passive film.

Impedance data is collected from 300 kHz – 10 mHz at 10 frequencies per decade with a 10 mV RMS voltage signal. For the purpose of capacitance measurements, impedance spectra are collected over a large voltage range with frequencies from 300 kHz – 1 Hz.

8.4 Results and Discussion

8.4.1 Impedance Spectra

Impedance spectra were collected from 500 kHz to 10 mHz for TiO_2-coated stainless steel 304 for potentials from -0.85 V to 0.15 V. The impedance modulus – Eq. (5.17) – is seen in Figure 8-1, the phase angle – Eq. (7.3) – is provided in Figure 8-2, and a complex plane plot of the admittance is given in Figure 8-3. Likewise, the impedance modulus and phase angle at the corrosion potential of TiO_2-coated SS304 is compared to bare SS304 in Figure 8-4.

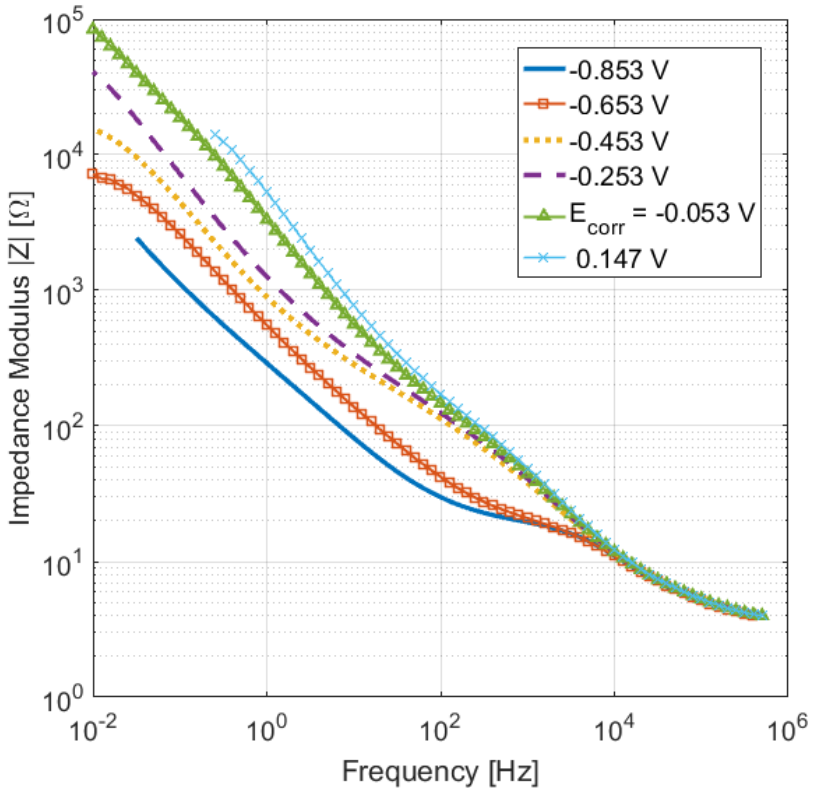

Figure 8-1: Impedance modulus versus frequency at several potentials – TiO_2 / SS304

Both the impedance modulus (Figure 8-1) and the impedance phase angle (Figure 8-2) show the effect of potential on the impedance response of the TiO_2-coated steel. The magnitude of the impedance modulus increases with increasing potential, and the shape shows that the impedance response consists of more than one capacitance, as is evidenced by the existence of multiple linear portions of the curves. At each potential, the curves converge at high frequency as the impedance tends toward the Ohmic resistance of the cell.

The phase angle, shown in Figure 8-2, clearly depicts the existence of a multi-capacitor response based on multiple local minima for each potential. It is apparent that the magnitude of the phase angle generally increases with increasing potential, which is indicative of a shift

toward more ideal capacitive behavior. The impedance response, especially at higher frequencies, is dominated by the protective TiO_2 thin film. Since the coating thickness and structure are not changing as the potential changes, the shift in phase angle must be due to a change in the electronic structure of the coating. The metal-oxide coating behaves as a semiconductor, so the applied potential determines the amount of band bending that occurs, resulting in either a depletion or an accumulation regime.

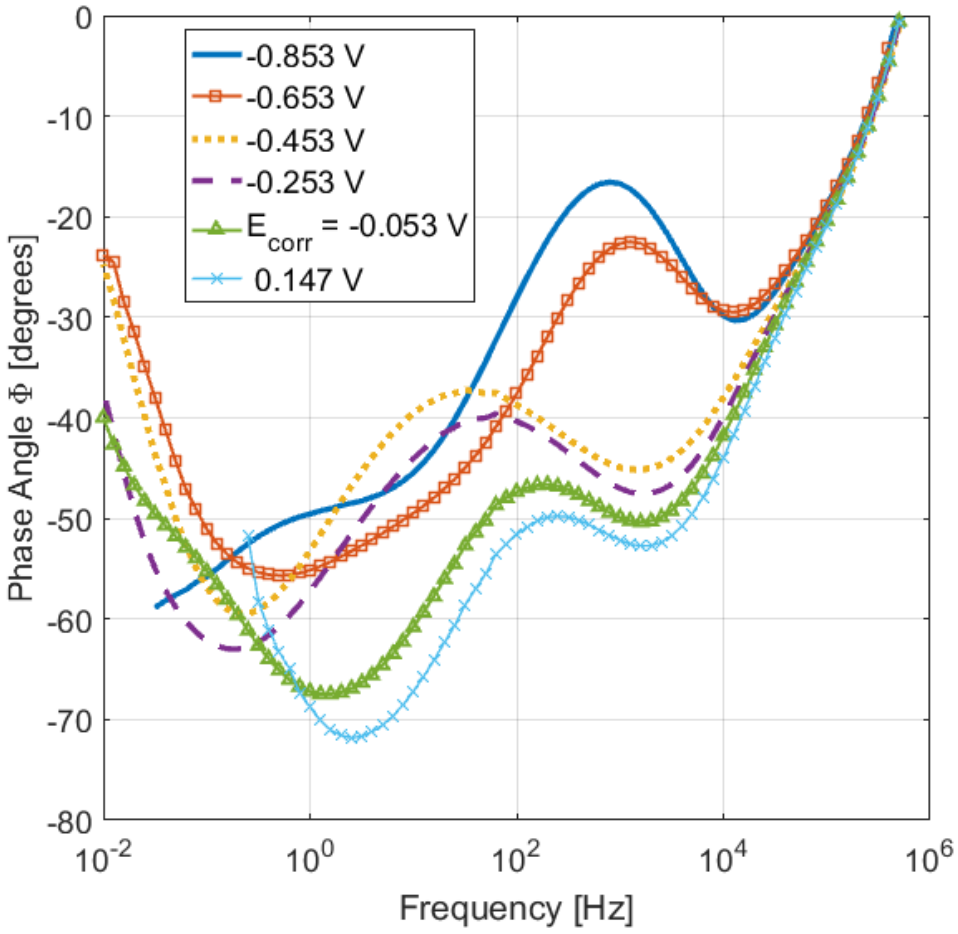

Figure 8-2: Phase Angle versus frequency at several potentials – TiO_2 / SS304

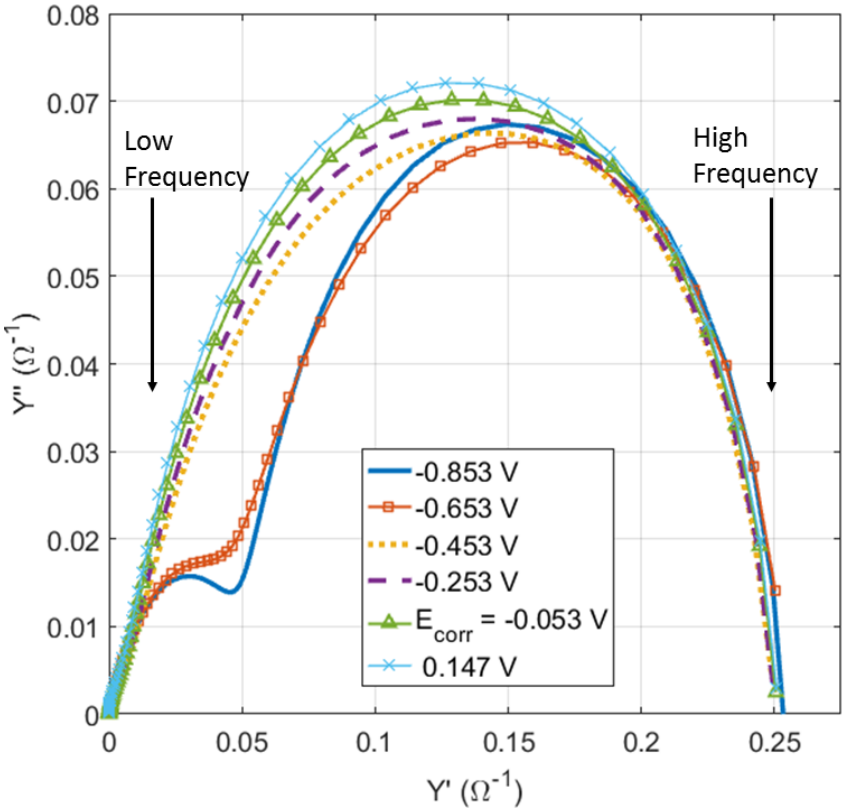

Figure 8-3: Complex admittance plot as a function of potential – TiO_2 / SS304. Arrows indicate regions of low or high frequency data points

Figure 8-3 also documents the shifting impedance response with the complex admittance plot. Admittance plots, in contrast to standard impedance (Nyquist) plots, highlight high frequency behavior, which is dominated by the capacitance of the coating. The admittance shows two distinct semicircles for the TiO_2-coated stainless steel electrode at -0.853 V. This becomes a single semicircle in the complex admittance plane as the voltage increases due to the low frequency semicircle being consumed by the high frequency one. As the applied potential becomes more and more noble to the flatband potential, the capacitance of the protective coating will produce an impedance response that is much larger than other capacitive

elements over a larger frequency range, which accounts for the loss of the two distinct semicircles in the admittance plane as the potential increases. Figure 8-3 shows that the high frequency capacitive behavior dominates the impedance response despite the existence of multiple capacitive elements, as is depicted in Figure 8-2.

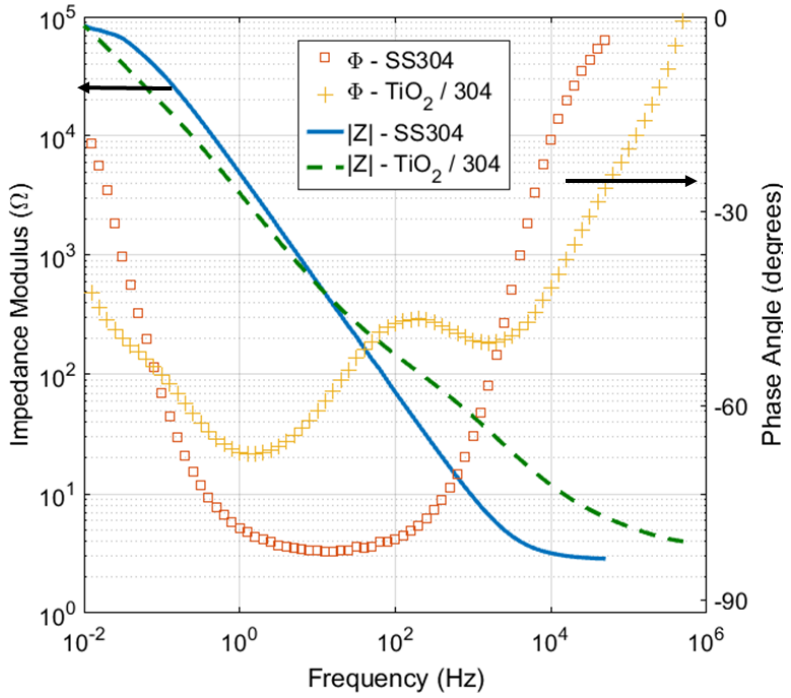

Figure 8-4: Bode plot – TiO_2 / 304 vs. SS304 (equilibrium potential)

The impedance response of the TiO_2-coated stainless steel is compared to that of uncoated stainless steel, both at their equilibrium potentials, in Figure 8-4. The impedance spectrum captured for the coated steel deviates significantly from that of the bare steel, which mirrors the response of a single capacitor (or CPE), which is clear from the shape of the phase angle as a function of frequency. A two-capacitor response is apparent from the shape of the

impedance modulus, which contains two distinct linear regions for the coated steel, as opposed to the one linear region for the bare steel. The low frequency capacitive response of the coated steel is likely due to a TiO_2 passive film that forms on the surface of the coating, which is overshadowed by the coating material at higher frequency. A lack of coating on the bare stainless steel accounts for the single linear region of the impedance modulus, produced by the impedance response of the passive film. The difference in shape of the phase angle and impedance modulus, along with the substantial increase in the polarization resistance compared to bare stainless steel, point to the TiO_2 coating possibly being an effective corrosion barrier.

8.4.2 Coating Capacitance

As was stated several times in the previous section, the capacitance of the coating material may be captured by the high frequency impedance data. The fact that the coating is likely several hundred times thicker than any passive film that may form means that it will have a much smaller capacitance and therefore, a much higher impedance, especially for high-frequency measurements.

The capacitance of the TiO_2 coating is determined by measuring impedance spectra from 500 kHz – 1 Hz over the potential range [0.1 V, -1.2 V] in 50 mV intervals. Figure 8-2, Figure 8-3, and Figure 8-4 exhibit obvious constant phase behavior, and the effective capacitance will be extracted using the power-law resistivity method presented in the work of Hirschorn et al. [137], [139] and given by Eq. (7.8). Based on the nature of the titanium (III) oxide coating, the transition away from CPE behavior occurs at a higher frequency than the passive film on stainless steel (Chapter 7). In cases where the transition to a capacitive response from a constant phase response is not observed, the maximum capacitance may be computed using the highest measured frequency, as is explained in Ref. [139].

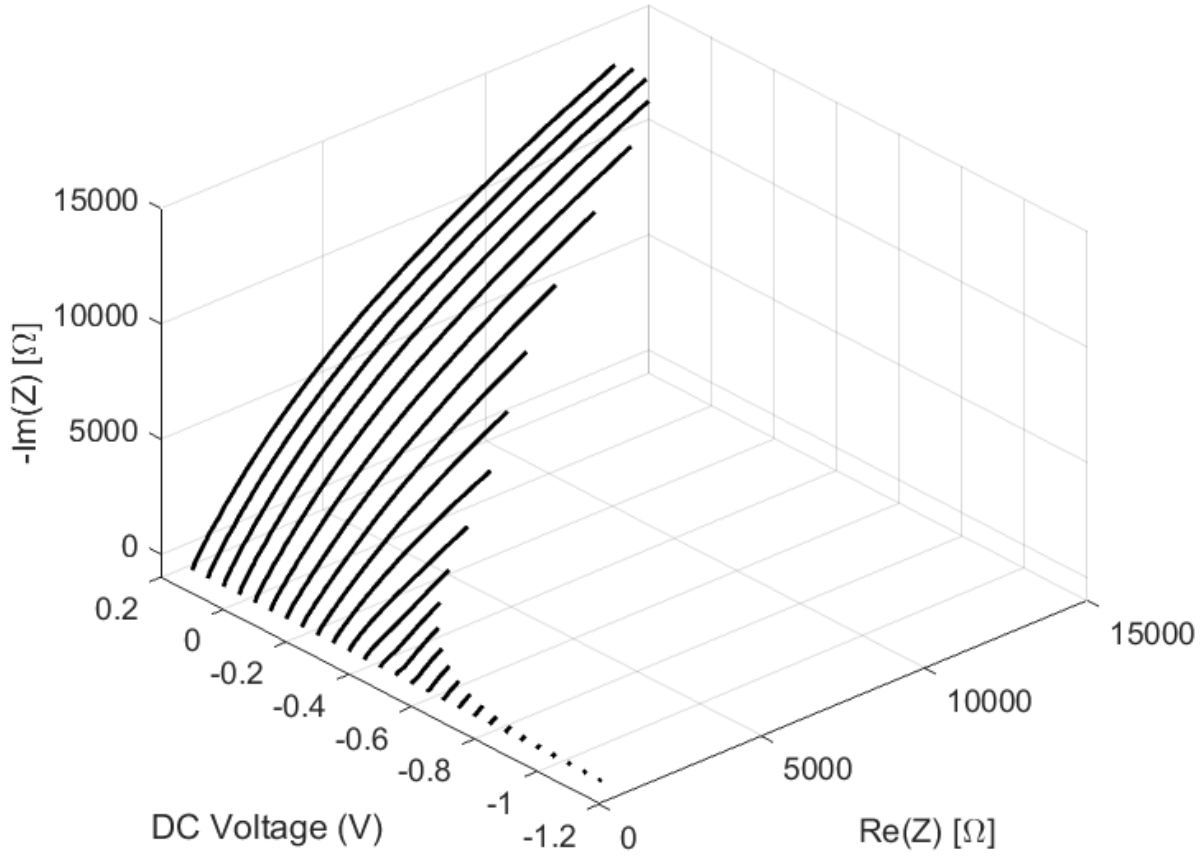

Figure 8-5: 3-D plot of impedance spectra measured from 500 kHz – 1 Hz over the potential range [0.1 V, -1.2 V] – TiO_2 / SS304

Figure 8-5 shows the impedance spectra of a TiO_2 / SS304 electrode used to calculate the effective coating capacitance. The impedance decreases rapidly with decreasing voltage after dropping below the equilibrium potential (~ -0.075 V). This is the same trend that can be seen in Figure 7-7 for bare SS304, except that the impedance does not increase again upon dropping below the flatband potential. In this case the coating and passive film are both primarily TiO_2 and will have the same electronic structure, unlike the bilayer passive film that forms on stainless steel, each layer with a separate electronic structure. This presents further evidence

that the TiO_2 coating is acting as a unique entity and is at least partially isolating the underlying substrate.

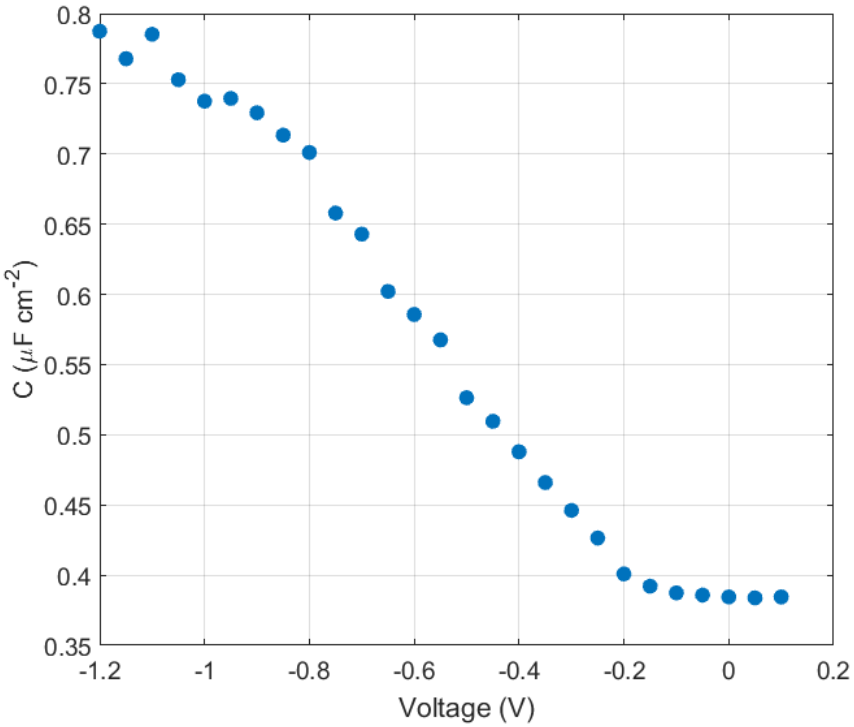

Figure 8-6: Calculated capacitance of TiO_2 / SS304 electrode using Eq. (7.8) and impedance spectra displayed in Figure 8-5

The coating capacitance in Figure 8-6 follows an inverse trend to the impedance spectra in Figure 8-5. The maximum capacitance is approximately 0.8 μF cm^{-2}, which is still mostly attributable to the coating. This is in contrast to the bare stainless steel (Figure 7-11) with maximum capacitance between 20 and 30 μF cm^{-2}, which could be ascribed to the Helmholtz layer. Thus, even at low voltage, the Helmholtz capacitance is negligible compared to the coating capacitance.

Calculating the effective capacitance allows for estimation of the dielectric constant of the coating assuming the thickness of the coating is known. This may be done using Eq. (7.10) by assuming a parallel plate capacitor with the TiO_2 coating as the dielectric between the plates. The capacitance of the coating at the equilibrium potential is 0.386 $\mu F\ cm^{-2}$, and the coating thickness is estimated to be 200 nm based on the deposition rate, which results in a relative dielectric constant of 87.2.

The capacitance used to determine the dielectric constant is likely equal to the space-charge capacitance of the TiO_2 coating, which should be correlated to the depletion region of the semiconductive coating. The thickness of this depletion region may be as low as one-fourth of the total thickness of the coating, which would significantly impact the dielectric constant. The relative dielectric constant of TiO_2 has been reported as anywhere from 7 [156] to well over 100 [157], [158] and is highly dependent on the crystal structure and the formation mechanism [159], as well as the measurement frequency. In light of this, the calculated relative dielectric constant should be considered the maximum possible value.

8.4.3 Mott-Schottky Analysis

The Mott-Schottky (M-S) plot of inverse capacitance squared versus voltage for TiO_2-coated stainless steel type 304 is given in Figure 8-7. The linear fit to the curve provides the slope and intercept used to calculate the defect density and flatband potential according to Eq. (7.12), which are useful in characterizing the coating.

The TiO_2 coating displays n-type behavior, which stems from an excess of oxygen vacancies. This points toward the fact that TiO_2 is an anion (oxygen) vacancy conductor. From the slope of the line in Figure 8-7 and the dielectric constant calculated previously ($\varepsilon_r = 87.2$), the dopant density in the coating may be estimated using Eq. (8.1), which comes from rearranging Eq. (7.12).

$$N_D = \frac{2}{\varepsilon_r \varepsilon_0 e \cdot m} \tag{8.1}$$

Where: N_D is the dopant (or defect) density,

e is the elementary charge (1.602 x 10^{-19} C),

And m is the slope of the linear fit to the M-S curve.

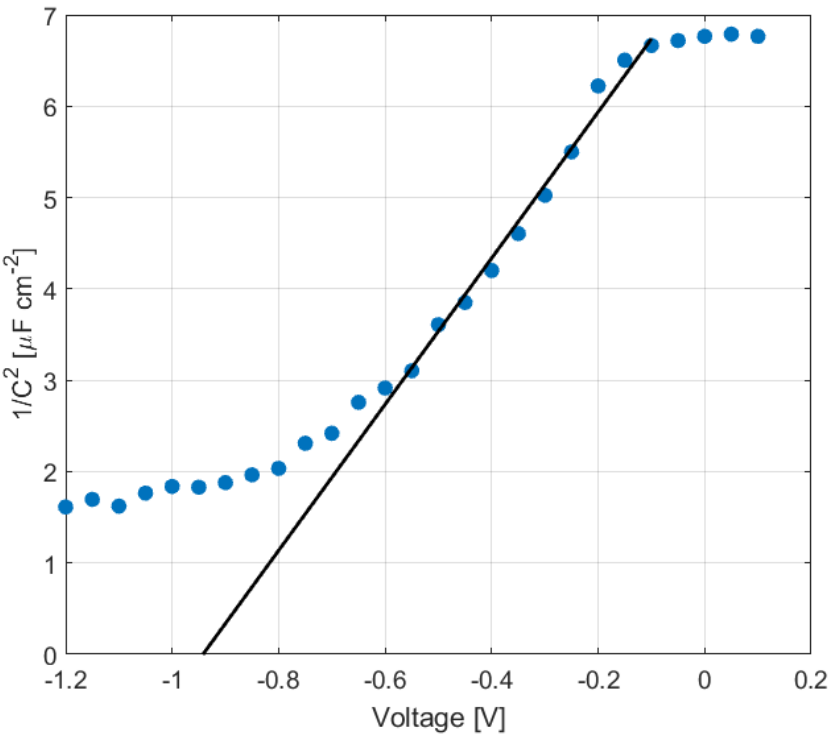

Figure 8-7: Mott-Schottky plot of TiO_2-coated SS304; circles are calculated values from data and the line represents a fit to the linear portion of the curve

The defect density calculated in this manner is 2.021 x 10^{17} cm^{-3}, which is several orders of magnitude lower than the defect density calculated for the passive film on stainless steel. This value no longer represents a highly-doped semiconductor, as is the case with passive layer

films, but rather is approaching the defect density of standard semiconductors. Depending on the true value of the relative dielectric constant, the actual defect density may range from 10^{17} cm^{-3} to 10^{18} cm^{-3}. Regardless of the accuracy of the calculated dielectric constant, this range of defect density represents a well-deposited coating, and is clearly indicative of the TiO_2 coating and not the passive film, which would have a much higher density of defects. Thus, this method may useful in diagnosing and determining coating quality following deposition.

The flatband potential (E_{FB}), which was discussed in Chapter 7, may be determined from the slope and intercept of the line depicted in Figure 8-7. The flatband potential is the intersection of the linear fit with the potential axis (x-axis) offset by the thermal energy. In equation form this is given by:

$$E_{FB} = -\left(\frac{b}{m} + \frac{kT}{e}\right) \tag{8.2}$$

Where m and b are the slope and intercept of the linear fit, respectively, k is Boltzmann's constant, and T is the absolute temperature. Again, Eq. (8.2) comes from the standard Mott-Schottky equation (Eq. (7.12)).

At 20°C, the flatband potential of the TiO_2-coated stainless steel electrode is calculated to be -0.967 V versus a saturated Ag/AgCl reference electrode. This was calculated assuming that the Helmholtz capacitance is negligible compared to the coating capacitance. Correcting the calculation using a Helmholtz capacitance of 25 μF cm^{-2} shifts the flatband potential by only 0.2 mV, proving that it is inconsequential in this case. The flatband potential for a TiO_2 electrode in an aqueous electrolyte solution has been given by Eq. (8.3), which depends solely on pH [160].

$$E_{FB} = -0.445 - 0.06 \cdot pH \text{ [V, vs. Ag/AgCl]} \tag{8.3}$$

The 1 M NaCl solution is prepared with distilled water and has a measured pH of 7.45, giving a flatband potential of -0.892 V vs. Ag/AgCl using Eq. (8.3). The difference between the two flatband potentials is 75 mV, which is within the uncertainty associated with these calculations. However, it could also be indicative of oxides other than TiO_2 existing within the coating, such as TiO or Ti_2O_3. It is likely while using reactive magnetron sputtering that there will be coating regions where different oxide compositions have been deposited. Depending on the relative concentrations of each type of oxide within the coating, the flatband potential may be shifted slightly.

8.5 Conclusions

Electrochemical impedance spectroscopy (EIS) has been used to characterize a stainless steel type 304 electrode coated with TiO_2 using reactive magnetron sputter deposition in 1 M NaCl solution. The measure impedance spectra are distinct from those measured for uncoated stainless steel presented in Chapter 7. This is a good indication that the TiO_2 coating is effective at isolating the substrate from the electrolyte solution.

The same methods used to study the passive film on austenitic stainless steel have been employed to study the semiconductive TiO_2 coating, to great effect. Impedance spectra are indicative of a multi-capacitor response, which is typical of a passive metal coated with an inert material. The maximum relative dielectric constant was calculated to be 87.2 using a parallel-plate capacitor approximation, and the true value is likely smaller than this based on the unknown thickness of the depletion region of the coating.

The coating defect density calculated from M-S analysis is on the order of 10^{17} cm^{-3}, which is typical for a slightly porous semiconductive coating. This is several orders of magnitude lower than the highly-doped oxide passive film on stainless steel, which speaks to the stability of the coating as a corrosion barrier. Finally, the flatband potential was measured to be -0.967

V vs. Ag/AgCl electrode and is more active by 0.075 V than the flatband potential calculated using Eq. (8.3) and the pH of the testing solution.

Based on these results, EIS proves to be a useful tool for characterizing the quality of coatings on passive metals. As was shown in Chapter 6, the assessment of inert coatings on active metals (i.e. A36 mild steel) may be accomplished using DC electrochemical techniques, as there will likely be a measurable difference in corrosion rate, especially as coating thickness increases. This may not be the case for coatings on passive metals, in which case AC electrochemical techniques can provide additional information to determine coating quality. Impedance measurements are sensitive to material properties that cannot be determined using DC methods.

CHAPTER 9

SUMMARY, CONCLUSIONS AND FUTURE WORK

9.1 Summary

Protective coatings on several types of steel have been assessed for their corrosion properties. The goal is to utilize these coatings in a multilayered, composite system for high-level nuclear waste storage containers. Current dry cask storage waste basket canisters are made of stainless steel and have the potential for failure due to stress corrosion cracking and other types of localized corrosion. The coatings presented in Chapter 4 are meant to prevent common types of failure for stainless steel, as well as to protect against hydrogen diffusion into the steel and mechanical wear.

Throughout the course of this research, only single layer coatings were tested in order to determine properties of individual materials. The first set of coated steels involved non-reactive depositions of all five compounds that were initially proposed. They included many batches of each coating material, each deposited using different parameters: power, pressure, and time. Following DC electrochemical testing, it was determined that the coatings were mostly too thin and porous to provide significant protection, although they showed promise on the A36 steel in that there was a measurable decrease in corrosion rate. This may be worth pursuing further considering that the outer shell of some dry cask designs is composed of carbon steel. It was clear that for each coating, the underlying substrate was still dictating the corrosion properties. Chapter 6 represents the culmination of this initial set of experiments. Some SEM images provided in this chapter show a correlation between protection against localized corrosion and thickness of the coating.

After the first set of coatings, time was spent studying the passive film on bare stainless steel while reactive magnetron sputtering was implemented to increase coating deposition rate. Chapter 7 explores the AC electrochemical techniques utilized to probe the passive film and presents results for type 304 and 316 stainless steels that largely agree with literature. The study of the passive film using EIS, while important for advancing knowledge on the subject, was seen as a preliminary test for proper experimental and analytical methods to apply to investigating coated steels. Essentially, Chapter 7 presents and validates a combined experimental and analytical method for removing the measurement frequency dependence of the capacitance that so frequently plagues EIS results in the literature. The methods discussed in this would be applied to TiO_2-coated stainless steel using reactive magnetron sputter deposition.

The study of stainless steel coated with a protective TiO_2 film is provided in Chapter 8. Impedance spectra that were collected exhibit behavior that is typical of passive metals coated with inert materials. The dielectric constant and defect density of the TiO_2 were calculated using electrochemical means and are consistent with what may be expected from a semiconducting coating. Electrochemical methods used in this study may be suitable to be used as diagnostic tools for coated metals. In this case, it is beneficial to have information about the composition and structure of the coating in order to iterate on the optimization of the deposition process.

9.2 Conclusions

Several conclusions may be drawn from the entirety of this research:

- Compound coatings deposited via magnetron sputter deposition are compatible with steel substrates. There was good adhesion between coating materials and the steels.
- Coatings show promise in decreasing the uniform corrosion rate of active metals. The decrease in corrosion rate will depend largely on the thickness and porosity of the coating.
- Coating defects and porosity must be largely minimized to provide enhanced resistance to localized corrosion. This may be achieved by increasing the number of layers and overall thickness of the protective coating.
- The capacitance calculated from impedance measurements should not depend on measurement frequency, as is often the case in the literature. Measurement of impedance spectra and appropriate treatment of the constant phase behavior often exhibited in electrode-electrolyte systems is capable of removing the frequency dependence of the capacitance.
- Oxide coatings behave similarly to oxide passive films, and the same electrochemical methods may be applied to studying both of them. Information may be gained about the coating structure and composition using electrochemical techniques. Oxide passive films have been studied extensively, which will benefit the investigation of oxide coatings through experimental comparison.
- Based on preliminary results, multilayer protective coatings may prove to be a viable alternative to newer alloys in protecting the integrity of HLW storage containers. Moreover, it is likely that the total coating thickness can be several micrometers (~ 5-10 μm) rather than the 50 μm that was initially proposed. It has yet to be determined if coating deposition can be economically competitive with other storage material options.

9.3 Future Work

The next step is to deposit and test the remaining reactively-sputtered coatings in order to determine the most optimal recipe for creating the desired coatings. Once the single layer coatings have been appropriately characterized, the focus will shift to the multilayer coating system seen in Figure 4-1. Adhesion among the coating layers is of primary importance, and will require precise deposition parameters. Having multiple layers will allow pinholes present in initial layers to be filled, greatly improving corrosion performance.

It was mentioned previously that the coatings are supposed to protect from hydrogen diffusion and mechanical wear, in addition to uniform and localized corrosion. Titanium nitride is often used as a diffusion barrier, particularly with regard to microelectronics manufacturing [161], [162], and molybdenum disulfide is a common solid lubricant used for wear resistance [80]–[82]. However, regardless of the known performance of individual materials, the coating system as a whole must be tested for diffusion and wear resistance, as it is currently unknown how the interplay of the materials will affect various properties. This is especially true because the properties of the thin films are dependent on the deposition environment, and the properties of each layer may change as an additional coating layer is deposited on top. The wear resistance may be simply studied using a tribometer, whereas hydrogen diffusion testing will rely on electrical resistance measurements made in an environment with controlled heating. Both of these projects are currently in the works.

The most important reason for using these materials to coat the stainless steel waste canister is to minimize the potential for stress corrosion cracking (SCC); the specifics of SCC were discussed in Chapter 2. Traditional SCC testing requires specimen of specific sizes and shapes for determination of stress intensity factors, and test procedures are classified into three groupings: constant total strain tests, constant load tests, and constant strain rate tests. Specialty samples need to be fabricated and coated in order to perform any quantitative SCC testing.

However, for qualitative testing focusing on a comparison between materials (i.e. coated and non-coated steel), the rules pertaining to sample size and geometry may be relaxed. Figure 9-1 is a picture of an apparatus designed and built by the precision machine shop at NC State that can perform constant load SCC experiments. The testing structure allows for simultaneous loading and submersion in a corrosive solution and is designed to hold 1" diameter disks, which have been used for the entirety of this study. This piece of equipment may be used as an alternative to traditional SCC testing, especially if it is coupled with the electrochemical methods that were the focus of this research.

Figure 9-1: Experimental apparatus for constant load testing of SCC

The following chapters - 10, 11, and 12 - consist of three published works that focus on the gamma-ray shielding of the coating materials discussed previously, as well as innovative blends of concrete and glass for enhanced shielding of waste storage packages.

CHAPTER 10

STUDY OF THE SHIELDING PROPERTIES OF PROTECTIVE COATINGS AND CONCRETE COMPOSITIONS FOR HLW STORAGE

Published in Ann. Nucl. Energy: "Shielding properties of protective thin film coatings and blended concrete compositions for high level waste storage packages," M. A. Fusco, A. L. Winfrey, M. A. Bourham, Ann. Nucl. Energy, Vol. 89, pp. 63-69, March 2016. DOI:10.1016/j.anucene.2015.11.026.

Various thin film coatings have been proposed to protect stainless steel high level waste (HLW) containers from premature failure due to localized corrosion, hydrogen embrittlement, and mechanical wear. These coatings include TiN, ZrO_2, MoS_2, TiO_2, and Al_2O_3, to be deposited either in multiple layers or as a thicker, single-layer composite. Linear attenuation coefficients of these materials have been simulated using MicroShield and measured experimentally for various photon energies. Additionally, spent fuel casks with overpacks made of two different types of concrete were simulated to compare exposure rate at the cask surface. In the energy range that is significant for high level waste storage all coating materials possess very similar attenuation behavior. A specialty concrete, containing magnetite (Fe_3O_4) and lead oxide (PbO), reduces the exposure rate at the outer surface of the overpack by several orders of magnitude. The higher-Z elements not present in ordinary concrete greatly increase attenuation of intermediate-energy gammas (0.4 – 1.0 MeV). The thin film coatings do not

affect the shielding capabilities of the HLW packaging, as their total proposed thickness is nearly three orders of magnitude less than the mean free path (MFP) of the primary photons of interest.

10.1 Introduction

Storage of spent nuclear fuel from commercial reactors and government-controlled high level waste (HLW) is one of the most important issues facing the nuclear industry. On-site dry cask storage is the only current long term storage option for commercial spent fuel, and thus, limiting exposure outside of the cask is of high priority. Dry storage casks consist primarily of a steel canister and concrete overpack, often with a glass layer in between [9]. HLW canisters are typically made of stainless steel because of its good mechanical strength and corrosion resistance [1], [20], [21]. However, stainless steel suffers from intergranular corrosion due to carbide buildup at grain boundaries and stress corrosion cracking (SCC) due to residual stresses from welding in the presence of chloride ions [27]. Additionally, mechanical wear and embrittlement from hydrogen diffusion pose a threat to the long term integrity of spent fuel canisters. A lack of in-situ monitoring coupled with the relative unpredictability of localized corrosion and embrittlement from gas diffusion makes canister lifetime difficult to predict. The US NRC mandates that high level waste containers must remain intact for 300 – 1000 years [163], making materials research for HLW storage imperative.

In order to combat premature failure of stainless steel canisters, various thin-film coatings have been proposed [60]. These coatings include titanium nitride (TiN), molybdenum disulfide (MoS_2), and Zirconia (ZrO_2), titania (TiO_2), and alumina (Al_2O_3) as an eventual composite, and have been shown to be good barriers to localized corrosion, hydrogen diffusion, and mechanical wear [38], [61]. The middle coating layer is a composite of the three oxides, and is commonly referred to as zirconolite.

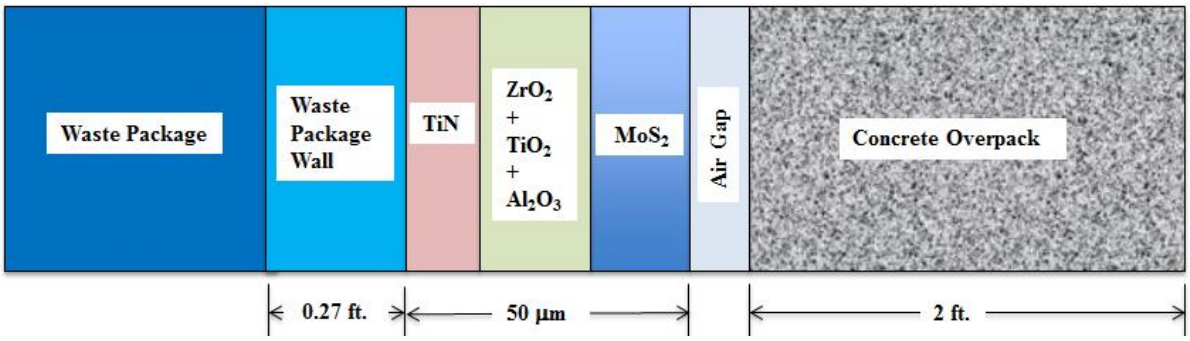

Figure 10-1: Multilayer coatings for high level waste storage (not to scale)

If these coatings are to be utilized to protect HLW containers, their attenuation properties must be known. Mass attenuation coefficients provide an adequate measure of the shielding capabilities of each material. The mass attenuation coefficient is independent of density, allowing for direct comparison between materials. A simulation study on the heavy particle impact on such multi-layered coatings, as in Figure 10-1, has shown that 2MeV particles can cause damage in the first 10µm of the TiN layer if neutrons leak through cracks and reach the coatings [164].

Recently there has been interest in specialty concrete for radiation shielding applications. The composition of concrete can be modified using additives and different forms of aggregates, making it an ideal material to be tailored toward specific uses. A computational study on various compositions of concrete for gamma attenuation, has shown that adding magnetite (Fe_3O_4) and lead oxide (PbO) in specific concentrations to standard concrete increases attenuation and greatly reduces exposure rate outside the spent fuel cask [13], and a specific concrete mixture, referred to as 'concrete-6' in their paper will be used as a comparison to ordinary concrete in the present study.

10.2 Methods

10.2.1 Computational Methods

Linear attenuation coefficients are calculated using MicroShield 9.05 [165]. The mass attenuation coefficient is calculated from the linear attenuation coefficient divided by the mass density of the absorber material and is given by the exponential attenuation law:

$$\frac{\mu}{\rho} = \frac{-1}{\rho x} \ln\left(\frac{I}{I_0}\right) \tag{10.1}$$

Where μ is the linear attenuation coefficient (cm^{-1}), ρ is mass density (g/cm^3), μ/ρ is the mass attenuation coefficient (cm^2/g), x is the absorber thickness (cm), I_0 is the initial photon intensity, and I is the transmitted photon intensity.

MicroShield computes the theoretical attenuation coefficient at desired photon energies using material composition and density. It has also been used to assess the exposure rate outside a typical spent fuel cask, as well as to assess the change in shielding effectiveness using multilayer protective coatings and magnetite/lead oxide-doped concrete "concrete 6" [13]. This concrete consists of 13.98% cement, 7.63% water, 23.5% aggregate (mainly SiO_2), 39.195% magnetite, and 15.678% lead oxide. The complete chemical composition of this proposed concrete mixture is given in [13].

The cask utilized in this study consists of a cylindrical volume of spent fuel with a height of 20 ft. and 8.727-ft. radius. The steel canister is 0.27 ft. thick, and the concrete overpack is 2 ft. thick. Three coating layers are added to the outside of the steel canister, which combined are 50 μm thick. The radiation source used in the MicroShield simulations comes from Surry plant spent fuel depleted using ORIGEN at 38.6 GWd/MTU [6] and is given in Table 10-1. The photon activity by energy group is scaled to represent 16 MTU per storage cask. At 0.4 to

0.5 MTU per assembly in a typical PWR, this assumes between 32 and 40 assemblies per cask. This is conservative given that the NRC considers between 2 dozen and 6 dozen assemblies per cask depending on the type [166]. The dose point is taken half way up the cask at the outer surface as illustrated in Figure 10-2.

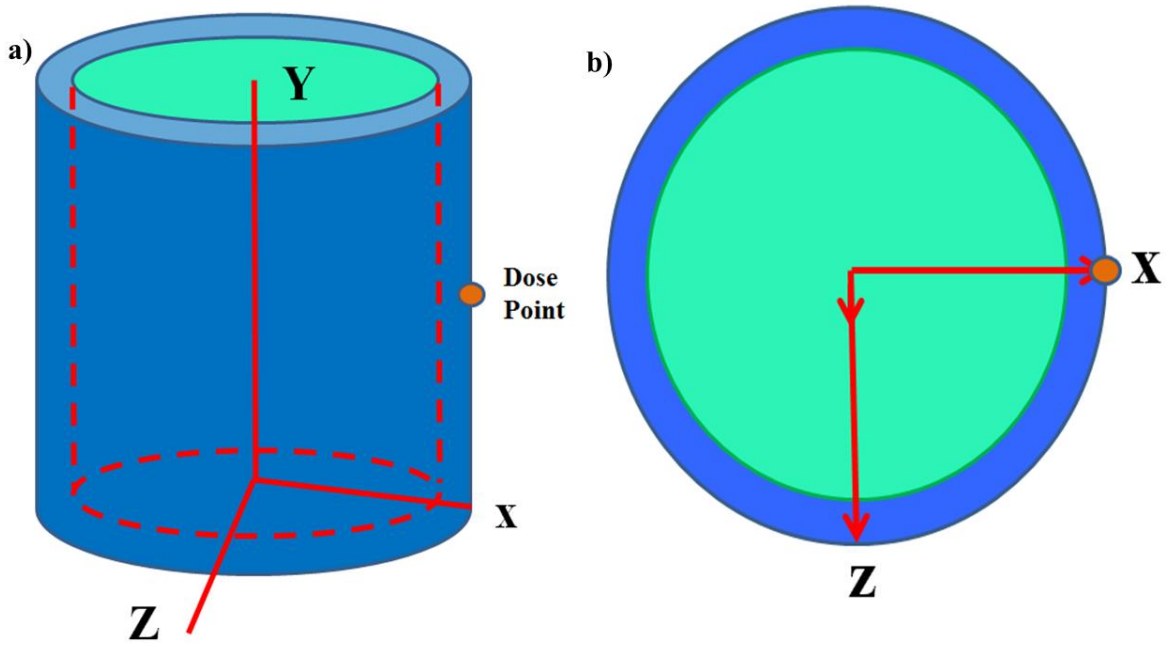

Figure 10-2: MicroShield cask geometry elevation (a) and top view (b)

Table 10-1: Source specification for spent fuel cask simulation – 38.6 GWd/MTU Surry Plant

Mean Photon Energy (MeV)	Activity/MTU (Photons/sec)	% Energy Activity
0.015	3.08E+09	0.00000
0.02	7.03E+09	0.00000
0.03	1.55E+14	0.31680
0.04	4.67E+13	0.12730
0.05	2.82E+12	0.00960
0.06	4.61E+13	0.18850
0.08	2.38E+12	0.01300
0.10	2.22E+13	0.15130
0.15	1.59E+10	0.00020
0.20	3.74E+12	0.05100
0.30	4.39E+11	0.00900
0.40	7.19E+11	0.01960
0.50	6.34E+11	0.02160
0.60	2.32E+15	94.8505
0.80	2.25E+13	1.22650
1.00	1.53E+13	1.04250
1.50	1.93E+13	1.97260
2.00	2.91E+06	0.00000
Total	2.66E+15	

The source specification for spent fuel cask simulation shows that the 0.6 MeV photon energy group contributes almost 95% of the energy activity, mostly from the decay of Cs-137. Also of interest are three higher energy groups: 0.8, 1.0, and 1.5 MeV, which have fairly high activity and are more difficult to shield than the lower energy gammas. These will likely contribute much of the total exposure rate. There are several energy groups in the tens of keV range that have high activity, but they are quite easily shielded and will not contribute significantly to exposure.

10.2.2 Experimental Methods

In order to corroborate theoretical calculations using the MicroShield code, gamma attenuation experiments have been performed. The radiation sources are 1" disks of Ba-133, Cs-137, and Co-60 to determine attenuation coefficients at four photon energies: 356 keV, 661.7 keV, 1173 keV, and 1332.5 keV, respectively. The detector is a 2" x 2" sodium iodide (NaI) scintillator, with built-in photomultiplier tube (PMT) and preamplifier, connected to a high voltage power supply, shaping amplifier, and multichannel analyzer (MCA). The three gamma sources are tested separately to avoid self-shielding. The detector is placed 60 cm directly above the source, and the disks are placed one-third of the way between source and detector, assuring most photons reaching the detector pass through the disk. Figure 10-3 illustrates the experimental set up for gamma attenuation measurements.

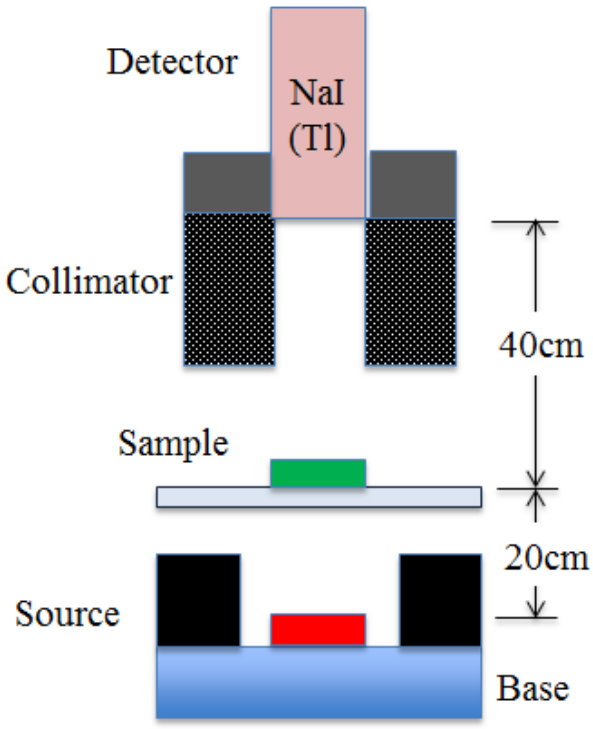

Figure 10-3: Gamma attenuation experimental setup

The full energy peaks measured using the MCA software are fit to a Gaussian plus linear background using the curve fit function in MATLAB, such that the fitting function takes the form:

$$f(x) = a \cdot \exp\left(-\left(\frac{x-b}{c}\right)^2\right) + dx + e \tag{10.2}$$

Where a, b, c, d, and e are fitting coefficients and x is the MCA channel number. Eq. (10.2) is then integrated over the entire photopeak to obtain the peak area. Ratios of integrated peak areas are used to calculate linear attenuation coefficients using Eq. (10.3):

$$\mu = \frac{1}{x}\ln\left(\frac{A_0}{A}\right) \tag{10.3}$$

Where: A_0 is the integrated photopeak area with no attenuation sample in place,
A is the integrated photopeak area with the sample present,
And x is the thickness of the steel disk.

10.3 Materials

Densities of the materials studied are given in Figure 10-4, which includes the substrate materials of type 304 and type 316 stainless steel and the coating materials (TiN, ZrO_2, MoS_2, TiO_2, Al_2O_3 and Zirconolite), in addition to the blended concrete 6 and the ordinary concrete. Zirconolite in this study is a stoichiometric combination of ZrO_2, TiO_2, and Al_2O_3, although the relative compositions of each oxide may be altered to create more desirable properties.

The samples tested are 1" diameter steel disks, both bare and coated. Thin film coatings are achieved using magnetron sputter deposition. The stainless steel substrates are two different thicknesses: stainless steel type 304 is 0.8975 mm thick and stainless steel type 316 is 1.498 mm thick. Focused ion beam (FIB) techniques reveal the coatings to be no thicker than several hundred nanometers. The oxide coatings, which sputter very slowly, are all less than 100 nm thick, whereas titanium nitride has the fastest deposition rate with a maximum thickness of roughly 900 nm.

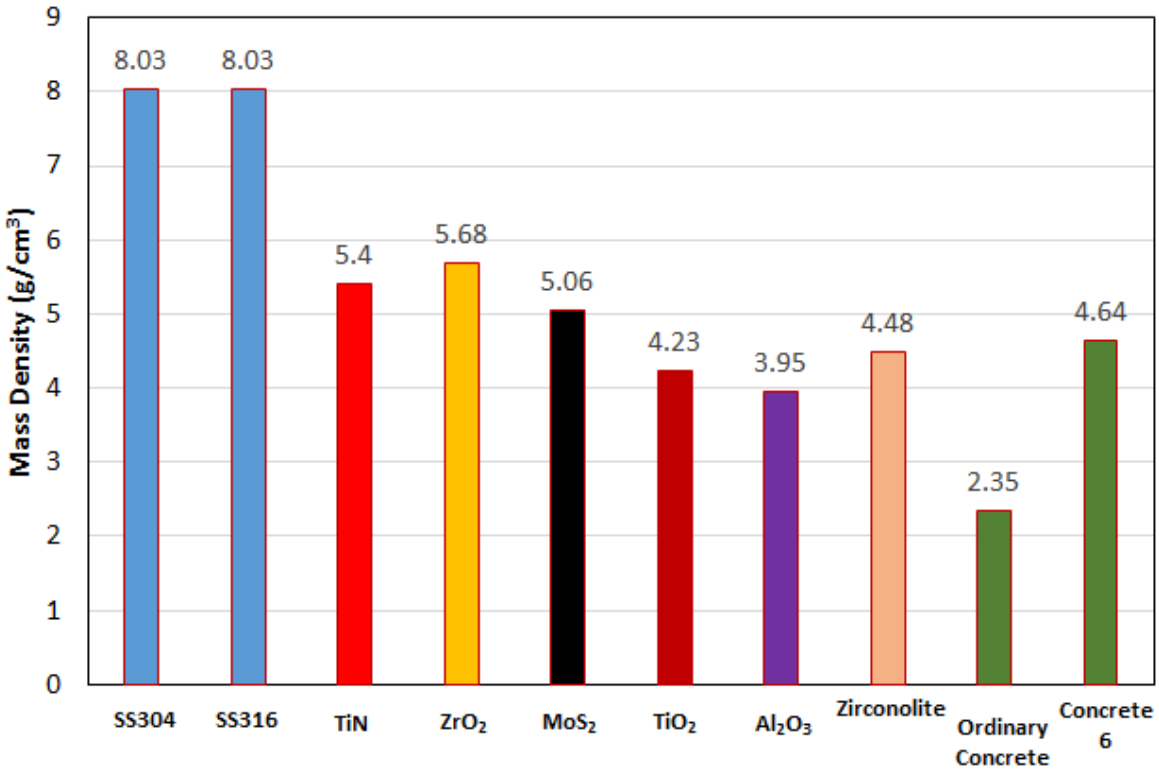

Figure 10-4: Mass density of materials used in this study

10.4 Results and Discussion

10.4.1 Linear Attenuation Coefficient

The linear attenuation coefficients for the materials studied were calculated from measurements obtained using the setup in Figure 10-3. The attenuation coefficients are displayed in Figure 10-5 with 95% confidence bounds, which correspond to the confidence bounds of the coefficients of the curve fit (Eq. (10.2)). Standard error using Poisson statistics was also determined for each value of linear attenuation, but the curve fitting produces greater

uncertainty than the experiment itself. Stainless steel type 304 and 316 have very similar compositions and thus have nearly identical attenuation properties. The attenuation of type 316 stainless steel is presented rather than type 304 because the disks are thicker, allowing for more precise measurement of the linear attenuation coefficient. Moreover, only the titanium nitride coating on stainless steel type 316 was chosen to represent the coated steels because it is the thickest coating on the thickest substrate, thus giving the best opportunity to measure a difference in attenuation from the bare steel.

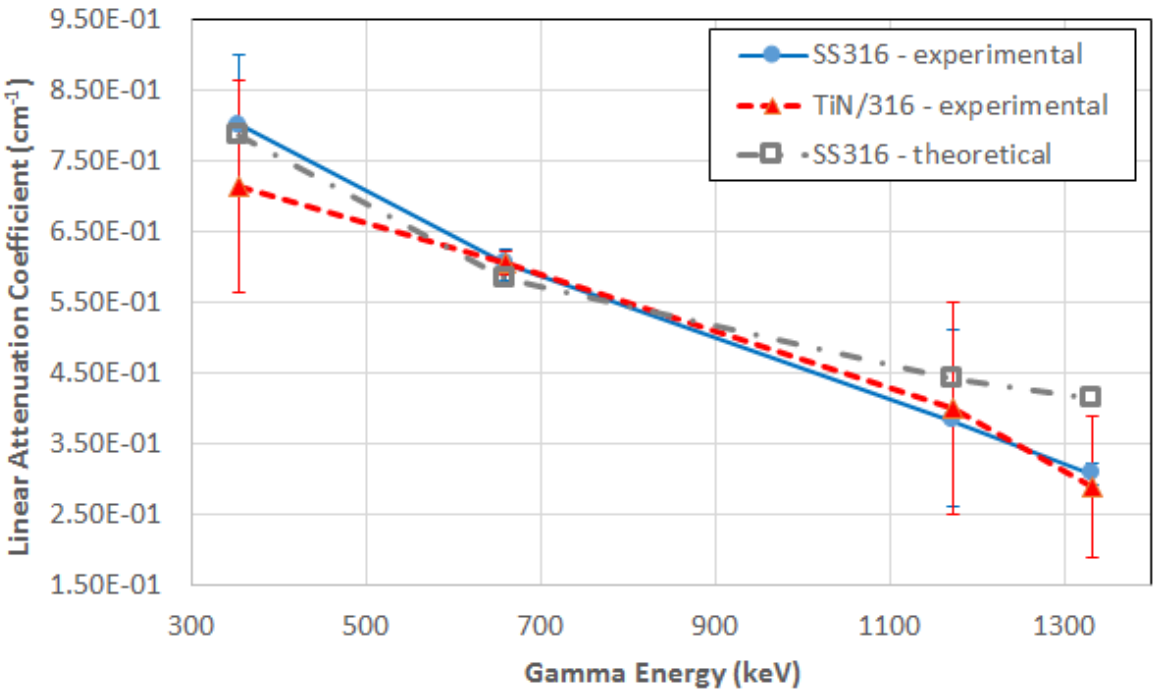

Figure 10-5: Comparison of experimental linear attenuation coefficients as a function of incident gamma energy for bare and TiN-coated stainless steel 316 with theoretical values

Experimental linear attenuation coefficients for stainless steel type 316 at four distinct incident photon energies are similar to predicted values. In all but one case, the theoretical value lies within the 95% confidence band of the experimental value. It lies outside the confidence range for the 1332.5 keV Co-60 gamma ray. Higher energy gammas require greater thickness to accurately measure the attenuation. The attenuation value for 662 keV gammas is both accurate and precise because the photopeak suffers neither from low signal-to-noise ratio (as with the Co-60 peaks) nor having other peaks close by to convolute the analysis. The titanium nitride coating, as well as all other coating materials, does not significantly affect the attenuation of the stainless steel substrate. It was not possible to measure the attenuation of the TiN separate from the steel because of the film thickness. The theoretical linear attenuation coefficient for TiN is 0.392 cm^{-1} for 661.7 keV gammas. Calculating this value from experimental data for a 1 μm-thick coating amounts to a difference of less than 0.004% between photopeak areas, which is well within the uncertainty bounds for radiation detection.

10.4.2 Mass Attenuation Coefficient and Mean Free Path

The mass attenuation coefficients for the coatings based on MicroShield calculations are given in Figure 10-6. As expected, over most of the energy spectrum the mass attenuation coefficient for each coating compound decreases monotonically. The increase in mass attenuation coefficient of ZrO_2 and MoS_2 in the low energy range corresponds to the K-edge. The K shell binding energies for Zr and Mo are 18 keV and 20 keV, respectively [167]. Photoelectric absorption becomes more efficient when the incident photon energy approaches the binding energy of the appropriate electron shell, which causes the observed peak in attenuation coefficient. The other elements present (Ti, Al, O, and N) have K-shell binding energies in the few-keV range. Mass attenuation coefficients are very similar among coating materials in the energy range of interest for nuclear waste applications.

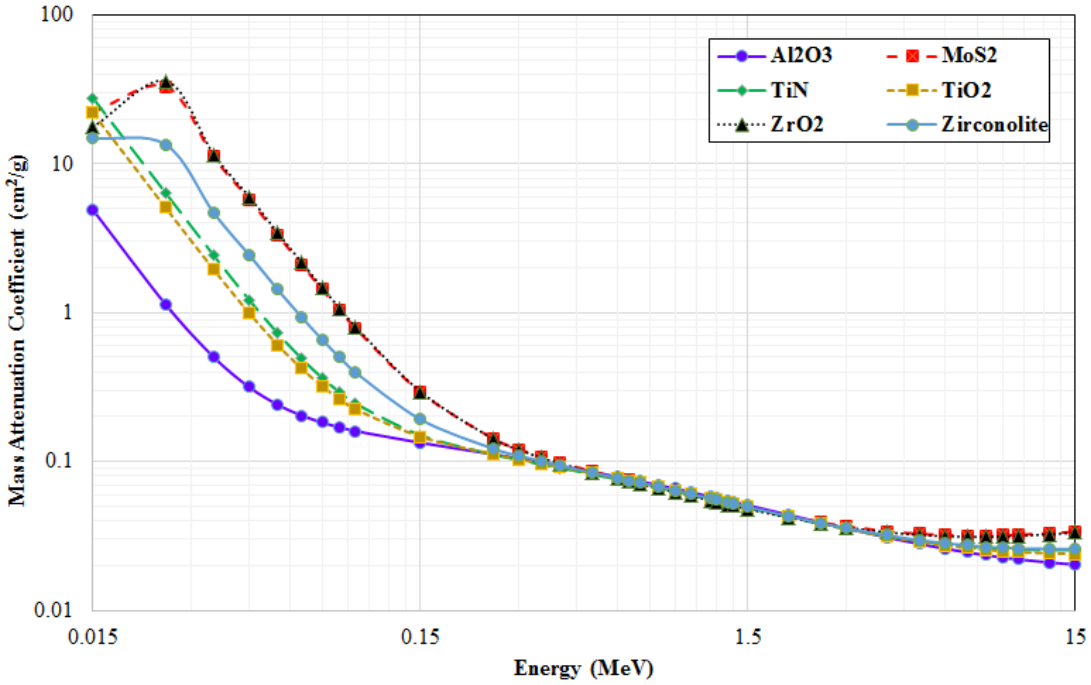

Figure 10-6: Mass attenuation coefficient as a function of energy for coating materials

Based on the predicted attenuation coefficients, the mean free path (MFP) in each material as a function of incident photon energy has been calculated and is shown in Figure 10-7. The minimum MFP in any of the coating materials is 50 μm, which occurs for 0.025 MeV (25 keV) photons in zirconia. The entire multilayer coating system is proposed to be 50 μm thick, so the coatings together will constitute less than a single MFP for even the lowest energy photons. A majority of the source activity stems from photons with a mean energy of 600 keV (Table 10-1). The MFP for these photons is between 2 and 3.5 cm depending on the material. This is nearly 1000 times larger than the total multilayer coating thickness, thus it is safe to assume that buildup will not be an issue for these coating materials.

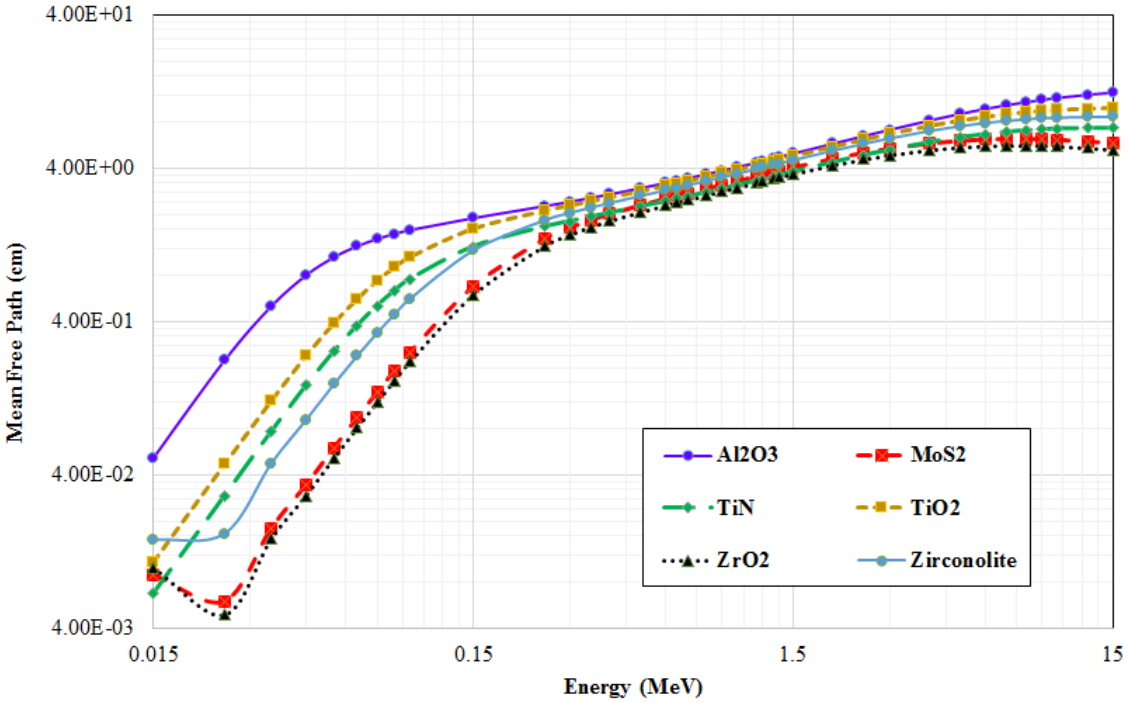

Figure 10-7: Mean free path in coating materials as a function of energy

10.4.3 Exposure Rate

The exposure rate, in mR/hr, taken at the outer surface of the storage cask is several orders of magnitude lower using 2 ft. of concrete-6 rather than ordinary concrete, as is seen in Figure 10-8. The attenuation of concrete-6 is much better than ordinary concrete, especially above 0.3 MeV incident photon energy. The higher-Z elements not present in ordinary concrete greatly increase attenuation of intermediate-energy gammas (0.4 – 1.0 MeV). Figure 10-9 shows that the effectiveness of concrete-6 over ordinary concrete is maximized for photons between 0.4 and 0.6 MeV, which is where the ratio of exposure rate between the two overpack materials is at a minimum. This is the energy range into which a majority of photons emitted from spent fuel fall, according to Table 10-1. The coatings proposed for the outer surface of the steel

canister have a negligible impact on the exposure rate. The total coating thickness of 50 μm is several orders of magnitude less than the MFP of the gammas of interest, as was discussed in the previous section.

Concrete-6 proves to be increasingly more effective at shielding gammas than ordinary concrete as the thickness of the dry cask overpack increases. An overpack thickness of 5 ft. of ordinary concrete is necessary to reduce the exposure rate outside the cask to the same level as 2.5 ft. of concrete-6. The total exposure rate as a function of the overpack thickness is shown in Figure 10-10.

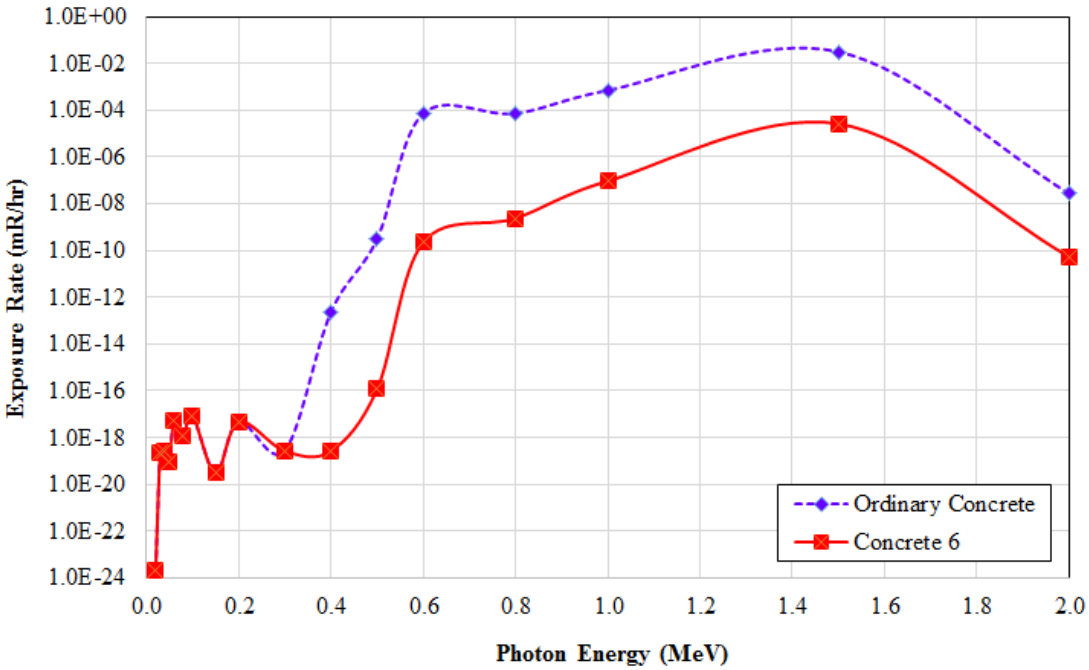

Figure 10-8: Exposure rate at cask surface as a function of incident photon energy – concrete comparison

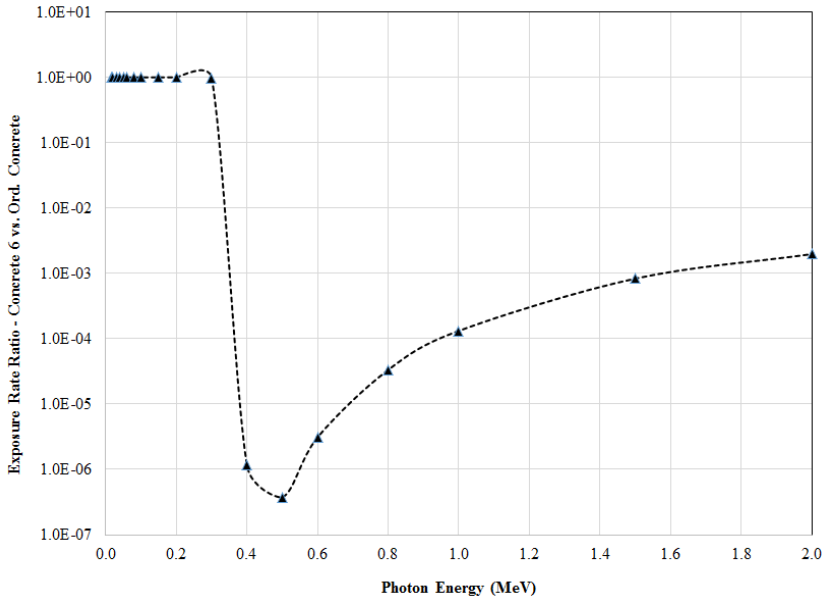

Figure 10-9: Ratio of exposure rate as a function of incident photon energy – Concrete 6 versus ordinary concrete

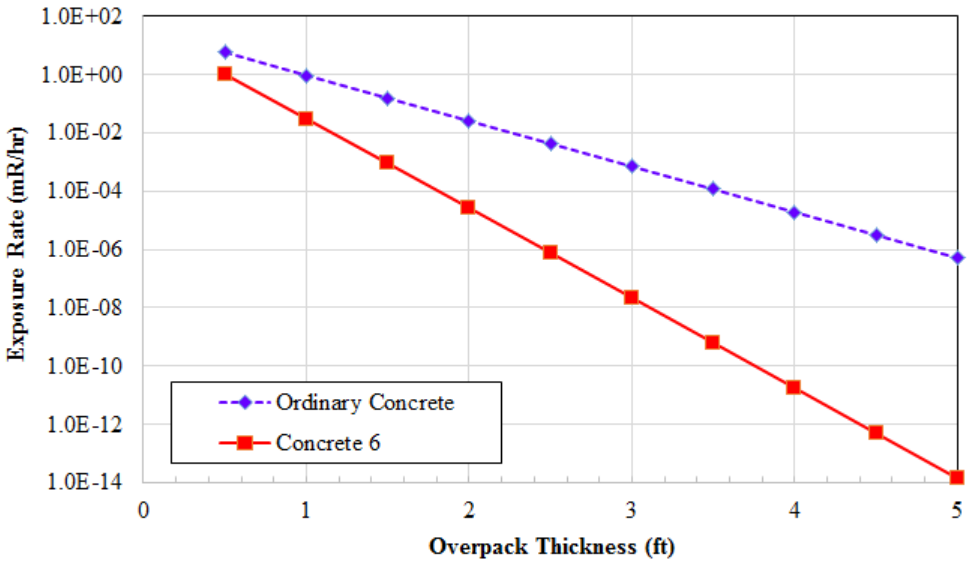

Figure 10-10: Exposure rate as a function of overpack thickness (log scale)

10.5 Conclusion

The shielding properties of thin films to be deposited on stainless steel for protection against localized corrosion, hydrogen diffusion, and mechanical wear have been investigated. Microshield calculations showed mass attenuation coefficients to be nearly identical among coating materials in the energy range of interest for shielding (0.4 MeV – 1.5 MeV). Experimental measurements show good agreement with predicted attenuation coefficients, based on material properties, for the bare stainless steel type 316. Coated steels show very similar attenuation to the bare substrate, which is expected based on the sub-micron thickness of each single-layer coating. The MFP of 0.6 MeV gammas in these materials is between 2 and 3.5 cm, and buildup in the coatings is negligible based on the proposed thickness of 50 μm. Based on full cask simulations using MicroShield, the five coating materials discussed previously (TiN, ZrO_2, TiO_2, Al_2O_3, and MoS_2) do not affect the exposure rate outside the cask to any measurable degree. Whereas these coatings do not provide additional shielding, they can be utilized for HLW storage without adversely affecting the shielding properties of the storage container.

Also in this study, a specialized type of concrete (concrete-6) containing Fe_3O_4 and PbO, introduced in a published work [13], was compared to ordinary concrete as an overpack material. Based on simulations, concrete-6 is able to decrease the total exposure rate outside a typical spent fuel cask by nearly three orders of magnitude. Double the thickness of ordinary concrete is required to achieve the same exposure rate as concrete-6. Given that there has yet to be a permanent storage solution for HLW and commercial spent nuclear fuel, a specialty concrete similar to concrete-6 warrants additional investigation into the feasibility of its use as shielding for HLW containers.

CHAPTER 11

STUDY OF GAMMA-RAY SHIELDING OF OXIDE GLASS SHIELDING MATERIALS

Published in Ann. Nucl. Energy: "Gamma-ray mass attenuation coefficient and half value layer factor of some oxide glass shielding materials," E-S. A. Waly, M. A. Fusco, M. A. Bourham, Vol. 96, pp. 26-30, October 2016, DOI: 10.1016/j.anucene.2016.05.028

The variation in dosimetric parameters such as mass attenuation coefficient, half value layer factor, exposure buildup factor, and the photon mean free path for different oxide glasses for the incident gamma energy range 0.015-15 MeV has been studied using MicroShield v5.03. It has been inferred that the addition of PbO and Bi_2O_3 improves the gamma ray shielding properties. Thus, the effect of chemical composition on these parameters is investigated in the form of six different glass compositions, which are compared with specialty concrete for nuclear radiation shielding. The composition termed 'Glass 6' in this paper has the highest mass attenuation and the smallest half value layer and may have potential applications in radiation shielding. An example dry storage cask utilizing an additional layer of Glass 6 as an intermediate shielding layer, simulated in MicroShield, is capable of reducing the exposure rate at the cask surface by over 20 orders of magnitude compared to the case without a glass layer. Based on this study, Glass 6 shows promise as a gamma-ray shielding material, particularly for dry cask storage.

11.1 Introduction

Due to the overwhelming concern about release of radionuclides from various sources, as well as the increasing use of gamma ray-emitting isotopes in industry, medicine, and agriculture, it has become necessary to study the shielding properties of new and improved materials. There is always a need to develop new materials that can be used under the potentially harsh conditions of radiation exposure and act as shielding materials for extended periods of time.

The most conventional material used for the purpose of radiation shielding for nuclear reactors and nuclear waste storage is concrete. It is a mixture of light nuclei (primarily hydrogen) and heavy nuclei, giving it the ability to be an effective shield against neutron and gamma radiation. Concrete is relatively inexpensive and easy to cast in many shapes and sizes, in addition to being strong and structurally sturdy. However, prolonged exposure to nuclear radiation results in heating of the concrete, which causes a decrease in density and a possible loss of cooling water and/or gas. Another drawback of concrete is that it is not transparent to visible light, and one cannot see through the concrete to monitor what goes on inside.

As an alternative to concrete, glasses can also act as effective shielding materials. They are typically transparent to visible light and their properties can be modified significantly by changing composition and adopting variations in preparation techniques [12], [168]. During recent years, there has been increasing interest in the synthesis, structure, and physical properties of heavy metal oxide glasses due to their high refractive index, high infrared transparency, high density, and good shielding of gamma rays [15]–[18], [169]–[171]. In particular, lead oxide and bismuth oxide have been used as additives in several silicate and borate glasses in order to achieve superior physical and shielding properties [172]–[174].

The present work has been undertaken to evaluate different types of glass systems as gamma-ray shields, which include changes in chemical composition. These glasses will be compared to a specialty concrete composition for radiation shielding applications.

Additionally, dry storage casks utilizing thin layers of these glass compositions are simulated computationally to determine changes in exposure rate.

11.2 Computational Methods and Materials

Linear attenuation coefficients are calculated from the exponential attenuation law:

$$I = I_0 \exp\left(-\mu_t x\right) \tag{11.1}$$

Where I_0 is the initial intensity, I is the transmitted intensity, x is the penetration depth, and μ_t is the total linear attenuation coefficient at a specific photon energy. The mass attenuation coefficient is defined as:

$$\frac{\mu}{\rho} = \frac{1}{\rho t} \ln\left(\frac{I_0}{I}\right) \tag{11.2}$$

Where ρ is the mass density and t is the absorber thickness. The mass attenuation coefficient for a mixture of materials is:

$$\left(\frac{\mu}{\rho}\right)_{total} = \sum_i w_i \left(\frac{\mu}{\rho}\right)_i \tag{11.3}$$

Where the total mass attenuation coefficient $(\mu/\rho)_{total}$ is the sum of the mass attenuation coefficient of the individual components $(\mu/\rho)_i$ multiplied by the weight fraction w_i of component i. Finally, the half value layer (HVL), which is the thickness at which the

transmitted intensity is one-half the initial intensity, is determined from Eq. (11.1) and depends only on the linear attenuation coefficient:

$$HVL = \frac{\ln(2)}{\mu} \tag{11.4}$$

The MicroShield v5.03 software package [175] is used as the principle computational tool in this study. MicroShield® uses properties of individual materials to compute theoretical mass attenuation coefficients using Eq. (11.3), as well as exposure buildup factors based on input material composition and density. The program can handle many different geometries, including a cylindrical spent fuel cask, which is of primary interest. Mass attenuation coefficients and buildup factors are computed for each composite material across a photon energy range of 15 keV to 15 MeV.

Six compositions of glass for radiation shielding composed of various metal oxides are considered in this study. The relevant properties of the metal oxides used to simulate the compositions of glass are provided in Table 11-1. The composition of each of the six glasses is given in Table 11-2, along with its resulting mass density. Each of the glass compositions contains at least 25% PbO by weight, as lead absorbs photons very efficiently based on its high atomic number and density. Clearly the density of the glass increases as the content of either PbO, Bi_2O_3, or CdO increases because of the high density of each. Table 11-3 shows the composition of the specialty concrete, termed ‘Concrete 6’ [13], used as the overpack material in the simulation of the waste storage cask. The cement in the concrete is Portland and the aggregate is 80% SiO_2 and 20% $CaCO_3$. Densities for the materials described in Table 11-1,Table 11-2, and Table 11-3 are exhibited in Figure 11-1.

Table 11-1: Physical properties of relevant metal oxides

Glass oxide	M (g/mol)	ρ (g/cm^3)	V (cm^3/mol)
PbO	223.2	9.53	23.421
Bi_2O_3	465.95	8.9	52.36
CdO	128.41	8.15	15.76
Al_2O_3	101.96	3.95	25.81
SiO_2	60.08	2.65	22.67
B_2O_3	69.62	2.46	28.3

Where M is the molar mass, ρ is the mass density, and V is the molar volume (M/ρ).

Table 11-2: Chemical composition (% by weight) and mass density of glasses simulated in this work

Glass Type	Composition						Density (g/cm^3)
	PbO	**Al_2O_3**	**B_2O_3**	**SiO_2**	**CdO**	**Bi_2O_3**	
Glass 1	0.25	0.1	0.65	---	---	---	4.3765
Glass 2	0.45	0.1	0.45	---	---	---	5.7905
Glass 3	0.5	0.1	---	0.4	---	---	6.22
Glass 4	0.3	---	0.2	---	0.5	---	7.726
Glass 5	0.3	---	0.2	---	---	0.5	7.801
Glass 6	0.8	0.1	---	0.1	---	---	8.284

Table 11-3: Chemical composition (% by weight) of 'Concrete 6'

Concrete 6 Composition						
Cement	**Water**	**Aggregate**	**Additive**			**Density**
13.98%	7.63%	23.517%	39.195% magnetite (Fe_3O_4) 15.678% lead oxide (PbO)			4.64
Composition	**CaO**	**SiO_2**	**Al_2O_3**	**Fe_2O_3**	**MgO**	**SO_3**
Weight Percent	8.8074	21.8892	0.4194	0.699	0.4194	0.4194
	Na_2O	**K_2O**	**H_2O**	**$CaCO_3$**	**Fe_3O_4**	**PbO**
	0.04194	0.09786	7.63	4.7034	39.195	15.678

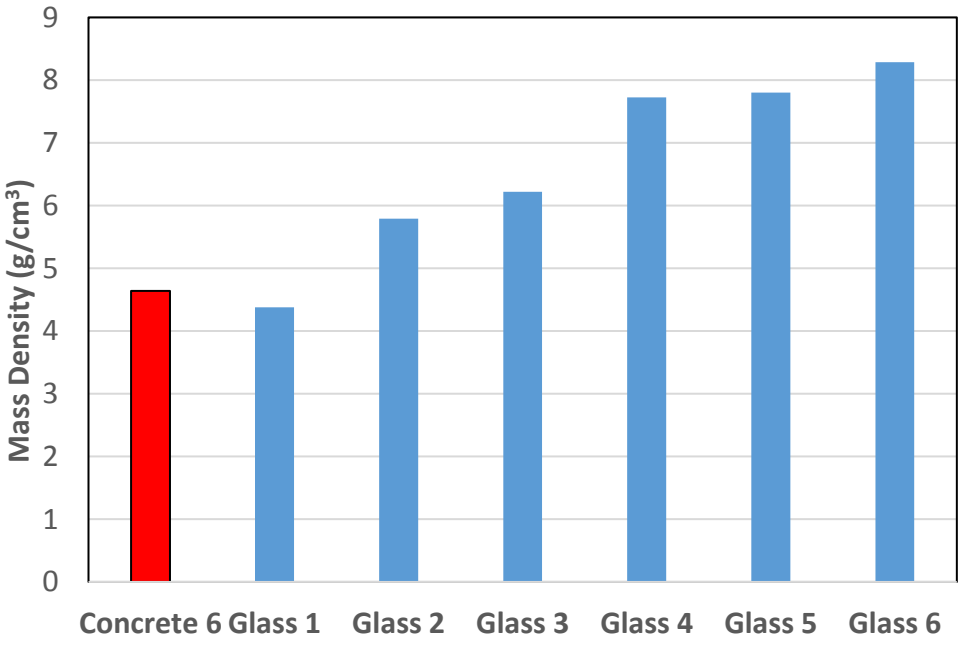

Figure 11-1: Mass density of materials investigated

11.3 Results and Discussion

11.3.1 Mass Attenuation Coefficient

The mass attenuation coefficient as a function of incident photon energy for the six compositions of glass and 'Concrete 6' is given in Figure 11-2. The photon energy range may be divided into three regions based on the type of interaction that dominates. In the low energy region, which extends from 15 keV to several hundred keV, attenuation decreases sharply with increasing energy. Photoelectric absorption is the dominant interaction mechanism for low energy gammas, which has a strong dependence on atomic number. A higher effective atomic number of the medium means photons are more likely to be absorbed as there are more electrons with which to interact. The increase in attenuation is attributable to the Pb K-edge. The K shell binding energy of lead is approximately 88 keV [167], which results in an increase in absorption efficiency for photons of incident energy slightly higher the binding energy.

The intermediate energy range covers a region from 0.5 MeV to several MeV, over which Compton scattering is the predominant interaction mechanism for gamma rays. The cross section for Compton scattering has a very weak dependence on atomic number, which is why all 7 materials converge to similar values for the mass attenuation coefficient. In this energy range, attenuation still decreases monotonically with increasing photon energy, albeit more slowly than in the low energy region.

The high energy range comprises all gammas with energy above several MeV (~ 3-5 MeV). Pair production becomes dominant for high energy photons. Unlike the other two interaction mechanisms, the pair production cross section increases with increasing photon energy. This accounts for the slight upturn in mass attenuation at high energy. Also, pair production increases slightly with increasing atomic number, giving rise to the minor spread in attenuation among the simulated materials at the end of the energy spectrum.

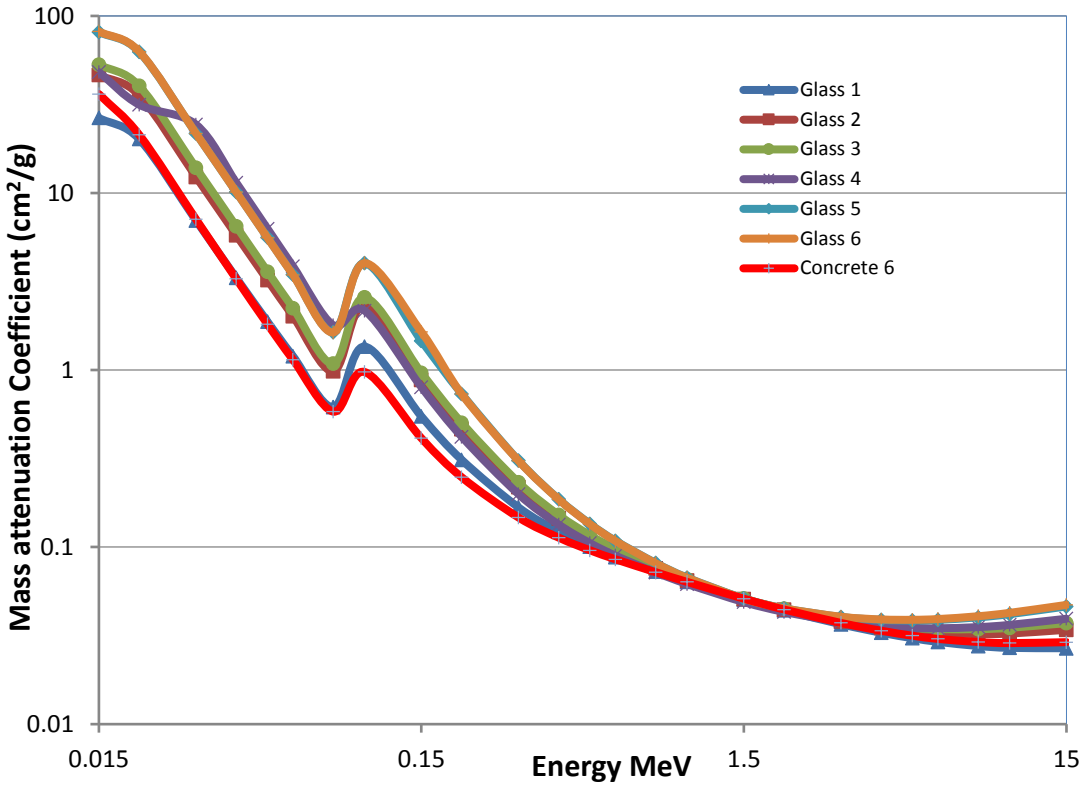

Figure 11-2: Mass attenuation coefficient versus incident photon energy

11.3.2 Half Value Layer

The half value thickness is calculated from attenuation coefficients using Eq. (11.4). Table 11-4 contains HVL values over a range of photon energies, and Figure 11-3 presents Table 11-4 graphically. The HVL is seen to increase as photon energy increases, as is expected based on the attenuation coefficients in Figure 11-2. The half value thickness is smaller for the glass compared to Concrete 6 with the exception of Glass 1, which is the only glass composition with a smaller mass density than the concrete. HVL roughly scales with density considering that Glass 6 is nearly twice as dense as Concrete 6, and its HVL is approximately half that of

Concrete 6 for most of the photon energies. The much larger difference between Concrete 6 and Glasses 2-6 for 0.1 MeV photons may be ascribed to the larger concentration of lead in each of the glass compositions, which has an absorption increase for photon energies in the vicinity its K-edge (0.088 MeV).

Table 11-4: Half Value Layer (cm) for several photon energies (0.1, 0.5, 1, 3, and 5 MeV)

Energy	Concrete 6	Glass 1	Glass 2	Glass 3	Glass 4	Glass 5	Glass 6
5 MeV	4.72	5.179	3.571	3.185	2.669	2.307	2.153
3 MeV	3.999	4.322	3.152	2.869	2.469	2.203	2.070
1 MeV	2.347	2.488	1.846	1.696	1.508	1.32	1.248
0.5 MeV	1.556	1.575	1.061	0.954	0.886	0.657	0.621
0.1 MeV	0.153	0.117	0.052	0.043	0.043	0.022	0.021

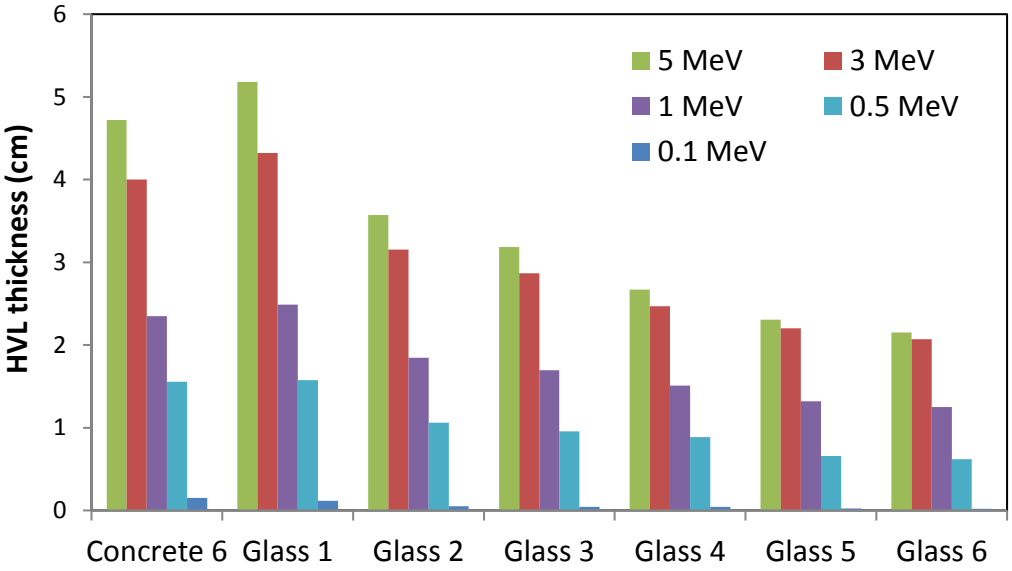

Figure 11-3: Half value layer at different photon energies (0.1, 0.5, 1, 3, and 5 MeV)

11.3.3 Exposure Buildup Factor

The variation of the exposure buildup factor with incident photon energy at fixed penetration depths of 0.5, 5, 10, 15, 25, and 30 mean free paths (MFP) for Glass 1 is shown in Figure 11-4. The buildup factor peaks for incident photons with mean energy of 0.5 MeV. This is explained with the photon interaction mechanisms. Compton scattering dominates in the intermediate energy range, leading to a greater proportion of scattering interactions over absorption. This causes a degradation of photon energy without complete removal of the photon, hence the higher buildup factor and increased escape probability. The low energy range where photoelectric absorption dominates shows very small buildup factors because scattering is minimal. For energies above several MeV the buildup factors are smaller than at the peak, but they are still significant. Pair production generates two 511 keV gammas, which will likely undergo Compton scattering based on the relative cross sections of the three main interaction

mechanisms at that energy. This generates a larger exposure buildup factor than in the low energy region, where absorption does not lead to the production of additional photons.

Figure 11-5 shows the exposure buildup factor as a function of penetration depth in MFP of the six glass compositions and Concrete 6 for an incident photon energy of 15 MeV. The buildup factors follow the trends of the mass attenuation coefficients (Figure 11-2) at 15 MeV, and the difference between the glass types is larger as the material thickness increases. Pair production scales with atomic number and Compton scattering scales with mass density, which accounts for the grouping of materials in Figure 11-5. The combination of high-Z elements and high mass density accounts for the very high buildup factors for Glass 5 and Glass 6.

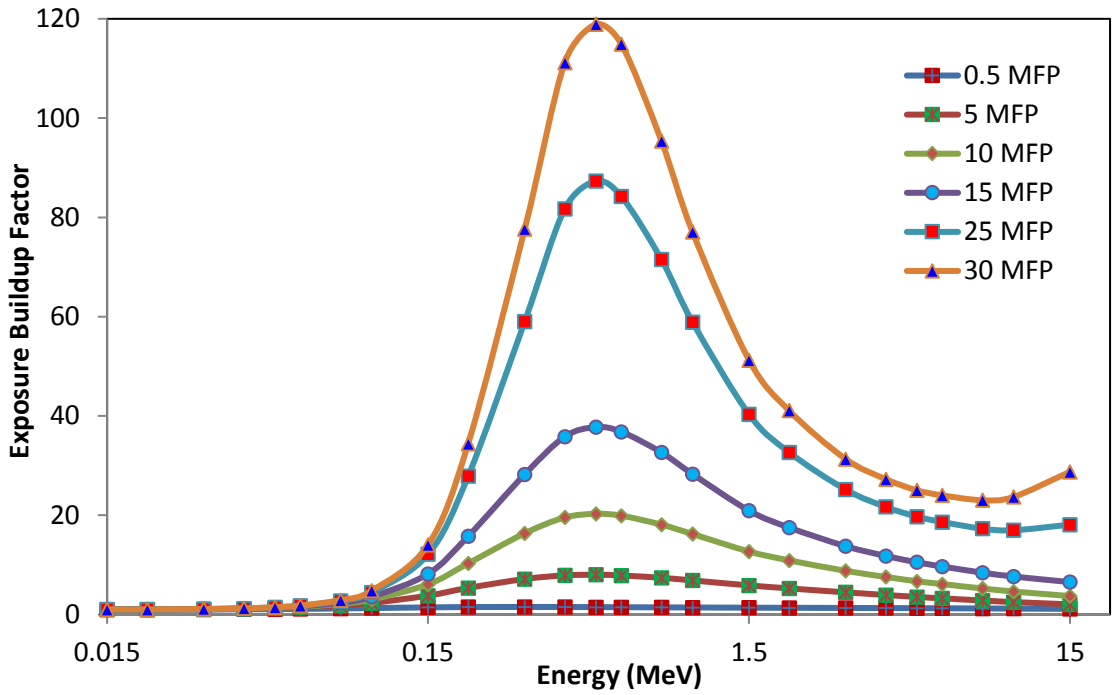

Figure 11-4: Exposure buildup factor versus incident photon energy at different mean free paths (0.5, 5, 10, 15, 25, and 30 MFP) – Glass 1

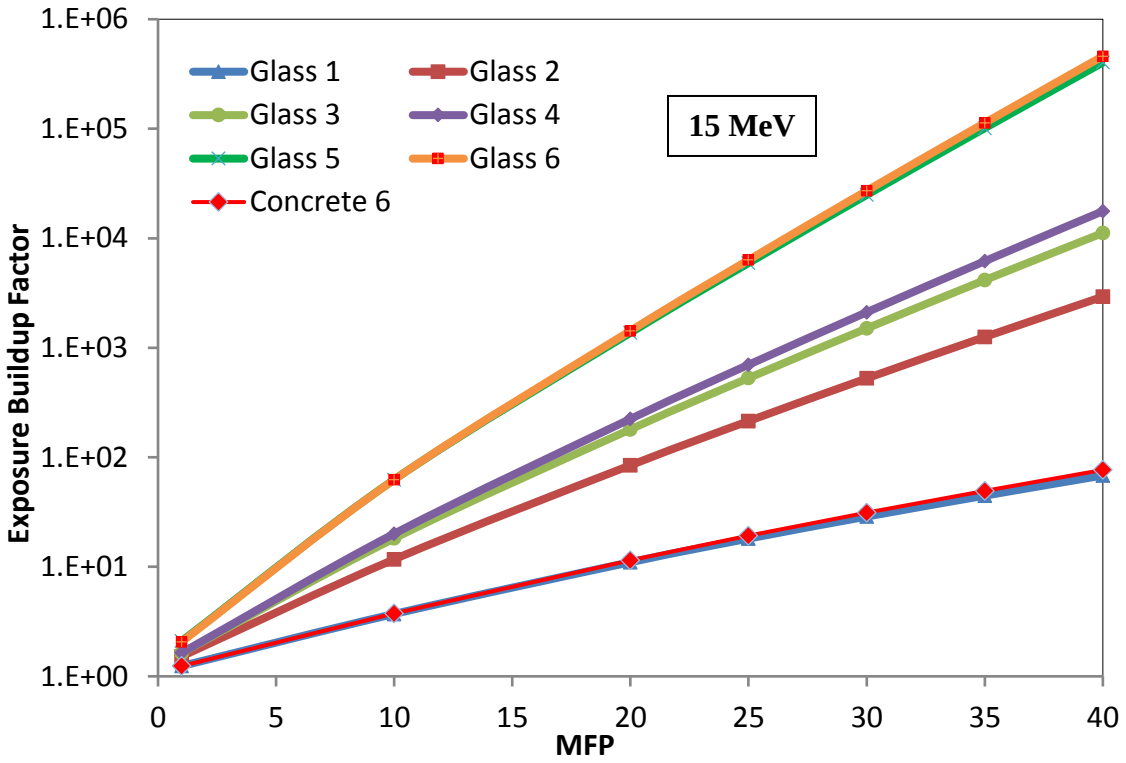

Figure 11-5: Dependence of exposure buildup factor on penetration depth for glasses and concrete at fixed incident photon energy of 15 MeV

11.3.4 Exposure Rate – Dry Cask

The compositions of glass in Table 11-2 may be put to practical application by utilizing them as shielding layers for dry casks for spent fuel storage. The cross sectional view of the cylindrical cask geometry for the MicroShield simulation is depicted in Figure 11-6. Case 1 has a two layer shield: an inner 303cu steel canister shell of 0.27 ft. thickness and a 2 ft.-thick Concrete 6 overpack. Case 2 implements a 0.2 ft.-thick glass shield between the steel and concrete, and the thickness of Concrete 6 is decreased to 1.8 ft. to maintain the same total cask

diameter. The thin glass layer provides increased shielding without significantly increasing buildup.

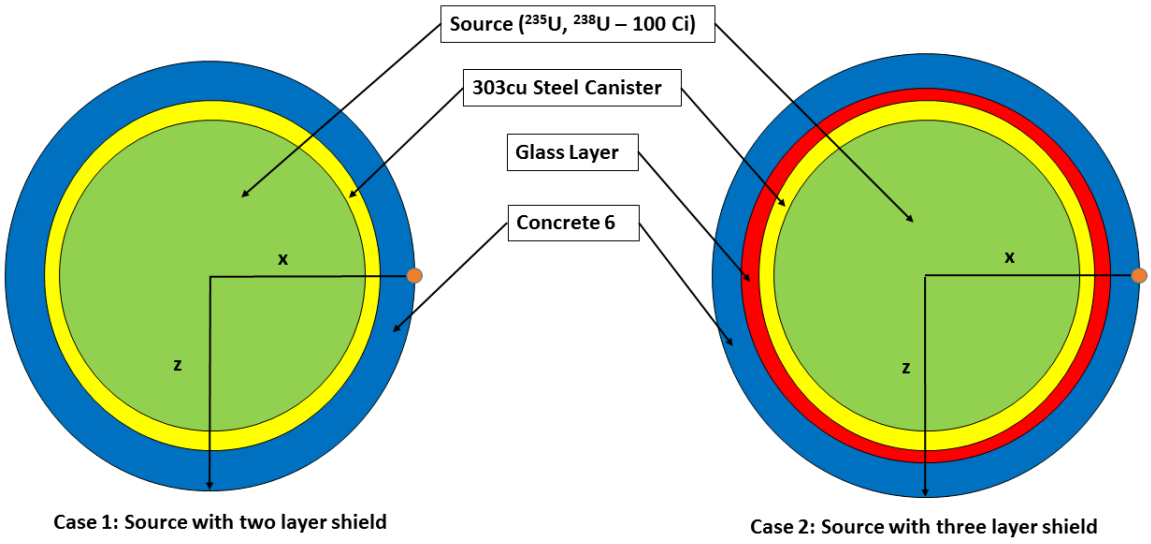

Figure 11-6: Cross sectional cask geometry for two cases – with and without glass shielding layer; dose point is noted on the cask surface

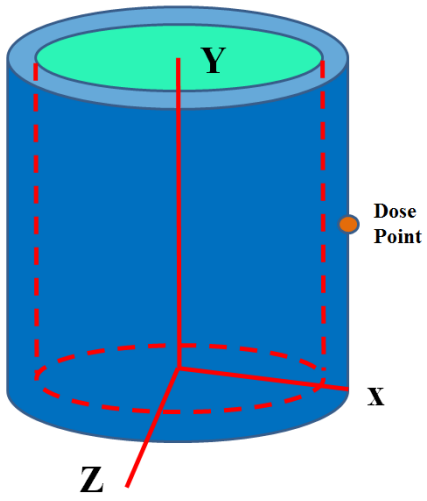

Figure 11-7: MicroShield cask geometry – side view

The source is a combination of ^{235}U and ^{238}U with total activity of 100 Ci and is 20 ft. high with an 8.727 ft. radius. The dose location at which exposure rate is calculated is 10 ft. high (half cask height) on the outer surface of the cask. The dose location is noted by an orange circle from the top view in Figure 11-6 and from the side view in Figure 11-7.

The exposure rate (mR/hr) at the dose point shown in Figure 11-6 and Figure 11-7 is compared between case 1 (no glass layer) and case 2 with each of the six different glass compositions. Figure 11-8 shows the exposure rate comparison for the 0.2214 MeV ^{235}U photon. Each composition of glass provides greater shielding than the case with only concrete because of the higher mass attenuation. Glass 6 provides the greatest reduction in dose with an exposure rate of 6.16E-76 mR/hr compared to 1.73E-53 mR/hr for case 1. A 2.4 inch thick layer of Glass 6, which is composed of 80% PbO, is capable of decreasing the exposure rate by more than 20 orders of magnitude.

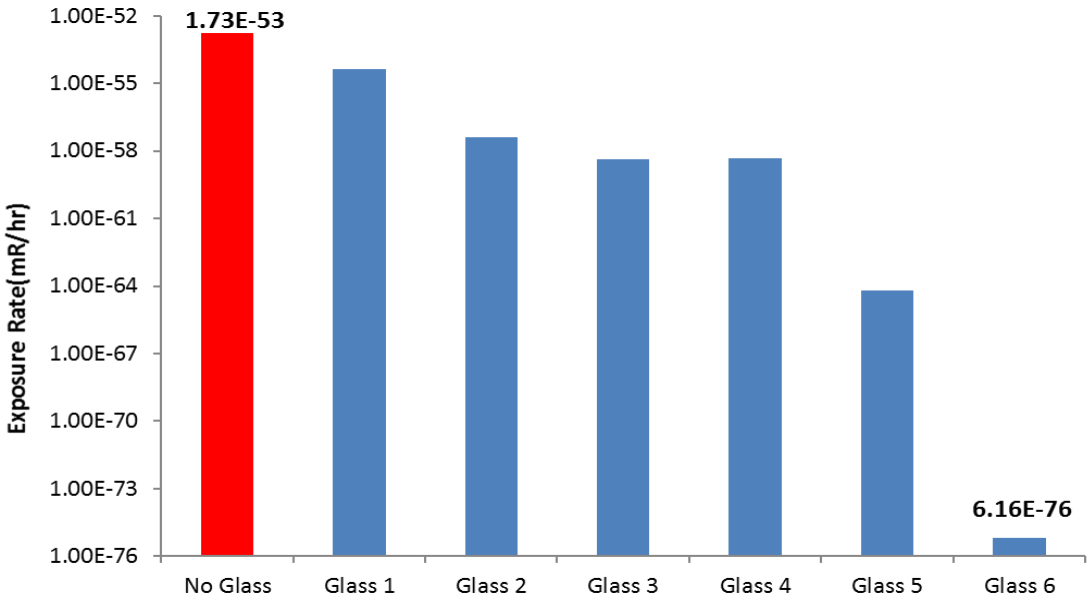

Figure 11-8: Variation of exposure rate (mR/hr) for storage casks with and without a glass shielding layer – 0.2214 MeV photons

11.4 Conclusion

From the present investigations, different compositions of glasses, especially those with higher content of PbO and Bi_2O_3, have been shown to be promising gamma ray shielding materials. Mass attenuation coefficients for each of the six glass compositions are observed to be higher than the specialty shielding concrete (Concrete 6) over a range of photon energies from 15 keV to 15 MeV. The high attenuation of the glass compositions allows for a thin wall of glass to enhance photon absorption without significantly altering buildup. As can be seen in Fig. 5, the exposure buildup factors for the primarily lead- and bismuth-containing glasses can become very large depending on the thickness. However, for photon energies of interest, the 0.2 ft. glass layer is less than 10 MFPs thick. For the case of 0.2214 MeV photons, a layer of Glass 6 is able to reduce the exposure rate outside of an example spent fuel cask by over 20 orders of magnitude without increasing the overall dimensions of the cask.

It is worth noting that Concrete 6 has previously been shown to greatly reduce the exposure rate outside a spent fuel cask over a range of photon energies from 15 keV to 2 MeV, with its effectiveness peaking between 0.4 and 0.6 MeV, where a majority of photons emitted from spent fuel lie [7]. Introduction of a glass shielding layer in tandem with specialty radiation shielding concrete allows the overpack thickness to be reduced substantially without sacrificing shielding efficiency. This provides a lighter cask, which may be particularly useful during transport of spent fuel or other high level waste.

As was mentioned previously, these glass compositions have the added benefit of being transparent to visible light. This is particularly useful for shielding applications in which being in view of the radiation source is advantageous.

CHAPTER 12

IMPACT OF SPECIALTY GLASS AND CONCRETE ON GAMMA SHIELDING IN MULTI-LAYERED PWR DRY CASKS

Article Published in Prog. Nucl. Energy: "Impact of specialty glass and concrete on gamma shielding in multi-layered PWR dry casks," E-S. A. Waly, M. A. Fusco, M. A. Bourham, Vol. 94, pp. 64-70, January 2017, DOI: 10.1016/j.pnucene.2016.09.017

There is a strong likelihood that dry casks will be relied upon for many decades to come as the storage system for nuclear spent-fuel high-level waste (HLW), which places importance on robust shielding materials for cask construction. A dry cask with multi-layered shielding has been simulated in MicroShield v9.05 to determine exposure rates due to gamma-rays at the outer cask surface. The cask consists of a 0.27 ft. thick stainless steel type 303Cu waste basket, a 0.2 ft. thick lead oxide glass shielding layer (named as Glass 6), and a 1.8 ft. thick overpack made of a specialty high density concrete (named as Concrete 6). Three spent fuel configurations have been used as photon sources, which include one high burnup (72 GWd/MTU) and two medium burnup (38.6 GWd/MTU) fuels. The cumulative exposure rate over all photon energies from 15 keV to 2 MeV is 6.81E-6 mR/hr at the outer cask surface for the high burnup spent fuel. This is roughly one order of magnitude smaller than if the glass layer were replaced with an equivalent thickness of Concrete 6 and is 3-4 orders of magnitude smaller than replacing the specialty concrete with ordinary, standard density concrete. Varying the ratio of the glass thickness to the concrete thickness significantly impacts the shielding

effectiveness, which should be considered along with structural and thermal stability for dry cask designs.

12.1 Introduction

Spent fuel pools at many of the commercial nuclear power plants across the United States are reaching their capacity limits, even with "re-racking" to increase the number of fuel assemblies that can be safely stored. Currently, the only available option following removal from pool storage is for the assemblies to be placed in dry cask systems. The spent fuel assemblies are left in pool storage to cool for several years after removal from the reactor before they are placed in dry storage containers and stored on-site. In some cases, they may instead be transported to a more centralized storage facility.

Based on the high levels of radiation emitted from spent fuel, it must be transported and stored in very sturdy containers that provide complete containment, physical protection, shielding, heat removal, and criticality safety. The International Atomic Energy Agency (IAEA) has compiled and published a list of cask manufacturers and models that are in use around the world [176], from which it is clear that there are many combinations of materials and cask configurations that are adequate for spent fuel storage. Typical dry casks employ a stainless steel inner canister with a concrete overpack, which may be rebar-reinforced, and/or an outer steel shell, along with a neutron shielding layer consisting of a high density material with low effective atomic number. Exposure due to gamma-rays is of primary concern for spent fuel storage and must be minimized, whereas neutron emission from spent fuel is low and can be shielded quite easily. With this in mind, more efficient shielding configurations for dry casks may be able to simultaneously reduce gamma exposure and cask volume, thus saving on construction, transportation, and monitoring costs.

In this study, the shielding properties of a multi-layered spent fuel cask using specialty gamma-ray shielding materials are investigated using computational simulations. The cask consists of three layers: the inner waste package canister made of AISI type 303Cu stainless steel, an intermediate shielding layer of a specialty high-density glass named as 'Glass 6' from the work of Waly et al. [177], and a concrete overpack consisting of a material named as 'Concrete 6' from the work of Waly and Bourham [13].

12.1.1 Materials

Stainless steel type 303Cu is an austenitic 18-8 stainless steel, meaning that it nominally contains 18% Cr and 8% Ni by weight, which is common among the 300-series stainless steels. The 'Cu' designation indicates that it is alloyed with 1.5% - 3.5% copper by weight. The addition of copper to austenitic stainless steels has been shown to significantly increase machinability and ductility [178].

There has been much interest recently in specialty compositions of glass oxides for radiation shielding [15]–[18], [170]. Glass oxides have the advantage of being transparent to visible light, and with the proper composition may be made with very high density and high thermal stability, both of which are important for radiation shielding applications. It is also simple to create glass that is an effective neutron shield by adding boron to the composition, which is already a prevalent ingredient of standard glass mixtures. Augmenting the dry casks with an appropriate glass layer could remove a portion of the thermal burden from the concrete overpack, which is prone to thermal stresses and cracking from prolonged radiation absorption [179].

Lead oxide (PbO) glasses have received significant attention based on the very high gamma ray interaction cross sections and high density of lead. Glasses with substantial concentrations of PbO have been prepared for study by several researchers, typically using the melt quenching technique [18], [179]–[181]. The addition of up to 60 mol% PbO in glass mixtures has been

shown to improve thermal stability [181]. However, high PbO concentrations may bring about a decrease in the rigidity of the glass [10,11], though this also depends on the other components of the glass. The composition and density of the named Glass 6 used in this study may be found in Table 12-1, which has been determined to provide very effective gamma-ray shielding [177].

Table 12-1: Chemical composition and density of Glass 6 [177].

Glass type	**Composition (%)**			**Density (g/cm^3)**
	PbO	Al_2O_3	SiO_2	
Glass 6	80	10	10	8.284

Concrete has proven itself to be an extremely versatile material, particularly in structural and shielding applications, based on the ability to tailor the concrete additives for specific purposes. Adding high density and high atomic number components as aggregates in concrete to increase shielding effectiveness has been sufficiently well documented [12], [14], [182]–[187]. This is especially important for spent nuclear fuel storage and transportation. The ability to decrease the overpack thickness without sacrificing desirable radiation shielding and structural properties is essential for increasing the efficiency of cask design. Decreasing the volume of the spent fuel cask could decrease transportation, loading, and storage costs, along with a decrease in the space required for placement of dry casks. With that goal in mind, a specialty concrete with substantial concentrations of magnetite and lead oxide additives was presented by Waly and Bourham [13]. The composition and density are given in Table 12-2.

Table 12-2: Chemical composition and density of Concrete 6 [13].

Material density	**Concrete 6 Composition**			
	Cement	**Water**	**Aggregate**	**Additive**
4.64 g/cm^3	13.98%	7.63%	23.517%	39.195% magnetite (Fe_2O_3) 15.678% lead oxide (PbO)

12.1.2 PWR Spent Fuel Composition

The radionuclide concentration and corresponding activity of spent fuel from two sample pressurized water reactors (PWRs) was calculated to support proposed spent fuel ratio (SFR) experiments at Sandia National Laboratories [6]. The high burnup isotopic composition for spent fuel from the H. B. Robinson nuclear plant and the medium burnup data for the Surry plant spent fuel are used in this study. The depletion calculations were performed using ORIGEN2 and ORIGEN-ARP, both of which are codes developed at Oak Ridge National Laboratory [188]. The H. B. Robinson spent fuel was depleted according to a 72 GWd/MTU burnup followed by an 8 year decay, whereas the Surry spent fuel depletion was calculated for a 38.6 GWd/MTU burnup also followed by an 8 year decay. The Surry spent fuel calculations were performed assuming both an average reactor power and a realistic power profile. A total of three different spent fuel compositions are used for this study, all of which may be found in detail in Sandia National Laboratories report [6]. The composition for the 72 GWd/MTU H. B. Robinson spent fuel is presented in Table 12-3. The majority of the activity in the spent fuel is from Sr-90, Y-90, Cs-137, Ba-137m, and Pu-241 and will be the most important isotopes to consider for shielding purposes. A comparative study of the three spent fuel cases is presented in this paper to determine the effectiveness of the selected shielding materials.

Table 12-3: All nuclides for 72 GWD/MTU H. B. Robinson spent fuel – ORIGEN2 [21].

Nuclide	8.0YR Decay, Activity (Ci/MTU)	Nuclide	8.0YR Decay, Activity (Ci/MTU)
H-3	7.24E+02	Pm-148m	9.69E-18
Be-10	1.04E-05	Pm-148	5.46E-19
C-14	1.42E+00	Eu-150	1.36E-04
Si-32	6.89E-08	Sm-151	5.20E+02
P-32	6.89E-08	Eu-152	1.15E+01
S-35	1.81E-09	Gd-152	4.30E-18
Cl-36	2.63E-02	Gd-153	7.33E-02
Ar-37	3.47E-26	Eu-154	1.67E+04
Ar-39	1.72E-04	Eu-155	6.74E+03
K-42	1.59E-12	Tb-160	2.36E-09
Ca-41	4.52E-04	Ho-166m	5.68E-02
Ca-45	1.41E-06	Tm-170	1.44E-07
Sc-46	2.19E-12	Tm-171	1.60E-03
V-50	8.66E-16	Ta-182	1.33E-09
Cr-51	2.86E-31	W-181	1.23E-08
Mn-54	2.21E-03	W-185	1.70E-11
Fe-55	1.01E+00	Re-188	3.57E-14
Fe-59	1.58E-20	Ir-192	1.94E-07
Co-58	5.39E-12	Ir-192m	1.94E-07
Co-60	3.59E+01	Ir-194	3.62E-09
Ni-59	2.15E-02	Pt-193	5.14E-06

Table 12-3. Continued

Nuclide	8.0YR Decay, Activity (Ci/MTU)	Nuclide	8.0YR Decay, Activity (Ci/MTU)
Ni-63	3.44E+00	Tl-206	4.57E-08
Zn-65	2.60E-02	Pb-204	1.72E-16
Se-79	8.29E-01	Bi-208	7.43E-08
Kr-85	5.43E+03	Bi-210	4.58E-08
Sr-89	1.13E-12	Po-210	1.49E-08
Sr-90	7.77E+04	Tl-208	4.73E-02
Y-90	7.77E+04	Pb-212	1.32E-01
Y-91	3.94E-10	Bi-212	1.32E-01
Zr-93	3.29E+00	Po-212	8.43E-02
Nb-93m	1.94E+00	Po-216	1.32E-01
Mo-93	1.76E-03	Rn-220	1.32E-01
Nb-94	4.19E-04	Ra-224	1.32E-01
Zr-95	1.39E-08	Th-228	1.31E-01
Nb-95	3.08E-08	Th-230	1.20E-04
Nb-95m	1.03E-10	Th-231	1.95E-03
Tc-99	2.30E+01	Th-234	3.04E-01
Rh-102	4.33E-01	Pa-231	5.10E-05
Ru-103	4.29E-17	Pa-233	5.98E-01
Rh-103m	3.87E-17	Pa-234m	3.04E-01
Ru-106	2.52E+03	Pa-234	3.96E-04
Rh-106	2.52E+03	U-232	1.44E-01

Table 12-3. Continued

Nuclide	8.0 YR Decay, Activity (Ci/MTU)	Nuclide	8.0 YR Decay, Activity (Ci/MTU)
Pd-107	3.89E-01	U-233	4.32E-05
Ag-108	2.39E-03	U-234	9.53E-01
Ag-108m	2.69E-02	U-235	1.95E-03
Ag-109m	1.60E-02	U-236	2.44E-01
Cd-109	1.60E-02	U-237	3.58E+00
Ag-110	5.03E-02	U-238	3.04E-01
Ag-110m	3.78E+00	U-240	8.98E-06
Cd-113m	1.30E+02	Np-235	9.18E-05
In-113m	1.61E-08	Np-237	5.98E-01
Sn-113	1.61E-08	Np-238	2.21E-01
In-114	9.82E-17	Np-239	1.51E+02
In-114m	1.03E-16	Np-240m	8.98E-06
Cd-115m	2.72E-17	Pu-236	2.76E-01
In-115	2.62E-14	Pu-237	6.32E-19
In-115m	1.89E-21	Pu-238	1.58E+04
Sn-119m	7.26E-02	Pu-239	3.69E+02
Sn-121m	4.81E-01	Pu-240	7.54E+02
Sn-123	4.07E-04	Pu-241	1.46E+05
Te-123m	4.38E-06	Pu-242	6.92E+00
Sb-124	6.92E-12	Pu-243	3.60E-05
Sb-125	6.92E-12	Am-241	2.92E+03
Te-125m	4.42E+02	Am-242m	4.41E+01
Sn-126	2.06E+00	Am-242	4.39E+01

Table 12-3. Continued

Nuclide	8.0 YR Decay, Activity (Ci/MTU)	Nuclide	8.0 YR Decay, Activity (Ci/MTU)
Sb-126	2.88E-01	Am-243	5.06E+01
Sb-126m	2.06E+00	Am-245	3.91E-08
Te-127	9.10E-05	Cm-241	3.61E-26
Te-127m	9.29E-05	Cm-242	3.77E+01
Xe-127	2.47E-25	Cm-243	3.58E+02
Te-129	1.30E-22	Cm-244	3.74E+04
Te-129m	2.00E-22	Cm-245	6.92E+00
I-129	7.21E-02	Cm-246	4.63E+00
Cs-134	2.33E+04	Cm-247	3.60E-05
Cs-135	9.39E-01	Cm-248	2.68E-04
Cs-137	1.54E+05	Bk-249	2.69E-03
Ba-137m	1.46E+05	Bk-250	8.27E-08
Ce-141	7.46E-22	Cf-249	5.00E-03
Ce-142	5.57E-05	Cf-250	1.83E-02
Ce-144	4.98E+02	Cf-251	2.12E-04
Pr-144	4.98E+02	Cf-252	1.42E-02
Pr-144m	5.98E+00	Es-254	8.26E-08
Pm-146	1.10E+00	Total	7.30E+05
Pm-147	1.10E+04		

12.2 Computational Methods

MicroShield v9.05 [165] has been used to compute the photon activity from the isotopic breakdown of the three spent fuel cases discussed in the previous section, as well as to perform shielding assessments and calculate attenuation coefficients for the shielding materials. MicroShield is a deterministic code used for a variety of gamma-ray shielding applications in industry including in three licensing applications for new U.S. reactor designs submitted to the U.S. NRC in 2007 [189]–[191]. Being a deterministic code, it must employ some assumptions, particularly in the buildup, which are not well documented. Despite this, MicroShield has been shown to closely match MCNP calculations for all but the lowest energy gamma-rays [192]. Low energy photons (~ < 0.15 MeV) can deviate substantially from Monte Carlo calculations based on the treatment of buildup in MicroShield, particularly in the vicinity of a K-edge. However, photon energies greater than 0.4 MeV are less affected by buildup calculations, which represents the energy range of interest for dry cask storage (see Table 12-4).

12.2.1 Multi-Layered Cask Geometry

The dry storage cask for this work is modeled as a cylindrical source of radiation (spent fuel) surrounded by concentric cylinders acting as containers and/or shielding layers. The design of the multi-layered cask geometry is displayed in Figure 12-1. The source dimensions are 8.727 ft. radius and 20 ft. height for a total source volume of 4785.3 ft^3 (1.355E+8 cm^3). The innermost layer consists of 0.27 ft. of stainless steel type 303Cu, followed by a 0.2 ft. thick layer of the Glass 6, which is an oxide glass previously studied for shielding [177]. Finally, the outer layer is the Concrete 6 overpack that is 1.8 ft. thick, which is a form of blended concrete with magnetite and lead oxide additives with high shielding efficiency for gamma rays [13]. This will also be compared to the case of a 2 ft. thick concrete overpack with no glass layer to

conserve the total shielding thickness. The dose is measured at the outer surface of the cask 10 ft. from the bottom (half way up the cask).

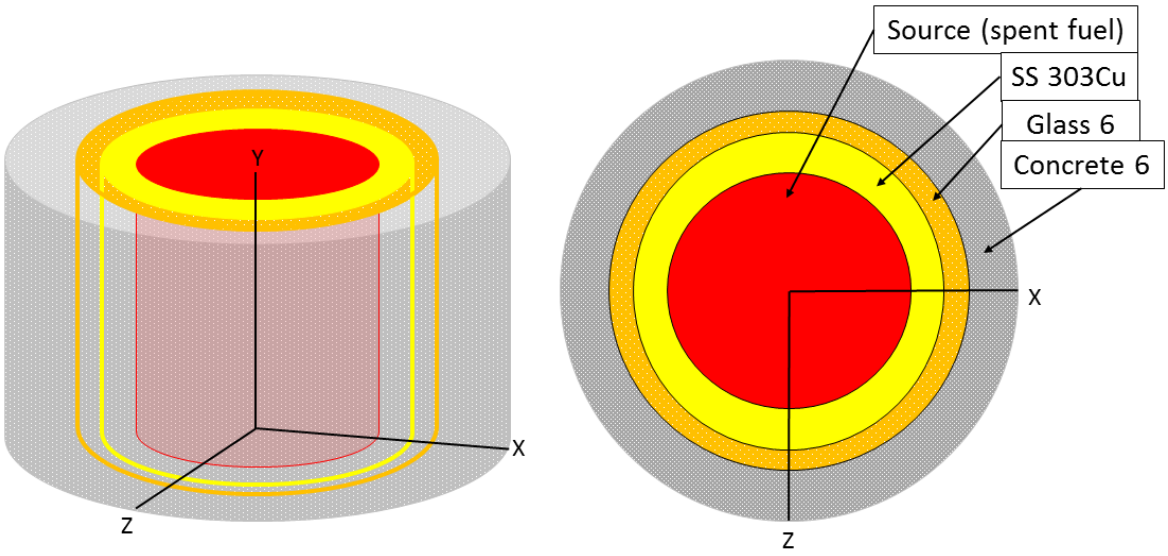

Figure 12-1: Multi-layered spent fuel dry cask – MicroShield geometry. Cylindrical source surrounded by three concentric cylindrical shielding layers

12.2.2 Photon Activity of Spent Fuel

Gamma-rays are the primary source of radiation exposure from high-level nuclear waste. Neutrons are also of concern, though the emission levels are much lower, and they may be efficiently shielded using high-density, low-Z materials. As such, only photons emitted from spent fuel will be considered in shielding calculations.

The spent fuel compositions found in Ref. [6] are used as inputs to MicroShield to build photon activities binned by energy group for each burnup configuration. The calculated photon activities may then be used as source terms for shielding calculations. Gamma-ray activity for the 72 GWd/MTU H. B. Robinson spent fuel and for the 38.6 GWd/MTU Surry spent fuel

(average and realistic power) is provided in Table 12-4 and Table 12-5 for 18 energy groups from 0.015 MeV to 2 MeV. The total source volume used for activity calculation is 4785.3 cubic feet; as indicated in the previous section for the multi-layered dry cask geometry.

Photon activities from Table 12-4 and Table 12-5 are plotted in Figure 12-2. The 72 GWd/MTU H. B. Robinson spent fuel has higher photon activity at all considered energies from 0.015 to 2.0MeV. This is expected because the higher burnup produces higher concentrations of fission products, which emit a majority of the radiation from spent fuel. The activity is dominated by the 0.6 MeV average energy photon group, which is primarily composed of the 662 keV gamma ray emitted following the decay of Cs-137 to the metastable state of Ba-137. The high burnup H. B. Robinson fuel also has a significant contribution from the photon group with average energy of 0.8 MeV, making up roughly 16.4% of the energy activity.

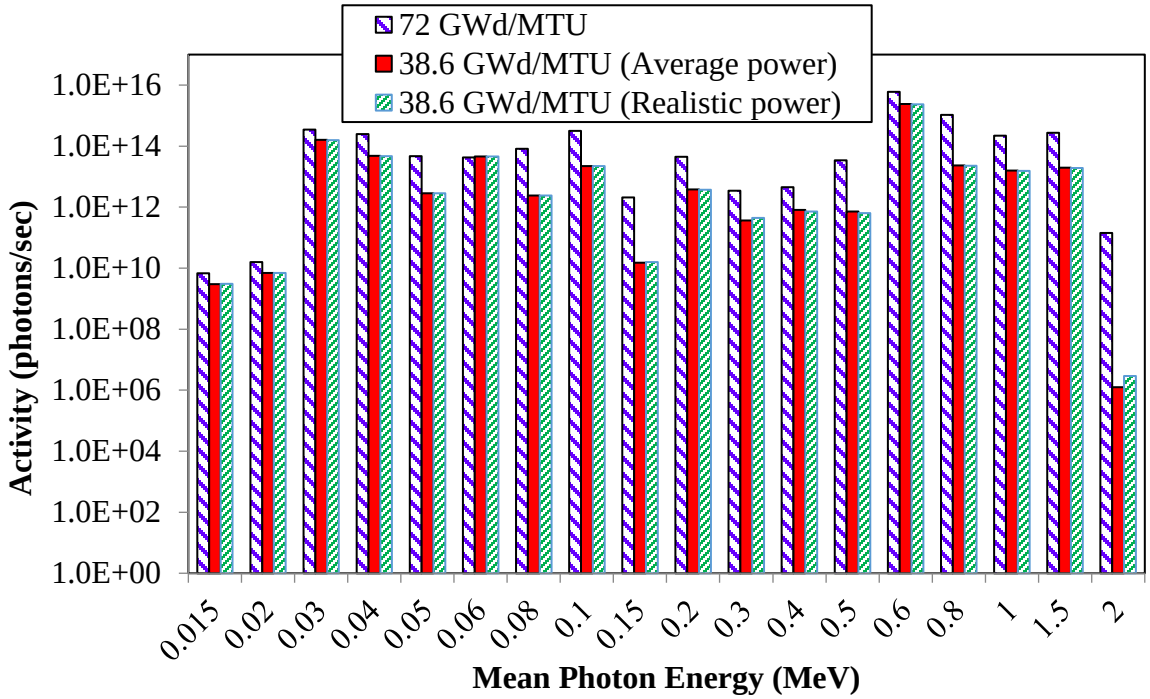

Figure 12-2: Photon activity by average group energy for three spent fuel burnup profiles

Table 12-4: Photon activity from 72 GWD/MTU H. B. Robinson spent fuel - MicroShield

Gamma Photon Group	Group Mean Photon Energy (MeV)	Activity Photons/sec	Volume source Photons/sec/cm^3	% Energy Activity
1	0.015	6.80E+09	5.02E+01	0.000
2	0.020	1.58E+10	1.16E+02	0.000
3	0.030	3.45E+14	2.55E+06	0.202
4	0.040	2.51E+14	1.85E+06	0.195
5	0.050	4.68E+13	3.45E+05	0.046
6	0.060	4.30E+13	3.17E+05	0.050
7	0.080	8.14E+13	6.01E+05	0.127
8	0.100	3.13E+14	2.31E+06	0.610
9	0.150	2.10E+12	1.55E+04	0.006
10	0.200	4.50E+13	3.32E+05	0.175
11	0.300	3.43E+12	2.53E+04	0.020
12	0.400	4.53E+12	3.34E+04	0.035
13	0.500	3.40E+13	2.51E+05	0.331
14	0.600	5.96E+15	4.40E+07	69.63
15	0.800	1.05E+15	7.78E+06	16.42
16	1.000	2.18E+14	1.61E+06	4.251
17	1.500	2.70E+14	1.99E+06	7.893
18	2.000	1.43E+11	1.05E+03	0.006
	Total	8.669E+15		

Table 12-5: Photon activity per MTU for 38.6 GWD/MTU Surry spent fuel (average and realistic power profiles) - MicroShield

Gamma Photon Group	Group Mean Photon Energy (MeV)	Average Power Activity Photons/sec	Realistic Power Activity Photons/sec
1	0.015	2.99E+09	3.08E+09
2	0.020	7.02E+09	7.03E+09
3	0.030	1.61E+14	1.55E+14
4	0.040	4.81E+13	4.67E+13
5	0.050	2.87E+12	2.82E+12
6	0.060	4.58E+13	4.61E+13
7	0.080	2.42E+12	2.38E+12
8	0.100	2.23E+13	2.22E+13
9	0.150	1.52E+10	1.59E+10
10	0.200	3.76E+12	3.74E+12
11	0.300	3.61E+11	4.39E+11
12	0.400	8.13E+11	7.19E+11
13	0.500	7.13E+11	6.34E+11
14	0.600	2.40E+15	2.32E+15
15	0.800	2.35E+13	2.25E+13
16	1.000	1.57E+13	1.53E+13
17	1.500	1.97E+13	1.93E+13
18	2.000	1.26E+06	2.91E+06
	Total	2.75E+15	

12.3 Results and Discussion

12.3.1 Attenuation Coefficient

The linear attenuation coefficient for each of the three shielding materials considered in this study has been calculated using MicroShield and is displayed in Figure 12-3. The Glass 6 layer possesses the highest attenuation coefficient at all photon energies up to 2 MeV based on its high density and lead concentration. The jump in attenuation for the 0.1 MeV group may be ascribed to the K-edge of lead due to its K-shell binding energy of 88 keV [167]. This explains why it is not seen in the attenuation of the stainless steel, which lacks any concentration of lead, and also why it is more pronounced in Glass 6, which contains 80% PbO, compared to the 15.7% PbO of the blended Concrete 6.

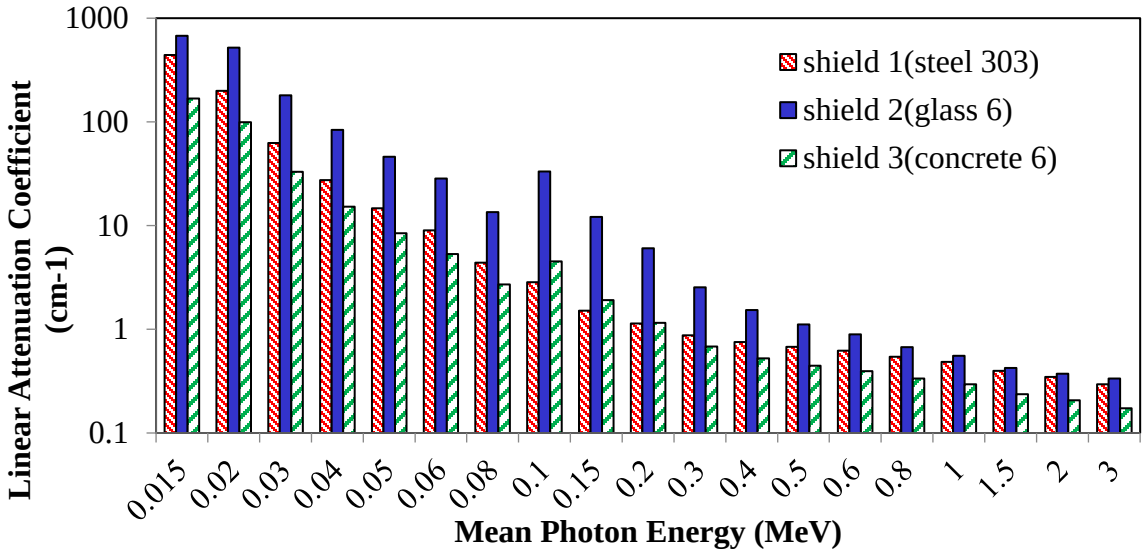

Figure 12-3: Linear attenuation coefficient versus average photon group energy for three shielding materials

12.3.2 Exposure Rate

The exposure rate in mR/hr without buildup at the outer cask surface is plotted versus photon energy in Figure 12-4 for the three source configurations. Energies below 0.4 MeV are not shown as the exposure due to these energies is negligible. The maximum exposure rate occurs for the 1.5 MeV average energy group and is around 1.0E-7 mR/hr for the highest burnup fuel. Figure 12-5 shows the exposure rate with buildup included in the calculations for the three source configurations. The low energy photon groups become much more significant contributors to exposure rate when buildup is included, as well as the highest individual group exposure rate increases by more than an order of magnitude.

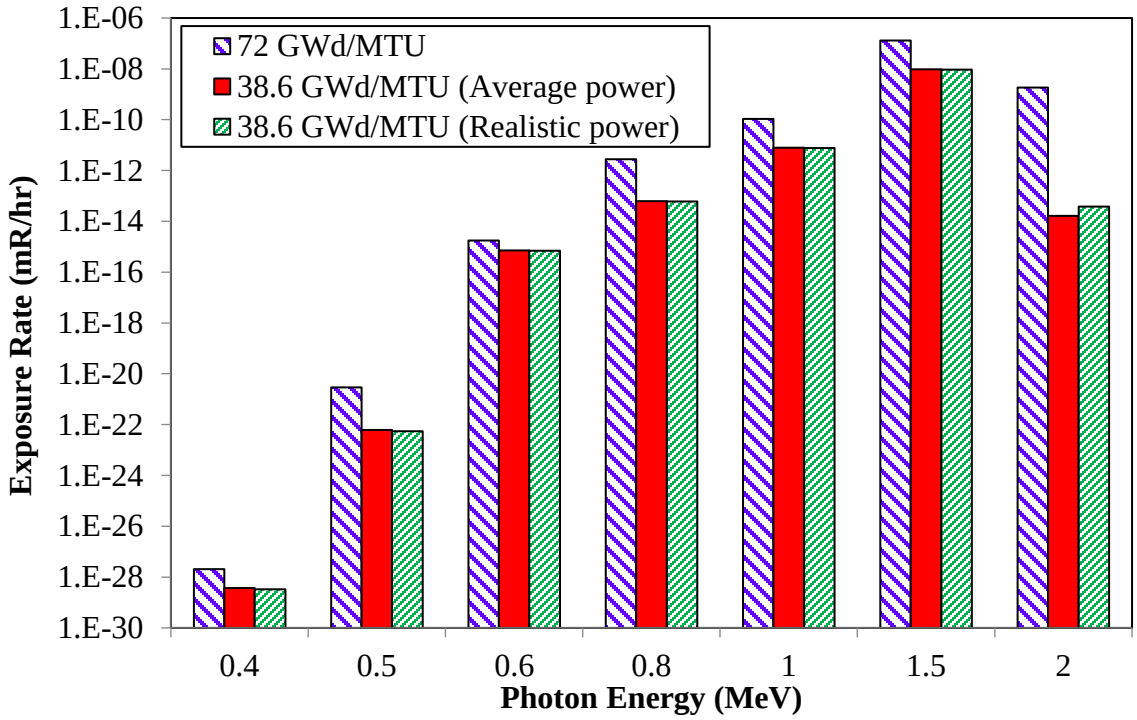

Figure 12-4: Exposure rate (no buildup) at outer cask surface for three radiation sources

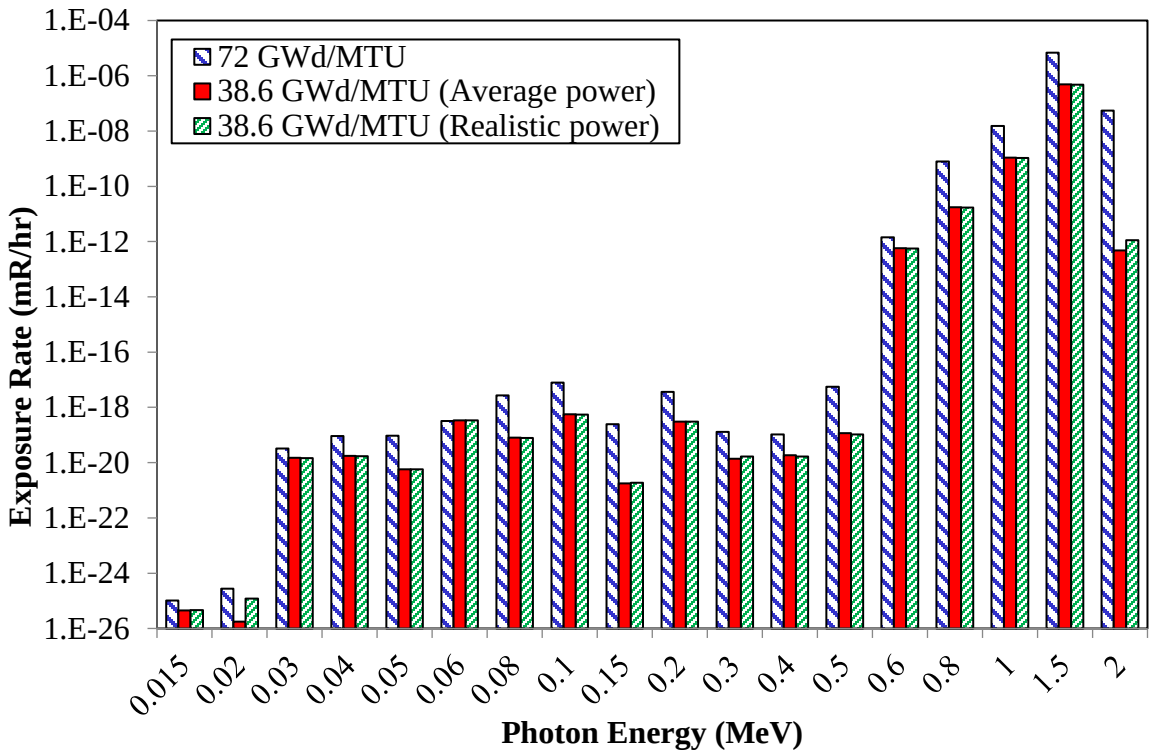

Figure 12-5: Exposure rate (with buildup) at outer cask surface for three radiation sources

Figure 12-6 details the effect of including buildup in the exposure rate calculations for the high burnup H. B. Robinson spent fuel. Including buildup increases the exposure rates by as much as several orders of magnitude for the higher gamma energies, giving a maximum exposure rate of 6.87E-6 mR/hr. Buildup clearly has a larger impact on low energy photons, resulting in an increase of exposure rate by 8 orders of magnitude for 0.4MeV gamma rays. This trend only increases continuously for lower energy photons. However, the exposure rate of the low energy gammas are still mostly insignificant after including buildup in the calculations, though they may be observed in Figure 5. In any case the exposure is dominated by high energy gammas, which are significantly less affected by buildup calculations. The total exposure rate over all energies is 1.34E-7 and 6.87E-6 mR/hr without and with buildup,

respectively. For comparison, the total exposure over all energies of the medium-burnup spent fuel from the Surry Power Plant is 4.97E-7 mR/hr for the average power and 4.79E-7 mR/hr for the realistic power profile.

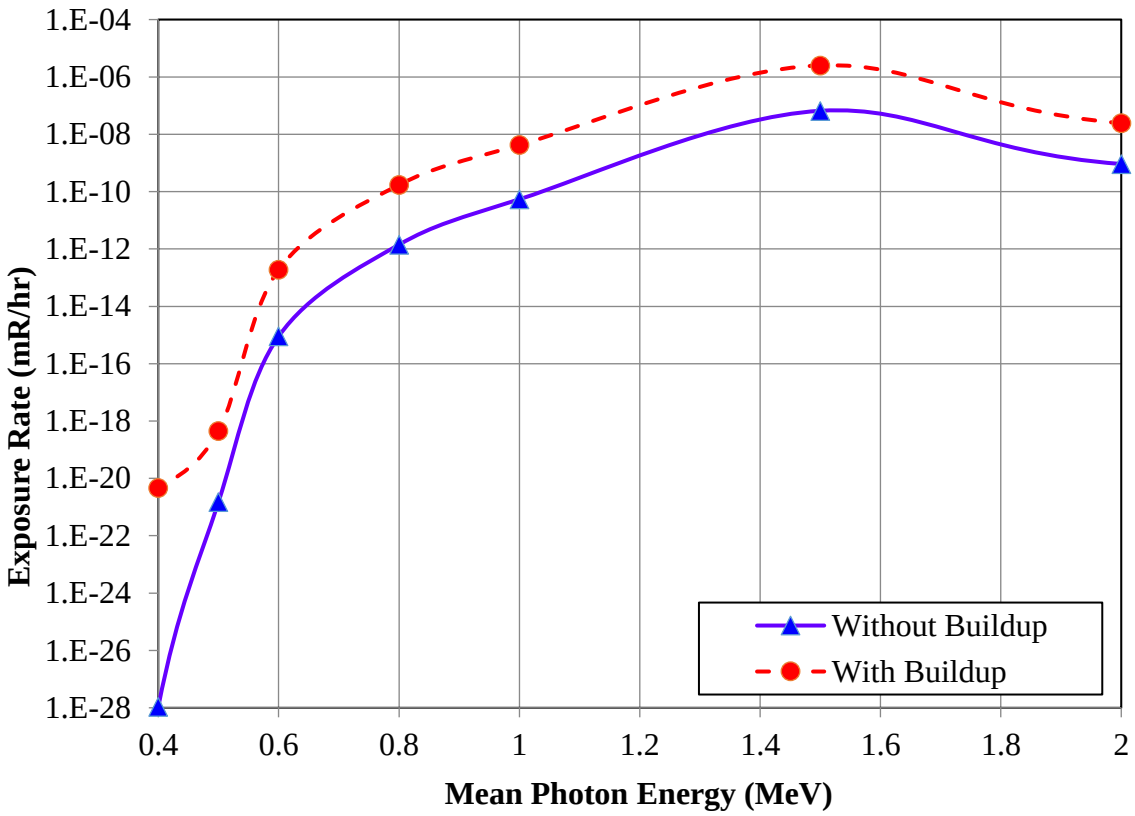

Figure 12-6: Exposure rate with and without buildup – 72 GWD/MTU H. B. Robinson spent fuel

Figure 12-7 provides a comparison of the exposure rates (with buildup) of 4 different cask configurations using the 72 GWd/MTU H. B. Robinson spent fuel data. The configurations are: 0.2 ft. Glass 6 and 1.8 ft. Concrete 6, 0.2 ft. Glass 6 and 1.8 ft. ordinary concrete, 2 ft. Concrete 6, and 2 ft. ordinary concrete. The latter two configurations have replaced the 0.2 ft.

of shielding glass with additional concrete, thus preserving the total cask thickness. All four configurations have 0.27 ft. of stainless steel type 303Cu as the innermost container.

The type of concrete that is used as the overpack material makes the largest difference in exposure rate. Use of Concrete 6 over ordinary concrete decreases the total exposure rate by 3 orders of magnitude for the same overpack thickness. Moreover, replacing 0.2 ft. of concrete with Glass 6 decreases the total exposure rate by an additional order of magnitude. This speaks to the immense shielding efficiency of high density glass that a 0.2 ft. (2.4 in.) layer can have such an impact on the exposure rate.

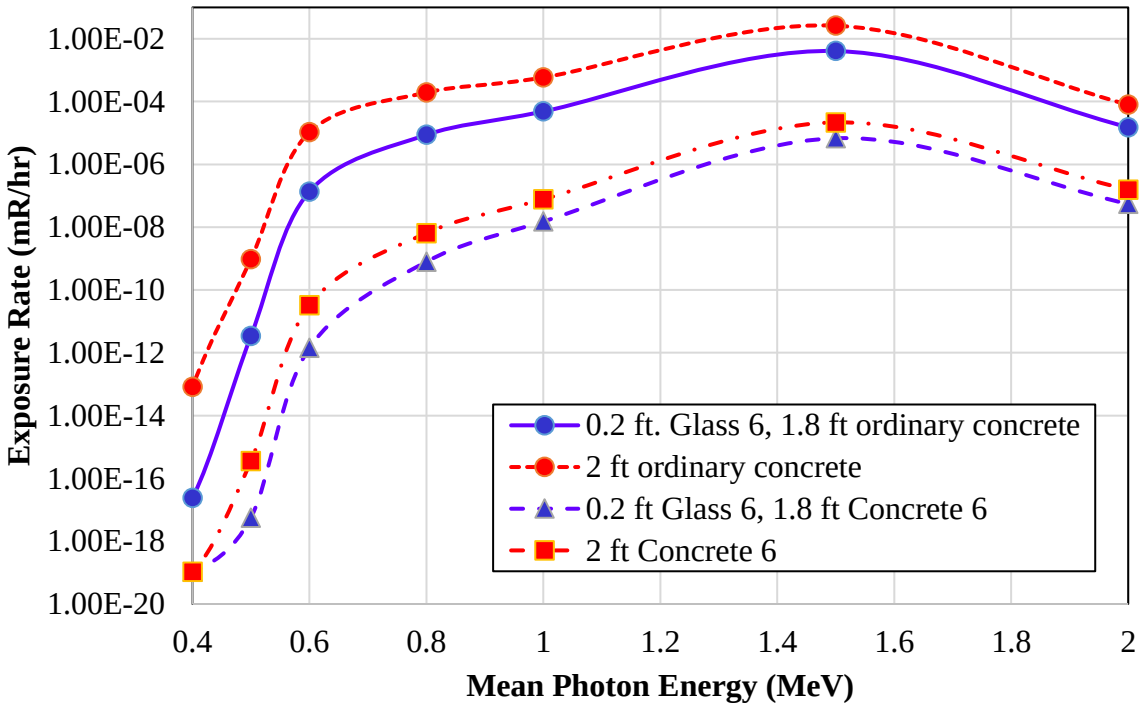

Figure 12-7: Exposure rate (with buildup) of 4 different cask configurations – 72 GWD/MTU H. B. Robinson spent fuel

12.3.2.1 Variation of Shielding Layer Thickness

Figure 12-8 shows the exposure rate as a function of the thickness of the Glass 6 shielding layer for two fuel burnup levels: 72 GWd/MTU and 38.6 GWd/MTU (realistic power profile). In this case, the thickness of the concrete 6 layer is adjusted to maintain a combined thickness of 2 ft. of glass and concrete. The exposure rate decreases exponentially with an increasing thickness of glass 6 based on its superior photon attenuation properties. The fuel burnup only affects the magnitude of the exposure rate and not the decrement of exposure with thickness. Exponential fits to the data are provided on the plot, where y is the exposure rate and x is the glass thickness.

The impact of the ratio of glass to concrete thickness is demonstrated in Figure 12-9. Ratios of glass 6 to concrete 6 thickness are varied from 1:1 to 1:9; for a combined thickness of 2 ft., a thickness ratio of 1:9 represents 0.2 ft. of glass 6 and 1.8 ft of concrete 6, which is the ratio used in Figure 12-7. Clearly the exposure rate decreases as the combined thickness of the two layers increases, and it decreases more rapidly for larger glass 6 to concrete 6 ratios. Exponential fit coefficients to the data in Figure 12-9 are provided in Table 12-6, where y is the exposure rate and x is the combined thickness of glass and concrete layers. The exponent ('b') varies greatly with the cask composition, showing the effectiveness of Glass 6 as a gamma shield. Higher ratios of glass to concrete thickness are most effective at reducing the exposure rate at the cask external surface. However, structural and thermal stability of the storage casks also must be taken into account, which may cause a different ratio to be better suited for implementation.

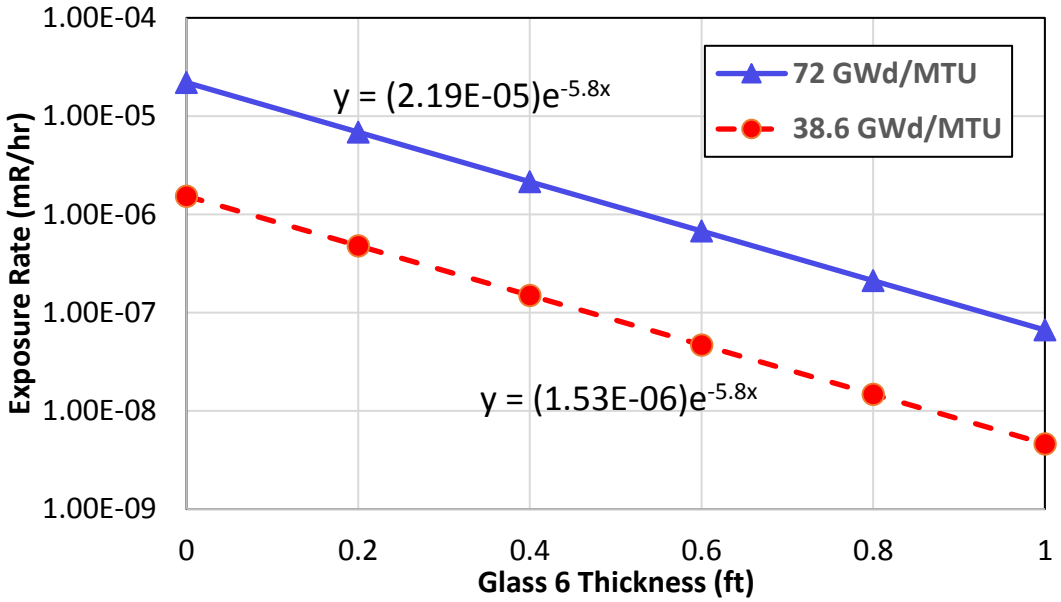

Figure 12-8: Exposure rate (log scale) versus thickness of Glass 6 layer for two different fuel burnups – thickness of Concrete 6 adjusted to maintain total overpack thickness of 2 ft.

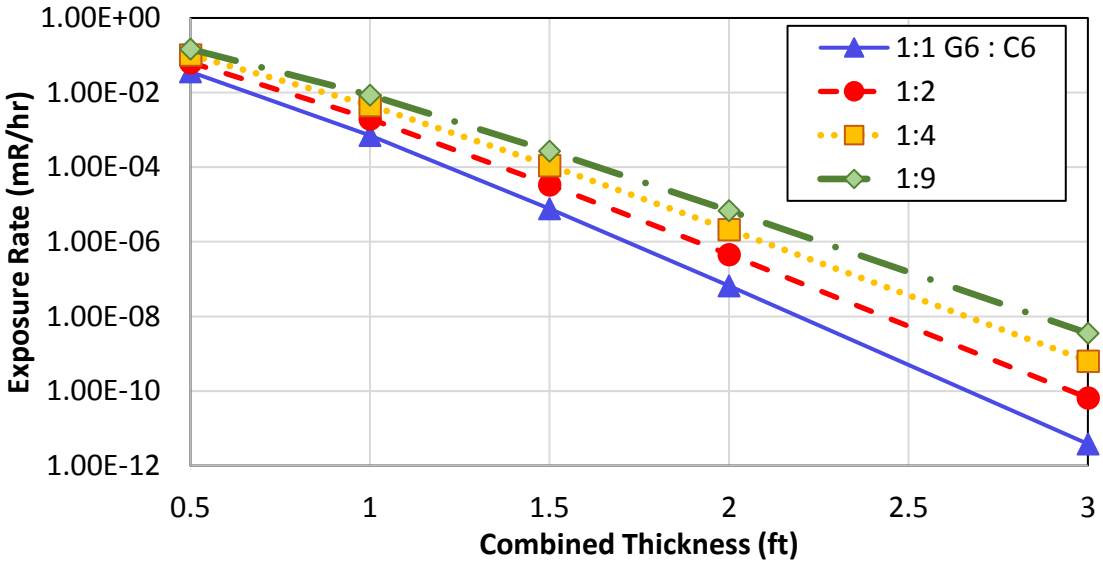

Figure 12-9: Exposure rate (log scale) versus combined thickness of Glass 6 and Concrete 6 for various ratios of Glass 6 to Concrete 6 thickness – 72 GWD/MTU burnup fuel.

Table 12-6: Exponential fit parameters – exposure rate versus combined thickness of glass and concrete layers

	$y = a \cdot \exp(-bx)$		
Glass 6 : Concrete 6 Ratio	**a**	**b**	**R^2**
1 : 1	5.869	9.252	0.9984
1 : 2	6.649	8.347	0.9980
1 : 4	7.370	7.624	0.9977
1 : 9	7.981	7.081	0.9973

12.4 Conclusion

From the present investigations, the direct gamma-ray exposure to radiation workers due to storage of high-level nuclear waste may be significantly decreased by the proper selection of shielding materials for spent fuel storage containers. A three layer cylindrical storage cask made up of a stainless steel type 303Cu basket, a thin layer of high-density oxide glass (named as Glass 6), and an overpack made of specialty concrete for radiation shielding (named as Concrete 6), for a total shielding thickness of 2.27 ft., is capable of producing a total exposure rate at the outer cask surface of 6.81E-6 mR/hr for the highest burnup fuel that was considered. This is nearly an order of magnitude smaller than a configuration of the same thickness without the oxide Glass 6 layer, and it is 3 to 4 orders of magnitude smaller than equivalent configurations using ordinary concrete as the overpack material instead of the blended Concrete 6. The variation in glass and concrete layer thicknesses shows that the ratio of the thickness of glass to concrete changes the shielding effectiveness for a given combined thickness of both layers. However, regardless of the ratio chosen, the exponential attenuation

behavior is observed and the exposure rate is reduced substantially over the use of more typical dry cask materials.

The ability to create shielding glass and concrete of varying composition and density introduces the possibility of creating high-level waste storage containers that may have thinner configurations and be of lighter weight without compromising radiation shielding performance. This has implications on transportation, loading, and storage costs, which are likely to decrease for dry casks with smaller total volume. Moreover, the versatility of glass and concrete make them desirable materials for a number of other shielding applications. This is especially true for glass compositions for shielding; the transparency of glass to visible light makes it ideal for visual examination of a radiation source requiring shielding. Also, the superior thermal stability of oxide glasses over concrete and other common shielding materials makes them attractive alternatives in some circumstances.

REFERENCES

[1] M.-S. Yim and K. L. Murty, "Materials issues in nuclear-waste management," *JOM*, vol. 52, no. 9, pp. 26–29, 2000.

[2] N. Tsoulfanidis and R. G. Cochran, "Radioactive Waste Management," *Nucl. Technol.*, vol. 93, pp. 263–304, 1991.

[3] J. K. Shultis and R. E. Faw, *Fundamentals of Nuclear Science and Engineering*, 2nd ed. Boca Raton, FL: CRC Press, 2008.

[4] J. C. Farmer, G. E. Gdowski, R. D. McCright, and H. S. Ahluwahlia, "Corrosion models for performance assessment of high-level radioactive-waste containers," *Nucl. Eng. Des.*, vol. 129, no. 1, pp. 57–88, 1991.

[5] J. A. Beavers, N. G. Thompson, and R. N. Parkins, "Stress-corrosion cracking of low strength carbon steels in candidate high level waste repository environments: Environmental effects," *Nucl. Chem. Waste Manag.*, vol. 5, no. 4, pp. 279–296, 1985.

[6] R. E. Naegeli, "Calculation of the Radionuclides in PWR Spent Fuel Samples for SFR Experiment Planning," 2004.

[7] M. A. Fusco, A. L. Winfrey, and M. A. Bourham, "Shielding properties of protective thin film coatings and blended concrete compositions for high level waste storage packages," *Ann. Nucl. Energy*, vol. 89, pp. 63–69, 2016.

[8] E. Easton, “Dry Cask Storage of Nuclear Spent Fuel.”

[9] W. C. Bare and L. D. Torgerson, “Dry Cask Storage Characterization Project - Phase 1: CASTOR V/21 Cask Opening and Examination,” 2001.

[10] Electric Power Research Institute, “Dry Cask Storage Characterization Project,” 2002.

[11] R. Mccullum, “An Overview of Dry Cask Storage,” 2012.

[12] D. Rezaei-Ochbelagh and S. Azimkhani, “Investigation of gamma-ray shielding properties of concrete containing different percentages of lead,” *Appl. Radiat. Isot.*, vol. 70, no. 10, pp. 2282–2286, 2012.

[13] E.-S. A. Waly and M. A. Bourham, “Comparative study of different concrete composition as gamma-ray shielding materials,” *Ann. Nucl. Energy*, vol. 85, pp. 306–310, 2015.

[14] U. Kaur, J. K. Sharma, P. S. Singh, and T. Singh, “Comparative studies of different concretes on the basis of some photon interaction parameters,” *Appl. Radiat. Isot.*, vol. 70, no. 1, pp. 233–240, 2012.

[15] S. Gupta and G. S. Sidhu, “Measurement of Total and Partial Mass Attenuation Coefficients of Oxide Glasses : A Radiation field reparation of Papers for International Journal of Modern Engineering and Research (16 Bold),” vol. 3, pp. 3830–3835, 2013.

[16] S. Kaur and K. J. Singh, “Comparative Study of Lead Borate and Lead Silicate Glass Systems Doped With Aluminum Oxide as Gamma-Ray Shielding Materials,” no. 5, pp. 172–175, 2013.

[17] S. R. Manohara, S. M. Hanagodimath, L. Gerward, and K. C. Mittal, "Exposure buildup factors for heavy metal oxide glass: A radiation shield," *J. Korean Phys. Soc.*, vol. 59, no. 23, p. 2039, 2011.

[18] P. Limkitjaroenporn, J. Kaewkhao, P. Limsuwan, and W. Chewpraditkul, "Physical, optical, structural and gamma-ray shielding properties of lead sodium borate glasses," *J. Phys. Chem. Solids*, vol. 72, no. 4, pp. 245–251, 2011.

[19] R. D. McCright, W. G. Halsey, G. E. Gdowski, and W. L. Clarke, "Candidate Container Materials for Yucca Mountain Waste Package Design," in *Proc. Nuclear Waste Packaging Focus '91 Conf.*, 1991.

[20] J. Farmer, V. Pasupathi, P. Nair, G. Gordon, G. Gdowski, S. Carroll, T. Steinborn, T. Summers, F. Wong, R. Rebak, R. Lian, J. Lee, F. Hua, and J. Payer, "Technical Basis Document No. 6: Waste Package and Drip Shield Corrosion," 2003.

[21] J. D. Lambert, S. Bakhtiari, I. Bodnar, C. Kot, and J. Pence, "NRC Job Code V6060: Extended In-Situ and Real Time Monitoring Task 3: Long-Term Dry Cask Storage of Spent Nuclear Fuel." pp. 1–55, 2012.

[22] H. Spilker, M. Peehs, H.-P. Dyck, G. Kaspar, and K. Nissen, "Spent LWR fuel dry storage in large transport and storage casks after extended burnup," *J. Nucl. Mater.*, vol. 250, no. 1, pp. 63–74, 1997.

[23] U. S. D. of E. Office of Civilian Radioactive Waste Management, "Viability Assessment of a Repository at Yucca Mountain," 1998.

[24] K. L. Murty and I. Charit, *An Introduction to Nuclear Materials*. Weinheim, Germany: Wiley-VCH Verlag & Co., 2013.

[25] J. N. Wanklyn, "The Role of Molybdenum in the Crevice Corrosion of Stainless Steels," *Corros. Sci.*, vol. 21, no. 3, pp. 211–225, 1981.

[26] A. Kocijan, C. Donik, and M. Jenko, "Electrochemical and XPS studies of the passive film formed on stainless steels in borate buffer and chloride solutions," *Corros. Sci.*, vol. 49, no. 5, pp. 2083–2098, 2007.

[27] R. W. Revie and H. H. Uhlig, *Corrosion and Corrosion Control*, 4th ed. John Wiley & Sons, 2008.

[28] D. E. Jiang and E. a. Carter, "Diffusion of interstitial hydrogen into and through bcc Fe from first principles," *Phys. Rev. B - Condens. Matter Mater. Phys.*, vol. 70, no. 6, pp. 1–9, 2004.

[29] D. A. Jones, *Principles and Prevention of Corrosion*. New York, NY: Macmillan Publishing Company, 1992.

[30] C.-O. A. Olsson and D. Landolt, "Passive films on stainless steels - Chemistry, structure and growth," *Electrochim. Acta*, vol. 48, no. 9 SPEC., pp. 1093–1104, 2003.

[31] C. M. Abreu, M. J. Cristóbal, R. Losada, X. R. Nóvoa, G. Pena, and M. C. Pérez, "Comparative study of passive films of different stainless steels developed on alkaline medium," *Electrochim. Acta*, vol. 49, no. 17–18, pp. 3049–3056, 2004.

[32] K. Hashimoto, K. Asami, and K. Teramoto, "An X-ray photo-electron spectroscopic study on the role of molybdenum in increasing the corrosion resistance of ferritic stainless steels in HC1," *Corros. Sci.*, vol. 19, pp. 3–14, 1979.

[33] B. N. Popov, *Corrosion Engineering*, 1st ed. Oxford, UK: Elsevier B. V., 2015.

[34] Y. X. Qiao, Y. G. Zheng, W. Ke, and P. C. Okafor, "Electrochemical behaviour of high nitrogen stainless steel in acidic solutions," *Corros. Sci.*, vol. 51, no. 5, pp. 979–986, 2009.

[35] S. Ningshen, U. Kamachi Mudali, V. K. Mittal, and H. S. Khatak, "Semiconducting and passive film properties of nitrogen-containing type 316LN stainless steels," *Corros. Sci.*, vol. 49, no. 2, pp. 481–496, 2007.

[36] R. Ritzenhoff and A. Hahn, "Corrosion Resistance of High Nitrogen Steels," in *Corrosion Resistance*, H. Shih, Ed. InTech, 2012, pp. 55–80.

[37] R. A. Cottis, "Stress Corrosion Cracking," 2000.

[38] R. Checchetto, M. Bonelli, L. Gratton, a Miotello, a Sabbioni, L. Guzman, Y. Horino, and G. Benamati, "Analysis of the hydrogen permeation properties of TiN-TiC bilayers deposited on martensitic stainless steel," *Surf. Coatings Technol.*, vol. 83, no. 1–3, pp. 40–44, 1996.

[39] P. R. Roberge, *Corrosion Engineering Principles and Practice*. McGraw-Hill Companies, Inc., 2008.

[40] H. M. Chung and W. J. Shack, "Irradiation-Assisted Stress Corrosion Cracking Behavior of Austenitic Stainless Steels Applicable to LWR Core Internals," 2006.

[41] H. H. Uhlig, "Passivity in metals and alloys," *Corros. Sci.*, vol. 19, no. 7, pp. 777–791, 1979.

[42] H. H. Uhlig, "Structure and Growth of Thin Films Exposed To Oxygen," *Corros. Sci.*, vol. 7, pp. 325–339, 1967.

[43] C. Y. Chao, L. F. Lin, and D. D. MacDonald, "A Point Defect Model for Anodic Passive Films I. Film Growth Kinetics," *J. Electrochem. Soc.*, vol. 128, no. 6, p. 1187, 1981.

[44] D. D. Macdonald, "The Point Defect Model for the Passive State," *J. Electrochem. Soc.*, vol. 139, no. 12, p. 3434, 1992.

[45] D. D Macdonald, "Passivity the key to our metals-based civilization," *Pure Appl. Chem.*, vol. 71, no. 6, pp. 951–978, 1999.

[46] D. D. MacDonald, "The history of the Point Defect Model for the passive state: A brief review of film growth aspects," *Electrochim. Acta*, vol. 56, no. 4, pp. 1761–1772, 2011.

[47] D. Macdonald, S. Biaggio, and H. Song, "Steady State Passive Films Interfacial Kinetic Effects and Diagnostic Criteria," *J. Electrochem. Soc.*, vol. 139, no. 1, pp. 170–177, 1992.

[48] C. Y. Chao, L. F. Lin, and D. D. MacDonald, "A Point Defect Model for Anodic Passive Films III. Impedance Response," *J. Electrochem. Soc.*, vol. 128, no. 6, p. 1874, 1981.

[49] L. Zhang, D. D. Macdonald, E. Sikora, and J. Sikora, "On the Kinetics of Growth of Anodic Oxide Films," *J. Electrochem. Soc.*, vol. 145, no. 3, p. 898, 1998.

[50] N. B. Hakiki, S. Boudin, B. Rondot, and M. Da Cunha Belo, "The electronic structure of passive films formed on stainless steels," *Corros. Sci.*, vol. 37, no. 11, pp. 1809–1822, 1995.

[51] M. F. Montemor, M. G. S. Ferreira, N. E. Hakiki, and M. Da Cunha Belo, "Chemical composition and electronic structure of the oxide films formed on 316L stainless steel and nickel based alloys in high temperature aqueous environments," *Corros. Sci.*, vol. 42, no. 9, pp. 1635–1650, 2000.

[52] M. G. S. Ferreira, M. Da Cunha Belo, N. E. Hakiki, G. Goodlet, M. F. Montemor, and A. M. P. Simoes, "Semiconducting properties of oxide and passive films formed on AISI 304 stainless steel and Alloy 600," *J. Braz. Chem. Soc.*, vol. 13, no. 4, pp. 433–440, 2002.

[53] G. Lorang, M. Da Cunha Belo, A. M. P. Simoes, and M. G. S. Ferreira, "Chemical composition of passive films AISI 304 stainless steel," vol. 141, no. 12, p. 3347, 1994.

[54] C. O. A. Olsson, "The influence of nitrogen and molybdenum on passive films formed on the austenoferritic stainless steel 2205 studied by AES and XPS," *Corros. Sci.*, vol. 37, no. 3, pp. 467–479, 1995.

[55] L. F. Lin, C. Y. Chao, and D. D. MacDonald, "A Point Defect Model for Anodic Passive Films II. Chemical Breakdown and Pit Initiation," *J. Electrochem. Soc.*, vol. 128, no. 6, p. 1194, 1981.

[56] N. Pessall and C. Liu, "Determination of critical pitting potentials of stainless steels in aqueous chloride environments," *Electrochim. Acta*, vol. 16, no. 11, pp. 1987–2003, 1971.

[57] B. E. Wilde and E. Williams, "The use of current/voltage curves for the study of localized corrosion and passivity breakdown on stainless steels in chloride media," *Electrochim. Acta*, vol. 16, no. 11, pp. 1971–1985, 1971.

[58] W. Tian, N. Du, S. Li, S. Chen, and Q. Wu, "Metastable pitting corrosion of 304 stainless steel in 3.5% NaCl solution," *Corros. Sci.*, vol. 85, pp. 372–379, 2014.

[59] P. Ernst and R. C. Newman, "Explanation of the effect of high chloride concentration on the critical pitting temperature of stainless steel," *Corros. Sci.*, vol. 49, no. 9, pp. 3705–3715, 2007.

[60] L. Winfrey and M. Bourham, "Enhanced Shielding Performance of HLW : Storage Packages via Multi- Component Coatings." DOE NEUP R&D Awards, 2013.

[61] C. C. Scheffing, K. Jagannadham, M. S. Yim, and M. Bourham, "Properties of Titanium-Nitride for High-Level Waste Packaging Enhancement," *Rad. Waste Mgmt. Dispos.*, vol. 156, pp. 213–221, 2006.

[62] C. Li, Y. Wang, L. Guo, J. He, Z. Pan, and L. Wang, "Laser remelting of plasma-sprayed conventional and nanostructured Al2O3-13 wt.%TiO2 coatings on titanium alloy," *J. Alloys Compd.*, vol. 506, no. 1, pp. 356–363, 2010.

[63] H. B. Bomberger, P. J. Cambourelis, and G. E. Hutchinson, "Corrosion Properties of Titanium in Marine Environments," *J. Electrochem. Soc.*, vol. 101, no. 9, pp. 442–447, 1954.

[64] N. C. Saha and H. G. Tompkins, "Titanium nitride oxidation chemistry: An x-ray photoelectron spectroscopy study," *J. Appl. Phys.*, vol. 72, no. 7, pp. 3072–3079, 1992.

[65] M. Wittmer, J. Noser, and H. Melchior, "Oxidation kinetics of TiN thin films," *J. Appl. Phys.*, vol. 52, no. 11, pp. 6659–6664, 1981.

[66] J.-E. Sundgren, "Structure and properties of TiN coatings," *Thin Solid Films*, vol. 128, no. 1–2, pp. 21–44, 1985.

[67] Y. Wang, S. Jiang, M. Wang, S. Wang, T. D. Xiao, and P. R. Strutt, "Abrasive wear characteristics of plasma sprayed nanostructured alumina/titania coatings," *Wear*, vol. 237, no. 2, pp. 176–185, 2000.

[68] C. X. Shan, X. Hou, and K.-L. Choy, "Corrosion resistance of TiO2 films grown on stainless steel by atomic layer deposition," *Surf. Coatings Technol.*, vol. 202, no. 11, pp. 2399–2402, 2008.

[69] P. F. Manicone, P. Rossi Iommetti, and L. Raffaelli, "An overview of zirconia ceramics: Basic properties and clinical applications," *J. Dent.*, vol. 35, no. 11, pp. 819–826, 2007.

[70] K. Kukli, M. Ritala, J. Aarik, T. Uustare, and M. Leskela, "Influence of growth temperature on properties of zirconium dioxide films grown by atomic layer deposition," *J. Appl. Phys.*, vol. 92, no. 4, pp. 1833–1840, 2002.

[71] M. Ritala and M. Leskelä, "Zirconium dioxide thin films deposited by ALE using zirconium tetrachloride as precursor," *Appl. Surf. Sci.*, vol. 75, no. 1–4, pp. 333–340, 1994.

[72] P. De Lima Neto, M. Atik, L. A. Avaca, and M. A. Aegerter, "Sol-Gel ZrO_2 Coatings for Chemical Protection of Stainless Steel," *J. Sol-Gel Sci. Technol.*, vol. 1, pp. 177–184, 1994.

[73] U. Diebold, "The surface science of titanium dioxide," *Surf. Sci. Rep.*, vol. 48, no. 5–8, pp. 53–229, 2003.

[74] M. Pelaez, N. T. Nolan, S. C. Pillai, M. K. Seery, P. Falaras, A. G. Kontos, P. S. M. Dunlop, J. W. J. Hamilton, J. A. Byrne, K. O'Shea, M. H. Entezari, and D. D. Dionysiou, "A review on the visible light active titanium dioxide photocatalysts for environmental applications," *Appl. Catal. B Environ.*, vol. 125, pp. 331–349, 2012.

[75] G. X. Shen, Y. C. Chen, and C. J. Lin, "Corrosion protection of 316 L stainless steel by a TiO2 nanoparticle coating prepared by sol-gel method," *Thin Solid Films*, vol. 489, no. 1–2, pp. 130–136, 2005.

[76] H. Yun, J. Li, H.-B. Chen, and C.-J. Lin, "A study on the N-, S- and Cl-modified nano-TiO2 coatings for corrosion protection of stainless steel," *Electrochim. Acta*, vol. 52, no. 24, pp. 6679–6685, 2007.

[77] R. Chaim, G. Stark, L. Gal-Or, and H. Bestgen, "Electrochemical Al203 coatings on SiC substrates," *J. Mater. Sci. Lett.*, vol. 13, pp. 487–890, 1994.

[78] X. Nie, E. I. Meletis, J. C. Jiang, A. Leyland, A. L. Yerokhin, and A. Matthews, "Abrasive wear/corrosion properties and TEM analysis of Al2O3 coatings fabricated using plasma electrolysis," *Surf. Coatings Technol.*, vol. 149, no. 2–3, pp. 245–251, 2002.

[79] A. I. Abdulagatov, Y. Yan, J. R. Cooper, Y. Zhang, Z. M. Gibbs, A. S. Cavanagh, R. G. Yang, Y. C. Lee, and S. M. George, "Al2O3 and TiO2 atomic layer deposition on copper for water corrosion resistance.," *ACS Appl. Mater. Interfaces*, vol. 3, no. 12, pp. 4593–4601, 2011.

[80] R. Holinski and J. Gänsheimer, "A study of the lubricating mechanism of molybdenum disulfide," *Wear*, vol. 19, no. 3, pp. 329–342, 1972.

[81] J. P. G. Farr, "Molybdenum disulphide in lubrication. A review," *Wear*, vol. 35, no. 1, pp. 1–22, 1975.

[82] W. O. Winer, "Molybdenum Disulfide as a Lubricant: A Review of the Fundamental Knowledge," *Wear*, vol. 10, pp. 422–452, 1967.

[83] R. G. Dickinson and L. Pauling, "The crystal structure of molybdenite," *J. Am. Chem. Soc.*, vol. 45, no. 6, pp. 1466–1471, 1923.

[84] J. L. Vossen and K. Werner, Eds., *Thin Film Processes II*. Elsevier Inc., 1991.

[85] D. M. Mattox, "Fundamentals of Ion Plating," *J. Vac. Sci. Technol.*, vol. 10, no. 1973, p. 47, 1973.

[86] V. P. Balema, "Chemical Deposition Techniques in Materials Design," *Material Matters*, pp. 3–4, 2006.

[87] J. L. Vossen and W. Kern, Eds., *Thin Film Processes*. New York, NY: Academic Press, Inc., 1978.

[88] S. M. George, A. W. Ott, and J. W. Klaus, "Surface Chemistry for Atomic Layer Growth," *J. Phys. Chem.*, vol. 100, no. 31, pp. 13121–13131, 1996.

[89] S. M. George, "Atomic layer deposition: An overview," *Chem. Rev.*, vol. 110, no. 1, pp. 111–131, 2010.

[90] S. K. Young, "Overview of Sol-Gel Science and Technology," 2002.

[91] M. Paunovic and M. Schlesinger, *Fundamentals of Electrochemical Deposition*. John Wiley & Sons, Inc., 2006.

[92] P. Sarkar and P. S. Nicholson, "Electrophoretic deposition (EDP): Mechanisms, Kinetics, and Applications to Ceramics," *J. Am. Ceram. Soc.*, vol. 79, no. 8. pp. 1987–2002, 1996.

[93] O. O. Van der Biest and L. J. Vandeperre, "Electrophoretic Deposition of Materials," *Annu. Rev. Mater. Sci.*, vol. 29, pp. 327–352, 1999.

[94] S. M. Rossnagel and J. Hopwood, "Magnetron sputter deposition with high levels of metal ionization," *Appl. Phys. Lett.*, vol. 63, no. 24, pp. 3285–3287, 1993.

[95] P. M. Martin, Ed., *Handbook of Deposition Technologies for Films and Coatings - Science, Applications, and Technology*. Elsevier Inc., 2010.

[96] M. A. Lieberman and A. J. Lichtenberg, *Principles of Plasma Discharges and Materials Processing*, 2nd Ed. Hoboken, NJ: John Wiley & Sons, Inc., 2005.

[97] P. Sigmund, "Theory of Sputtering. I. Sputtering Yield of Amorphous and Polycrystalline Targets," *Phys. Rev.*, vol. 184, no. 2, pp. 383–416, 1969.

[98] J. A. Thornton, "Magnetron sputtering: basic physics and application to cylindrical magnetrons," *J. Vac. Sci. Technol.*, vol. 15, no. 2, pp. 171–177, 1978.

[99] D. Depla, S. Mahieu, and R. De Gryse, "Magnetron sputter deposition: Linking discharge voltage with target properties," *Thin Solid Films*, vol. 517, no. 9, pp. 2825–2839, 2009.

[100] S. Berg and T. Nyberg, "Fundamental understanding and modeling of reactive sputtering processes," *Thin Solid Films*, vol. 476, no. 2, pp. 215–230, 2005.

[101] M. Konuma, *Film Deposition by Plasma Techniques*. Springer, 1991.

[102] I. Safi, "Recent aspects concerning DC reactive magnetron sputtering of thin films: a review," *Surf. Coatings Technol.*, vol. 127, pp. 203–219, 2000.

[103] S. W. Dean, "Electrochemical Techniques for Corrosion Engineering," in *Electrochemical methods of corrosion testing*, 1986.

[104] O. A. Petrii, R. R. Nazmutdinov, M. D. Bronshtein, and G. A. Tsirlina, "Life of the Tafel equation: Current understanding and prospects for the second century," *Electrochim. Acta*, vol. 52, no. 11, pp. 3493–3504, 2007.

[105] M. Stern and A. L. Geary, "Electrochemical Polarization," *J. Electrochem. Soc.*, vol. 104, no. 9, p. 559, 1957.

[106] J. R. Macdonald and W. B. Johnson, "Fundamentals of Impedance Spectroscopy," in *Impedance Spectroscopy Theory, Experiment, and Applications*, 2nd ed., E. Barsoukov and J. R. Macdonald, Eds. Hoboken, NJ: John Wiley & Sons, Inc., 2005, pp. 1–26.

[107] D. D. Macdonald and M. C. H. McKubre, "Corrosion of Materials," in *Impedance Spectroscopy Theory, Experiment, and Applications*, 2nd ed., E. Barsoukov and J. R. Macdonald, Eds. Hoboken, NJ: John Wiley & Sons, Inc., 2005, pp. 343–429.

[108] D. W. Marquardt, "An Algorithm for Least-Squares Estimation of Nonlinear Parameters," *J. Soc. Indust. Appl. Math.*, vol. 11, no. 2, pp. 431–441, 1963.

[109] J. A. Nelder and R. Mead, "A Simplex Method for Function Minimization," *Comput. J.*, vol. 7, no. 4, pp. 308–313, 1965.

[110] P. Cordoba-Torres, T. J. Mesquita, and R. P. Nogueira, "Influence of geometry-induced current and potential distributions on the characterization of constant-phase element behavior," *Electrochim. Acta*, vol. 87, pp. 676–685, 2013.

[111] P. Córdoba-Torres, T. J. Mesquita, and R. P. Nogueira, "Toward a better characterization of constant-phase element behavior on disk electrodes from direct

impedance analysis: Methodological considerations and mass transport effects," *Electrochim. Acta*, vol. 92, pp. 323–334, 2013.

[112] K. S. Cole and R. H. Cole, "Dispersion and Absorption in Dielectrics I. Alternating Current Characteristics," *J. Chem. Phys.*, vol. 9, no. 4, p. 341, 1941.

[113] B. D. Hirschorn, "Distributed time-constant impedance responses interpreted in terms of physically meaningful properties," University of Florida, 2010.

[114] E. D. Bidoia, L. O. S. Bulhoes, and R. C. Rocha-Filho, "Pt/HClO4 interface CPE: influence of surface roughness and electrolyte concentration," *Electrochim. Acta*, vol. 39, no. 5, pp. 763–769, 1994.

[115] T. Pajkossy, "Capacitance dispersion on solid electrodes: anion adsorption studies on gold single crystal electrodes," *Solid State Ionics*, vol. 94, no. 1–4, pp. 123–129, 1997.

[116] Z. Kerner and T. Pajkossy, "Impedance of rough capacitive electrodes : the role of surface disorder," vol. 448, pp. 139–142, 1998.

[117] Z. Kerner and T. Pajkossy, "On the origin of capacitance dispersion of rough electrodes," *Electrochim. Acta*, vol. 46, no. 2–3, pp. 207–211, 2000.

[118] T. Pajkossy, "Impedance spectroscopy at interfaces of metals and aqueous solutions - Surface roughness, CPE and related issues," *Solid State Ionics*, vol. 176, no. 25–28, pp. 1997–2003, 2005.

[119] C. C. Scheffing, "Properties of a Multilayer Coating for Applications in High Level Waste Packaging," North Carolina State University, 2005.

[120] L. Williams and R. J. Taylor, "iR Correction: Part I. A Computerised Interrupt Method," *J. Electroanal. Chem. Interfacial Electrochem.*, vol. 108, no. 3, pp. 293–303, 1980.

[121] ASTM, "Standard Test Method for Conducting Cyclic Potentiodynamic Polarization Measurements for Localized Corrosion Susceptibility of," *Annual Book of ASTM Standards*, vol. 86, no. G61-86. pp. 1–5, 2010.

[122] M. Bouklah, B. Hammouti, M. Lagrenée, and F. Bentiss, "Thermodynamic properties of 2,5-bis(4-methoxyphenyl)-1,3,4-oxadiazole as a corrosion inhibitor for mild steel in normal sulfuric acid medium," *Corros. Sci.*, vol. 48, no. 9, pp. 2831–2842, 2006.

[123] M. a M. Ibrahim, S. S. Abd El Rehim, and M. M. Hamza, "Corrosion behavior of some austenitic stainless steels in chloride environments," *Mater. Chem. Phys.*, vol. 115, no. 1, pp. 80–85, 2009.

[124] M. H. Wahdan, "The synergistic inhibition effect and thermodynamic properties of 2-mercaptobenzimidazol and some selected cations as a mixed inhibitor for pickling of mild steel in acid solution," *Mater. Chem. Phys.*, vol. 49, no. 2, pp. 135–140, 1997.

[125] a. Zarrouk, B. Hammouti, H. Zarrok, S. S. Al-Deyab, and M. Messali, "Temperature effect, activation energies and thermodynamic adsorption studies of L-Cysteine Methyl Ester Hydrochloride as copper corrosion inhibitor in nitric acid 2M," *Int. J. Electrochem. Sci.*, vol. 6, no. 12, pp. 6261–6274, 2011.

[126] R. S. Oguike, "Corrosion Studies on Stainless Steel (FE6956) in Hydrochloric Acid Solution," *Adv. Mater. Phys. Chem.*, vol. 4, no. 8, pp. 153–163, 2014.

[127] E. A. Gulbransen, "The Transition State Theory of the Formation of Thin Oxide Films on Metals," *J. Electrochem. Soc.*, vol. 83, no. 1, pp. 301–317, 1943.

[128] M. Dahmani, a. Et-Touhami, S. S. Al-Deyab, B. Hammouti, and a. Bouyanzer, "Corrosion inhibition of c38 steel in 1 M HCl: A comparative study of black pepper extract and its isolated piperine," *Int. J. Electrochem. Sci.*, vol. 5, no. 8, pp. 1060–1069, 2010.

[129] V. Meille, "Review on methods to deposit catalysts on structured surfaces," *Appl. Catal. A Gen.*, vol. 315, pp. 1–17, 2006.

[130] A. M. Ferrar, "Measurement and Uncertainty Analysis of Transonic Fan Response to Total Pressure Inlet Distortion," Virginia Polytechnic Institute and State University, 2015.

[131] D. D. Macdonald, A. Sun, N. Priyantha, and P. Jayaweera, "An electrochemical impedance study of Alloy-22 in NaCl brine at elevated temperature: II. Reaction mechanism analysis," *J. Electroanal. Chem.*, vol. 572, no. 2, pp. 421–431, 2004.

[132] G. J. Brug, a. L. G. van den Eeden, M. Sluyters-Rehbach, and J. H. Sluyters, "The analysis of electrode impedances complicated by the presence of a constant phase element," *J. Electroanal. Chem. Interfacial Electrochem.*, vol. 176, no. 1–2, pp. 275–295, 1984.

[133] C. H. Hsu and F. Mansfeld, "Technical note : Concerning the conversion of the constant phase element parameter Y0 into a Capacitance," *Corrosion*, vol. 57, no. 9, pp. 747–748, 2001.

[134] M. E. Orazem, I. Frateur, B. Tribollet, V. Vivier, S. Marcelin, N. Pebere, a. L. Bunge, E. a. White, D. P. Riemer, and M. Musiani, "Dielectric Properties of Materials Showing Constant-Phase-Element (CPE) Impedance Response," *J. Electrochem. Soc.*, vol. 160, no. 6, pp. C215–C225, 2013.

[135] S. P. Harrington and T. M. Devine, "Analysis of Electrodes Displaying Frequency Dispersion in Mott-Schottky Tests," *J. Electrochem. Soc.*, vol. 155, no. 8, p. C381, 2008.

[136] V. M.-W. Huang, V. Vivier, M. E. Orazem, N. Pébère, and B. Tribollet, "The Apparent Constant-Phase-Element Behavior of a Disk Electrode with Faradaic Reactions," *J. Electrochem. Soc.*, vol. 154, no. 2, p. C99, 2007.

[137] B. Hirschorn, M. E. Orazem, B. Tribollet, V. Vivier, I. Frateur, and M. Musiani, "Constant-Phase-Element Behavior Caused by Resistivity Distributions in Films: I. Theory," *J. Electrochem. Soc.*, vol. 157, no. 12, pp. C452–C457, 2010.

[138] B. Hirschorn, M. E. Orazem, B. Tribollet, V. Vivier, I. Frateur, and M. Musiani, "Constant-Phase-Element Behavior Caused by Resistivity Distributions in Films: II. Applications," *J. Electrochem. Soc.*, vol. 157, no. 12, pp. C458–C463, 2010.

[139] B. Hirschorn, M. E. Orazem, B. Tribollet, V. Vivier, I. Frateur, and M. Musiani, "Determination of effective capacitance and film thickness from constant-phase-element parameters," *Electrochim. Acta*, vol. 55, no. 21, pp. 6218–6227, 2010.

[140] A. Guntershulze and F. Keller, "Die Dielektriztatskonstanten einer Anzahl Oxyde," *Z. Phys.*, vol. 75, no. 1, pp. 78–83, 1932.

[141] U. Stimming and J. W. Schultze, "A semiconductor model of the passive layer on iron electrodes and its application to electrochemical reactions," *Electrochim. Acta*, vol. 24, no. 8, pp. 859–869, 1979.

[142] N. E. Hakiki, M. Da Cunha Belo, A. M. P. Simoes, and M. G. . Ferreira, "Semiconducting Properties of Passive Films Formed on Stainless Steel," *J. Electrochem. Soc.*, vol. 145, no. 11, pp. 3821–3829, 1998.

[143] N. E. Hakiki, M. F. Montemor, M. G. S. Ferreira, and M. da Cunha Belo, "Semiconducting properties of thermally grown oxide films on AISI 304 stainless steel," *Corros. Sci.*, vol. 42, no. 4, pp. 687–702, 2000.

[144] B. Lovrecek and J. Sefaja, "Semiconducting aspects of the passive layer on chromium," *Electrochim. Acta*, vol. 17, no. 6, pp. 1151–1155, 1972.

[145] G. Okamoto and T. Shibata, "Stability of passive stainless steel in relation to the potential of passivation treatment," *Corros. Sci.*, vol. 10, no. 5, pp. 371–378, 1970.

[146] A. Di Paola, "Semiconductor Properties of Passive Films on Stainless Steel," *Electrochim. Acta*, vol. 34, no. 2, pp. 203–210, 1989.

[147] M. E. Curley-Fiorino and G. M. Schmid, "The Effect of the Cl Ion on the Passive Film on Anodically Polarized 304 Stainless Steel," *Corros. Sci.*, vol. 20, no. 3, pp. 313–329, 1980.

[148] J. J. Kim and Y. M. Young, "Study on the passive film of type 316 stainless steel," *Int.*

J. Electrochem. Sci., vol. 8, no. 10, pp. 11847–11859, 2013.

[149] A. M. P. Simoes, M. G. S. Ferreira, B. Rondot, and M. Cunha Belo, "Study of Passive Films Formed on AISI 304 Stainless Steel by Impedance Measurements and Photoelectrochemistry," *J. Electrochem. Soc.*, vol. 137, no. 1, pp. 82–87, 1990.

[150] Y. F. Cheng and J. L. Luo, "Electronic structure and pitting susceptibility of passive film on carbon steel," *Electrochim. Acta*, vol. 44, no. 17, pp. 2947–2957, 1999.

[151] T. L. S. L. Wijesinghe and D. J. Blackwood, "Photocurrent and capacitance investigations into the nature of the passive films on austenitic stainless steels," *Corros. Sci.*, vol. 50, no. 1, pp. 23–34, 2008.

[152] N. Li, Y. Li, S. Wang, and F. Wang, "Electrochemical corrosion behavior of nanocrystallized bulk 304 stainless steel," *Electrochim. Acta*, vol. 52, no. 3, pp. 760–765, 2006.

[153] R. De Gryse, W. P. Gomes, F. Cardon, and J. Vennik, "On the Interpretation of Mott-Schottky Plots Determined at Semiconductor/Electrolyte Systems," *J. Electrochem. Soc.*, vol. 122, no. 5, p. 711, 1975.

[154] M. A. Fusco, Y. Ay, A. H. M. Casey, M. A. Bourham, and A. L. Winfrey, "Corrosion of single layer thin film protective coatings on steel substrates for high level waste containers," *Prog. Nucl. Energy*, vol. 89, pp. 159–169, 2016.

[155] M. J. Carmezim, A. M. Simoes, M. F. Montemor, and M. Da Cunha Belo, "Capacitance behaviour of passive films on ferritic and austenitic stainless steel," *Corros. Sci.*, vol.

47, no. 3 SPEC. ISS., pp. 581–591, 2005.

[156] N. Rausch and E. P. Burte, "Thin TiO2 Films Prepared by Low Pressure Chemical Vapor Deposition," *J. Electrochem. Soc.*, vol. 140, no. 1, p. 145, 1993.

[157] F. A. Grant, "Properties of rutile (titanium dioxide)," *Rev. Mod. Phys.*, vol. 31, no. 3, pp. 646–674, 1959.

[158] H. Tang, K. Prasad, R. Sanjines, P. E. Schmid, and F. Levy, "Electrical and optical properties of TiO2 anatase thin films," *J. Appl. Phys.*, vol. 75, no. 4, pp. 2042–2047, 1994.

[159] A. Wypych, I. Bobowska, M. Tracz, A. Opasinska, S. Kadlubowski, A. Krzywania-Kaliszewska, J. Grobelny, P. Wojciechowski, A. Wypych, I. Bobowska, M. Tracz, A. Opasinska, S. Kadlubowski, A. Krzywania-Kaliszewska, J. Grobelny, and P. Wojciechowski, "Dielectric Properties and Characterisation of Titanium Dioxide Obtained by Different Chemistry Methods," *J. Nanomater.*, vol. 2014, pp. 1–9, 2014.

[160] B. Enright, C. Redmond, and D. Fitzmaurice, "Spectroscopic Determination of Flatband Potentials for Polycrystalline Ti02 Electrodes in Mixed Solvent Systems," *J. Phys. Chem*, vol. 98, pp. 6195–6200, 1994.

[161] Y. H. Shin and Y. Shimogaki, "Diffusion barrier property of TiN and TiN/Al/TiN films deposited with FMCVD for Cu interconnection in ULSI," *Sci. Technol. Adv. Mater.*, vol. 5, no. 4, pp. 399–405, 2004.

[162] S. Q. Wang, I. Raaijmakers, B. J. Burrow, S. Suthar, S. Redkar, and K. B. Kim,

"Reactively sputtered TiN as a diffusion barrier between Cu and Si," *J. Appl. Phys.*, vol. 68, no. 10, pp. 5176–5187, 1990.

[163] U.S. Nuclear Regulatory Commission, "Radioactive Waste: Production, Storage, Disposal; NUREG/BR-0216, Rev. 2." pp. 1–30, 2002.

[164] S. Radwan, L. Winfrey, and M. Bourham, "Simulation of particle impact on protective coating of high-level waste storage packages," *Prog. Nucl. Energy*, vol. 81, pp. 196–202, 2015.

[165] GroveSoftware, "MicroShield." 2012.

[166] U.S. Nuclear Regulatory Commission, "Typical Dry Cask Storage System," 2015. [Online]. Available: http://www.nrc.gov/waste/spent-fuel-storage/diagram-typical-dry-cask-system.html.

[167] F. P. Larkins, "Semiempirical Auger-Electron Energies for Elements $10 < Z < 100$," *At. Data Nucl. Data Tables*, vol. 20, no. 4, pp. 311–387, 1997.

[168] R. S. Kaundal, S. Kaur, N. Singh, and K. J. Singh, "Investigation of structural properties of lead strontium borate glasses for gamma-ray shielding applications," *J. Phys. Chem. Solids*, vol. 71, no. 9, pp. 1191–1195, 2010.

[169] T. Singh, G. Kaur, and P. S. Singh, "Study of Gamma Ray Exposure Buildup Factor for Some Ceramics with Photon Energy, Penetration Depth and Chemical Composition," *J. Ceram.*, vol. 2013, pp. 1–6, 2013.

[170] N. Singh, K. J. Singh, K. Singh, and H. Singh, "Comparative study of lead borate and bismuth lead borate glass systems as gamma-radiation shielding materials," *Nucl. Instruments Methods Phys. Res. Sect. B Beam Interact. with Mater. Atoms*, vol. 225, no. 3, pp. 305–309, 2004.

[171] H. Kumar and T. Singh, "Vanadium Compounds : As Gamma Rays Shielding Material," *Asian J. Eng. Appl. Technol.*, vol. 1, no. 2, pp. 53–58, 2012.

[172] M. H. Kharita, R. Jabra, S. Yousef, and T. Samaan, "Shielding properties of lead and barium phosphate glasses," *Radiat. Phys. Chem.*, vol. 81, no. 10, pp. 1568–1571, 2012.

[173] N. Chanthima and J. Kaewkhao, "Investigation on radiation shielding parameters of bismuth borosilicate glass from 1 keV to 100 GeV," *Ann. Nucl. Energy*, vol. 55, pp. 23–28, 2013.

[174] C. Bootjomchai, J. Laopaiboon, C. Yenchai, and R. Laopaiboon, "Gamma-ray shielding and structural properties of barium-bismuth-borosilicate glasses," *Radiat. Phys. Chem.*, vol. 81, no. 7, pp. 785–790, 2012.

[175] GroveSoftware, "MicroShield." 1998.

[176] J. S. Lee, "Operation and Maintenance of Spent Fuel Storage and Transportation Casks/Containers," 2007.

[177] E. S. A. Waly, M. A. Fusco, and M. A. Bourham, "Gamma-ray mass attenuation coefficient and half value layer factor of some oxide glass shielding materials," *Ann. Nucl. Energy*, vol. 96, pp. 26–30, 2016.

[178] B. . Gonzalez, C. S. . Castro, V. T. . Buono, J. M. . Vilela, M. . Andrade, J. M. . Moraes, and M. . Mantel, "The influence of copper addition on the formability of AISI 304 stainless steel," *Mater. Sci. Eng. A*, vol. 343, pp. 51–56, 2003.

[179] R. S. Kaundal, S. Kaur, N. Singh, and K. J. Singh, "Investigation of structural properties of lead strontium borate glasses for gamma-ray shielding applications," *J. Phys. Chem. Solids*, vol. 71, no. 9, pp. 1191–1195, 2010.

[180] K. J. Singh, N. Singh, R. S. Kaundal, and K. Singh, "Gamma-ray shielding and structural properties of PbO-SiO2 glasses," *Nucl. Instruments Methods Phys. Res. Sect. B Beam Interact. with Mater. Atoms*, vol. 266, no. 6, pp. 944–948, 2008.

[181] Y. Cheng, H. Xiao, W. Guo, and W. Guo, "Structure and crystallization kinetics of PbO-B2O3 glasses," *Ceram. Int.*, vol. 33, no. 7, pp. 1341–1347, 2007.

[182] I. Akkurt, H. Akyildirim, B. Mavi, S. Kilincarslan, and C. Basyigit, "Gamma-ray shielding properties of concrete including barite at different energies," *Prog. Nucl. Energy*, vol. 52, no. 7, pp. 620–623, 2010.

[183] I. Akkurt, H. Akyildirim, B. Mavi, S. Kilincarslan, and C. Basyigit, "Radiation shielding of concrete containing zeolite," *Radiat. Meas.*, vol. 45, no. 7, pp. 827–830, 2010.

[184] A. M. El-Khayatt, "Radiation shielding of concretes containing different lime/silica ratios," *Ann. Nucl. Energy*, vol. 37, no. 7, pp. 991–995, 2010.

[185] O. Gencel, A. Bozkurt, E. Kam, and T. Korkut, "Determination and calculation of

gamma and neutron shielding characteristics of concretes containing different hematite proportions," *Ann. Nucl. Energy*, vol. 38, no. 12, pp. 2719–2723, 2011.

[186] D. Rezaei Ochbelagh, S. Azimkhani, and H. Gasemzadeh Mosavinejad, "Effect of gamma and lead as an additive material on the resistance and strength of concrete," *Nucl. Eng. Des.*, vol. 241, no. 6, pp. 2359–2363, 2011.

[187] S. J. Stanković, R. D. Ilić, K. Janković, D. Bojović, and B. Lončar, "Gamma radiation absorption characteristics of concrete with components of different type materials," *Acta Phys. Pol. A*, vol. 117, no. 5, pp. 812–816, 2010.

[188] O. W. Hermann and R. M. Westfall, "ORIGEN-S: SCALE system module to calculate fuel depletion, actinide transmutation, fission product buildup and decay, and associated radiation source terms," 1984.

[189] "U.S. EPR Final Safety Analysis Report, Section 12.3: Radiation Protection Design Features," 2007.

[190] "Design Control Document for the US-APWR - Chapter 12: Radiation Protection," 2007.

[191] "AP1000 Design Control Document, Section 12.3: Radiation Protection Design Features," 2007.

[192] A. D. Oliveira and C. Oliveira, "Comparison of deterministic and Monte Carlo methods in shielding design," *Radiat. Prot. Dosimetry*, vol. 115, no. 1–4, pp. 254–257, 2005.